SEISMIC ANALYSIS OF KNEE ELEMENTS FOR STEEL FRAMES

by

Denis Emile Clément

A Thesis submitted for the Degree of Doctor of Philosophy
at the University of Oxford

Lincoln College

Trinity Term, 2002

Abstract

Seismic design of knee elements for steel frames

Denis Emile Clément

Lincoln College

A Thesis submitted for the Degree of Doctor of Philosophy

at the University of Oxford

Trinity Term, 2002

The 1994 Northridge and 1995 Kobe earthquakes, which were moderate in seismological terms, showed that many buildings were subjected to demolition or very expensive repairs because of severe damage in principal members, mainly in the column-beam connections. As a result, the development of dissipative systems was encouraged, which limit the damage parts to easily replaceable elements, in case of moderate earthquakes. One such system is the knee braced frame. Knee braced frames are a modified form of cross bracing in which the brace is cut short and connected to the mid point of a knee element spanning between the adjacent beam and column. The key component is the knee element, which controls both the initial elastic stiffness of the frame, and the onset of yield and subsequent energy dissipation. The knee elements are required to ensure energy absorbtion through repeated large deformations without suffering collapse or instability. This thesis describes the development of different knee element designs and their performance assessments. It is shown that the dissipative mechanism of the web yielding in shear is advantageous because it is independent of the moment distribution and it does not affect the connections and extends the dissipative zones to all its length. Extensive finite element modelling and experimental testing have been undertaken. In the shear yielding mode excellent performance was achieved using standard hot rolled sections, modified by the addition of web stiffeners to prevent localised buckling failure. Weakening of the knee

element's web so that it yields very early in an earthquake has potential benefits, but is shown to be unsafe as it promotes premature failure of the element. A knee element model for non-linear dynamic analysis of an entire building has been developed. Time-history analyses showed that knee braced frames with the developed knee element have a large global ductility and an outstanding performance. Results obtained with different pushover analysis methods (Eurocode 8, FEMA-356 and ATC-40) have been compared to those obtained with the time history analyses. Moreoverhe FEMA-356 method, which includes a more accurate representation of the structure's significant post-yield stiffness, gave the closest agreement with the time history analyses and is recommended for the design of knee braced frames.

Dedication

"The weakest link in a chain is the strongest because it can break it"

Stanislaw J Lec

I dedicated this thesis to my parents, for their love, support and their encouragement.

23^{th} July 2002, Denis Emile Clément

Acknowledgements

I would like to express my gratitude to my supervisors Dr Martin S Williams and Dr Anthony Blakeborough for their invaluable support and precious advice during this research project. I would like to thank Professor Edmund Booth for the stimulating discussion and his advice on seismic provisions. I am grateful to Professor Mike Brady and Dr Kostas Marias for their help and advice in image processing. I would like to thank Clive Baker for his essential technical help concerning the experimental testing.

I would like to thank Corus for providing me generously with hot rolled sections for the knee elements.

I would like to thank the Swiss national Fund (FNRS), the ACUBE Fund of the A^3E^2PF Lausanne and the Engineering and Physical Science Research Council U.K. (EPSRC) for their financial support.

Contents

Symbols

Latin lower case letters

a	Width
a_g	Ground acceleration
b	Spacing, Width
c	Constant, Damping
c_p	Specific heat
d	Hole diameter, Depth between fillet, Lever arm
d_r	Interstorey drift
e	Edge distance
f	Flexibility coefficient, Frequency
g	Gravitation acceleration, Uniformly permanent force
h	Height
k	Stiffness, Conductivity
l	Length
m	Mass, Fatigue parameter
n	Number, Fatigue parameter
p	Power density
q	Behaviour factor (Force)
q_e	Displacement behaviour factor
q_u	Behaviour factor for equivalent system, (Force)
r	Radius, Root radius
t	Web thickness, Time
u	Temperature, Displacement
x	Horizontal direction, Horizontal displacement

w Deflection, Distributed load, Energy density

y Vertical direction, Vertical displacement

z Longitudinal direction

Latin upper case letters

A Area, Accidental action, Wave amplitude, Acceleration

B Width

C Damping coefficient, Constant

D Depth, Damage index, Displacement

E Elastic modulus, Seismic action effect

F Force

G Shear modulus, Permanent action, Spectral density function

H Height, Warping constant, Energy

I Second moment of area, Intensity function

J Torsional constant

K Stiffness

L Length, Span

M Moment, Mass

N Axial force, Number

P Concentrated load, Pixel

Q Variable action, Equivalent temperature variation due to heat generation

R Reaction force, Radius, Behaviour factor

R_d Design value of resistance

S Shear force, Spectral response, Soil parameter

T Temperature, Thickness of flange, Period, Time

$\tilde{T}$ Transform function

U Energy

V Voltage, Volume

Z Section modulus

Greek lower case letters

α Angle of knee element, Mass damping factor

α_{SH} Strain hardening ratio

β Angle of brace, Stiffness damping factor

γ Angle, Importance factor, Criteria percentage

δ Displacement, Deflection

ε Strain

ζ Normalised deformation, Criteria percentage

η Damping correction factor, Energy ratio, Combination coefficient

θ Rotation

κ Heat diffusion constant

λ Seismic corrective factor, Slenderness factor, Yield-strain proportional factor

μ Ductility

ν Poison ratio, Serviceability reduction factor

ξ Damping ratio

π Pi

σ Stress

τ Shear stress

φ Angle, Combination factor

χ Remaining strength capacity ratio

ϕ Phase angle

ω Frequency, Energy density

Greek upper case letters

Γ Transformation factor

Φ Mode shape, Displacement vector

Ψ Combination factor

Subscripts

a	Acceleration
b	Shear base
cr	Critic
d	Displacement, Design
e, el	Elastic
epp	Elastic-perfectly-plastic
eq	equivalent
f	Failure
fl	Flange
i	Initial
l	Lateral
m	Mechanism, Mean
n	Control node
p, pl	Plastic
r	Redundancy, Residual
rot	Rotation
s	Overstrength, Seismic, Stabilised
t	Tension, True, Target
ts	Tensile
u	Ultime
w	Web
y	Yield
H	Hole
I	Input
K	Kinematic
L	Left
R	Right, Row
S	Shear
VM	Von Mises

Convention

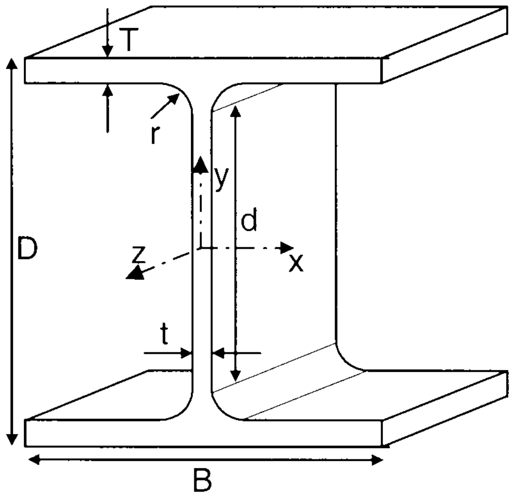

Abbreviations

Structural elements and systems

B	Beam
BS	Bracing system
CBF	Concentrically braced frame
EBF	Eccentric braced frame
KBF	Knee braced frame
KE	Knee element
$MDOF$	Multiple degree of freedom
MRF	Moment resisting frame
$SDOF$	Single degree of freedom

Sections

RHS	Rectangular hollow section
SHS	Square hollow section
UB	Universal beam
UC	Universal column

Knee element specimens

$\{UB; UC\}$ + weight per meter + $\{F; H, N, P\}$ + {number;-}

UB	Universal beam section
UC	Universal column section
F	With full stiffeners (followed by the number of stiffeners)
H	With holes (followed by the hole diameter in mm)
N	Normal, unaltered, without holes or additional stiffeners
P	With partial stiffeners (followed by the number of stiffeners)

Chapter 1

Introduction

1.1 Background

A significant fraction of the world's population is living in regions of known seismic hazard. This number is increasing because of the rapid growth of cities and mega-cities situated in seismic areas. Economic, educational, cultural and other attractions prevail over the seismic danger. In the last 100 years, with the exception of the 1923 Tokyo and the 1976 Tangshan earthquake, big cities have not suffered from strong earthquakes (magnitude>7). Unfortunately this may not last.

Strong economic pressure keeps the price for a seismic design only a few percent higher than for a standard structure. It is incumbent therefore on the engineer to develop economical seismic designs.

In the 1994 Northridge and 1995 Kobe earthquakes, most structures built after 1980 did not collapse and successfully fulfilled the prime requirement to preserve human life, but a large number of buildings that had survived the earthquake without collapsing had to be demolished or were subject to expensive repairs (Bertero et al. 1994, Blakeborough et al. 1997, Burdekin 1996, 1997, Chandler and Pomonis 1997, Holmes and Sommer 1996). The direct costs (indirect costs such as loss of business and production being excluded) were for the Northridge earthquake around \$16 billion and for the Kobe earthquake around \$100 billion. These earthquakes were in seismological terms not large for these regions; for example, in Japan, inland earthquakes of magnitude 7 and larger have occurred six times in the last 100 years (FEMA, 2002). There is need to develop structures that not only survive the strongest expected earthquake of the area without collapsing, but also suffer very limited or no damage in earthquakes with larger probability of occurrence in the structure's life.

These principles are reflected in the latest draft of Eurocode-8 (2001):

1. No collapse requirements

   The structure shall be designed and constructed to withstand the seismic design action (of a 475 years return period seismic hazard), without local and global collapse, thus retaining its structural integrity and a residual load bearing capacity after the seismic events.

2. Damage limitation requirements

   The structure shall be designed and constructed to withstand the seismic design action (of a 95 years return period seismic hazard), without the occurrence of damage and the associated limitation of use, the costs of which would be disproportionately high in comparison with the costs of the structure itself.

These guidelines are valid only for ordinary structures (e.g. apartments and offices). Structures for public use (e.g. stadiums), emergency utilities (e.g. hospitals) and industry with potential risks (e.g. nuclear powerstations) have to satisfy stricter design requirements.

An earthquake with more than 10% probability of exceedence in 10 years includes earthquakes with a return period ranging up to 95 years. An earthquake with more than 10% probability of exceedence in 50 years includes earthquakes with a return period ranging up to 475 years.

The design seismic action is generally selected on the basis of a chosen return period and need not coincide with the maximum event that may occur at a given site. The Eurocode-8 (2001) assumes that through proper selection of the value of the return period and proper calibration of the design procedure and associated safety elements, the target probability of failure is satisfied.

1.2 Different strategies for seismic design

To design a structure to resist earthquakes purely in the elastic range is not viable. Different strategies to resist earthquake have been elaborated. The main four strategies are:

1. Isolate the structure from the ground motion.
2. Include an active system that compensates or cancels out the effect of the earthquake.
3. Include tuned vibration absorbers which will absorb most of the energy.
4. Include energy absorbing features which damp the structure.

1.2.1 Isolation of structure

A seismic isolation system essentially decouples the structure from potentially damaging earthquakes and consists of supports that are very flexible or have sliding and friction properties (Figure 1-1). To avoid movements due to wind, horizontal supports may be added to the structure. During an earthquake these supports, which have a brittle failure at a specific horizontal load, will give way and allow the structure to be decoupled. Appropriate damping may also be provided to reduce the relative movements. The structure has to sustain only small oscillations, which are induced by the friction and the damping.

Base isolation suits only for free standing buildings and important gaps (up to 800mm for very seismic areas) must be kept free of any obstruction. The sliding or friction properties have to be maintained to assure the reliability of the system.

Many installations have been made in buildings and on bridges, where the isolation is placed generally on the top of the piers.

1.2.2 Active systems

Active systems are powered control systems, which reduce the response of structures. Figure 1-2 shows a flow diagram of active systems (Symans and Constantinou 1998). In general such systems are complex and need power that must be secured during the earthquake.

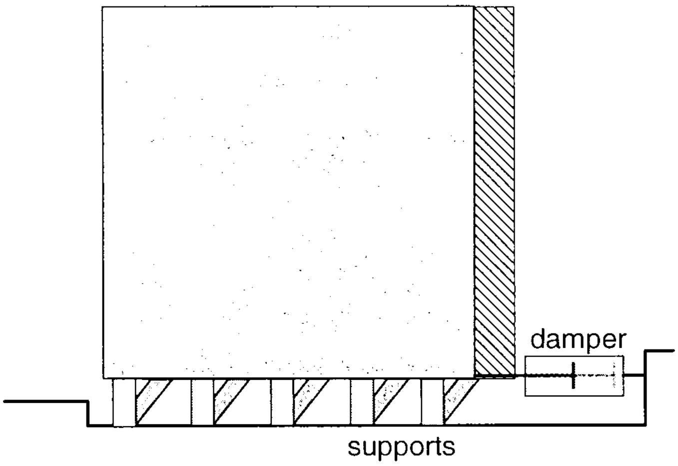

Figure 1-1: Structure mounted on a base isolation system coupled with a damper

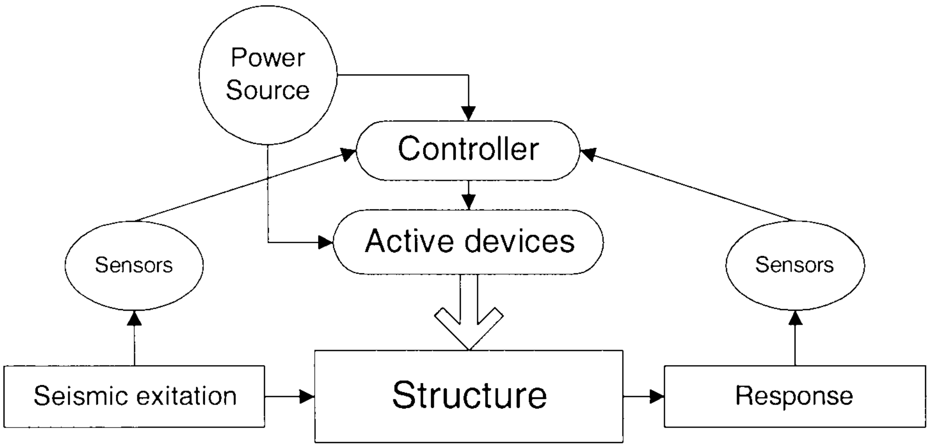

Figure 1-2: Diagram of active system

Active tendon mechanisms (ATMs) and active tuned mass dampers (ATMDs) are examples of active systems.

The ATMs are composed of prestressed tendons connected to servo-hydraulic actuators. An algorithm controls the actuators in response to measured data and stored optimised reaction schemes (Agrawal et al. 1994).

ATMDs are composed of a mass, which is driven with large accelerations so that the reaction to its inertia forces tends to cancel the effects of the earthquake. In practice this system is limited in size (Chang and Yang 1995).

Ensuring the stability of the control algorithms, the reliability of the actuators and the efficiency of active systems is a very difficult task. For the moment, active systems do not seem very appropriate as seismic protection, although they are successfully used to reduce oscillations due to wind.

1.2.3 Tuned vibration absorbers

Tuned vibration absorbers consist of mass-spring-dashpot systems which are tuned to a frequency lower than the principal structural frequency, (Figure 1-3 a).

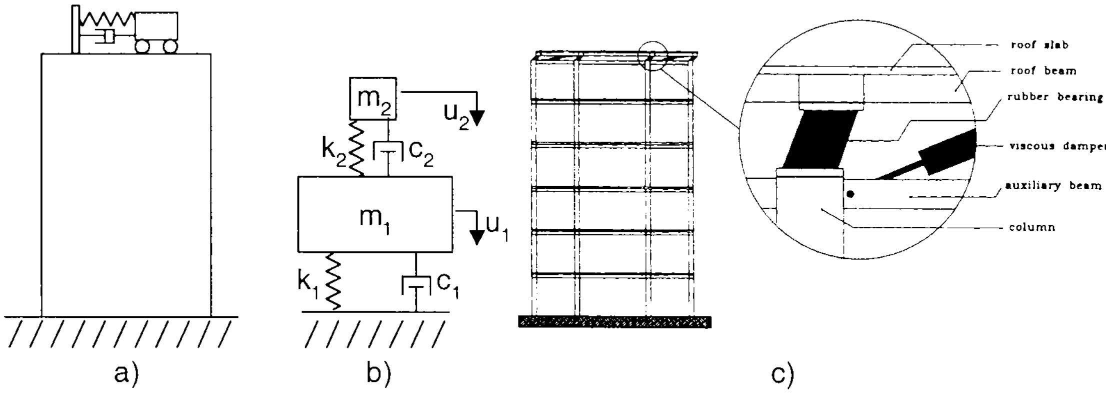

Figure 1-3: Tuned vibration absorbers

The added mass changes the structure's modeshape so that it attracts most of the energy released by the earthquake, by undergoing large movements. The simplest model, for a structure with a tuned vibration absorber is a two degree of freedom system, Figure 1-3 b). If the damping of the structure is zero, then the optimum frequency ratio of the tuned vibration absorber $f_{2.opt}$ and the optimum damping $\xi_{2.opt}$, for reducing the structure displacement u_1, are given by Equation 1.1. For value of $\xi_1 \neq 0$, $f_{2.opt}$ will be smaller than in the case $\xi_1 = 0$.

$$f_{2.opt} = \frac{1}{1 + m_2/m_1} \quad \text{and} \quad \xi_{2.opt} = \sqrt{\frac{3m_2/m_1}{8(1 + m_2/m_1)^3}} \tag{1.1}$$

This system is widely and successfully used in footbridges (Bachmann and Weber 1995). For buildings, very large masses (m_2) and displacements (u_2) are required to reduce the structure displacement (u_1) to an acceptable level. This may occupy a lot of space. The aseismic roof system (Figure 1-3 c) is a way using of the roof as a tuned vibration absorber (Villaverde 1999).

1.2.4 Damped structures

The basic energy relationship of the structure is represented by (Filiatrault and Cherry 1990):

$$H_I = H_K + H_S + H_\xi + H_H \tag{1.2}$$

H_I is the earthquake input energy, H_K is the kinematic energy of the structure, H_S is the elastic strain energy in the structure, H_ξ the viscous damping energy and H_H the hysteretic damping energy. By increasing H_H or H_ξ, for a given H_I, the elastic strain in the structure is decreased.

Incorporating viscous damping (adequately designed and placed) in the structure reduces the lateral displacement and the base shear during an earthquake (Chang et al. 1995). Hysteretic damping is obtained by a non-linear response of structural elements, presenting cyclic hysteretic curves in their force-displacement diagram. The capacity of structural systems to resist seismic action in the non-linear range permits, in general, a design for forces much smaller than those corresponding to linear elastic response.

Elements that provide the structure with viscous damping or hysteretic damping are called dissipative elements. These may be friction devices, solid visco-elastic devices, fluid viscous devices or hysteretic structural dampers. Hysteretic structural dampers use directly the plastic deformation capacity of the material they are made of to contribute to the process of energy absorption. Steel and alloys can sustain significant plastic deformation before they fail. A hysteretic structural damper can be any structural element that can show a stable post-elastic behaviour; for example, a steel beam developing a stable plastic hinge or a well designed and detailed reinforced concrete flexural beam allowing the reinforcement bars to yield without brittle failure or concrete crushing. Eccentrically braced frames, moment resisting frames and knee braced frames are designs in which structural elements can act as efficient hysteretic structural dampers. Some designs may require large lateral drift to allow the cyclic yielding of the dissipative zones to develop, resulting in important non-structural damage. Other designs do not lend themselves to using the hysteretic properties of their structural elements. A review of a selection of passive damping systems is presented in chapter 2.

1.3 Scope of the research

The present thesis concerns the development of knee bracing system for steel frames. Knee bracing is a form passive damping that combines the advantages of low cost, providing ductility, restricting the damage to the small elements called knees (which are the key elements of the structure) and offering the possibility to replace the damaged elements relatively easily. The knee element, despite being the key element, has been paid little attention until now and therefore the focus of the current research.

In Chapter 2 different passive damping systems are discussed and the advantages of knee bracing are highlighted. In Chapter 3 an analytical study is then performed and the characteristics that the knees should possess to provide the frame with the adequate stiffness, energy dissipation and ductility, are listed. Different plastic mechanisms for the knee element are presented and arguments in favour for the shear mode mechanism are put forward. The hot rolled sections that are the most likely to develop the dissipating mechanism and possess high endurance are identified. Different knee element designs which consist of modified hot rolled sections are proposed and their performance evaluated with finite element analysis. The choice of the specimens for physical testing are given. In Chapter 4 the test set up, comprising among others the development of a thermal imaging camera analysis method and the calibration of novel loadcells are presented. In Chapter 5 the results of the physical testing are presented, the performance and characteristics assessed, weaknesses identified and the "best" design determined. In Chapter 6 extensive finite element analysis has been performed under both monotonic and cyclic loading. The sensitive parameters, the details that need to be included, the accuracy and the limitations of the finite element analysis have been identified. Finally, in Chapter 7, the knee element behaviour was modelled in a non-linear model in order to perform push-over analysis (static analysis) and time history analysis (dynamic analysis) of a whole building. For that purpose a 5-storey building example containing knee braced frames was designed and its performance assessed. Since the present research leaves some questions unanswered, suggestions of future work is given after the final conclusions.

Chapter 2

Review of passive systems and of design procedures

2.1 Introduction

The four principal ways to design against earthquake damage are: base isolation, active systems, tuned vibration systems and passive damping systems. The passive damping system is the most suitable for ordinary structures. Base isolation is very effective but expensive and only applicable to free standing structures. Active systems are extremely complex for seismic protection and their reliability can be questionable. Tuned vibration absorbers require enormous moving masses and places to situate them. A large number of passive damping systems exist and a review of some of them is presented in this Chapter. The list of dampers presented has no ambition to be exhaustive.

Particular attention is given to hysteretic structural dampers which have the advantages of simplicity and minimal maintenance requirements. The characteristics of structures containing hysteretic structural dampers are analysed and knee bracing is identified as a particularly attractive form of hysteretic damper. Lastly, it is explained how codes and especially Eurocode-8 (2001) treat the design of hysteretically damped steel structures (or non-linear structures).

2.2 Friction, solid visco-elastic and fluid viscous dampers

2.2.1 Visco-elastic Dampers

Probably the simplest visco-elastic damper is composed of layers of visco-elastic material, usually polymers (e.g. acrylic copolymer), deforming in shear, Figure 2-1.

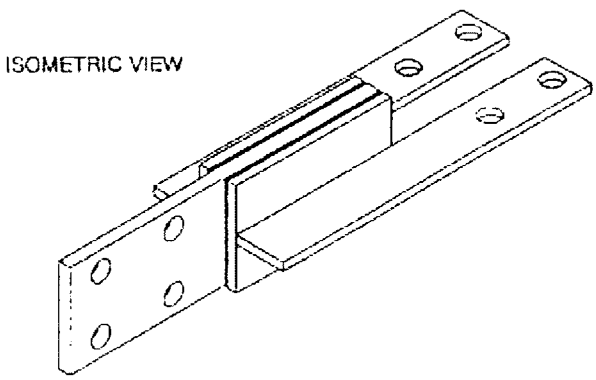

Figure 2-1: Viscoelastic damper composed of n layers of viscoelastic material

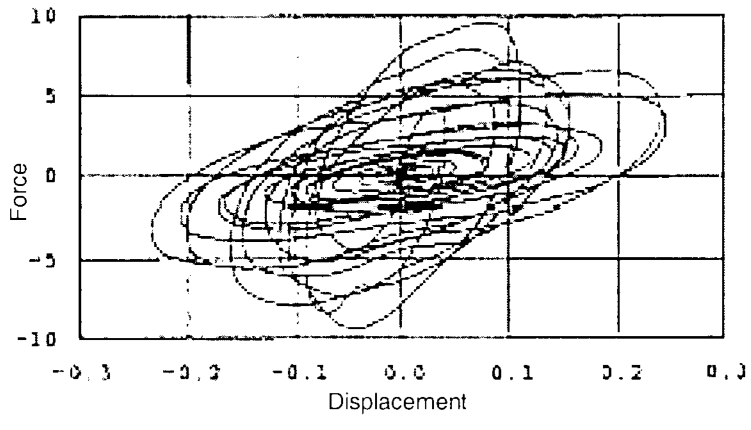

Figure 2-2: Hysteresis loops of a viscoelastic dampers

Visco-elastic dampers have no threshold or activation force level, and thus they dissipate energy for all levels of earthquake excitation. They exhibit elliptical hysteresis loops, as in the example shown in Figure 2-2, which is typical of materials with velocity-dependent properties.

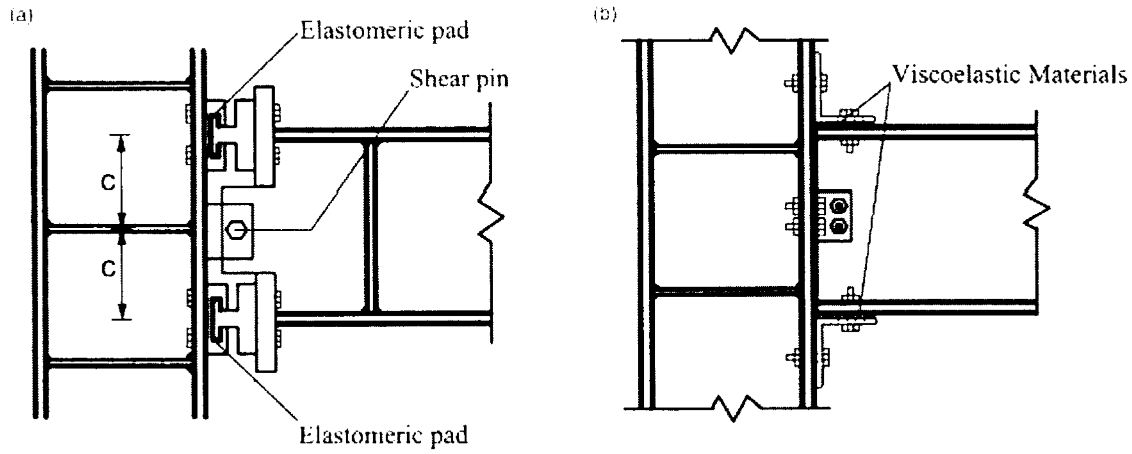

Figure 2-3: Beam column connection with energy dissipation devices. (a) Elastomeric pad and (b) viscoelastic materials. (Xu and Zhang 2001)

Visco-elastic dampers can be easily placed at the end of a single diagonal brace. They have been used in a number of structural applications. Chang et al. (1995) has analysed behaviour of visco-elastically damped structures and Shukla and Datta (1995) has worked on optimisation of their use in buildings for seismic design.

Xu and Zhang (2001), has proposed bolted non-linear semi-rigid beam-column connections, using two elastomeric pads and a shear pin, Figure 2-3 (a), or placing two visco-elastic materials between the beam flanges, Figure 2-3 (b). These non-linear semi rigid connections, can be tuned to increase the global vibration energy absorbtion.

2.2.2 Fluid viscous dampers

Fluid viscous dampers have found numerous applications in shock and vibration isolation systems (Large fluid dampers were used to reduce the recoil of large canons, for automotive suspensions, etc.). In seismic design, they have been incorporated in base isolation systems, in roof isolation systems and in braced framed structures.

A passive fluid viscous damper can be built from just a hydraulic cylinder with a piston. By adding a controllable by-pass valve, Figure 2-4, fast modulation of the damping coefficient can be obtained. This modulation can be coupled to the motion of the structure itself in order to obtain a semi-active device (Gavin et al. 2001).

Magnetorheological fluid changes its properties in the presence of a magnetic field.

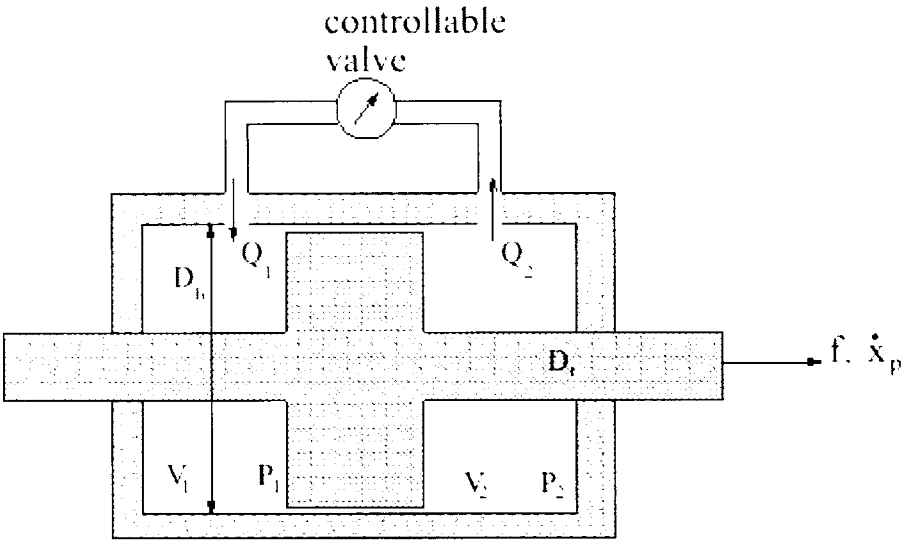

Figure 2-4: Semi-active fluid viscous damper

Electrorheological fluid changes its properties in the presence of a electric field. Both changes take place in a matter of milliseconds. Using one of these liquids in a fluid damper, allows one to modify its characteristics in real time to adapt to changing excitation (Ehrgott and Masri 1993, Johnson et al. 1998).

2.2.3 Friction dampers

Friction dampers, in contrast to visco-elastic dampers, are not activated for forces less than a threshold which corresponds to the slip force. They usually show extremely regular and repeatable behaviour. The slip load, even during an earthquake, shows no noticeable variation. Their force-displacement response is independent of the loading frequency. Pall and March (1982) have proposed to add friction devices to improve the dissipation capacity of X-concentrically braced frames. The friction device is shown in Figure 2-5, and consists of four hinged links arranged to form a quadrilateral shape, and of two diagonal links also hinged at the joints which are connected externally to the diagonal braces.

The diagonals of the quadrilateral are made of two separate parts which are partially superimposed by mean of a friction brake joint located in the middle. For a lateral force F_1 the braces in compression reach their buckling load P_{cr}, while the brace in tension

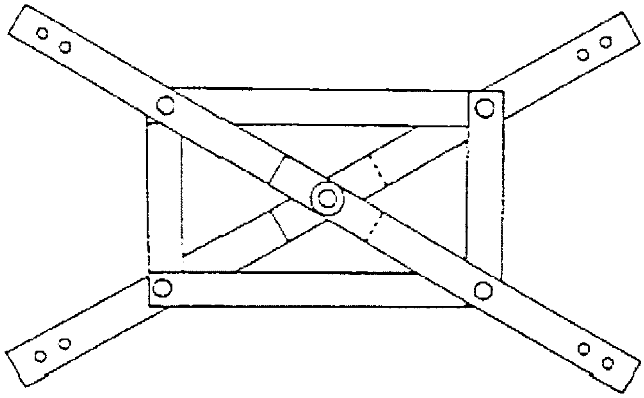

Figure 2-5: Pall friction devise

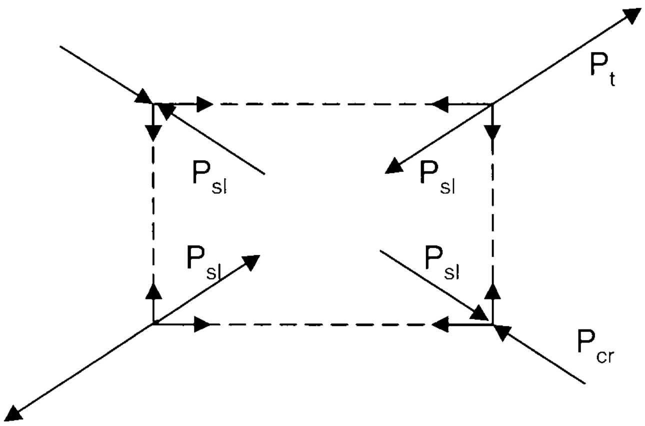

Figure 2-6: Distribution of forces at slippage phase of both joints in a friction dampers

remains elastic. With further increase of F, the critical slip load will be reached for the diagonal link in tension only (the force in the compression braces remains constant after having reached the buckling load). With further increase of F the force in the compression links increases (force transmitted through the vertical and horizontal links as shown in Figure 2-6) and eventually reaches the critical slip load.

The performance of this friction device in a X-concentrically braced frame have been examined by Colojanni and Papaia (1993). They realised that optimising the design is not a easy task and furthermore that design criteria cannot be generalised.

Slotted bolted connections, as seen in Figure 2-7, consist of a main connecting plate with elongated holes parallel to the line of loading placed between two outer members. A

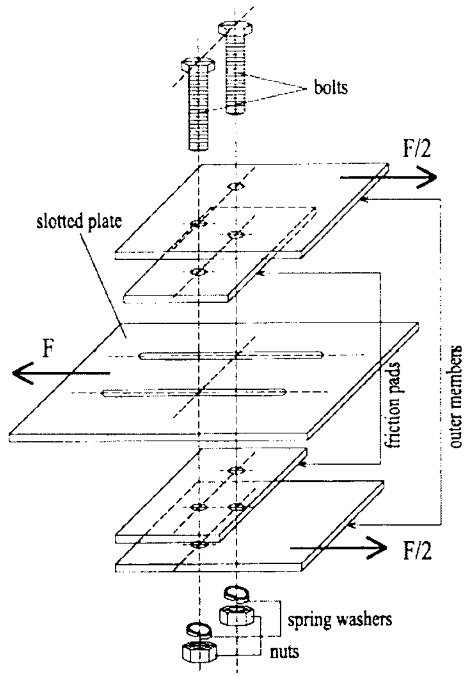

Figure 2-7: Slotted bolted connection

friction lining pad is sandwiched between each outer member and the main plate. When the tensile or compression force applied to the connection exceeds the limiting frictional forces, the slotted plate slips relative to the lining pads. Energy is dissipated by means of friction between the sliding surfaces (Balendra et al. 2001). Slotted bolted connections can be placed at the end of a single diagonal bracing or as part of a chevron bracing system (Giacchetti et al. 1989).

Many friction devices exist, which have been used in a wide range of structural applications. Some devices even come from other engineering fields (for example, Sumitomo Metal Industry developed a friction device for seismic design which was originally a shock absorber in railway rolling stock).

2.3 Steel hysteretic dampers

Steel possesses real advantages for seismic designs, attributable to its ductility and its cyclic strength. Steel, if protected from corrosion, does not change its properties with time and therefore most steel hysteretic dampers do not need maintenance.

2.3.1 Torsional-Beam Steel Dampers

Torsional beam steel dampers, as shown in Figure 2-8, are used to anchor tanks. They dissipate energy through inelastic twisting of the mild-steel bar induced by vertical movement of the tank. (Malhotra 1998).

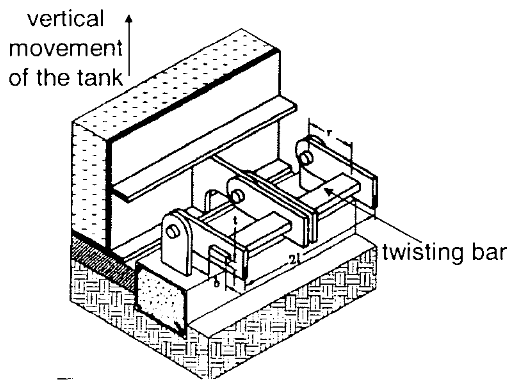

Figure 2-8: Torsional beam steel dampers (Malhotra 1998)

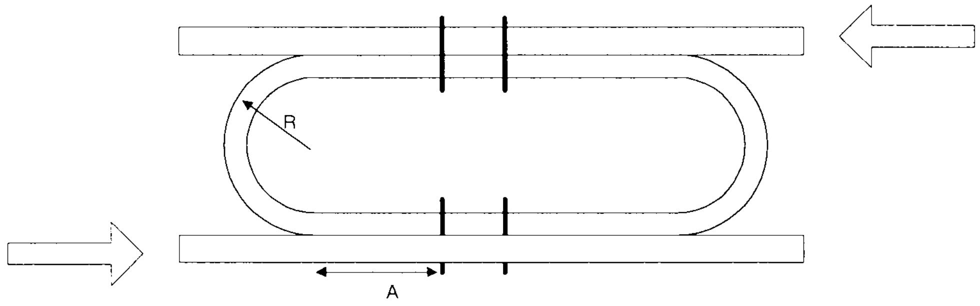

Figure 2-9: U-Element

2.3.2 U-shaped mild steel strips dampers

The rolling bending and the energy dissipating characteristic of a U-shaped mild strip, Figure 2-9, has been investigated by Aguire and Sanched (1992). They tested 38mm wide and 13mm thick strips, with an optimal value for R=45mm and A=100mm and showed that they could sustain 100 stable cycles of 25mm. The yield displacement was 3mm. U-shapes are easy to fabricate. Multiple U-shaped elements can be put in parallel to obtain higher strength. U-shaped elements can be placed at the end of a single diagonal bracing.

2.3.3 Shape memory hysteretic dampers

The shape memory effect in metals was first observed in the 1930s. In 1962, the phenomenon was observed in Nickel-Titanium ($NiTi$, or Nitinol). Shape-memory alloys have the capacity to undergo large strains and subsequently recover their initial configurations. The basis for this behaviour is that, rather than deforming in the usual manner of metals, shape-memory alloys undergo transformations from the austenitic to the martensitic crystal phase (Hodgson, 1988). Sasaki (1989), Graesser and Cozzarelli (1991) and Witting (1992) have investigated flexural, torsional, shear, axial modes and energy dissipation under seismic-type loading. The stress-induced behaviour of Nitinol, loaded in tension, is referred to as super-elasticity, which is illustrated in Figure 2-10. Aiken et al. (1993) have performed physical testing on a small-scale model with cross bracing made of pre-strained Nitinol wires. Shape memory metal are very expensive relative to common steel.

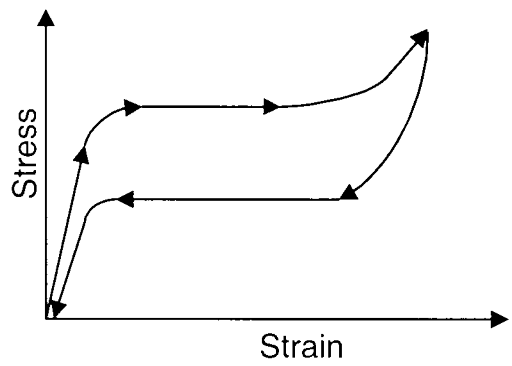

Figure 2-10: Superelastic behaviour of a shape memory metal

2.3.4 Off-centre bracing system and toggle brace damper system

The off-centre bracing system, Figure 2-11, possesses a off-diagonal eccentricity e which provides the structure with a geometrically non-linear behaviour. Placed only in the first storey it can be designed to behave like a base isolation system, with adequate reserved strength, to safeguard against instability and collapse (Moghaddam and Estekanchi

1999). Two force-displacement hysteresis curves that can be obtained for different element lengths are given in Figure 2-12.

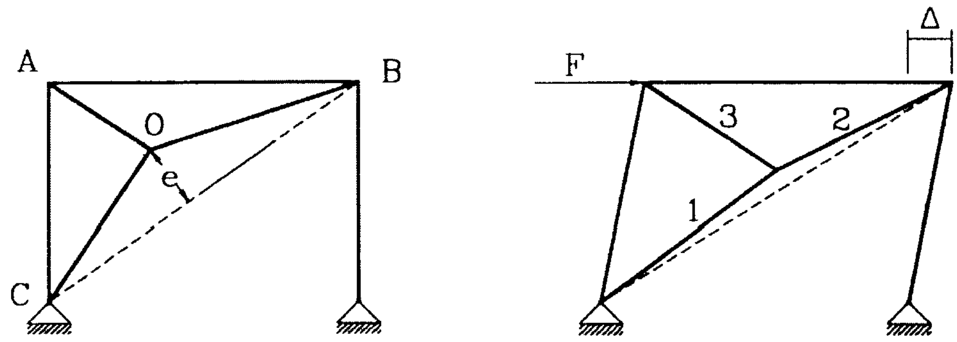

Figure 2-11: Off-centre bracing system

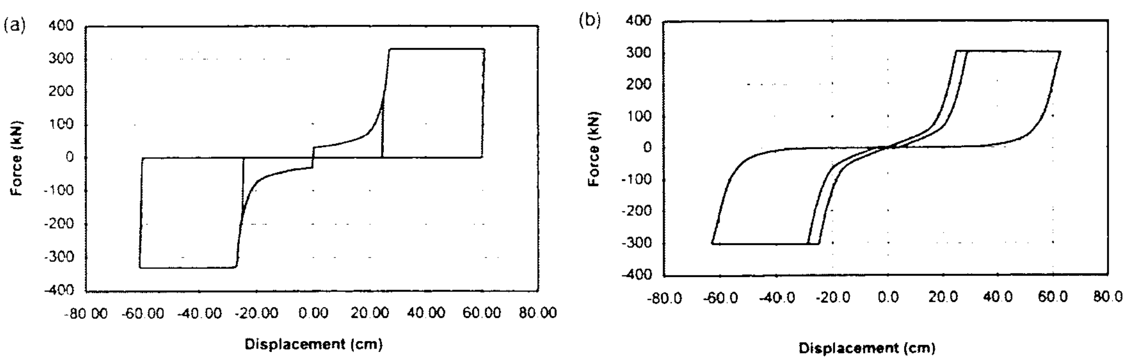

Figure 2-12: Force-displacement hysteresis curves of off-centre bracing systems

The toggle brace damper system, is an off-centre bracing system where the element 3, Figure 2-11, is replaced by a fluid viscous dampers. This configuration improves the use of fluid viscous dampers by magnifying the damper displacement and reducing the required damper force, while still producing the desired damping effect. Fluid viscous energy dissipation devices require special detailing when operating at very small strokes, which results in an increased volume of the device and thus an increase in cost (Constantinou et al., 1997).

2.3.5 Base isolator and energy dissipator

ALGA S.p.A has developed several seismic devices for bridges. One of them is a base isolator and energy dissipator. This device consists of the combination of 16 C-shaped elements with radial symmetry, allowing a uniform behaviour for an earthquake acting in any direction as shown in Figure 2-13 a). Figure 2-13 b) shows the deformed device at its maximum displacement. The energy dissipation is achieved by plastic hinges in bending in the C-shaped elements. The plastic hinges do not appear at the same time and do not have the same plastic rotations.

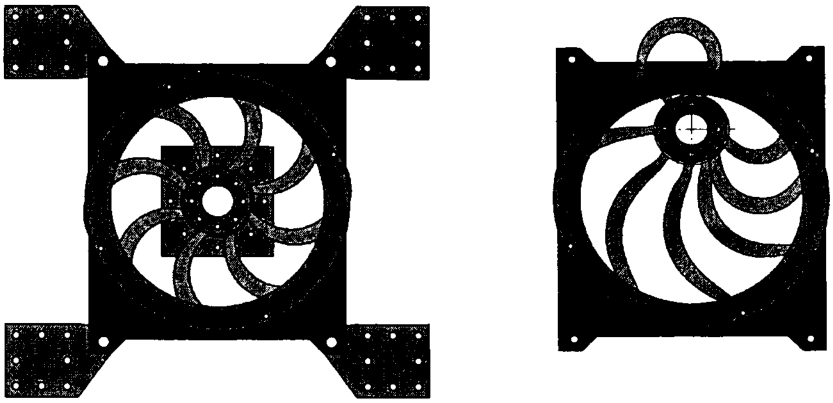

a) b)

Figure 2-13: An energy dissipator for bridges (ALGA 2001)

On the Anatolian Motorway between Düzce and Bolu in Turkey, two major viaducts have been equipped with this kind of base isolator and energy dissipator from Seismic Devices ALGA S.p.A. The devices, specially built for the applications, show stable hysteretic curves, have an ultimate displacement of ±480mm and an ultimate load of 250kN. Yielding occurs at a displacement of 38mm and a load of 155kN. The device has a ductility of $\sim$ 12.5 and a ratio F_u/F_y ≈1.6 (ALGA 2001).

The two viaducts were not far from the epicentre of the recent earthquakes that struck Turkey on 17 August and 12 November 1999 during which the hysteretic dampers performed satisfactorily (ALGA 2001).

2.3.6 Triangular-plate added damping and stiffness (TADAS)

Ductile end diaphragms have been proposed for seismic-resistant construction (Tsai et al.1993) and especially for seismic retrofit strategy to protect the substructures of existing girder bridges from damage during earthquakes (Zahrai and Bruneau,1999). The TADAS-system, Figure 2-14 a), consists of a number n of triangular plates, generally welded on a base plate bolted to the bottom beam and an upper part composed of $n+1$ thick rectangular plates attached to the braces as shown in Figure 2-14 b).

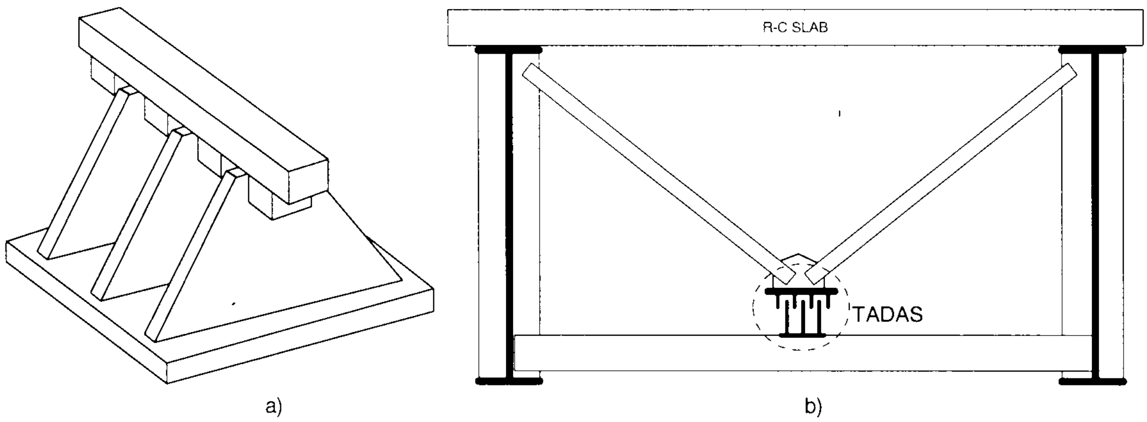

Figure 2-14: a) Details of the TADAS-device, b) Girder bridge equipped with a TADAS-device

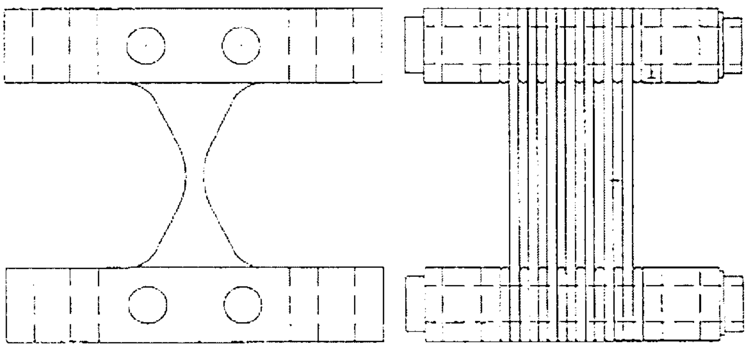

Figure 2-15: ADAS Element

When the girder is subject to lateral forces the rectangular plates come into contact with the triangular elements, which bend. There is no vertical bond between the lower and upper parts. Different gap sizes between the triangles and rectangular plates can be used to prevent simultaneous yielding. This allows the lowering of the yield load, while keeping a large residual strength capacity after yield. The TADAS devices analysed by Zahrai & Bruneau have a ductility of ~4 and a ratio F_u/F_y ≈2.2.

2.3.7 Added damping and stiffness (ADAS)

ADAS elements consists of multiple X-shaped mild steel plates in parallel between top and boundary conditions as showed in Figure 2-15. They are designed to dissipate energy through the flexural yielding deformation. Behaviour of individual ADAS elements has been studied by Whittaker et al. (1991), Fierro et al. (1993) and Tehranizadeh (2001).

2.3.8 Campenon Bernard hysteretic device

Campenon Bernard has patented an interesting hysteretic damper (Campenon Bernard 2000). The basic element consists of an elongated part, called the 'bar', that, when a lateral force is applied at its end, bends onto a rounded shaped template called the 'gabarit', Figure 2-16. The plastic hinge will first form at the base of the bar and then progressively move upwards with the bar-gabarit contact point.

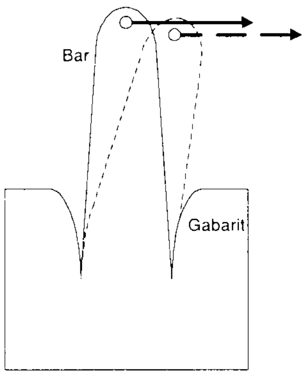

Figure 2-16: Basis element of Campenon Bernard hysteretic device

With the width b of the bar taken as constant, the horizontal force needed to bend the bar more increases, because the lever arm (the vertical distance between the contact point and the end of the bar) decreases. Figure ?? shows the force-displacement diagram for a force pulling at the end of the bar at different angles α to the horizontal ($b = 0.05m$, $\ell = 0.3m$, and the plastic strain limit $\varepsilon = 10\%$). The width b can be varied along the

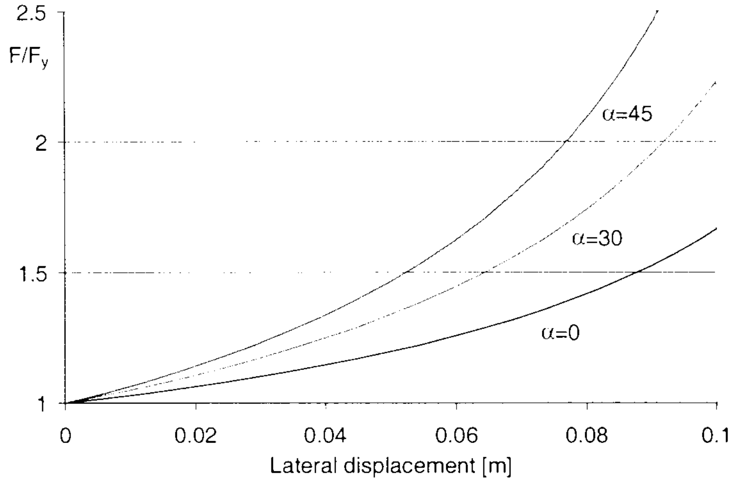

Figure 2-17: Force-displacement plot of a Campenon Bernard device

height of the bar in order to obtain the adequate force-displacement curve. The radius of the gabarit limits the plastic strain ε to a certain value. By geometrical relationships it can be easily shown that $\varepsilon = b/(2R)$. The gabarit can be given the adequate shape to keep the b/R ratio constant.

This hysteretic damper design has been used as seismic protection on the second Tagus bridge in Portugal (Capra and Wastiaux 2000), where the gabarit was built-into reinforced concrete and a UC steel section was used as the bar. The bridge deck in case of an earthquake would abut or bump against the steel column beam, which would bend and thus dissipate energy. Figure 2-18 shows two devices for application in steel buildings and Figure 2-19 shows the second of these connected to the cross-bracing of a steel frame. In these two cases the 'gabarit' and the bar are cut from a single thick plate of metal. These devices resist more then 20 cycles of the maximum amplitude allowed by the device, still showing stable hysteresis (Capra 2000). However the connection point not only moves laterally but also vertically for large displacements, and this needs to be taken into account when calculating the global frame behaviour. The previous excursions have also to be taken in account, as the deformation of the bar can take the form shown in Figure 2-20. This is an interesting development that possesses enough parameters (length, gabarit radius, width...) to vary, in order to tune and optimise its response. Fatigue and crack propagation at the end of the slot between the bar and the gabarit need to be assessed.

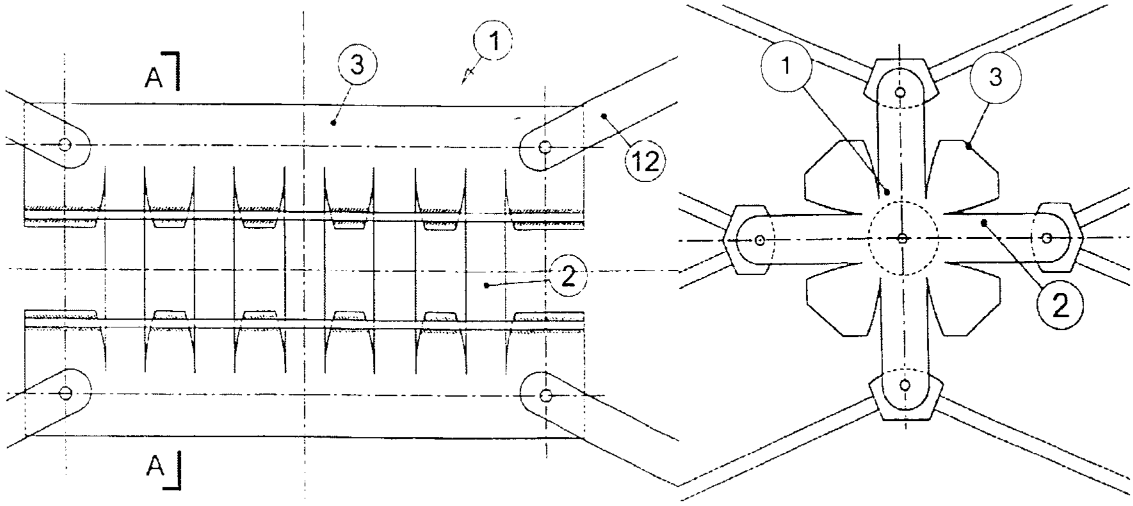

Figure 2-18: Two Campenon Bernard hysteretic dampers for steel building

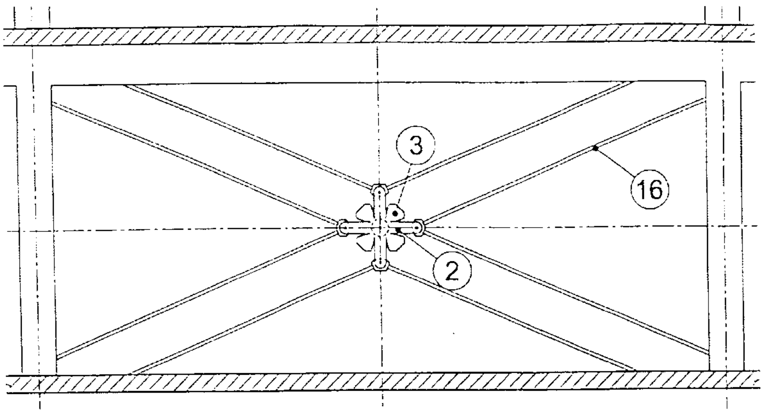

Figure 2-19: Campenon Bernard hysteretic damper in a steel frame

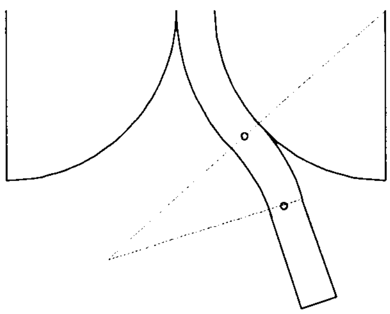

Figure 2-20: Deformation in the bar

2.3.9 Filled sections

Foam-filled sections are developed for automotive structures, where they are used to absorb impact energy during frontal collision. The presence of the foam filler changes the crushing mode of the thin-walled beam from one localized fold to multiple propagating folds. This modified mechanism prevents the drop in load carrying capacity due to the formation of more plastic hinge lines, producing a limited sectional crush. Therefore, more bending energy can be dissipated, Santosa et al. (2000). In Figure 2-21 the deformation of a non-filled section and a foam filled section undergoing the same impact is shown.

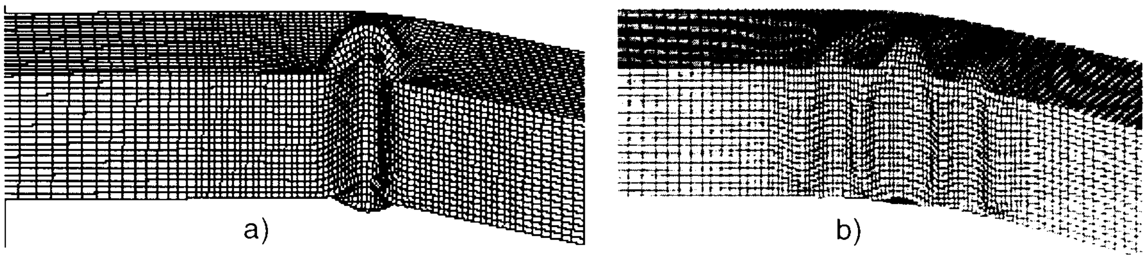

Figure 2-21: a) Non-filled section, b) foam filled section (Santosa et al. 2000)

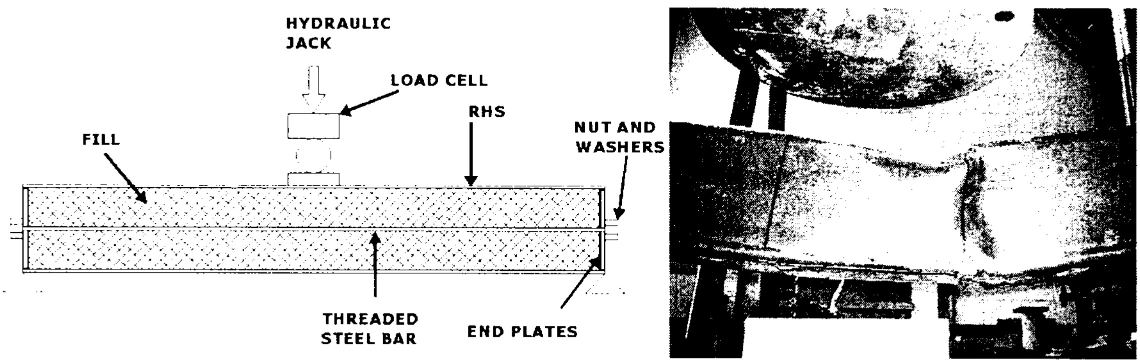

Figure 2-22: a) Testing set up and b) failure of a rectangular hollow section with confined gravel (Darby 2001)

In a similar way, energy dissipation of steel sections can be improved by filling rectangular hollow sections with a confined granular material, e.g. sand, gravel. Even for small deformation the fill material dissipates energy. The fill beneficially affects the stiffness and avoids premature local buckling (Darby 2001). Figure 2-22 shows the test set up and

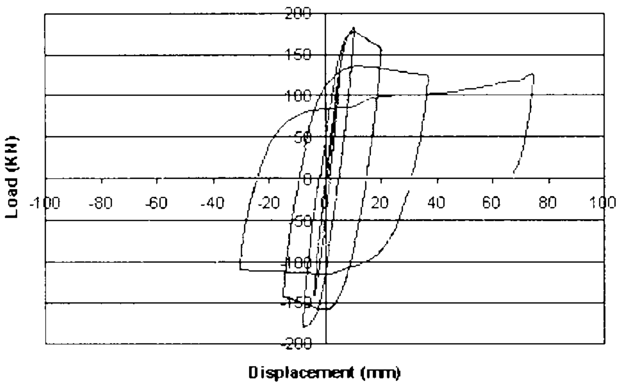

Figure 2-23: Hysteretic curves of a rectangular hollow section with confined gravel (Darby 2001)

the deformed shape of a rectangular hollow section with confined gravel and Figure 2-23 shows the hysteretic curves it has experienced.

2.3.10 Moment resisting frames

Moment resisting frames ($MRFs$) are popular for allowing a large degree of freedom for architectural planning since they do not obstruct the spaces between columns. $MRFs$ with adequate connections are able to undergo large plastic deformation and therefore dissipate large amounts of energy. However the large deformations that arise lead to excessive non-structural damage. $MRFs$ have a low lateral stiffness and their use for tall buildings is consequently uneconomic.

The 1994 Northridge and 1995 Kobe earthquakes have been destructive for many steel joints, essentially in moment frame structures. The connections were believed to be ductile and capable of withstanding the repeated cycles of large inelastic deformation. A wide spectrum of unexpected brittle fractures did occur at the connections, ranging from minor cracking, to large fractures extending across the full depth of the columns, (Bertero et al. 1994, Tsai et al. 1995, Holmes and Sommer 1996, BRI 1996, Burdekin 1997, Miller 1998, Popov et al. 1998, Chandler and Lam 2001). The remedy to improved local ductility consisted in forcing the development of plastic hinges in beams of moment frames to take place away from the columns and the beam joints, by either a connection strengthening (Figure 2-24) or beam weakening (Figure 2-25).

Unfortunately connection strengthening, while guaranteeing high ductility, is quite

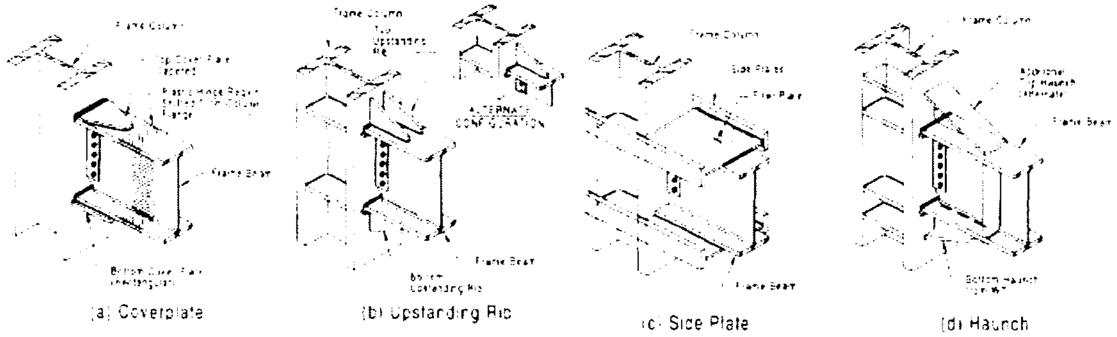

Figure 2-24: Example of reinforced moment connections (After Engelhardt and Sabol 1998)

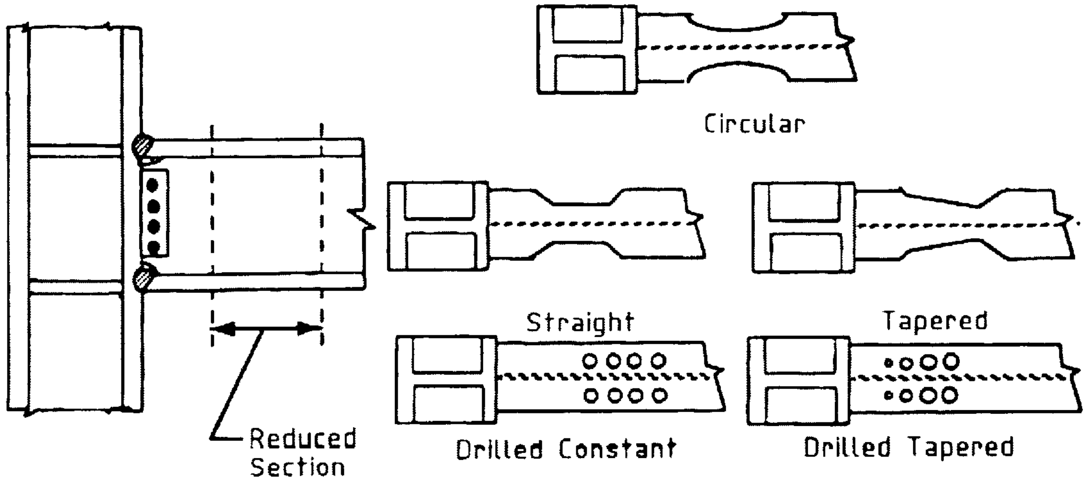

Figure 2-25: Different reduced beam section patterns (After Plumier 2000)

complex and thus expensive. This may diminish the competitiveness of MRF-steel structures relatively to reinforced concrete structures. Beam weakening avoid damage in the joints (Shen et al., 2000) and can be realised on existing structures, for example by drilling holes in flanges, which is more favourable than flame cutting on a beam in-place.

2.3.11 Concentrically braced frames and V-bracing

Concentrically braced frames ($CBFs$) and V-bracing (VBs), Figure 2-26, are very efficient in providing lateral stiffness. $CBFs$ and VBs are composed of very slender braces, which buckle in compression giving the structure a poor dissipation capacity. Their use, is limited to low rise buildings, where it is possible to provide relatively high lateral strength, thus reducing the need for ductile post-yield performance.

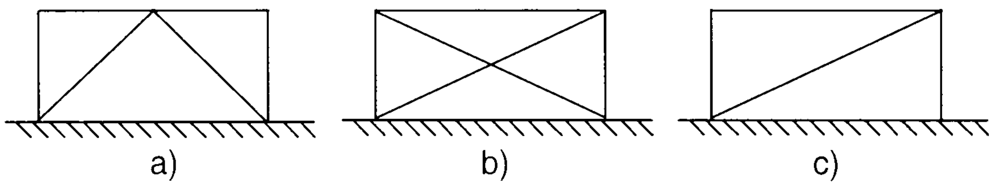

Figure 2-26: a) V-bracing b) X-bracing c) single diagonal bracing

2.3.12 Core loaded bracing or buckling resistant unbonded braces

Core loaded bracing consists of a core placed inside a mild steel sleeve filled with inert material. There is no transfer of axial load between the sleeve and the core. The sleeve prevents the core from buckling. The core can experience plastic strain in tension and in compression thus providing stable energy dissipation under reverse axial loading (Kalyanaraman et al. 1998). Similarly, Ove Arup has developed buckling resistant unbonded braces, Figure 2-27. These braces exhibit stable hysteretic behaviour during cyclic and earthquake loading. 17 full cycles of 2% plastic strain are necessary before failure occurs due to low cycle fatigue (Ove Arup 1999).

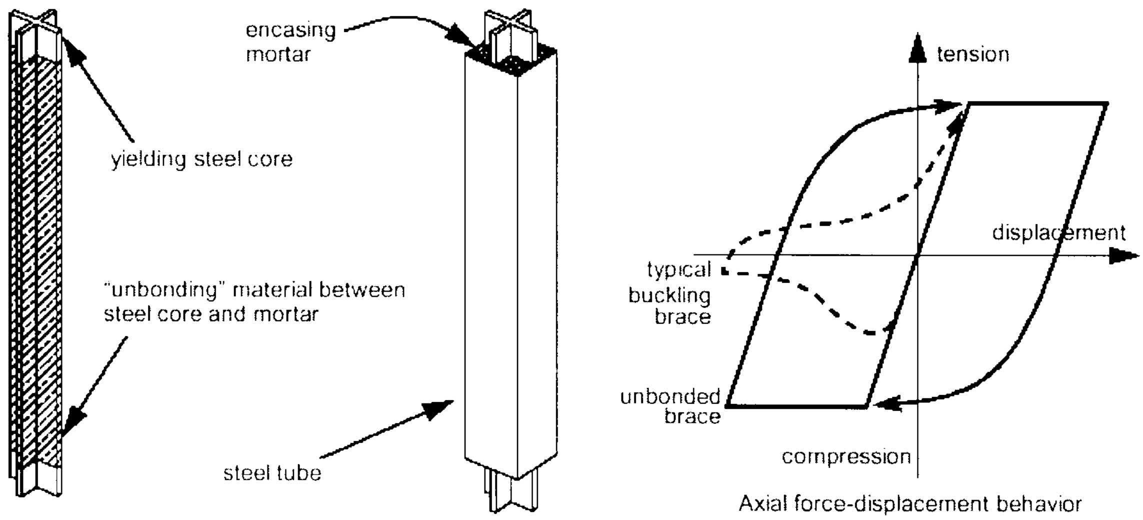

Figure 2-27: Arup's buckling resistant unbonded braces

2.3.13 Eccentric brace frames

Eccentrically braced frames ($EBFs$) are obtained by offsetting either a single brace or adjoining braces creating a short link. The axial forces of the braces are transmitted through combined shear and bending into the short segment of beam, called the "link", Figure 2-28.

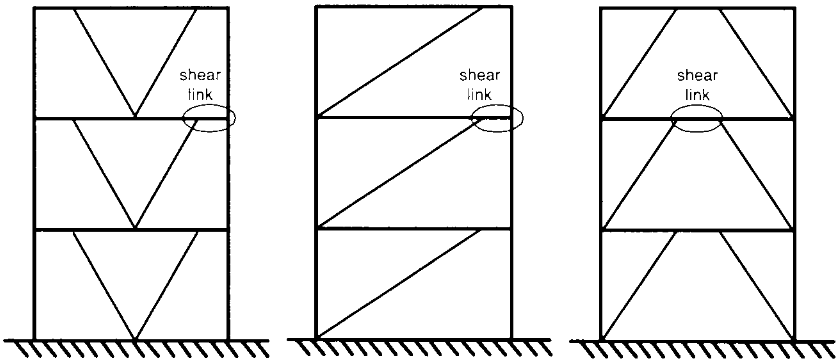

Figure 2-28: Eccentically braced frames

The links are kept small as they develop significant shear deformation during elastic response. During an earthquake these links are designed to yield and to fulfil their function of energy dissipation. The inelastic response of $EBFs$ is governed by the link behaviour. The modelling of these links has therefore been the subject of extensive investigations. Despite high shear forces combined with flexural moments in the active link, research by Kasai and Popov (1986) have shown that, in short links, shear yielding is not significantly influenced by the presence of bending moments. This was attributed due to the dominance of shear and the rapid spread of plasticity throughout the web following first shear yielding (Ricles and Popov 1994). Uncoupled yield surfaces for shear and bending can be used in simulation. It is recommended however, for a shear link, to use a value of M_p obtained by considering the flanges alone, since the web will only carry shear. Manheim and Popov (1983) have given a maximum length for shear links. Popov and Kasai (1986) have submitted evidence that, for large axial forces, the flange buckling can become a potential cause of premature failure. This possibility can be reduced by selecting a small b_f/t_f ratio and a short link length. Horizontal beams in $EBFs$ are mostly large UB-sections. The web slenderness ratio of these sections is in the range of 30 to 60 and therefore the webs are prone to buckling. This leads to significant loss of both carrying capacity and energy dissipating capability. In physical testing performed by Hjelmstad and Popov (1983), it was shown that with adequate stiffening of the web (vertical stiffeners from bottom to top flanges) the buckling could be delayed to higher amplitudes of loading. It was also shown that for links yielding predominantly in shear, equal sizing of the panel zones was optimal.

$EBFs$ have been used widely, and shear links with properly stiffened webs have proved that they can resist several large cyclic deformations and dissipate a considerable amount of energy. One disadvantage is that the links are integral parts of the frames (main structure) and therefore their repairs or replacements are complex and very expensive. Even shear links with bolted connections are still problematic to replace (Ramadan and Ghobarah, 1995). (They were only developed to avoid field welding and not to facilitate their replacement.) Another disadvantage is the high floor distortion that may also result from the seismic action.

2.3.14 Knee braced frames

Knee braced frames ($KBFs$) are a modified form of cross bracing in which the brace is cut short and connected to the mid point of a knee element spanning the adjacent beam and column. In Figure 2-29 different knee brace frames are shown. They are referred to as (a) K-knee braced frame (b) X-knee braced frame (c) knee braced frame with single brace (d) knee braced frame with single brace and with two knee elements.

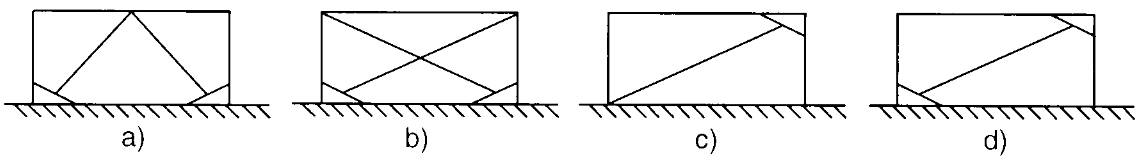

Figure 2-29: Different knee brace frames: $K-KBF$, $X-KBF$, single brace with 1 KE and single brace with 2 KEs

These bracing systems were first introduced by Aristizabal-Ochoa (1986). The key component of ($KBFs$) is the knee element, which controls both the initial elastic stiffness of the frame and the onset of yield and consequent energy dissipation. Knee braced frames attempt to combine the advantages of concentrically braced frames and eccentrically braced frames in providing simultaneous stiffness and ductility. While the knee braced frame provides ductility, it also keeps the floor distortion low compared to an eccentrically braced frame (Bourahla 1990). In case of a moderate earthquake the repair cost will be limited to the knee-elements and non-structural parts. The knee-element is connected by bolts to the beam, the column and the brace. It has a very modest size (~1m), and thus could be made easily accessible for inspection and possible replacement after an earthquake. To hold the brace to the frame during the replacement of the knee element should not be too difficult, provided some connection points for that purpose have been included in the initial design.

To assess the inelastic characteristics of $KBFs$, Balendra et al. (1990) tested a large scale model of a one storey KBF (height: 3.2m, width: 2.8m) using the pseudodynamic test procedure. They used the KBF-type of Figure 2-29 (c). A square hollow section (SHS $60 \times 60 \times 4.5$) was used as knee element. Their test frame was subjected to a sinusoidal excitation force. The amplitude was progressively increased. The knee element yielded in bending next to its connections and showed stable force displacement hysteresis curves until cracks propagated next to the connections. A ductility of 4 and a maximum storey drift of 1/170 of the height were obtained. More elaborated connections did allow them to increase the ductility to 5 (Balendra et al., 1991). Further tests of $KBFs$ with shear yielding knee element were also conducted (Balendra et al., 1994 & 1995). The knee element adopted was a built up 50×50mm I-section. They obtained a ductility of 6 and a maximum storey drift of 1/190 of the height. Failure occurred due to the tearing of the knee element's web. Later, they tested two-storey $KBFs$ (height: 2m, width: 3m), with shear yielding knee elements (Balendra et al., 1997). The knee elements they used were hot rolled I-sections (125×125×23.8 and 100×100×17.2) with web stiffeners and with their brace connection at a third of their length. This resulted in ductilities between 7 and 13. These results are promising and point out that suitably designed knee elements could provide $KBFs$ to withstand severe earthquakes. However, imposed loads other than lateral excitation forces were not included in the tests performed by Balendra et al. (1990 to 1997). In addition, relatively slender columns were used since they were testing only one-storey or two-storey $KBFs$. Methods and models for assessing the performance of higher KBF–buildings with larger and thicker structural members, needs to be developed. Design guidelines for the dimensioning of the structural members to provide the KBF with an adequate response are also needed.

2.4 Hysteretically damped steel structures: characteristics and design procedure

In Section 1.1 the two fundamental requirements (collapse & damage limitation requirements) of the latest draft of Eurocode-8 (2001) were described. In this section the design procedure for hysteretic damped steel structures and a method for establishing the design values are presented. Two approaches are possible, the design spectrum method and the non-linear time-history analysis with artificial or recorded earthquakes. The design spectrum method is the simplest of the two.

2.4.1 Basic representation of the seismic action (elastic response spectrum)

The earthquake motion at a given point of the surface is generally represented by an elastic ground acceleration spectrum (called an elastic response spectrum). Design spectra consist of envelopes of a range of possible events which might affect an elastic structure at a certain site. The subsoil category (rock, gravel, soft soil...) determines the periods T_B, T_C, and T_D and the intensity multiplier factor S which are given in Eurocode-8 (2001). In Eurocode-8 (2001) two types of elastic ground acceleration response spectrum were introduced to take into account the difference in frequency contents of strong earthquakes, small earthquakes and earthquakes with a remote epicentre (Figure 2-30). The envelope for strong earthquakes is given by:

$$\begin{aligned} 0 &\leq T \leq T_B: \ S_e(T) = a_g \cdot S \cdot (1 + (2,5 \cdot \eta - 1) \cdot T/T_B) \\ T_B &\leq T \leq T_C: \ S_e(T) = a_g \cdot S \cdot 2,5 \cdot \eta \\ T_C &\leq T \leq T_D: \ S_e(T) = a_g \cdot S \cdot 2,5 \cdot \eta \cdot T_C/T \\ T_D &\leq T \leq 4s: \ S_e(T) = a_g \cdot S \cdot 2,5 \cdot \eta \cdot T_C \cdot T_D/T^2 \end{aligned} \tag{2.1}$$

where η is a damping correction factor with reference value $\eta = 1$ for the viscous damping ratio $\xi = 5\%$. National authorities give a zoning of their national territories (the territory is subdivided into zones of different seismicity) and give the peak (or design) ground accelerations a_g associated with each zone.

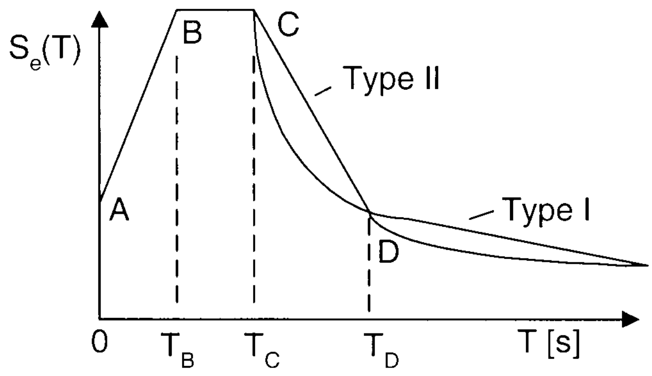

Figure 2-30: Elastic response spectrum

2.4.2 Design spectrum for hysteretically damped structures

The capacity of structures to resist seismic actions in the non-linear range permits, in general, a design for forces smaller than those corresponding to a linear elastic response. To avoid explicit non-linear structural analysis in design, the energy dissipation capacity of the structure, through mainly ductile behaviour of its elements, is taken into account by performing a linear analysis based on a reduced response spectrum, henceforth called the design spectrum.

In Eurocode-8 (2001), this reduction is accomplished by introducing a behaviour factor q in the equations of the elastic response spectrum which become:

$$\begin{aligned}
0 \ &\leq \ T \leq T_B : \quad && S_d(T) = a_g \cdot S \cdot \left[1 + \frac{T}{T_B} \cdot \left(\frac{2,5}{q} - 1\right)\right] \\
T_B \ &\leq \ T \leq T_C : \quad && S_d(T) = a_g \cdot S \cdot \left(\frac{2,5}{q}\right) \\
T_C \ &\leq \ T \leq T_D : \quad && \begin{Bmatrix} S_d(T) = a_g \cdot S \cdot \left(\frac{T_C}{T}\right) \cdot \left(\frac{2.5}{q}\right) \\ \geq 0.20 \cdot a_g \end{Bmatrix} \\
T_D \ &\leq \ T : \quad && \begin{Bmatrix} S_d(T) = a_g \cdot S \cdot \left(\frac{T_C \cdot T_D}{T^2}\right) \cdot \left(\frac{2.5}{q}\right) \\ \geq 0.20 \cdot a_g \end{Bmatrix}
\end{aligned} \tag{2.2}$$

q corresponds to the ratio between the seismic intensity which causes the ultimate limit state and the seismic intensity associated with the elastic limit state of the structure. q depends on the structural system, the ductility class and, in some cases, also on the ratio α_2/α_1. The different q factors are given in Table 2.1.

Type of structure	Ductility Class I	Ductility Class II
Moment resisting frames	$5\frac{\alpha_2}{\alpha_1}$	4
Concentric braced frames:		
Diagonal-bracing	4	4
V-bracing	2,5	2
Frames with eccentric bracing (bending or shear links)	$5\frac{\alpha_2}{\alpha_1}$	4
K-bracing (Figure 2-31)	not allowed	not allowed

Table 2.1: Behaviour factors (q)

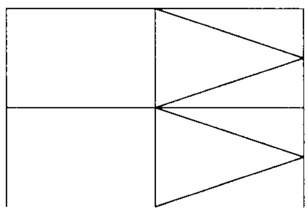

Figure 2-31: K-bracing (not allowed for seismic designs)

α_2/α_1 is the ratio of the horizontal seismic load required to cause collapse to that required to develop the first plastic hinge. α_2/α_1 must always be taken smaller than 1.6. If the building is non-regular the q values listed in Table 2.1 should be reduced by 20%.

In the United States, for example, the UBC 1997 code use a similar behaviour factor which is split into three constituents $R = R_s \cdot R_\mu \cdot R_R$. The factor R_s is the overstrength ratio (ratio between the supply resistance and the design one). R_μ is the ductility factor and R_R is the redundancy factor, which takes into account the number and distribution of plastic hinges in the structure needed for forming the collapse mechanism.

2.4.3 Simplified modal response analysis

For simple structures, with regular shape in plan and in elevation and with stiffness reducing with the height without abrupt changes, whose response is not expected to have any significant contribution from higher modes of vibration, a simple modal response analysis of two plane models can be performed. If the building does not possess the required characteristics a multi response spectrum analysis must be applied.

In Eurocode-8 (2001), the simplified modal response analysis consists of distributing the base shear force F_b as a static horizontal force at each storey using:

$$F_i = F_b \cdot \frac{s_i \cdot m_i}{\sum_{j=1}^{n} s_j \cdot m_j} \tag{2.3}$$

where F_i is horizontal force acting on the storey i, s_i the displacement of storey i in the fundamental mode shape and m_i the mass of storey i. The base shear is given by:

$$F_b = S_d(T_1) \cdot W \cdot \lambda \tag{2.4}$$

$S_d(T_1)$ is obtained from Equation 2.2, W is the total weight and λ is a corrective factor which is 1.00 in general and 0.85 if $T_1 \leq 2 \cdot T_c$. It is unclear where this correction factor comes from and why it has not simply been included in the design spectra.

The displacement d_s induced by the design seismic action is calculated on the basis of the elastic deformation d_e using

$$d_s = q_e \cdot d_e \tag{2.5}$$

where q_e is the displacement behaviour factor (usually assumed equal to the behaviour factor q).

It can be noticed that the benefit for hysteretically damped steel structures allowed in Eurocode-8 (2001) with this method concerns the strength only. There is no advantage in terms of lateral displacement relative to that of a fully elastic structure. Still, this benefit can be quite significant since some structures can have a behaviour factor up to 8. The section size of some the steel members might be considerably smaller and thus the cost of the building might be reduced.

2.4.4 Multi-modal response spectrum analysis

In the simplified modal response spectrum analysis only the fundamental mode is considered. In the present method a combination of modal responses is performed. Whenever all relevant modal responses can be regarded as independent of each other (when $T_j \leq 0.9 \cdot T_i$) the seismic action effect E_E is obtained by the square root of the sum of the squares ($SRSS$) method:

$$E_E = \sqrt{\sum E_{\mathrm{Ei}}^2} \tag{2.6}$$

where E_{Ei} is the seismic action effect due to the vibration mode i. For structures with closely spaced modes a more accurate procedure, the complete quadratic combination (CQC) should be used.

2.4.5 Time-history analysis using artificial or recorded accelerograms

Time-history analysis using artificial or recorded accelerograms is an alternative to the design spectrum method. The response of a structure to an accelerogram (representing the seismic ground motions) can be obtained by using structural non-linear dynamic software (performing direct numerical integration of the differential equations of motion). Artificial accelerograms can be generated to match the elastic response spectrum for a given site. A minimum of three accelerograms must be used to give a stable statistical mean and variance of the response quantities.

The adequacy of the response of a 5-storey building, containing knee braced frames, has also been evaluated using this method and is presented in Section 7.5.

2.5 Conclusion

In this review some damping systems have been described. The costs and the need for maintenance of fluid viscous, friction and solid visco-elastic dampers favours the use of structural hysteretic dampers for common structures.

Hysteretically damped structures such as eccentrically braced frames perform adequately during earthquakes but their dissipative elements are integral parts of the main structure and are expensive and complex to replace. The knee braced frame seems to be one of the promising designs that combines the advantages of low cost, high ductility, limitation of the damage to small elements and the possibility of replacing the damaged elements relatively easily. However the system is not yet developed sufficiently to be ready for design implementation. This thesis therefore aims to rectify this situation by presenting research on the performance of the knee braced frames and especially on the key element, the knee element.

The design procedures for hysteretically damped steel structures and especially those from the Eurocode-8 (2001) were presented.

Chapter 3

Knee braced frames and knee elements

3.1 Introduction

For intermediate size buildings in seismic areas, the use of hysteretic damped structures and in particular the knee braced frames, seems advantageous. The knee braced frame combines the advantage of showing large ductility (which allows design for reduced forces), limiting the damage to small elements called knees and offering the possibility of replacing the damaged elements relatively easily. Since a variety of knee braced frames exists, a single type on which to carry out the research was chosen. A detailed analytical study was then undertaken to establish the mechanism and the behaviour of the knee braced frames and in particular the role of the knee element. From this study the characteristics that a knee element should possess were determined.

Different plastic mechanisms for knee braced frames were studied. From this study it was shown that the shear yielding mode is preferable to the commonly preferred bending mode. The characteristics of standard hot rolled sections are presented to identify those which are most suitable for knee-elements yielding in shear. A review of shear capacity, in buckling, in particular inelastic shear buckling and of damage models, in particular of low cycle fatigue, is presented.

Different designs of knee-elements are proposed, analysed and optimised using finite element modelling. Finally several designs are chosen for physical testing in order to verify the finite element modelling results and the later calibration and improvement of models.

3.2 Choice of the knee braced frame type

As a result of a parametric study, Bourahla (1990) recommended the K-configuration, since under the same cyclic load the amount of energy dissipated was larger than for the X-configuration. In addition, the X-KBF has the disadvantage of having crossed braces requiring a more complex design. A brace with two knee elements does not bring any advantages but increases the number of connections and thus the cost. The work presented in this thesis therefore concentrates on the K-knee braced frame only. However results can be adapted and extended for use with other knee brace frame types.

3.3 Analytical study of knee braced frames

This section presents the analytical work on the knee braced frames undertaken to establish how the knee element influences the lateral deformation, stiffness and ductility of a $K-KBF$ structure.

3.3.1 Frame lateral drift

Figure 3-1 shows the deformation of a single bay $K-KBF$.

The lateral drift Δx_{Frame} is given by:

$$\Delta x_{Frame} = x_{D'} - x_D = (x_{D'} - x_{B'}) + (x_{B'} - x_B) - (x_D - x_B) \tag{3.1}$$

$$\Delta x_{Frame} = (L_{Brace} + \Delta L_{Brace}) \cos(\beta + \Delta\beta) + (\Delta_{Knee} \cdot \sin\alpha + 0.5 \cdot \Delta x_A) - (L_{Brace} \cdot \cos\beta) \tag{3.2}$$

Equation 3.2 is applicable for sway frames, moment resisting frames, strong-column weak-beam frames and strong-beam weak-column frames.

Vertical geometrical continuity requires:

$$y_D = y_{D'} + \Delta y_D \Longrightarrow (y_D - y_B) = (y_{D'} - y_{B'}) + (y_{B'} - y_B) + \Delta y_D \tag{3.3}$$

$$L_{Brace}\cdot\sin\beta = (L_{Brace}+\Delta L_{Brace})\sin(\beta+\Delta\beta)+(\Delta x_{Knee}\cdot\cos\alpha+0.5\cdot\Delta y_C)+\Delta y_D \quad (3.4)$$

From Equation 3.4 $\Delta\beta$ can be extracted to give:

$$\Delta\beta = \arcsin\left(\frac{(L_{Brace}\cdot\sin\beta - \Delta x_{Knee}\cdot\cos\alpha - 0.5\cdot\Delta y_D - \Delta y_C)}{(L_{Brace}+\Delta L_{Brace})}\right) - \beta \qquad (3.5)$$

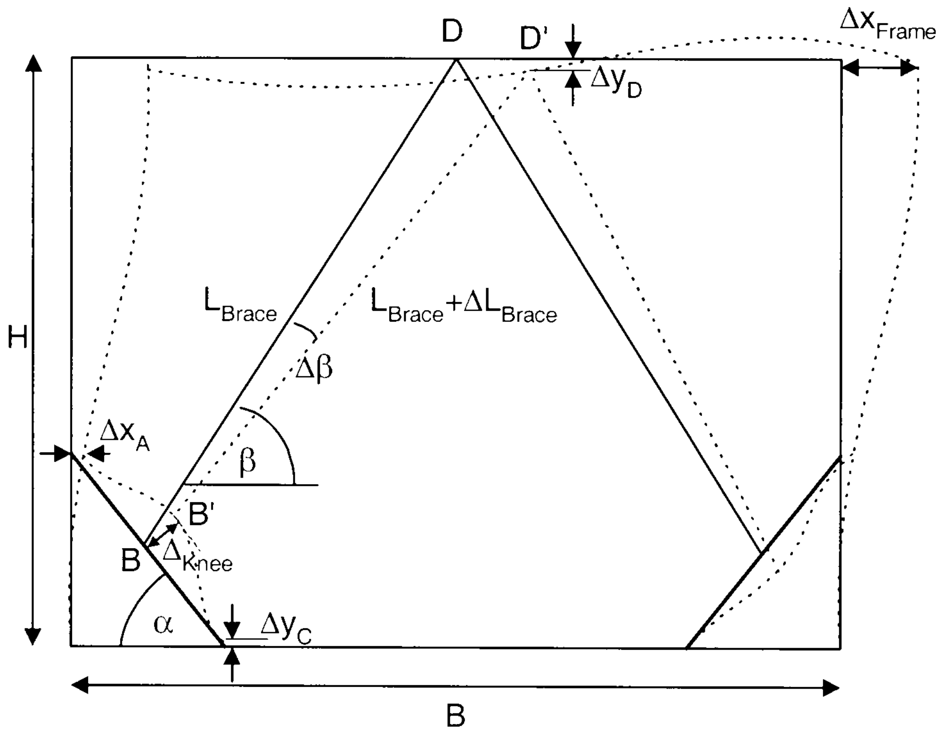

Figure 3-1: Deformation of a K- knee braced frame

When the knee-element starts yielding whilst the rest of the frame remains elastic, Δ_{Knee} dominates over Δx_A, Δy_C, Δy_D and ΔL_{Brace}. $\Delta\beta$ remains very small ($\leq 3°$) even for a large Δ_{Knee}. Neglecting the influence of Δx_A, Δy_C, Δy_D, ΔL_{Brace}, and approximating $\sin\Delta\beta \simeq \Delta\beta$ and $\cos\Delta\beta \simeq 1$, Equations 3.2 and 3.4 can be written as a function of Δ_{Knee}, α, L_{Brace} and β only:

$$\Delta x_{Frame} \simeq \Delta_{Knee}\cdot\sin\alpha - L_{Brace}\cdot\Delta\beta\cdot\sin(\beta) \qquad (3.6)$$

$$\Delta\beta \simeq -\frac{\Delta_{Knee}\cdot\cos\alpha}{L_{Brace}\cdot\cos\beta} \qquad (3.7)$$

which gives

$$\Delta x_{Frame} \simeq \Delta_{Knee} \cdot (\sin\alpha + \cos\alpha \cdot \tan\beta) = \Delta_{Knee} \cdot \frac{\sin(\alpha+\beta)}{\cos(\beta)} \qquad (3.8)$$

Equation 3.8 implies that the frame drifts almost linearly with the knee element deflection after the knee element has yielded and that the gradient (or constant of proportionality) is mainly dependent on the brace and the knee element inclinations. Figure 3-2 shows the gradient for different values of the brace and the knee element inclinations.

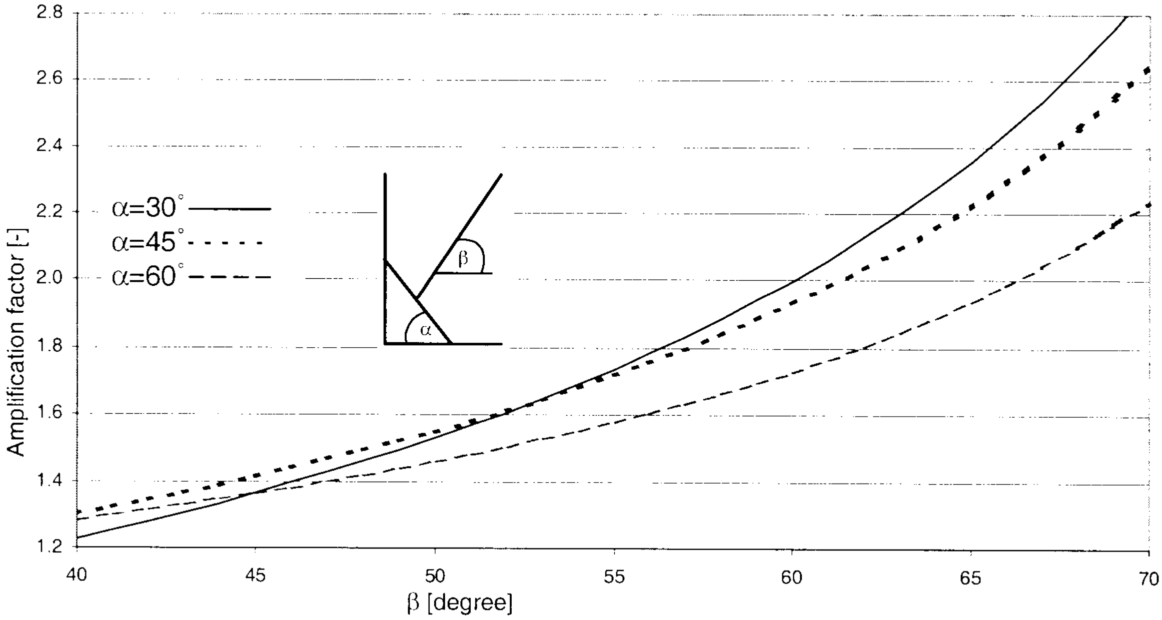

Figure 3-2: Interstorey-lateral-drift knee-element-deflection ratio as a function of brace and knee inclination (Equation 3.8)

Numerical analysis of the 5-storey building performed in Section 7.3, confirms that lateral drift is approximately proportional to the knee element deflection. The constants of proportionality are different in the three cases: (1) The whole structure is in the elastic range, (2) the knee element deforms plastically while the rest of the structure remains elastic, (3) the knee elements and elements of the frame deform plastically. Equation 3.8 gives the constant of proportionality for case (2), but the values it gives are around 20% smaller than those found in the numerical analysis. The difference is due to the fact that Equation 3.8 does not take into account the terms ΔL_{Brace}, Δx_A, Δy_C and Δy_D. For a closer approximation of the results. Equation 3.8 can be improved to:

$$\Delta x_{Frame} \simeq 1.25 \cdot \Delta_{Knee} \cdot \frac{\sin(\alpha + \beta)}{\cos(\beta)} \tag{3.9}$$

and this gives.

3.3.2 Forces and stiffness

A lateral load P on a K-knee braced frame will be transmitted down the structure via two different paths. One goes through the bracing system (BS) and the other through the column, as in a moment resisting frame (MRF).

$$P_{KBF} = P_{MRF} + P_{BS} \tag{3.10}$$

The force in a single brace is given by:

$$F_{Brace} = \frac{1}{2} \cdot \frac{P_{BS}}{\cos(\beta)} \tag{3.11}$$

and the shear and the axial forces transmitted to the knee element are given by:

$$S_{KE} = \frac{1}{2} \cdot \frac{\sin(\alpha + \beta)}{\cos(\beta)} \cdot P_{BS} \tag{3.12}$$

$$N_{KE} = \frac{1}{2} \cdot \frac{\cos(\alpha + \beta)}{\cos(\beta)} \cdot P_{BS} \tag{3.13}$$

The portion of the load taken by the moment resisting frame and the bracing system depends on their relative stiffness. It is quite tempting to approximate the knee braced frame by two separate independent systems, the bracing system (BS) and the moment resisting frame (MRF), as shown in Figure 3-3 and expressed in Equation 3.14.

$$K_{KBF} = K_{MRF} + K_{BS} \tag{3.14}$$

However this is not possible because the horizontal force transmitted through the column-knee connection and the vertical force transmitted through the beam-knee connection affect the deformation of the moment resisting frame, and the lateral and vertical

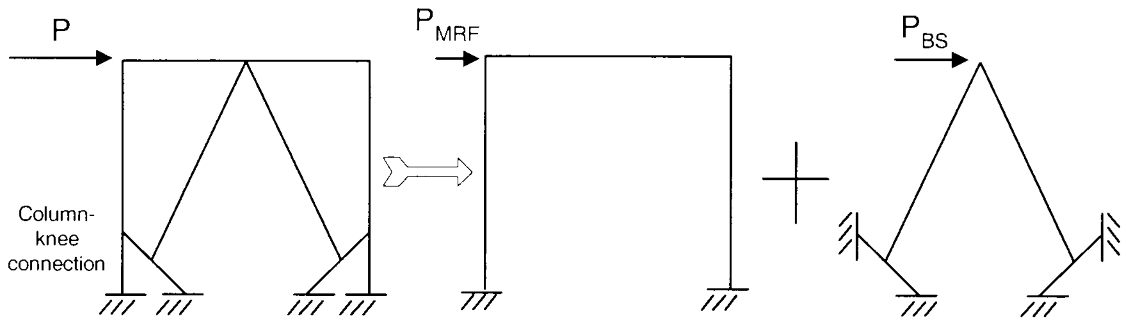

Figure 3-3: K- knee brace frame split into a moment resisting frame and a bracing system

movements of the knee connections affect the bracing system. A numerical calculation is necessary to evaluate forces in the different elements and the global behaviour of the knee braced frames. To have a high level of energy dissipation, the proportion of the force transmitted through the system containing the yielding element, must be high. Therefore the bracing system stiffness should be high compared to the stiffness of the moment resisting frame. In the numerical analysis of Section 7.3, the ratio K_{BS}/K_{MRF}, was found to be around 60 in the elastic range.

3.3.3 Ductility and energy dissipation

The knee braced frame is composed of multiple elements with different characteristics (stiffness, ductility, yield load). To understand how the global ductility and the energy dissipation are affected by the element characteristics, a system composed of a spring of stiffness K_{Spring}, in series with an elastic-plastic element of ductility μ_{Box}, is analysed. Figure 3-4 shows the bi-linear behaviour of the elastic-plastic element. This system can be used to model the bracing system where the spring represents the brace and where the elastic-plastic element represents the knee element.

The elastic-plastic element has an elastic stiffness K_{Box}, a post-yield stiffness $\alpha_{SH} \cdot K_{Box}$ (with $\alpha_{SH} < 1$) and a yield load of F_y, (Figure 3-5).

The yield displacement δ_y, due to the force F_y, and the additional plastic displacement δ_{pl}, due to a force increment ΔF, are given by:

$$\delta_{y.System} = \delta_{y.Spring} + \delta_{y.Box} = \frac{F_y}{K_{Spring}} + \frac{F_y}{K_{Box}} = F_y \cdot \left(\frac{K_{Box}}{1 + K_{Box}/K_{Spring}} \right)^{-1} \quad (3.15)$$

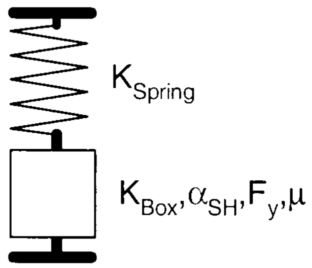

Figure 3-4: A spring and an elastic-plastic element in series

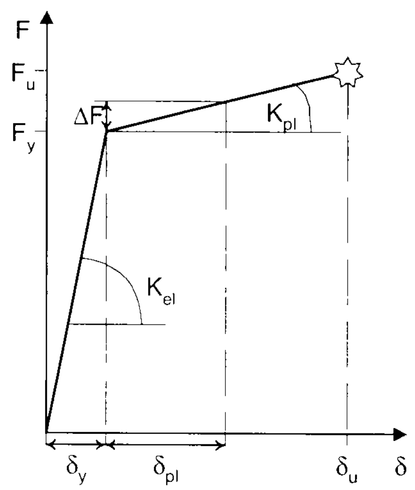

Figure 3-5: Bi-linear behaviour of the elastic-plastic element

$$\delta_{pl.System} = \frac{\Delta F}{K_{Spring}} + \frac{\Delta F}{\alpha_{SH} \cdot K_{Box}} = \Delta F \cdot \left(\frac{\alpha_{SH} \cdot K_{Box}}{1 + \alpha_{SH} \cdot K_{Box}/K_{Spring}} \right)^{-1} \tag{3.16}$$

The expression in brackets in Equations 3.15 and 3.16 are the apparent stiffness of the system before and after yield.

$$\alpha_{SH.System} = \frac{K_{pl.System}}{K_{el.System}} = \frac{(1 + K_{Box}/K_{Spring})}{(1 + \alpha_{SH} \cdot K_{Box}/K_{Spring})} \cdot \alpha_{SH} \tag{3.17}$$

$\Rightarrow$ This shows that $\alpha_{SH.System} \geq \alpha_{SH}$ and that $\alpha_{SH.System}$ decreases with increasing K_{Spring}/K_{Box}.

Considering that the ultimate load is reached when the elastic-plastic element deforms to its maximum ductility $\mu_{Box} = \delta_{u.Box}/\delta_{y.Box}$ (see Figure 3-5) the failure load is given by:

$$F_u = (1 + \alpha_{SH} \cdot (\mu_{Box} - 1)) \cdot F_y \tag{3.18}$$

Substitution of Equation 3.18 into Equation 3.16 gives:

$$\delta_u = \delta_y + \frac{\alpha_{SH} \cdot (\mu_{Box} - 1) \cdot F_y}{K_{Spring}} + \frac{(\mu_{Box} - 1) \cdot F_y}{K_{Box}} \tag{3.19}$$

The maximum ductility of the system is given by:

$$\mu_{System} = \frac{\delta_u}{\delta_y} = 1 + (\mu_{Box} - 1) \cdot \frac{1 + \alpha_{SH} \cdot K_{Box}/K_{Spring}}{1 + K_{Box}/K_{Spring}} \tag{3.20}$$

Figure 3-6 a) gives the ductility ratio $(\mu_{System} - 1) / (\mu_{Box} - 1)$.

$\Rightarrow$ This shows that $\mu_{System} < \mu_{Box}$ and that μ_{System} increases with increasing K_{Spring}/K_{Box}.

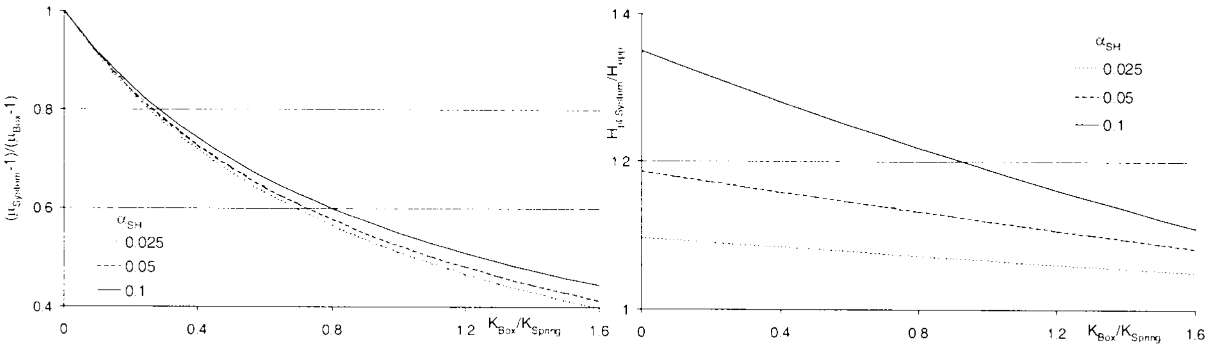

Figure 3-6: a) Ductility ratio and b) plastic energy ratio

The plastic energy, which is dissipated exclusively by the elastic-plastic element, is given by:

$$\begin{aligned}
H_{pl.System} &= \delta_{pl.Box} \cdot \left(F_y + \frac{\Delta F}{2}\right) \cdot (1 - \alpha_{SH}) \qquad (3.21) \\
&= \frac{(1 - \alpha_{SH})}{1 + \alpha_{SH} \cdot K_{Box}/K_{Spring}} \cdot \left(F_y + \frac{\alpha_{SH} \cdot \delta_{pl.System} \cdot K_{Box}}{2 \cdot (1 + \alpha_{SH} \cdot K_{Box}/K_{Spring})}\right) \cdot \delta_{pl.System} \\
&= \frac{(1 - \alpha_{SH})}{1 + \alpha_{SH} \cdot K_{Box}/K_{Spring}} \cdot \left(1 + \frac{\alpha_{SH} \cdot \gamma}{2 \cdot (1 + \alpha_{SH} \cdot K_{Box}/K_{Spring})}\right) \cdot H_{epp}
\end{aligned}$$

where H_{epp} is the energy dissipated by elastic perfectly plastic system and $\gamma = \delta_{pl.System}/\delta_{y.Box}$. Figure 3-6 b) shows $H_{pl.System}/H_{epp}$ as a function of α_{SH} and for $\gamma = 10$.

⇒This shows that the energy dissipated increases with increasing K_{Spring}/K_{Box}, but the gain remains relatively small.

3.3.4 Conclusion

- The bracing system stiffness should be much greater than that of the moment resisting frame.
- Choosing a larger brace section than needed to satisfy the buckling strength is beneficial, because the energy dissipation, the global stiffness and the ductility of knee braced frames are increased.
- The ductility of the knee braced frame is smaller than the ductility of the knee element.

3.4 Knee element requirements

Knee elements provide the opportunity to control the yield pattern of a building in an earthquake. To make best used of this opportunity, a numberof knee element requirements can be listed. Defining P_y as the concentrated force applied perpendicularly at mid-span at which the knee element starts yielding and P_u as the force at which the knee element fails, the knee element should:

1. not yield during normal service life or a very small earthquake: $P_y > P_{lower\ bound}$.
2. yield for the first important acceleration peak of a moderate earthquake: $P_y < P_{higher\ bound}$. This expresses the fuse or sacrificial function of the knee element. The knee element should take all the damage so the rest of the structure does not suffer damage. If the knee element does not start yielding, then damage may occur in the main structure and the economical benefit will not be achieved.
3. resist without failure the load generated by the strongest earthquake forecast for the building site: $P_u > P_{\max}$.

4. resist several large ductile stable hysteresis cycles without low cycle fatigue failure. As the previous requirement refers to strength this one refers to the 'endurance' of the knee element.

5. not suffer lateral torsional buckling nor local flange or web buckling. Buckling is a non-dissipative phenomenon and should be avoided.

6. have a high initial stiffness.

3.5 Plastic mechanism of knee elements

Different knee element energy dissipating mechanisms exist. They depend on the beam section properties and on the end fixity of the knee element. This section considers which mode is better and how the selected dissipating mechanism can be achieved.

3.5.1 Boundary conditions and yielding mode

When the knee element is a simply supported beam loaded at its centre by a concentrated load, only one plastic hinge is required to create a mechanism (as shown in Figure 3-7 (a)). When the knee element is built-in at both ends, and the section is homogeneous along the length of the beam, the mechanism has three hinges, as shown in Figure 3-7 (b).

The yield load P_y for case a) is given by:

$$P_y = 4\frac{M_y}{L} \tag{3.22}$$

And for case b) by:

$$P_y = 8\frac{M_y}{L} \tag{3.23}$$

When the knee element has semi-rigid connections, Figure 3-7 c), the hinge at mid span appears at a load P_{y1}. At a load P_{y2} ($>P_{y1}$) additional hinges form at the ends. Figure 3-8 shows the evolution of the bending moment and the deformation.

Using the slope deflection method and symmetry we can write:

$$\theta_A = -\theta_B, \ \theta_C = 0 \tag{3.24}$$

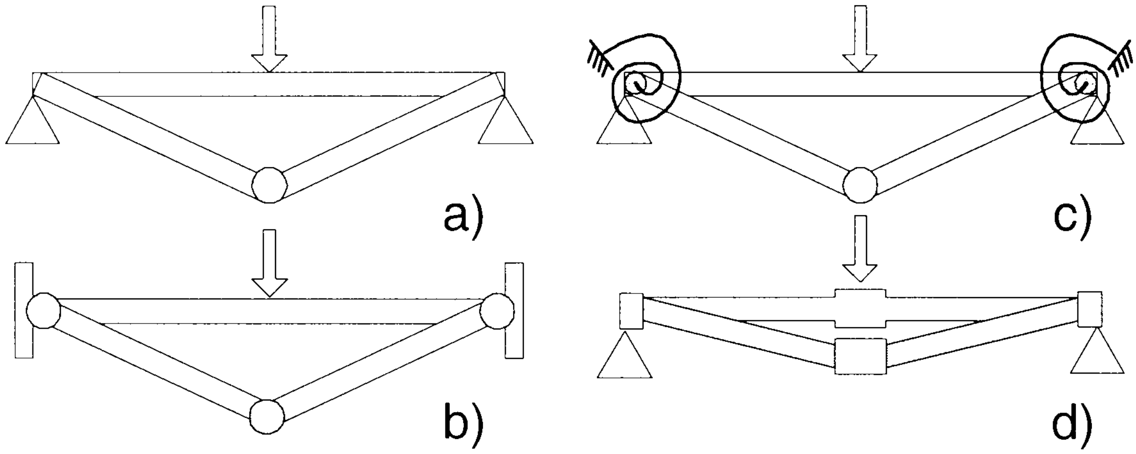

Figure 3-7: Plastic mechanism for different boundary conditions and section characteristics

$$M_{AB}^F + M_{AB}^D = \frac{PL}{8} + \frac{2EI}{L}(\theta_A) + K \cdot \theta_A = 0 \tag{3.25}$$

$$M_{AC}^F + M_{AC}^D = \frac{2EI}{L/2}\left(2\theta_A - \frac{3\delta}{L/2}\right) + K \cdot \theta_A = 0 \tag{3.26}$$

where L is the total length of knee element and K the rotational stiffness of the semi-rigid connections. The end rotation θ and the central deflection δ are given by:

$$\theta_A = -\frac{PL^2}{8(2EI + KL)} \tag{3.27}$$

$$\delta = \theta_A\left(\frac{L}{3} + \frac{KL^2}{24EI}\right) = -\frac{PL^3}{(192EI)} \cdot \frac{(8EI + KL)}{(2EI + KL)} \tag{3.28}$$

By considering the equilibrium of segment AC we can write:

$$M_C = \frac{PL}{4} - M_A(= M_y) \tag{3.29}$$

where $M_A = -K \cdot \theta_A$. Combining Equations 3.27 and 3.29 we obtain:

$$P_{M,y1} = \frac{8M_y}{L} \cdot \frac{(2EI + KL)}{(4EI + KL)} \tag{3.30}$$

Figure 3-7 d) shows a beam yielding in shear. Since the shear force is constant along

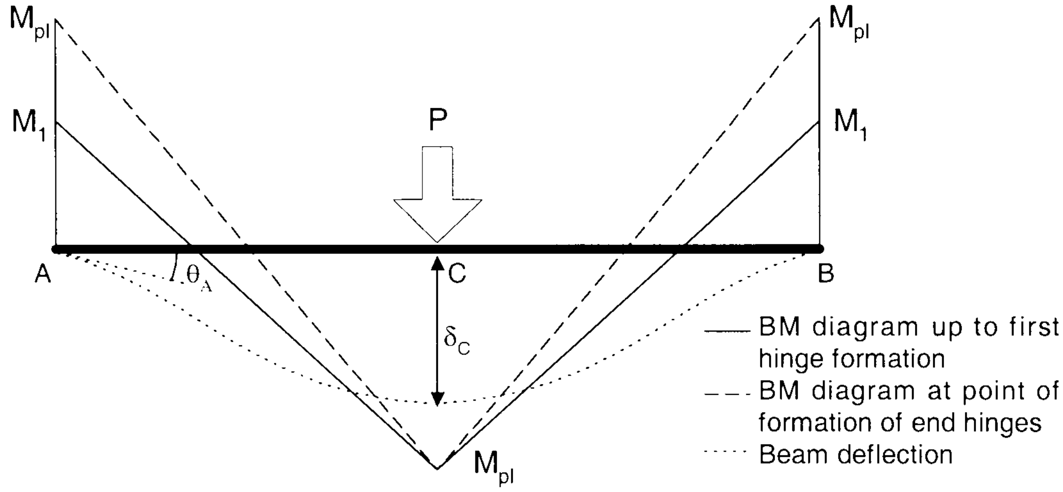

Figure 3-8: Moment and deformation of a knee with semi-rigid connections

the beam, it will yield on its whole length, except around the connection points which are locally strengthened. In this case the shear yield load does not depend on the boundary condition. The energy dissipation area is larger and more homogeneous than in the three other cases. This should make the element less sensitive to low cycle fatigue.

To show that the dissipative area is effectively larger and more homogeneous in shear yielding mode, finite element analysis using the ABAQUS package was performed on a series of 1m long I-beam models with a width B=152mm and a depth D=146mm. The beam models were using 3974 shell elements (3-noded triangle shell elements for the web and 4-noded quadrilateral shell elements for the flanges). The load was applied at mid span above the web over a length of 150mm. Beam 1 was pinned at both ends and had a web thickness t=15mm and flange thickness T=8mm. Beam 2 was built-in at both ends and had t=6mm and T=13mm. A monotonic load was applied until 10.5kJ was dissipated by plastic yielding. For beam 1 a bending hinge appeared at mid-span, the load was F =500kN and the central deflection δ=26.7mm. Beam 2 yielded in shear, the load was F =494kN and the central deflection δ=26mm.

For beam1 plasticity occurs mainly in a small strip in the bottom and top flanges. The web also experiences some plastic strain, Figure 3-9 a). For beam 2 the strain distribution is effectively more uniform, Figure 3-9 b).

The bending hinge shape and plastic strain distribution are affected greatly by the

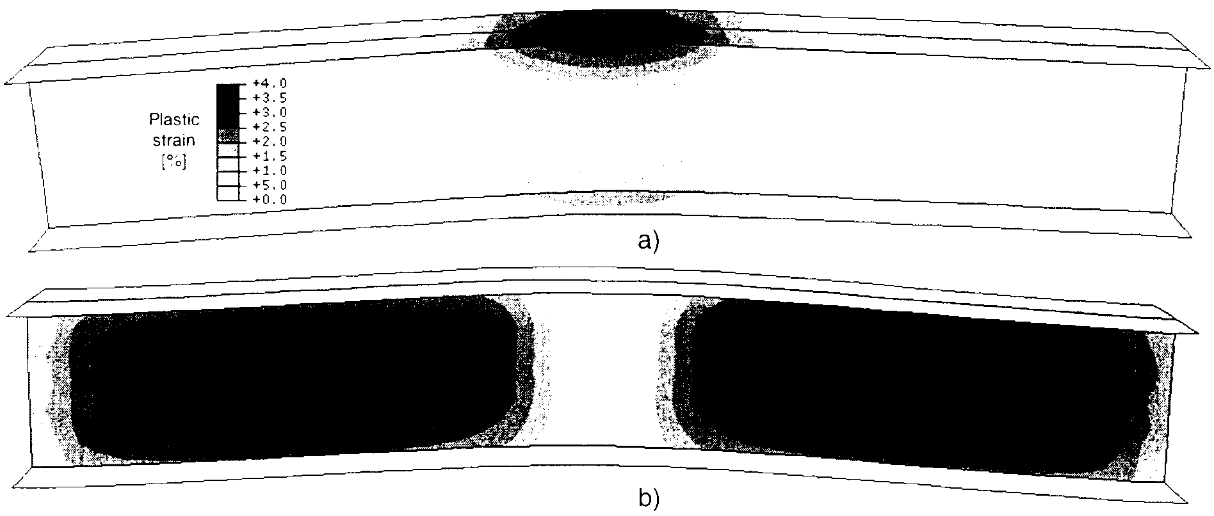

Figure 3-9: Plastic strain of a beam yielding a) in bending b) in shear

connection details (bolts, welds and stiffeners) (Popov et al. 1998). Estimating the yield strength and the ultimate capacity of a connection is a subtle task, especially when the moment distribution depends on the boundary conditions.

3.5.2 Choice of the yielding mode

It was decided to design and investigate knee elements yielding in shear. This was because:

1. the energy dissipation area is larger and more homogeneous and should improve the low cycle fatigue resistance,
2. yield occurs between the connections thus connection failures are avoided,
3. the yield load does not depend on the boundary conditions,
4. the yield load should be easier to estimate than the yield load of a connection and
5. the yield load does not depend on the axial load.

3.5.3 Section and length of knee elements yielding in shear

As a result of a parametric study, Bourahla (1990) showed that the optimal length of a built-in knee element for a medium size knee braced frame is between 0.2 and 0.35 times the storey height. For a 3m high storey this mean between 600mm and 1050mm. His study was based on a knee element yielding in bending. Nevertheless the optimal length of a knee element yielding in shear is expected to be similar, since the hysteresis curves of an element yielding in shear are similar to those yielding in bending.

If a section is to yield in shear, Equation 3.31 must be satisfied where $P_{M.y}$ is given by Equations 3.22 (pinned connection), 3.23 (built-in connection) and 3.30 (semi-rigid connection).

$$P_{S.y} < P_{M.y} \tag{3.31}$$

$$P_{S.y} = 2 \cdot S_y = 2 \cdot A_S \cdot \tau_y = 2 \cdot A_S \cdot \sigma_y / \sqrt{3} \tag{3.32}$$

where S_y is the elastic shear ressitance and A_S the shear area. A_S is greater than the web area. The root area and a part of the flanges situated above the root also participate to the shear resistance. In table 5.16 of Eurocode-3 (1993), for hot rolled I section, A_s is given by:

$$A_S = c_A \cdot A_w = 1.04 \cdot D \cdot t \tag{3.33}$$

It will be shown later that the post-yielding life of a knee element is increased if the flanges remain elastic until the web fails. The flanges, in addition to their moment carrying function (tension/compression), act as edge stiffeners for the yielding web increasing its resistance to buckling. If no instability phenomena occur:

$$\frac{P_{S.u}}{P_{S.y}} \approx \frac{f_u}{f_y} = c_f \quad \Longrightarrow P_{S.u} \approx c_f \cdot P_{S.y} \tag{3.34}$$

The flanges remain totally elastic if:

$$M_u < Z_y \cdot \sigma_y \tag{3.35}$$

where Z_y is the elastic section modulus. For a built-in knee element :

$$M = \frac{PL}{8} \tag{3.36}$$

Combining Equations 3.35 and 3.36, we obtain the condition for which the flanges remain totally elastic until the web fails:

$$\frac{P_{S,u} \cdot L}{8} < Z_y \cdot \sigma_y \tag{3.37}$$

Replacing terms from Equations 3.34 and 3.32 in Equation 3.37 we obtain:

$$\frac{c_f \cdot A_S \cdot \sigma_y \cdot L}{4 \cdot \sqrt{3}} < Z_y \cdot \sigma_y \tag{3.38}$$

The maximum built-in knee element length that satisfies Equation 3.38 is given by:

$$L_{\max} = \frac{4\sqrt{3}}{c_f} \cdot \frac{Z_y}{A_S} \tag{3.39}$$

Considering the deflection due to bending and due to shear, which is not negligible for short elements with high shear, the global stiffness K of a centrally loaded built-in element, is given by (Frey, 1993):

$$K = \left(\frac{1}{K_{shear}} + \frac{1}{K_{bending}}\right)^{-1} = \left(\frac{L}{4 \cdot G \cdot A_S} + \frac{L^3}{192 \cdot E \cdot I}\right)^{-1} = E \cdot \left(\frac{L \cdot (1 + \nu)}{2 \cdot A_S} + \frac{L^3}{192 \cdot I}\right)^{-1} \tag{3.40}$$

$L_{\max}$, $P_{S,y}$ and K, obtained with Equations 3.39, 3.32 and 3.40 with $c_f = 1.65$ and $c_A = 1.04$, were calculated for standard sections: Universal Column (UC), Universal Beams (UB), both taken about their strong axis, square hollow sections (SHS) and rectangular hollow sections (RHS) taken about their weak axis.

In Figure 3-10, $P_{S,y}$ is plotted against the $L_{\max}$. UC-sections have the lowest $P_{S,y}$ for a given $L_{\max}$. A few UB-sections have comparable performances. RHS-sections have on average 3 times (and SHS-sections 4 times) higher yield load (in shear) than UC-sections for the same $L_{\max}$. Requirement 2 (section 3.4) suggests that sections with a smaller yield load are more suitable.

In Figure 3-11, K is plotted against $P_{S,y}$ (only for sections with $L_{\max}$ >0.7m). The stiffness is roughly the same for all four section types, but slightly higher for UB and UC sections. Requirement 6 (Section 3.4) suggests that sections with a higher stiffness K are more suitable.

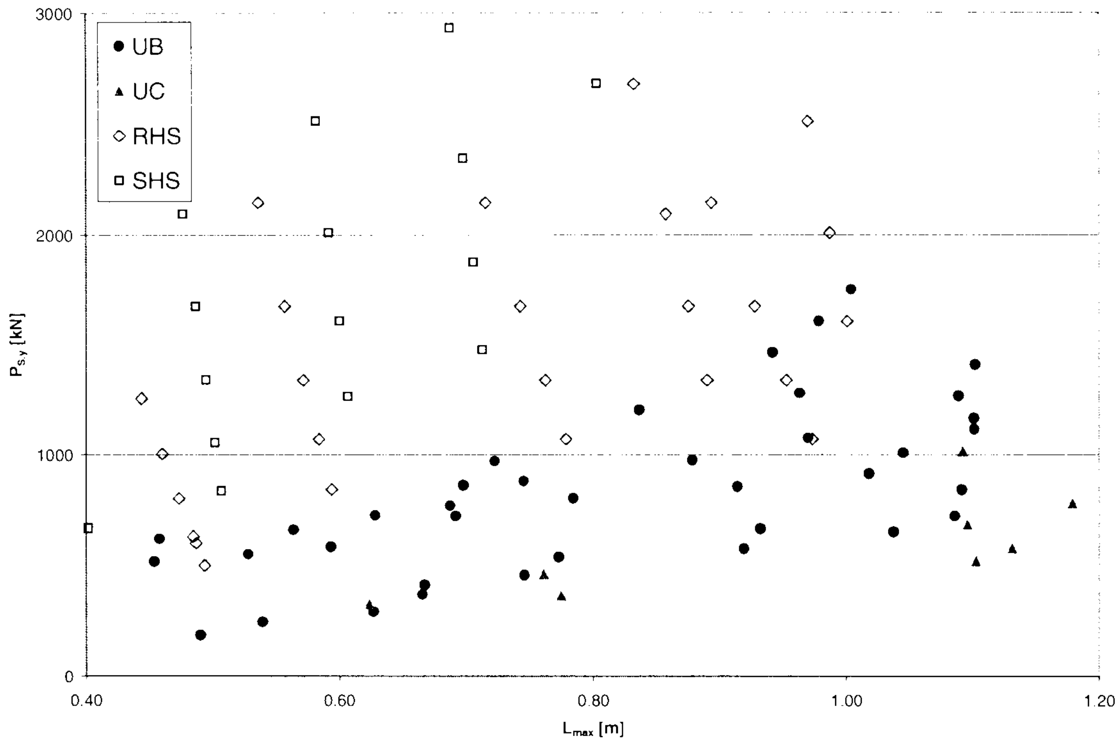

Figure 3-10: Maximum length and yielding load of standard sections

3.5.4 Conclusion

Short *UC*-sections and some *UB*-sections fulfil the condition of yielding in shear. In addition they possess the quality of a low yield load and a high stiffness.

3.6 Shear capacity of plates and sections

3.6.1 Behaviour mode of plates

How plates resist shear loads depends mainly on their slenderness ratio. If a plate is very slender, it buckles at stresses below the yield stress (Mode I, the elastic buckling, Figure 3-12). For smaller slenderness ratios it reaches the yield stress (mode II), experiences small plastic strain and fails by plastic buckling. The plastic strains are smaller than the strain where strain hardening starts and therefore the ultimate shear stress is τ_y. In Mode III strain hardening takes place until plastic buckling load is reached. Mode IV applies only to very thick plates, where the ultimate stress of the material is reached before any

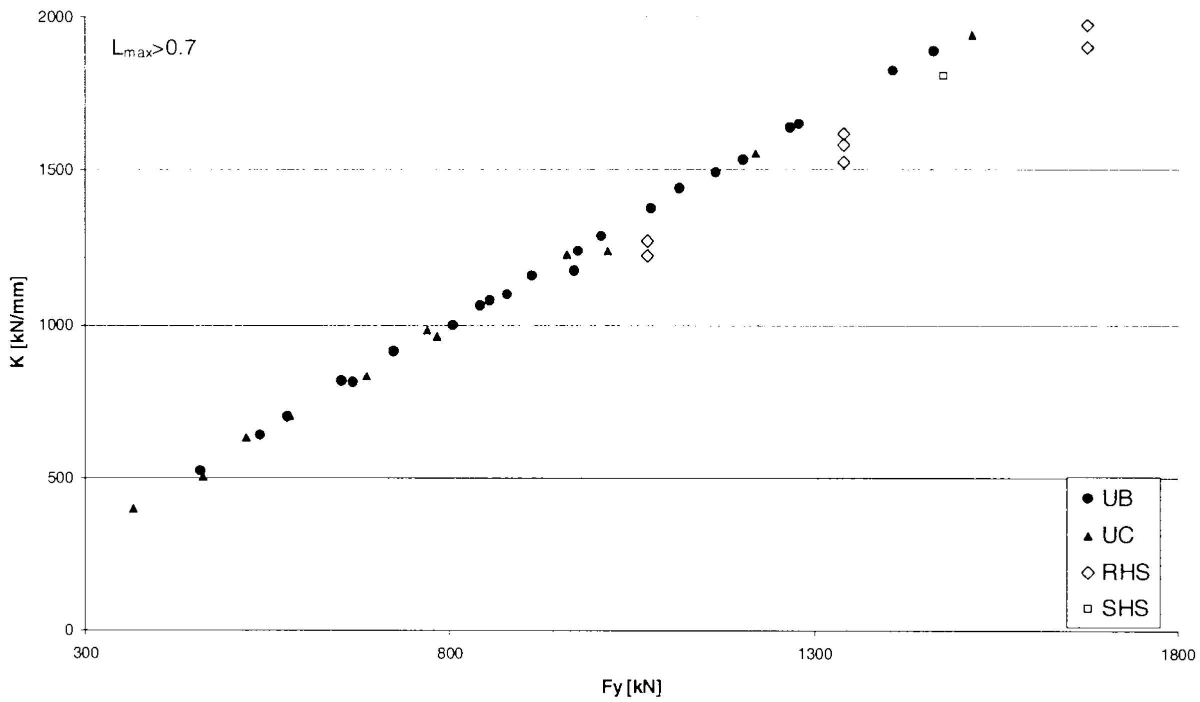

Figure 3-11: Stiffness and yielding load of standard sections

instability occurs.

3.6.2 Elastic shear buckling

The elastic critical (or buckling) shear stress τ_{cr} for plates is given by Allen and Bulson (1980):

$$\tau_{cr.el} = K\frac{\pi^2 \cdot E}{12\left(1-\nu^2\right)}\left(\frac{t}{d}\right)^2 \tag{3.41}$$

For a simply supported plate along all the edges, K is given by:

$$K = 5.35 + 4\left(\frac{d}{b}\right)^2 \quad \text{with } b > d \tag{3.42}$$

For a plate built-in along all the edges by:

$$K = 9 + 5.4\left(\frac{d}{b}\right)^2 \quad \text{with } b > d \tag{3.43}$$

where b is the longer side of the plate and d the width.

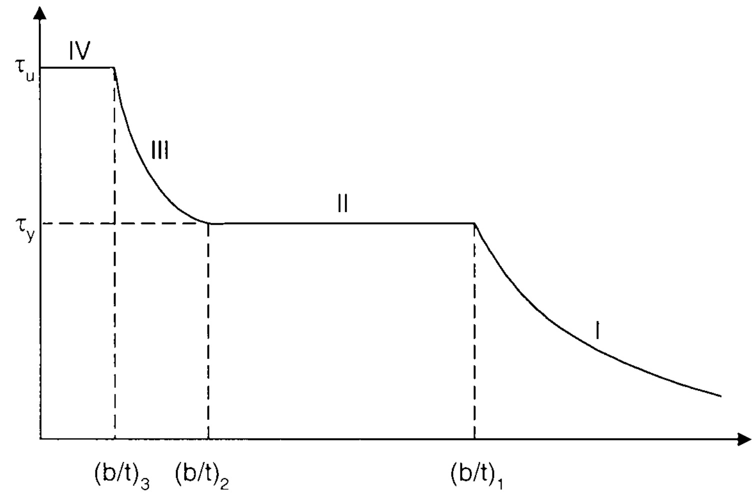

Figure 3-12: Critical shear stress in plates, Inoue (1996)

As the web of an I-section beam reaches its elastic critical shear capacity, a tension field is set up through the web (the direction does not usually coincide with the diagonal of the panel) and plastic hinges in the flanges form, Figure 3-13 (Basler and Thurlimann, 1960).

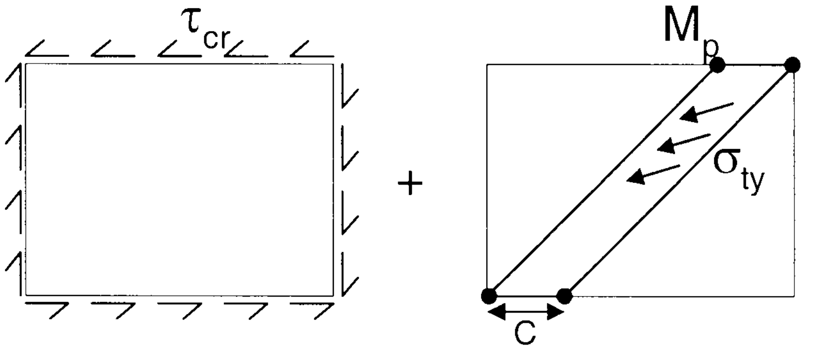

Figure 3-13: Ultimate load mechanism developed by Basler and Thurlimann

Porter et al. (1975) developed a method with an incremental loop, that can be carried out quickly running on a computer, to calculate the ultimate shear capacity S_{ult}. For Universal Beams and Universal Columns, the web is always thick enough to make $\tau_{cr,el}$ =

τ_y. In this case Porter's equation becomes:

$$S_{ult} = \frac{4M_{p.fl}}{b} + \tau_y \cdot d \cdot t \tag{3.44}$$

where $M_{p.fl}$ is the plastic moment of the flanges.

For the length of the plate taken equal to the depth between fillet, $d = D - 2(T + r)$, the contribution of the flanges are between 3 and 10% for UC-sections and between 1 and 5% for UB-sections.

3.6.3 Inelastic shear buckling

The inelastic buckling of plates has been analysed by a finite strip method by Inoue (1996). The material properties used in his analyses were $E = 206GPa$, $\nu = 0.3$, the tangent modulus in strain hardening range in uni-axial tension $E_{st} = E/33$, strain at the onset of strain hardening in uni-axial tension $\epsilon_{st} = 11 \cdot \epsilon_y$. For the plastic critical shear stress is given by:

$$\tau_{cr.pl} = K_p \frac{\pi^2 \cdot E}{12(1-\nu^2)} \left(\frac{t}{d}\right)^2 \tag{3.45}$$

where for a simply supported plate along all the edges:

$$K_p = 2.24 + 3.96 \left(\frac{d}{b}\right)^2 \text{ with } b > d \tag{3.46}$$

The slenderness $(b/t)_1$, (for which the critical elastic buckling stress is equal to the yielding stress), the slenderness $(b/t)_2$, (for which the critical plastic buckling stress is equal to the yielding stress), and the slenderness $(b/t)_3$, (for which the critical plastic buckling stress is equal to the ultimate material stress) for a simply supported plate along all the edges are given by:

$$\begin{aligned}
\left(\frac{b}{t}\right)_1 &= \sqrt{\frac{\pi^2 \cdot E}{12\,(1-\nu^2)\,\tau_y}\left[5.35 + 4\left(\frac{d}{b}\right)^2\right]} \\
\left(\frac{b}{t}\right)_2 &= \sqrt{\frac{\pi^2 \cdot E}{12\,(1-\nu^2)\,\tau_y}\left[2.24 + 3.96\left(\frac{d}{b}\right)^2\right]} \\
\left(\frac{b}{t}\right)_3 &= \sqrt{\frac{\pi^2 \cdot E}{12\,(1-\nu^2)\,\tau_u}\left[2.24 + 3.96\left(\frac{d}{b}\right)^2\right]}
\end{aligned} \tag{3.47}$$

Inoue did physical tests to compare with their analytical results. For $b/t \approx (b/t)_1$ they found good agreement. However for $b/t > 1.05 \cdot (b/t)_1$ Equation 3.45 gives a too high value for $\tau_{cr.pl}$.

Azhari and Bradford (1993) have included residual stresses in their study of simply supported and built-in plates (along all the edges). Their results (for monotonic loading) are presented in Figure 3-14.

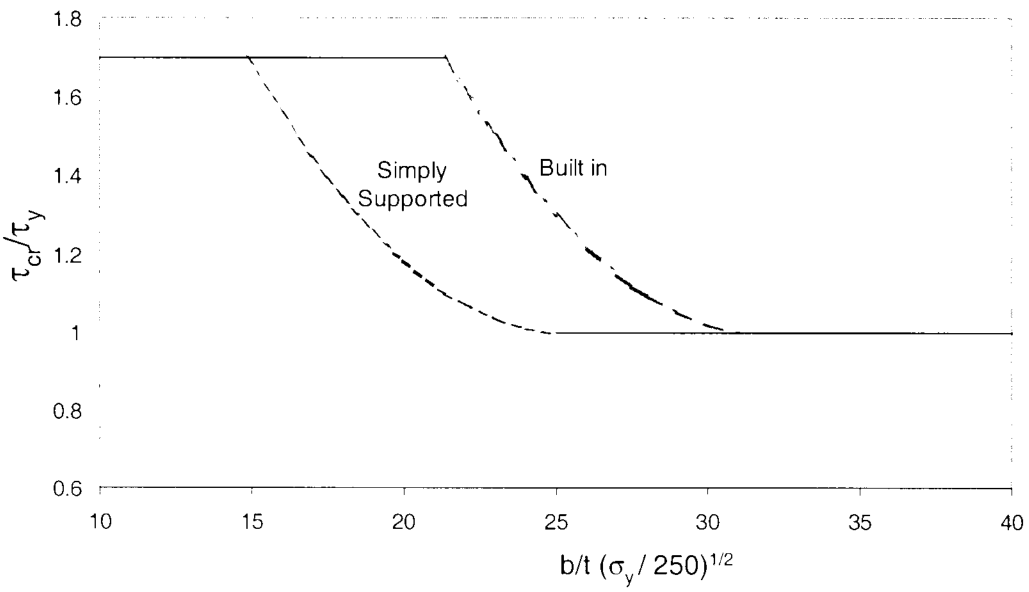

Figure 3-14: Plastic shear buckling of plates. (Azhari and Bradford, 1993)

Bradford and Azhari obtained much smaller $\tau_{cr.pl}$ than Inoue, for the same width-to-thickness ratio b/t. Standard I-sections come between the built-in and the simply supported curves but are closer to the built-in curves. Standard sections with slenderness ratios smaller than 20 are needed to reach the ultimate stress before the critical plastic buckling stress. Standard sections with a slenderness ratio above 28 buckle immediately after yielding. By reducing the slenderness ratio slightly, significant shear capacity can be gained. Table 3.1 gives the d/t for some small UC, UB, RHS and SHS sections and in Figure 3-15 the slenderness ratio d/t (only for sections with $L_{\max}$ >0.7m) is plotted against $P_{S,y}$.

Universal Column	d/t	Universal Beam	d/t	Hollow sections	d/t
152x152x23	20.3	127x76x13	23.0	120x120x5	21
152x152x30	18.7	152x89x16	26.5	120x120x12.5	6.6
152x152x37	15.3	178x102x19	31.2	200x200x5	37
203x203x46	22.0	203x102x23	32.6	200x200x12.5	9.5
203x203x52	20.1	203x133x25	29.7	150x100x5	17
203x203x60	17.3	203x133x30	27.4	150x100x12.5	5
203x203x71	15.6	254x102x22	38.8	200x100x5	17
203x203x86	12.4	254x102x25	36.9	200x100x16	3.3

Table 3.1: Slenderness ratio

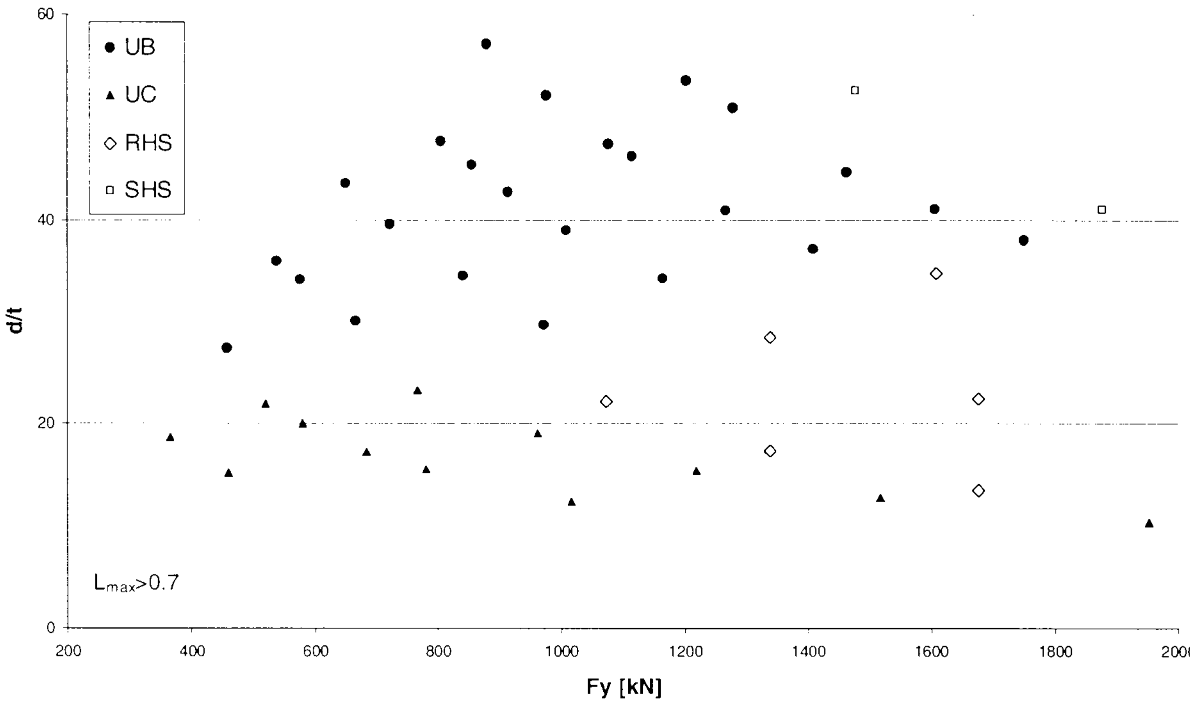

Figure 3-15: Slenderness and yielding load of standard sections

According to the Bradford and Azhari analyses, the UC, the very thick RHS-sections and very thick SHS sections have a τ_{cr} that tends towards τ_u and the UB-sections have a τ_{cr} that is not much higher than τ_y. Slenderness ratio is smallest for UC-sections for the same $P_{S,y}$, (Figure 3-15).

3.6.4 Conclusion

UC-sections are more suited for dissipating plastic energy in shear yielding.

In countries like Switzerland, which uses different standard sections, HEB and HEM sections should be considered for the knee element, SZS-C5 (1992).

3.7 Cumulative damage models

The structural failure of a section can be due to three different effects: local buckling, fatigue and brittle fracture. Buckling has been discussed in the previous section and can be eliminated with adequate stiffeners. Brittle fracture usually occurs in the connection areas. For beams yielding in shear the critical zones are away from the connections. This section presents some damage models concerning cyclic failure and especially low cycle fatigue.

3.7.1 High cycle fatigue

For high cycle fatigue (for number of cycles $> 10^4$) the cumulative linear Miner rule is often used to calculate the damage index D (when D reaches 1 failure of the element is considered to have occurred):

$$D = \sum_{i=1}^{k} \left(\frac{n_i}{N_{f,i}} \right) \tag{3.48}$$

where N_f is the number of cycles necessary to reach failure, which can be obtained with the Basquin law:

$$\Delta\sigma \cdot (N_f)^m = c_1 \tag{3.49}$$

where c_1 and m are material constants.

When the mean stress is not zero the Goodman rule gives an equivalent mean stress $\Delta\sigma_0$ applied from that gives the same number of cycles to failure as that of a $\Delta\sigma_m$ stress with zero mean stress:

$$\Delta\sigma_0 = \Delta\sigma_m \left(1 - \frac{\overline{\sigma}}{\sigma_{ts}} \right)^{-1} \tag{3.50}$$

where $\Delta\sigma_m$ is the applied stress range at mean stress $\overline{\sigma}$ and σ_{ts} the tensile strength.

3.7.2 Low cycle fatigue

High cycle fatigue affects structures under wind or traffic loads. Elements dissipating energy under seismic load are likely to fail due to low cycle fatigue. A large number of low cycle fatigue models exist. Some are modified high cycle fatigue models. Others add a term accounting for the damage due to the maximum excursion.

Ballio & Castigliani and Calado & Azevedo model

Ballio and Castigliani (1995) have proposed:

$$D = c\sum n_i \left(\frac{\Delta\delta_i}{\delta_y}\cdot\sigma(F_y)\right)^m \tag{3.51}$$

where n_i is the number of occurrences of cycles having an amplitude $\Delta\delta_i$, δ_y is the yield displacement and $\sigma(F_y)$ the stress level . c and m are constants depending on the fatigue strength category.

Similarly, Calado and Azevedo (1989 &1995) have proposed:

$$D = c\sum_{i=1}^{k}(\Delta\zeta_p)^m \tag{3.52}$$

where $\Delta\zeta_p$ is the plastic part of the normalized deformation, e.g. plastic strain $\Delta\varepsilon/\varepsilon_y$, rotation $\Delta\theta/\theta_y$ or deflection $\Delta\delta/\delta_y(=\mu)$.

From both models the following damage model can be derived:

$$D = c\sum_{i=1}^{k}\mu^m \tag{3.53}$$

Ballio and Castigliani (1994 & 1995) have performed cyclic tests on a large number of 1.6m long cantilevers beams of standard commercial cantilever sections ($HEA220$, $HEB220$), yielding in bending. In the tests deflections δ comprised in the range of $2\cdot\delta_y \leq \delta \leq 18\cdot\delta_y$ were imposed. They obtained excellent predictions using Equation 3.53 with $m = 2.28$, $c = 1/4708$ for $HEA220$ and $m = 3.34$, $c = 1/90754$ for $HEB220$.

From their results, it can be deduced that 25 cycles at ductility 10 is necessary to obtain failure for an $HEA220$ and 41 cycles for an $HEB220$.

$HEA220$ and $HEB220$ have a similar depth and width, but $HEB220$ has much thicker flanges and a thicker web. These tests seems to indicate that sections with slender flanges and webs will accumulate more damage than sections with bulkier flanges and webs.

Ballio (1995) also found that strain hardening effects are greater in $HEB220$ than in $HEA220$.

The Park & Ang and the Daali & Korol model:

Park and Ang (1985) have proposed:

$$D = c_1 \frac{\mu_{\max}}{\mu_m} + c_2 \cdot \sum \left(\frac{\mu_i - 1}{\mu_m} \right) \tag{3.54}$$

where $\mu_{\max}$ is the corresponding ductility for the maximal exursion and μ_m the monotonic ductility.

Similarly Daali and Korol (1995) have proposed:

$$D = c_1 \frac{\mu_{\max} - 1}{\mu_m - 1} + c_2 \cdot \sum \left(\frac{\mu_i - 1}{\mu_m - 1} \right)^n \tag{3.55}$$

They have also developed an empirical formula for estimating the monotonic ductility (in bending) as a function of geometric characteristics:

$$\mu_m = 1 - 9.2 \cdot \lambda + 10.71 \cdot \lambda^{\;0.293} \tag{3.56}$$

where $\lambda = \alpha_{fl} \cdot \alpha_w \cdot \alpha_l$, with α_{fl} the flange slenderness, α_w the web slenderness and α_l the lateral slenderness.

In Table 3.2 the monotonic ductility has been calculated for some 950mm long UC and UB sections using Equation 3.56.

We can see above that UC-sections are expected to fail at higher monotonic ductility than UB-sections.

Universal Column	μ_m	Universal Beam	μ_m
152x152x23	16	127x76x13	16
152x152x30	20	152x89x16	15
152x152x37	22	178x102x19	14
203x203x46	20	203x102x23	15
203x203x52	21	203x133x25	14

Table 3.2: Monotonic ductility

Energy based damage model

Damage models based on the energy dissipation H_{pl} of the hysteresis curves have been used for concrete structures and steel piers (Usami and Kumar 1998).

$$D = c \sum (H_{pl})^n \tag{3.57}$$

This model should give results similar to those based on ductility, as for an elastic perfect plastic structure the energy dissipation is proportional to $\mu - 1$.

3.7.3 Conclusion

From the experimental results found in literature, it can be deduced that UC-sections will have a higher low cycle fatigue resistance (in bending) than UB-sections.

3.8 Different knee element designs

Only very few sections of a reasonable length have a small enough shear strength (or a high enough bending strength) to yield in the shear mode. There is therefore an interest in modifying standard sections to vary the shear capacity to produce knee element that suit a particular structure.

It has been found that the sections the most likely to fulfil knee element requirements are the Universal Columns (UC). Therefore modifications were undertaken on UC $152 \times 152 \times 23$ and UC $152 \times 152 \times 30$, (the two smallest UC standard sections).

Reducing the shear yield load can be achieved by providing stress concentration or web weakening of the beam section. In this research it was decided to vary the yield capacity of a beam by weakening the web.

3.8.1 Beams with reduced web section

The shear capacity of a standard hot rolled section can be reduced by removing material from the web by flame cutting or by drilling holes. Drilling holes seems the most practical and reproducable way of reducing the web section and was adopted in the current research.

By drilling holes in the web, the section available to resist the shear force is reduced, additionally the holes provide stress concentrations. The yielding in shear should therefore start at a significantly lower load while the initial stiffness is only slightly reduced.

In this section, beam with holes in the web have been investigated by finite element analysis. Different hole arrangements have been evaluated.

Finite element modelling

The monotonic and cyclic response of centrally loaded built-in UC $152 \times 152 \times 23$ and UC $152 \times 152 \times 30$ sections with holes have been modelled using the finite element program *ABAQUS*. The meshing was performed with the software *I-DEAS*. Solid elements (10-noded tetrahedra) and shell elements (3-noded triangle and 4-noded quadratic elements) have been used. Models using solid elements are more accurate, but are computationally demanding. Models using shell elements, allow faster results to be obtained and create much smaller results files. Using symmetry conditions, only a quarter of the beam needed to be modelled.

Preliminary numerical results

For holes with diameters smaller than a certain size $d_{\min}$, significant stress concentration only takes place at the periphery of the hole, and the global knee element behaviour would hardly be affected. For holes with diameter greater than $d_{\min}$ and spaced at a reasonable distance s, a strip of plastic strain stretches between the holes, Figure 3-16, which affects the global knee element behaviour. From the finite element analysis it was found that $d_{\min} \simeq 10mm$ for UC $152 \times 152 \times 23$ and UC $152 \times 152 \times 30$ sections.

Oval-shaped holes were also analysed. Since oval-shaped holes are more complicated to create and their influence relative to the hole-area is not significantly different compared to circular holes, designs with oval-shaped holes were discontinued.

The subsequent research focused on the arrangement of circular holes and determining

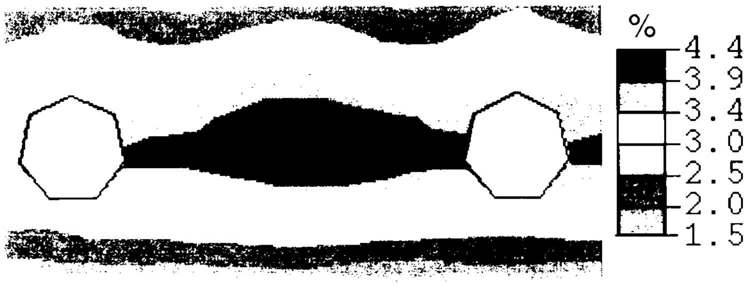

Figure 3-16: Plastic strain between two holes

the influence of hole spacing and hole diameters

First, beams with holes in a rectangular grid and beams with offset holes, Figure 3-17, were compared.

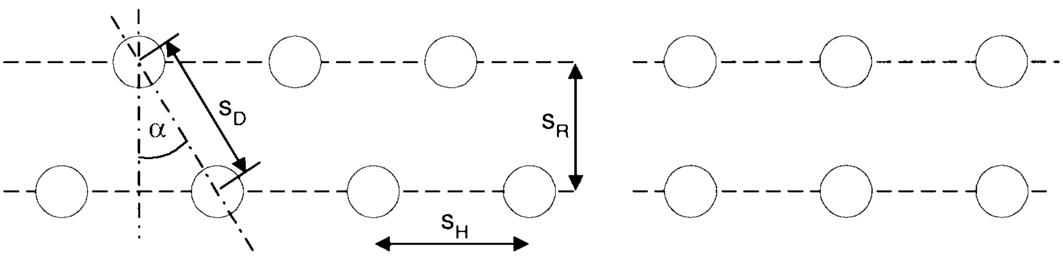

Figure 3-17: Offset hole rows and aligned hole rows

For the same imposed central deflection, higher plastic strain peaks were observed for the aligned displacement, a higher post-yielding stiffness and remaining strength capacity was observed for the offset row beam (the hole arrangements were chosen to make the initial stiffness and the yield load the same for both beams). The offset row arrangement is better if many rows are to be drilled, since the row spacing s_R for the aligned row needs to be greater than for an offset row. It is therefore believed that offset-row beams are more suitable and investigations were continued with that pattern.

The relationship between the geometric parameters in Figure 3-17 is given by:

$$\begin{aligned} \tan\alpha &= \frac{s_H}{2 \cdot s_R} \\ s_D &= \sqrt{\left(\frac{s_H}{2}\right)^2 + s_R^2} \end{aligned} \qquad (3.58)$$

Different angles for the arrangement of offset holes have been investigated. For value of s_H and s_R above $s_{\min.H}$ and $s_{\min.R}$ the initial stiffness is hardly affected. $s_{\min.H}$ and $s_{\min.R}$ depend of course on the hole diameter d. From the finite element analysis these minimum values are $s_{\min.R} \simeq 26mm$ and $s_{\min.H} \simeq 35mm$ for d in the range of 15 to 20mm. It was also found that for hole diameters larger than $d_{\max}$, the beam shows significant weakening, excessive deformation, which may favour crack initiation. From the numerical results $d_{\max} \simeq 25mm$ for UC 152 × 152 × 23 and UC 152 × 152 × 30 sections.

Figures 3-18 to 3-20 show the plastic strain for a central imposed deflection of 12mm for three different row spacing: $s_{R.1} = 52mm$, $s_{R.2} = 40mm$, $s_{R.3} = 26mm$. The hole spacing was $s_H = 52mm$ and the hole diameter $d = 20mm \Longrightarrow \alpha_1 = 26.5^\circ$, $\alpha_1 = 33^\circ$ and $\alpha_1 = 45^\circ$ (Equation 3.58). The beam is built-in at the ends and has a single stiffener in the centre. As before only a quarter of the beam needed to be modelled. Hole arrangement 1 produces essentially horizontal oval yielding zones between holes, but no yielding zones between holes in different rows. Hole arrangement 2 and hole arrangement 3 produce more lozenge shaped yielding zones because the adjacent rows are close enough to produce an interaction of stresses. This interaction enlarges the yielding zones. For hole arrangement 3, the plastic strain stretches vertically between the holes of row 1 and row 3 becomes even higher than the plastic strain stretching horizontally between holes of the same row.

All three beams possess almost the same force-displacement curves, differences are less than one percent. The plastic strains peak was the highest for hole arrangement 3. Additional numerical analysis showed that the "optimal" hole arrangement is when $\alpha \approx 30^\circ$ and $s_D \approx s_H$.

The maximum shear stress $\tau_{\max}$ in the web of a normal I-beam is given by (Frey, 1993):

$$\tau_{\max} = S \cdot \left[\frac{(D - t_{fl})^2}{8 \cdot I} + \frac{B \cdot t_{fl} \cdot (D - t_{fl})}{2 \cdot I \cdot t_w} \right] \tag{3.59}$$

where I, B, D, t_{fl}, t_w are respectively the stiffness the height, the width, the flange- and web-thickness.

An increase of the shear stress in the web is induced by the reduction of the vertical section but also by the reduction of the horizontal section. It is interesting to determine if it is the hole spacing as in Figure 3-20 or if it is the row spacing as in Figure 3-18 that is the dominant parameter.

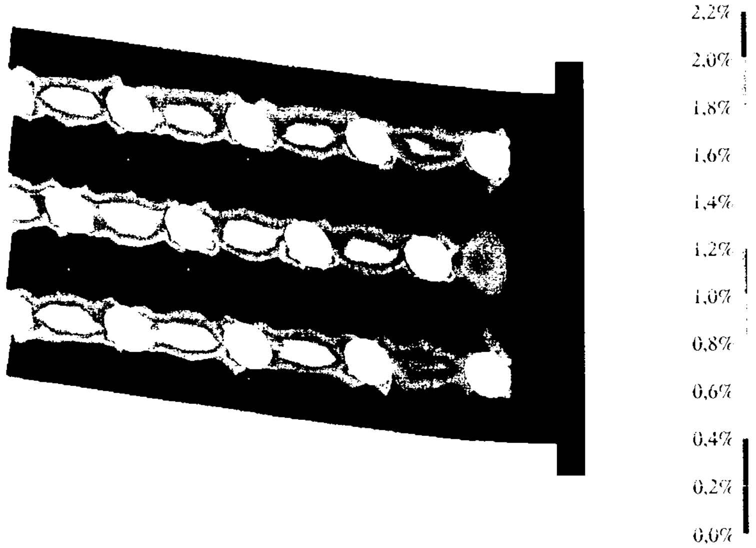

Figure 3-18: Plastic strain for hole arrangement 1

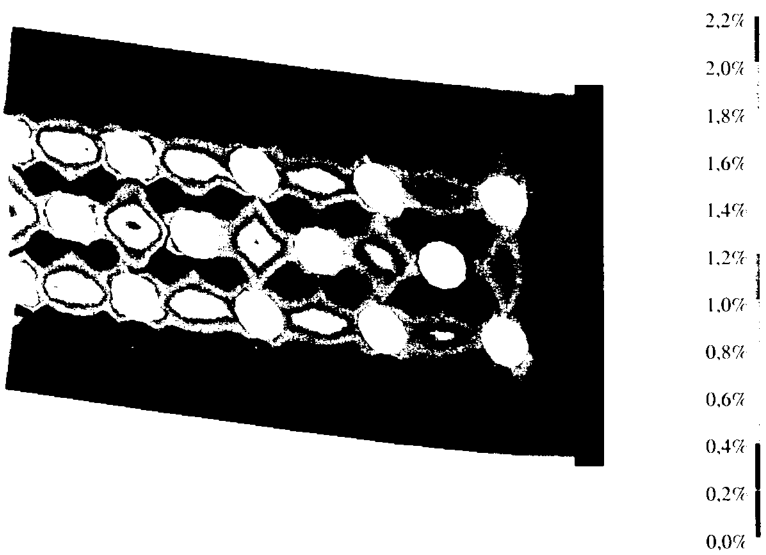

Figure 3-19: Plastic strain for hole arrangement 2

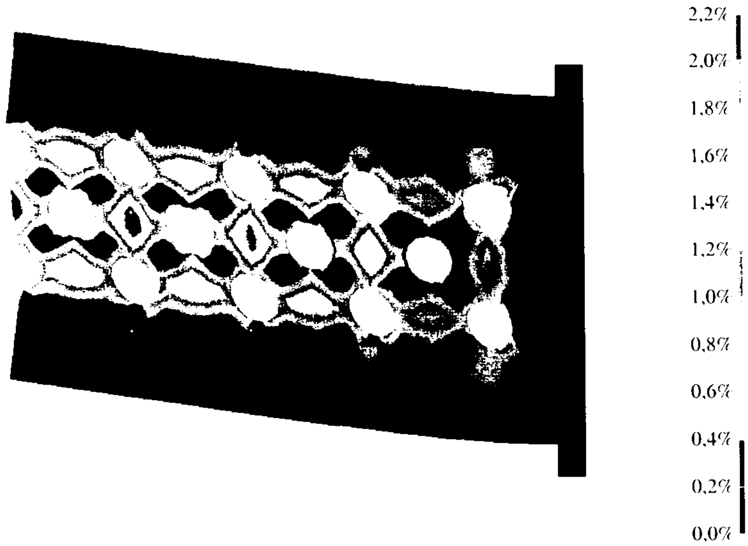

Figure 3-20: Plastic strain for hole arrangement 3

Since the shear force is constant along the beam we can write:

$$\overline{\tau_{reduced\_area}} \cdot A_{reduced\_area} = \overline{\tau_{full\_area}} \cdot A_{full\_area} \tag{3.60}$$

Taking the web area between two hole centres, the shear stress due to the hole spacing will increase approximately to:

$$\tau_{\max,H} = \tau_{\max} \cdot \frac{s_H}{(s_H - d)} \tag{3.61}$$

and due to the row spacing (offset row) will increase approximately to:

$$\tau_{\max,R} = \tau_{\max} \cdot \frac{s_R}{(s_R - d/2)} \tag{3.62}$$

Therefore the hole spacing effect is dominant when:

$$\frac{s_H}{(s_H - d)} > \frac{s_R}{(s_R - d/2)} \tag{3.63}$$

For a UC 152 × 152 × 23 section, with $d = 20mm$, $s_H = 52mm$, s_R has to be smaller than 26mm for the vertical effect to become dominant. But the vertical mode does not seem to have advantages over the horizontal mode, since generally hole arrangements giving that mode have in total a smaller effective dissipative area then for the ones giving the horizontal mode.

3.9 Specimens for physical testing

From the preliminary numerical results four different specimens with holes were prepared for physical testing. Normal sections (without holes) and sections with stiffeners were also prepared for comparison.

All specimens were 950mm long, including the two 400mm×400mm×12.5mm end-plates that were connected with eight (M24) bolts to the loadcells. The specimens were connected to the loading beam with eight (M16) bolts, as shown in Figure 3-21. The bolts used were all grade 12.9.

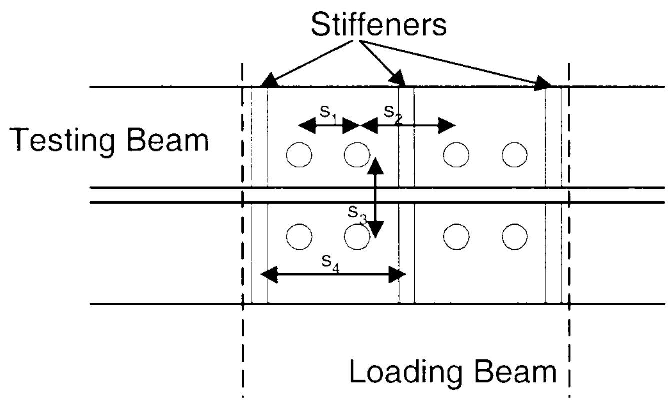

Figure 3-21: Detail of the specimen-loading beam connection ($s_1 = 40mm$, $s_2 = 70mm$, $s_3 = 45mm$, $s_4 = 112mm$)

For the specimens without holes three full 12.5mm thick stiffeners on both sides were placed at the centre, Figure a) (only half of the beam is represented, since it is symmetric), in order to redistribute the load transmitted by the loading beam. For the specimen with holes one full 12.5mmm thick stiffener and two small triangular 9.4mm thick stiffeners were placed, Figure 3-22 c).

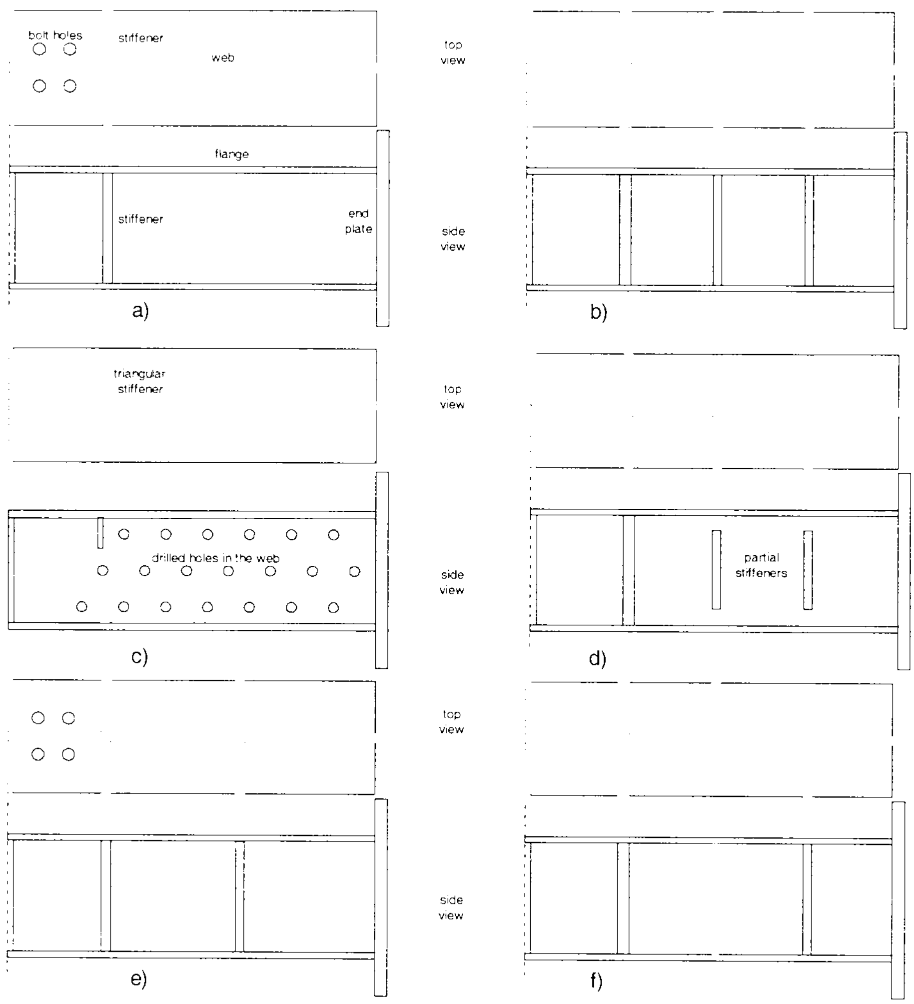

Figure 3-22: Half beams of different specimens for physical testing

Specimens 1 to 4

For these four specimens UC 152 × 152 × 30 sections were used, and the hole diameters, hole and row spacing are given in Table 3.3. The web area removed by hole drilling is also given. Specimens 1 and 2 had the same hole arrangement, Figure 3-22 c).

Specimen 5, the reference beam

Specimen 5, was a simple UC 152×152×30 section without holes and served as a reference beam, Figure 3-22 a).

N	$d_{hole}[mm]$	$s_H[mm]$	$s_R[mm]$	n_{row}	$n_{hole.total}$	$A_{holes}[mm^2]$
1	12.5	52	45	3	40	4908
2	20	52	45	3	40	12566
3	15	100	36	4	26	4594
4	15	100	25	5	38	7068

Table 3.3: Specimen with holes

Specimen 6

Specimen 6, was a UC 152 × 152 × 30 section with four additional full stiffeners (9.4mm thick) on both sides, Figure 3-22 e). This divided the web into clear rectangles of approximately 100mm×123mm (distance between the weldbeads of the stiffeners × depth between flange fillets).

Specimens 7 to 10

Specimens 7 to 10 were UC 152 × 152 × 23 sections. Specimen 7 was similar to specimen 5. Specimen 8 had four additional partial stiffeners (9.4mm thick), leaving a gap of 10mm between the flanges and the stiffeners, Figure 3-22 d). Specimen 9 had two additional full stiffeners, (9.4mm thick), Figure 3-22 e). The clear web rectangle was 160mm×123mm. Specimen 10 had four additional full stiffeners (9.4mm thick), but contrary to specimen 6 they were only placed on one side, Figure 3-22 f).

Specimens 11 and 12

Specimens 11 and 12 were UB 203×102×23 sections. Specimen 11 was similar to specimen 5. Specimen 12 was similar to specimen 6. The clear web rectangle was 100mm×169mm.

Remarks

All the specimens proposed are sections to be tested about their strong axis. Sections about their minor axis possess low yield load and high out-of-plane stability. However, observations made from a back to back channel 127 × 64 × 19.4 tested about its weak axis proved that it is extremely difficult to provide an adequate connection at the mid-point of the knee element and that the flanges rotated excessively when the section was loaded. This approach was therefore not considered suitable and abandoned.

Chapter 4

The testing facilities

4.1 Introduction

Nineteen knee-elements of twelve different designs were tested at the Structural Dynamics Laboratory at Oxford University. Since the testing and measurement equipment and method used were quite challenging and an important part of the present research they are presented in this chapter separately from the test results.

4.2 The structural dynamics laboratory

All the equipment is mounted on a large concrete base isolation block, to reduce transmission into the surrounding building of vibrations set up by a test. A steel rig, bolted onto anchors sunk into the concrete isolation block, has been built to hold a 950mm long specimen. This length has been estimated to be roughly the optimal size for a knee element in a knee braced frame, Bourahla (1990). The specimen is loaded at its centre by a single loading beam, driven by up to four actuators positioned in a line. Two loadcells measure the axial and shear forces and the bending moment at the ends of the specimen. The loadcell design, development and calibrations are described in Section 4.6.

Hydraulic power is provided by a large Dartec power pack comprising three pumps, each capable of delivering a flow rate of $90\ell/\text{min}$. For short bursts additional flow is provided by a bank of accumulators, which can deliver a further 100ℓ in twenty seconds. The flow is fed via two substations to Instron servo-hydraulic actuators. Two actuators have a dynamic load capacity of 100kN and the other two of 250kN and all have strokes of ±125mm. At a slow driving rate the actuators can apply respectively a load of 124kN and of 330kN. All four actuators put in parallel give a dynamic load capacity of 700kN and at a slow driving rate a load of 908kN.

The actuators are controlled by a Labtronic 8800 control console, manufactured by Instron-Schenck Testing Systems. The controller is in turn driven by Instron RS Plus software running on a PC, which communicates with the 8800 unit via a GPIB interface. Ramp, cyclic or specified history curves of either displacements or forces can be imposed. In addition an innovative real time substructure testing method, which is described in section 4.9, can also be run on the system.

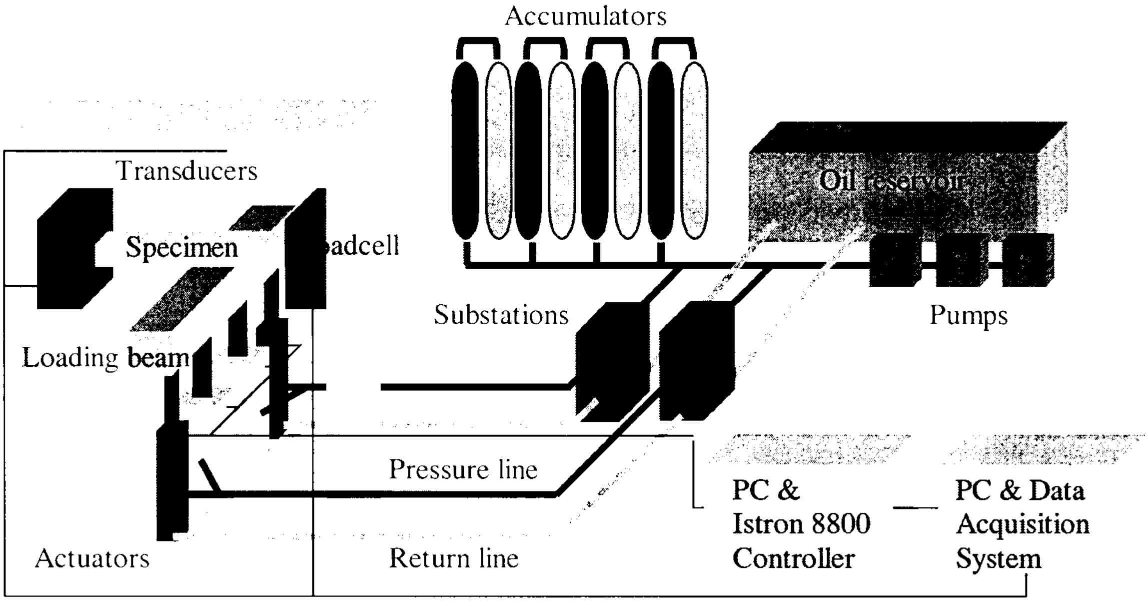

Figure 4-1: Schematic of the structural dynamics laboratory

The actuators are equipped with high precision loadcells and displacement transducers. In addition 11 cable extension position transducers spanned between the top beam of the rig and the specimen to record its deflection at multiple points and its torsional rotation in the middle.

The acquisition system consists of a 30 channel BEDO programmable amplifier system controlled by Hewlett Packard's *HP-VEE* software from a Dell P200 PC with a Microstar A-D card. Each channel can be set up for half or full bridges, with a 5V or

10V excitation, with an acquisition frequency up to 200Hz and can be amplified up to 1000 times. Acquisition frequency was set to 20Hz and increased to 50 Hz when using the thermal imaging system. Smoothing filters or cut-off filters are also available, but were not used in the experimental tests presented in this thesis. Nine channels are necessary for each of the two rig loadcells, two channels for each of the actuators used (one for the displacement, one for the force), one per cable extension position transducer and one for the thermal film sensor described in Section 4.8. In total 38 channels would have been necessary to monitor all the instruments. Since only 30 were available, in some tests only three or four of the eleven cable extension position transducers were used.

4.3 Cable extension position transducers

Eleven Celesco PT101 cable extension position transducers (Celesco, 2001), as shown in Figure 4-2, were available. They have an extension of 500mm and an accuracy of ±0.25%.

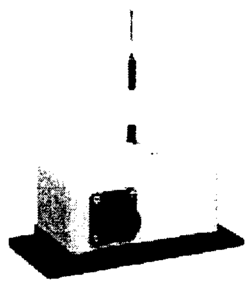

Figure 4-2: Cable extension position transducer

The transducers were placed as shown in Figure 4-3. Transducers b and h, at the ends of the specimen are used as reference points. Transducers d, e and f give the central deflection and the torsional rotation at mid span. Transducers c and g give the deflection at quarter and three quarter span. Transducers a and i, on the front plate of each loadcell, are used to detect eventual slippage of the bolted loadcell-specimen connection. Transducers j and k, horizontally placed, give the change in length of the specimen and the relative rotations of the loadcells. The testing rig had significant flexibility and rotations and displacements are not negligible. The stiffness of the rig is determined in Section 4.4.

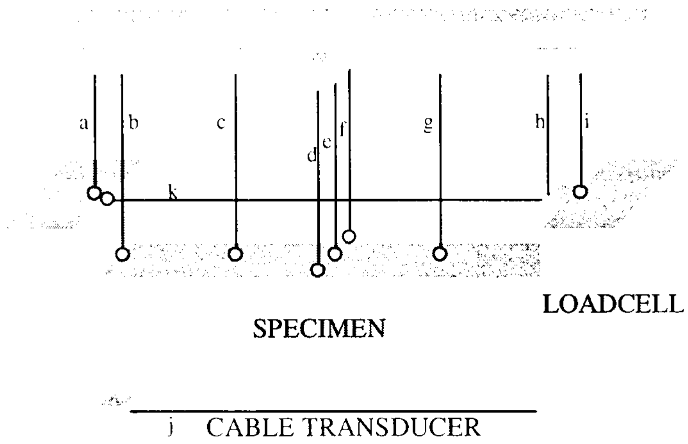

Figure 4-3: Transducer disposition on the testing rig

Under a static load with displacement of magnitude ±60mm the global accuracy is estimated at 0.3mm. But during a dynamic loading, vibrations in the cable affect the readings. No electronic filters were set in the $HP - VEE$-software, because the filtering would cut off a part of the real displacements and the original data would not be retrievable.

A fast fourier transform (FFT) on the acquired data was performed after the test. The FFT will give the frequency spectrum up to half of the sample frequency. A radical low-pass filter, with infinite attenuation for the frequencies above the cut-off frequency, can be applied to the data, in order to eliminate the perturbation created by the vibration.

In the experimental tests, mainly cycles of displacement at constant amplitude and constant frequency were imposed. Differences from a perfect sine wave can been seen in the real history deflection curve of the specimen, Figure 4-4. The differences are caused by the testing rig flexibility and small delays, which occur if the actuators reach their dynamic capacity limit. Even taking these irregularities into account, only a few frequencies are needed to approximate the displacement time-history. By filtering the data of a 0.5Hz cyclic test with a cut off frequency at 2.5Hz, most of the vibration perturbations are eliminated, as Figure 4-4 shows. Vibrations are a significant perturbation for small deflections, but become less important for larger deflections (e.g. for ±30mm central deflections the vibration perturbation remains smaller than ±0.7mm). This filtering method can not be applied when using the real time substructure testing (described in Section 4.9) with an earthquake as external load, since the real displacement spectrum may have important amplitude in the whole frequency band.

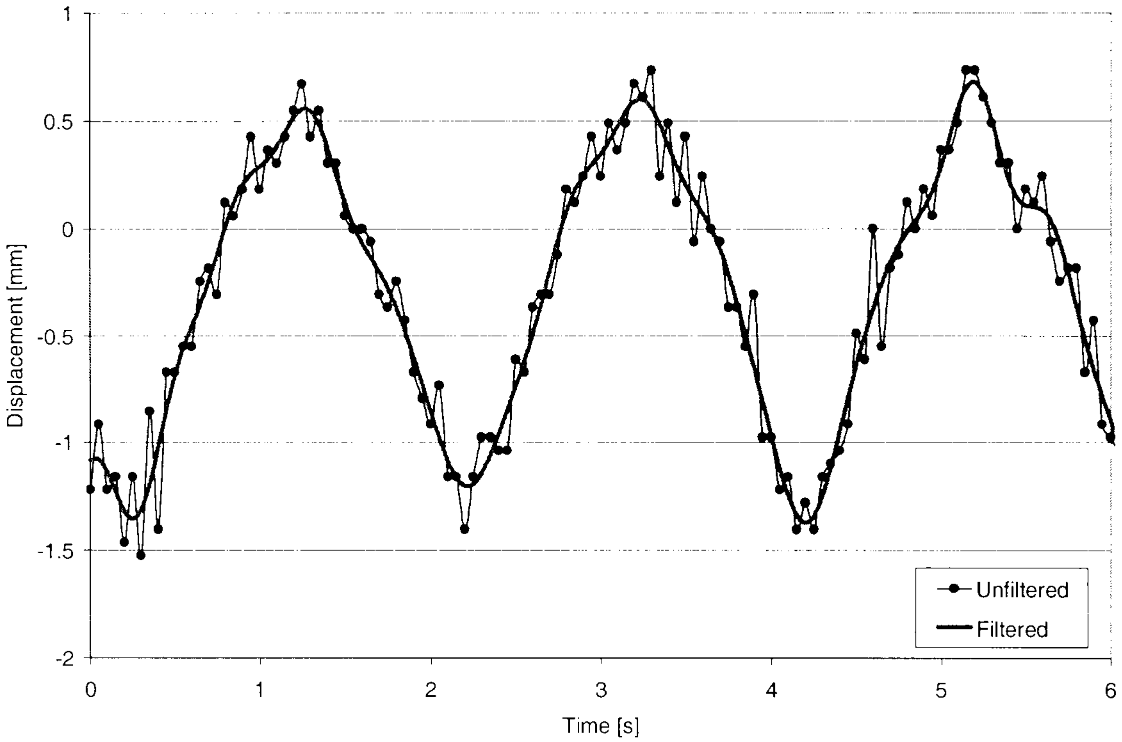

Figure 4-4: Original and filtered data of the knee element central deflection (cyclic test frequency =0.5Hz, filter cut-off frequency= 2.5Hz, acquisition frequency=20Hz)

4.4 Flexibility of the testing rig

As mentioned in Section 4.3, the rig in which the specimen is mounted is far from being rigid and significant rotations and displacements occur at the ends of the specimen. The change in length of the specimen and the relative rotation of the two loadcells were recorded. At the same time the horizontal forces and moments were measured. Data from three different knee element tests, (cyclic imposed displacement with increasing amplitude) were available.

It was assumed that the test rig stiffness was symmetric. The axial forces were symmetric since the specimen was loaded vertically. The moment measured by the two loadcells did not differ by more than a few percent in the tests selected. The change in length δ of the specimen and the relative rotation θ of the two loadcells are given by Equation 4.1.

$$\begin{bmatrix} \delta \\ \theta \end{bmatrix} = \begin{bmatrix} f_{N\delta} & f_{M\delta} \\ f_{N\theta} & f_{M\theta} \end{bmatrix} \begin{bmatrix} N \\ M \end{bmatrix} \tag{4.1}$$

where M is the average moment and N the average axial force in the two loadcells

By minimising the square of the errors of Equation 4.1, specifying $f_{M\delta} = f_{N\theta}$, the flexibility coefficients of the test rig can be deduced and are given in Table 4.1.

$f_{N\delta} = 1.7\cdot10^{-2}$ mm/kN	$f_{M\delta} = -1.8\cdot10^{-2}$ mm/kNm
$f_{N\theta} = -1.8\cdot10^{-5}$ rad/kN	$f_{M\theta} = 1.4\cdot10^{-4}$ rad/kNm

Table 4.1: Flexibility coefficients of the test rig

Figure 4-5 shows a) the sign convention, b) the deformation of the test rig due to tension in the specimen and (c) the deformation of the test rig due to the ends moments.

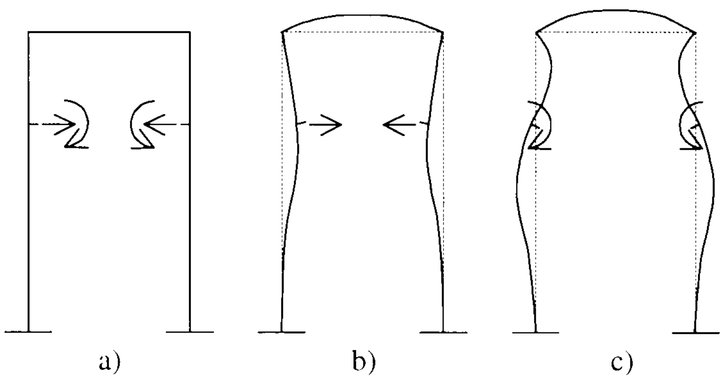

Figure 4-5: Flexibility of the testing rig

4.5 Problems and modifications

Unfortunately, the anchors which the test rig and the actuator base-plates were bolted on to, frequently failed at a load of less than half of that the manufacturer guaranteed. This interrupted a number of tests before their failure. The rig had to be shifted onto undamaged anchors. Different anchor shapes and different adhesives (e.g. epoxy compounds) have been tried out without much more success.

Originally the set up was made for using only two actuators. For the specimen designed by the author, it was foreseen that the loading capacity would need to be increased. Therefore the loading beam was extended and reinforced in order to use up to four actuators. Two new, more rigid, base-plates for the actuators were put in place. Reinforcement beams connecting the actuator's base-plates to the test rig were put in place to redirect a part of the vertical forces and therefore reduce the tension in the anchors. The reinforcement did work satisfactorily, and the test rig did not need to be moved any more until completion of the testing campaign.

Even if the testing rig frame itself has not been modified, the flexibility coefficients given in Table 4.1 have varied, since the rigidity of the footing and the anchors have changed. The flexibility coefficients have been therefore recalculated for each test.

4.6 Loadcells

4.6.1 History and design

Accurate measurements of the end forces on the specimen were necessary to compare to numerical and theoretical predictions. Early calculations showed that forces might be as large as 780kN in the axial direction, 350kN in shear and 200kNm in bending. An important requirement was that the loadcell should be as slim as possible. A wide loadcell would significantly increase the lever arm of the applied load and thus decrease the effective rotational stiffness of the loading frame. The loadcell would also have to provide a rigid connection between the 400mm square end plates of the specimen and the support frame.

Although the need for multi-axial force and moment measurement in structural testing is widespread, no commercially available loadcell could be found which met these design parameters. Purpose-made loadcells were therefore designed and built within the Oxford research group, Blakeborough et al. (2002). The author participated in the calibration and improvement phase of this process. Each loadcell comprises three spring elements sandwiched between two 50 mm thick plates as shown in Figure 4-6. Figure 4-7 shows the spring elements mounted on the cover plate before the back plate was mounted.

Each element is strain gauged to measure its deformations both normal to the plane of

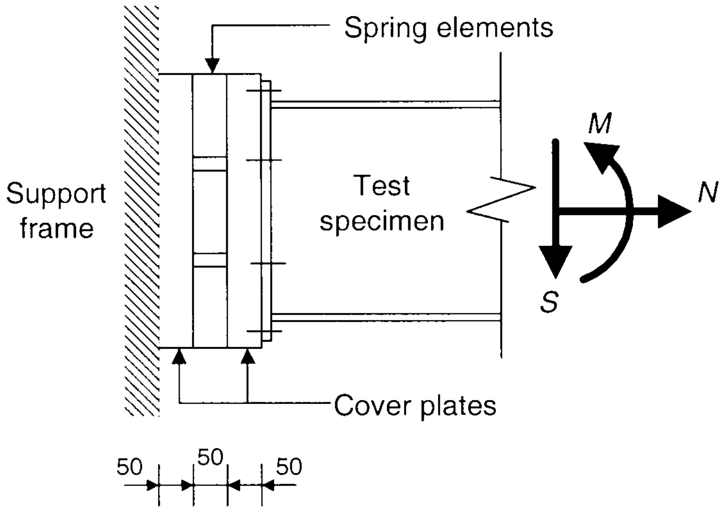

Figure 4-6: Shematic of the loadcell

the loadcell (i.e. corresponding to an axial force in the test specimen) and in the plane of the loadcell (i.e. the shear deformation). Each element is designed to behave as a double spring. The element is machined from a solid steel plate of dimensions 400×125×50mm thick. The front and back faces are each divided into five sub-sections by four semi-circular grooves, and alternate faces are recessed by a small amount. When the loadcell is assembled, two of the five sub-sections come into contact with the front plate, the other three lengths with the back plate, Figure 4-8. A normal or shear load applied to the element via the cover plates must follow a load path from the front contact faces to the back ones, via the four narrow sections between each pair of semi-circular notches. Most of the deformation occurs in these notched regions, since the notches both reduce the cross-sectional area to approximately 50% of that of the remainder of the plate, and act as geometric stress raisers.

4.6.2 Strain gauging

All strain gauges used were 45° double chevrons, designed to measure shear strain. For axial force measurement within each element one gauge was fixed measuring the shear strain on the top and bottom edges between each pair of notches and for shear force measurement two gauges were fitted in the root of each notch at the third points across the face of each element, as shown in Figure 4-9. Thus each element carried 24 gauges,

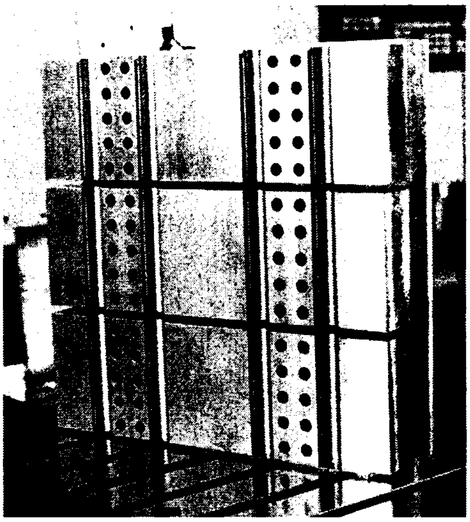

Figure 4-7: Photo of the three spring elements mounted on the cover plate

16 for shear and 8 for axial force measurement. The gauges were connected in full bridge circuits so as to sum each group of gauges, thus maximising the measured quantities and nulling the unwanted components. To measure the shear force, all the half chevrons on one face of an element showing positive strain under a positive shear load on the loading face were wired into one arm of a bridge, and all those showing negative strain into another. This arrangement was copied on the opposite face of the element to complete the four arms of the bridge.

Initially it was intended to use a similar bridge arrangement for axial force measurement, so as to give a single axial force output for each element. However, the author showed that this led to inaccurate bending moment results, since it was not possible to account for the variation of axial force across each element in the moment calculation. The author therefore proposed to connect the axial force gauges at the top and bottom of each element into separate bridge circuits, giving two separate axial force outputs per element.

4.6.3 Calibration

Calibration was performed on the fully assembled loadcell.

Two different types of calibration test were used. The first, referred to as the axial test, is shown in Figure 4-10 a). The loadcell was mounted horizontally in a Denison

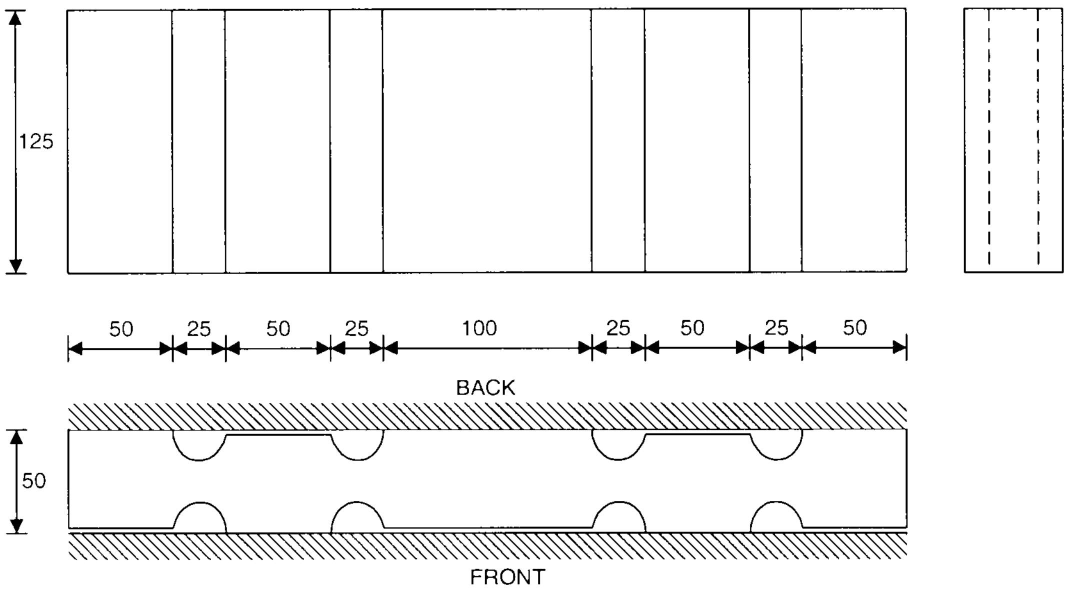

Figure 4-8: Loadcell element details

testing machine and a vertical load was applied. The loadcell was subjected to three cycles of amplitude 500kN, applied in 50kN steps. Three axial tests were performed, with the eccentricity, e, of the load from the loadcell centre-line varied between tests.

The second type of test, referred to as the cantilever test, is illustrated in Figure 4-10 b). The loadcell was mounted in a test rig and a short, steel cantilever was attached to it. Three cycles of vertical load were then applied to the cantilever using a hydraulic actuator. Three cantilever tests were performed, using different combinations of load, P, and lever arm, d, so as to vary the moment to shear ratio between tests.

The complete set of six calibration tests is summarised in Table 4.2.

Each test was given equal weighting in determining the calibration coefficients. The outputs from the loadcell comprised three voltages V_{S1}, V_{S2} and V_{S3} corresponding to the shear forces S_1, S_2 and S_3 in the three elements and six voltages V_{N1} to V_{N6} corresponding to the axial forces N_1 to N_6 in the top and bottom parts of each element. Each axial force is assumed to act at a distance a from the centre-line of the element, as shown in Figure 4-10 c).

The total shear and axial forces measured by the loadcell are then given by Equations 4.2 and 4.3.

$$S = S_1 + S_2 + S_3 = \sum_{i=1}^{6} C_{Si} \cdot V_{Si} \tag{4.2}$$

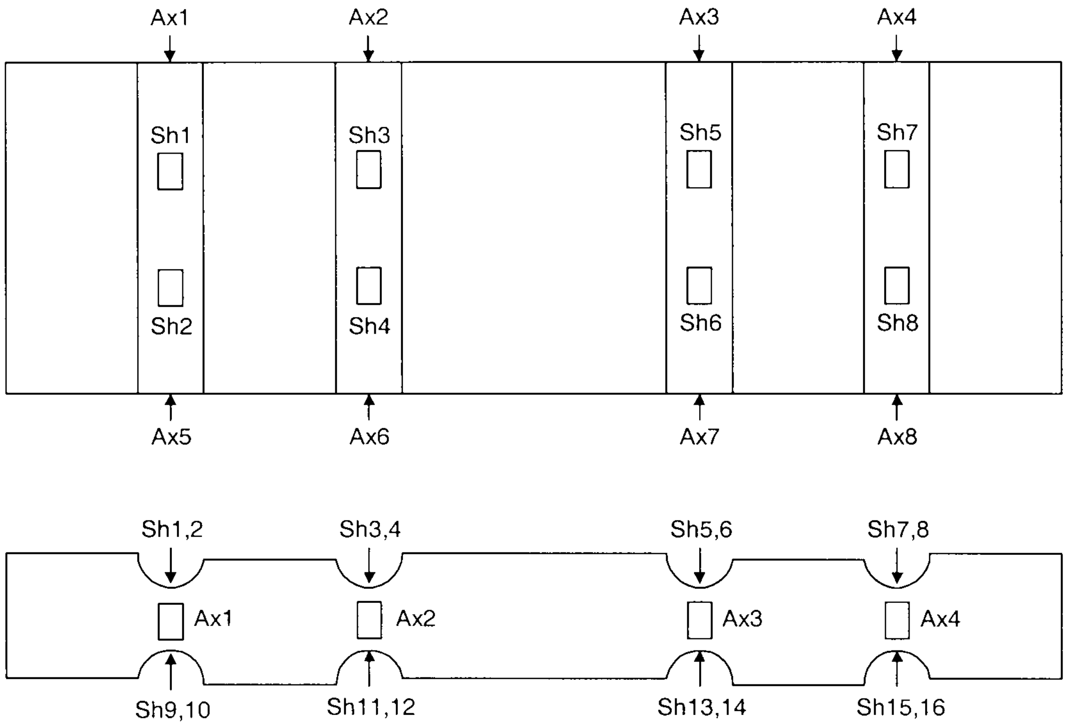

Figure 4-9: Strain gaging of the loadcell element

Test title	Details
Axial test 1	Load applied at $e = -0.138$m from the centre-line of the loadcell
Axial test 2	Load applied at the centre-line of the loadcell ($e = 0$)
Axial test 3	Load applied at $e = +0.138$m from centre-line of the loadcell
Cantilever test 1	Load of $P = 250$kN applied at $d = 0.13$m from front face of loadcell
Cantilever test 2	Load of $P = 200$ kN applied at $d = 0.28$m from front face of loadcell
Cantilever test 3	Load of $P = 150$kN applied at $d = 0.515$m from front face of loadcell

Table 4.2: Loadcell calibration tests

$$N = N_1 + N_2 + N_3 + N_4 + N_5 + N_6 = \sum_{i=1}^{6} C_{Ni} \cdot N_{Ni} \tag{4.3}$$

Appropriate values of the calibration coefficients C_{Si} and C_{Ni} were found by minimising the squares of the errors between the applied shear and axial forces in the calibration tests and those measured by the loadcell. For the axial forces, excellent results were achieved by using the same calibration coefficients for the two channels on a single element. However, it was found that slightly different calibration coefficients were required for tensile and compression loads – this is unsurprising, since the load path between the sensor elements and the cover plates differs slightly between the tensile and compression cases. To date,

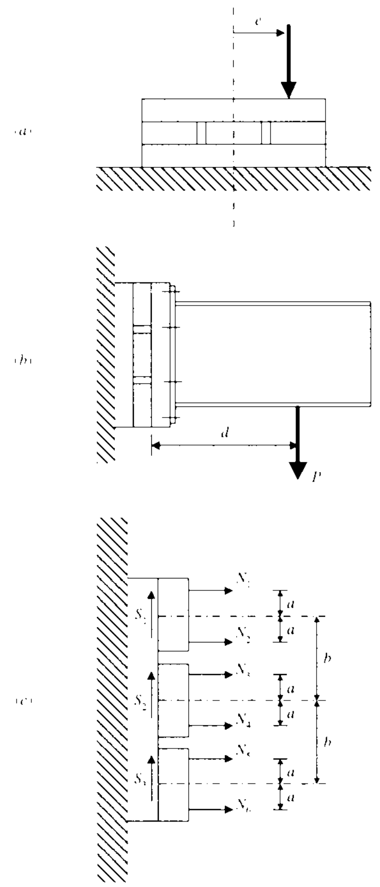

Figure 4-10: Loadcell calibration tests

two loadcells have been manufactured. The coefficients used for Loadcell 1 and Loadcell 2 are shown in Tables 4.3 and 4.4 in [kN/V].

LC1 Shear:	LC1 Axial:	Tension	Compression
$C_{S1} = 63.0$	$C_{N1}, C_{N2} =$	45.0	41.0
$C_{S2} = 60.3$	$C_{N3}, C_{N4} =$	44.0	40.0
$C_{S3} = 61.4$	$C_{N5}, C_{N6} =$	44.0	40.3

Table 4.3: Calibration coefficient for LoadCell 1

Lastly, referring to Figure 4-10, the moment on the loadcell is given by Equation 4.4.

$$M = a \cdot (N_1 - N_2 + N_3 - N_4 + N_5 - N_6) + b \cdot (N_1 + N_2 - N_5 - N_6) \tag{4.4}$$

The distance b between element centre-lines is 137.5mm. The value of a was found by minimising the squared error between the applied and measured moments. This yielded a=30mm for Loadcell 1 and a=31mm for Loadcell 2.

LC2 Shear:	LC2 Axial:	Tension	Compression
$C_{S1} = 67.0$	$C_{N1}, C_{N2} =$	43.6	41.7
$C_{S2} = 64.8$	$C_{N3}, C_{N4} =$	41.5	39.3
$C_{S3} = 64.3$	$C_{N5}, C_{N6} =$	40.8	39.0

Table 4.4: Calibration coefficient for LoadCell 2

The outputs from the calibration tests on Load Cell 1 using the above coefficients are shown in Figures 4-11 to 4-13, which show results for axial force, shear force and bending moment respectively. In each case the applied load and the loadcell output are plotted on common axes in the upper graph, with the lower graph showing the differences between the two plotted at larger scale. The level of agreement achieved is generally very good.

The maximum error as a proportion of the peak applied load is 5.0% for axial force, 3.2% for shear and 4.8% for moment. Over most of the range of operation the errors are much smaller than this.

Figure 4-12 shows that, in the first two axial calibration tests on Loadcell 1, some shear was unexpectedly generated in the loadcell elements. This is thought to be due to a slight error in the test set-up rather than a genuine interaction effect within the loadcell. In the calibration of Loadcell 2 great care was taken in the test set-up and no significant shear measurement was read. Careful studies have revealed no axial/shear interaction effects during the subsequent use of Loadcell 1 and Loadcell 2.

4.6.4 Implementation

Knee-element testing allows a further check on the performance of the loadcells, since the acquisition of forces and moment are redundant. Figure 4-14 shows the forces acting on the knee element as measured by the actuator loadcell and the two multi-axial loadcells. For equilibrium we would expect the horizontal force, vertical force and moment to be zero. Any deviation from these equilibrium conditions is likely to be largely due to errors in the loadcell readings.

$$\begin{aligned} &N_R - N_L = 0 \\ &P - S_R - S_L = 0 \\ &M_R - M_L - (S_L - S_R) \cdot L/2 = 0 \end{aligned} \tag{4.5}$$

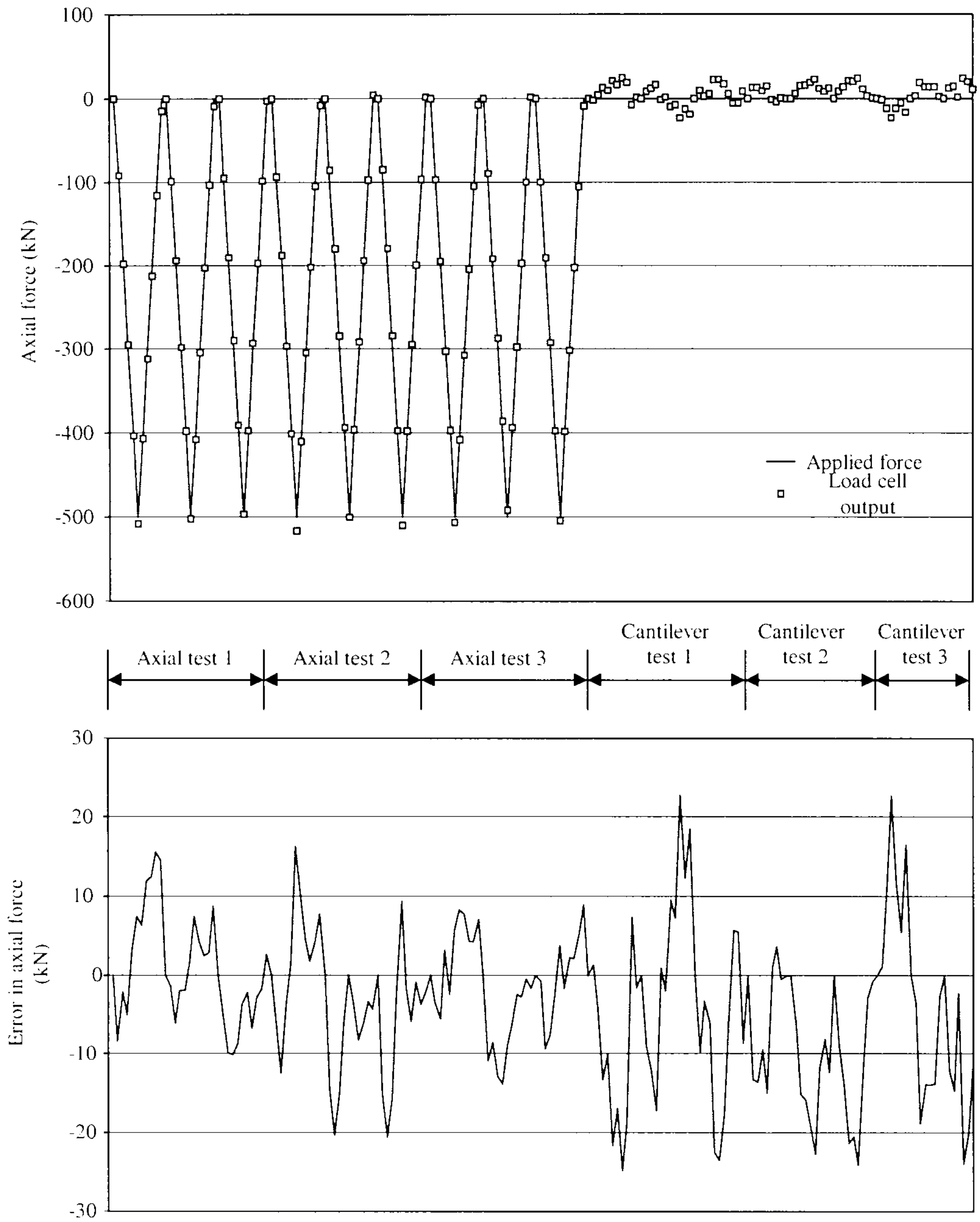

Figure 4-11: Calibration test: Axial force

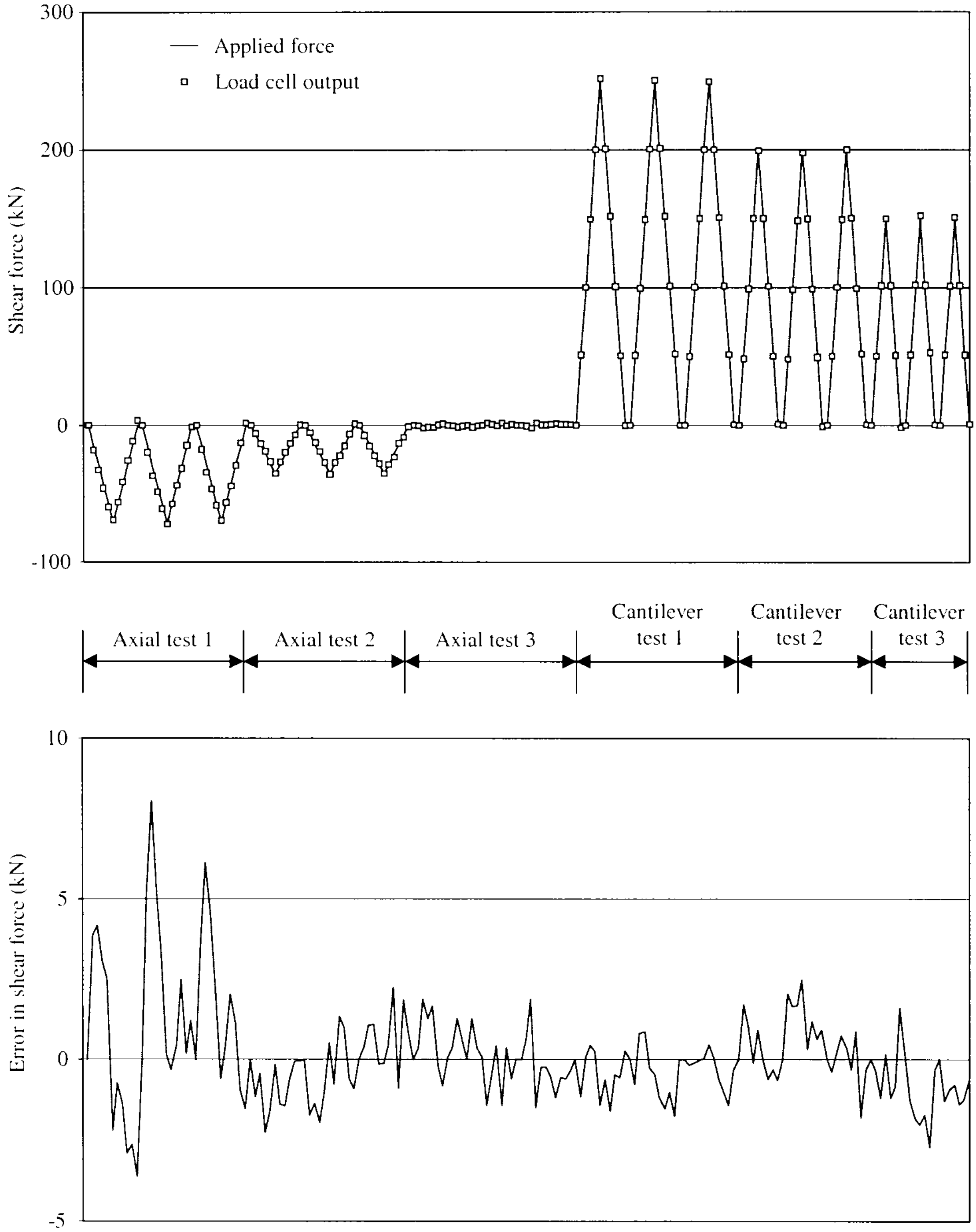

Figure 4-12: Calibration test: Shear force

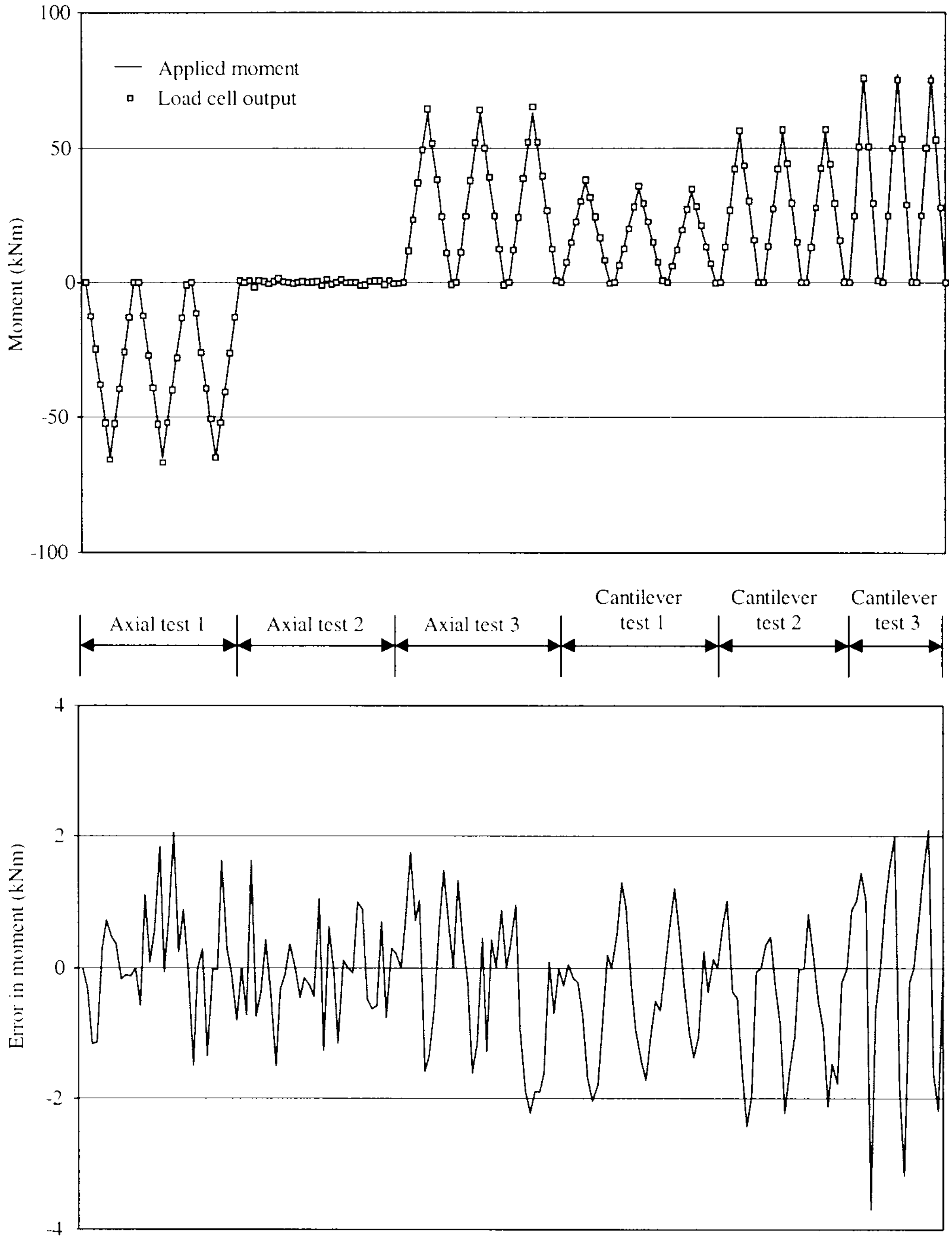

Figure 4-13: Calibration test: Moment

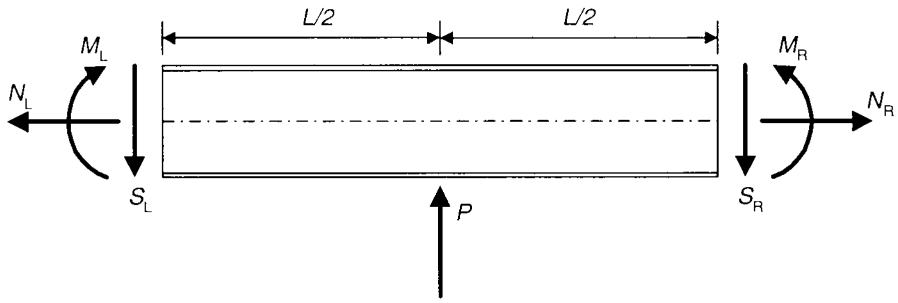

Figure 4-14: Equilibrum check of the force acting on a specimen

Figure 4-15 a) shows for a specimen undergoing large excursions into the plastic range but still behaving in a stable fashion. The variations in axial force at either end of the element, as measured by the loadcells, are shown together with the error in horizontal equilibrium (i.e. the amount by which Equation 4.5 is not satisfied). Similarly, Figure 4-15 b) shows the shear forces at either end and the vertical equilibrium error and Figure 4-15 c) shows the end moments and the overall moment equilibrium error. In all cases the error term remains small throughout.

It can be seen from Figures 4-15 a) to c) that the load distribution in the knee element has remained roughly symmetrical in this test, despite the high degree of plasticity present. Comparable levels of accuracy were found in a wide variety of knee element tests, including tests at higher loading rates where the element is undergoing a sudden and highly non-symmetrical buckling failure, Figure 4-16 a) to c).

4.6.5 Conclusion

The multi-axial loadcells have been successfully calibrated under both axial compression and combined shear and bending loads, and have been found to perform accurately and reliably in an extensive series of dynamic tests on steel knee elements. The loadcells were crucial for the analysis and the understanding of the experimental testing of knee-elements.

4.7 Thermal imaging system

An Agema 880 thermal imaging camera, shown in Figure 4-17, was made available for two months from the EPSRC loan pool.

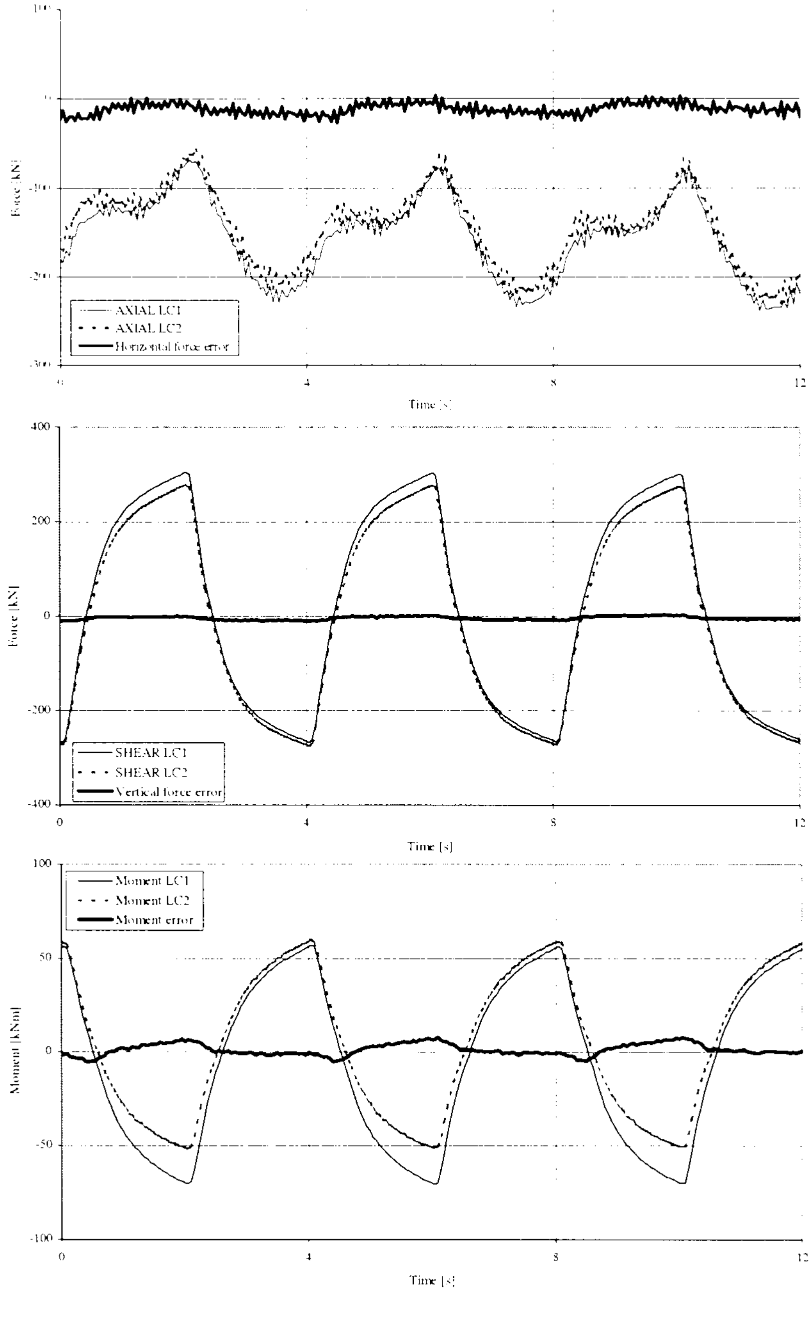

Figure 4-15: Example 1 of Axial, Shear and Moment measerements

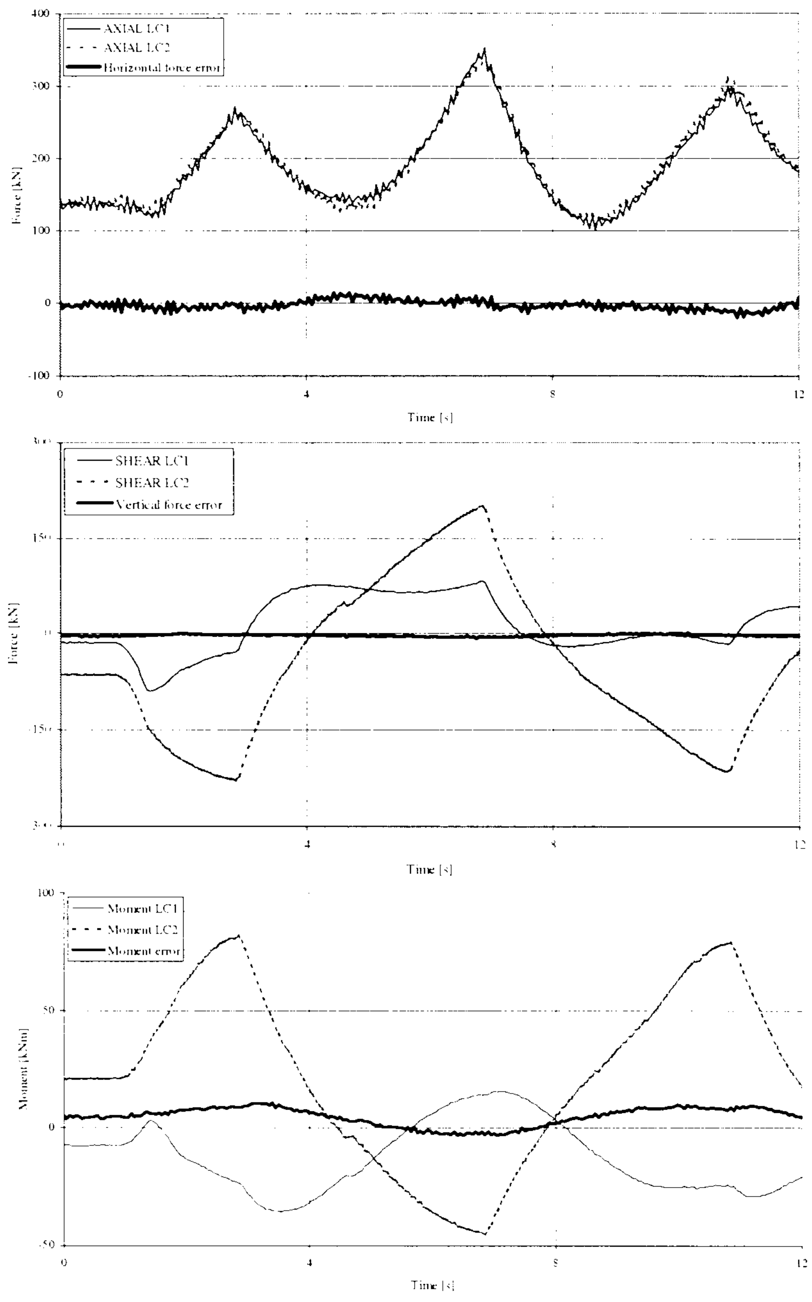

Figure 4-16: Example 2 of Axial, Shear and Moment measurements.

The Agema 880 is a cryogenically cooled long wave analysis system with a temperature range of $-20^{\circ}C$ to $+1500^{\circ}C$.

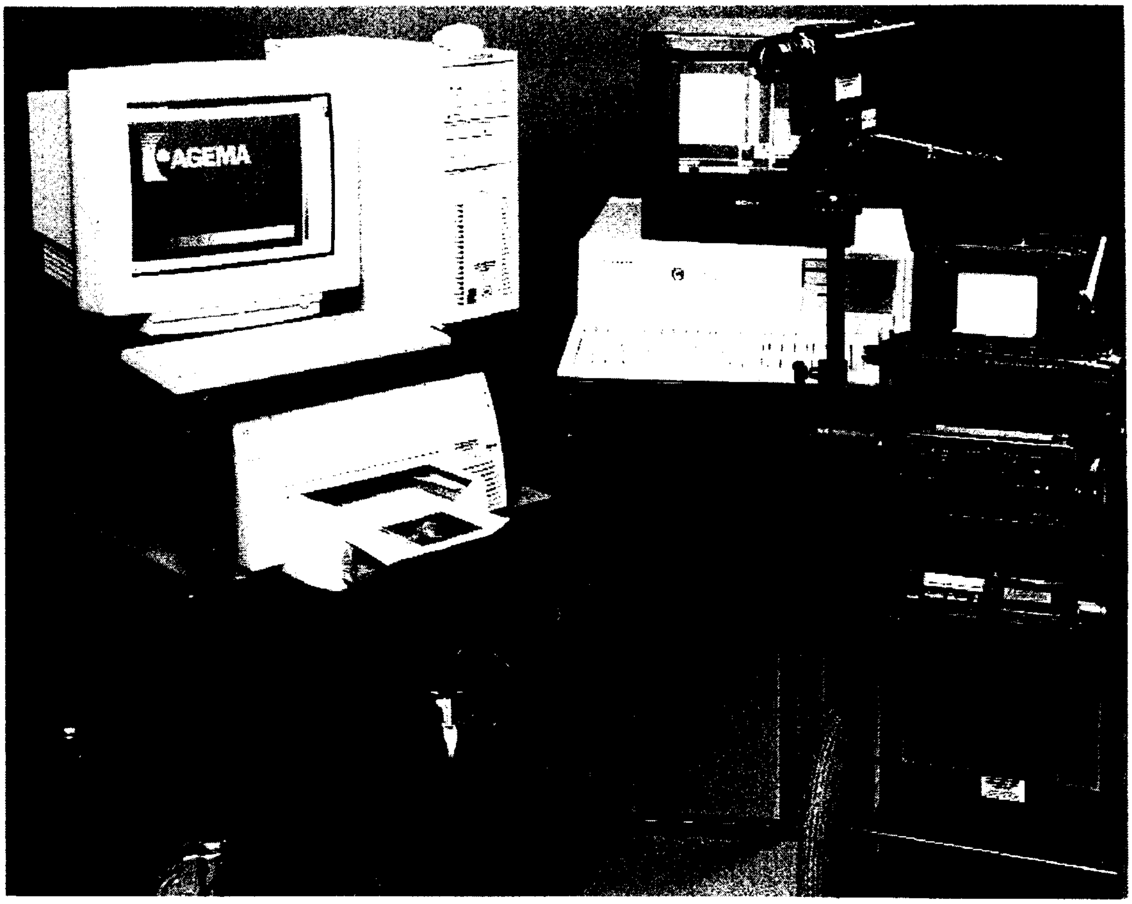

Figure 4-17: Thermal imaging system

The system operates the CATSE thermal analysis software package. The system allows storage of individual images or images sampled at a rate of 0.5Hz. In addition the camera is also fitted with a burst 25Hz image acquisition system. In burst mode, the images are stored in the buffer, which limits the acquisition time to approximately 20s. In burst mode the system scans and stores as fast as it can, and therefore the true acquisition frequency is between 22 and 28Hz. After the acquisition the images are transferred to the computer hard disk at a rate of 6 images/min, which imposes a considerable break between each measurement sequence. The tested elements therefore have time between the tests to cool down and to stabilise to a uniform temperature distribution.

The definition of the images is 140pixels$\times$140pixels. The acquisition system stores the value in 256 bands (8 bit unsigned integer), which are not equally spaced. The sensitivity depends on the width of the temperature range. For the smallest range width the sensitivity at 20°C is around 0.1°C. For the largest range width used during the physical tests, (+15°C to +115°C), the sensitivity is around 0.6°C.

The images were converted with the *IRWIN* software package into *MATLAB*-files and Bitmap-files for analysis.

The thermal imaging system used was assembled in the late eighties and its value then was of £ 86,000. Nowadays, of course, smaller and cheaper thermal imaging cameras exist, with much better resolution and accuracy, with accurate selectable acquisition frequencies and without the need to be cooled with liquid nitrogen. Though quite modest compared to the latest technology the results with this system yielded essential information.

In order to determine the emissivity of the specimen, which is a crucial parameter of the thermal imaging camera, the web of the specimen was heated with a hot air gun, as uniformly as possible up to 100°C, and was then allowed to cool. Synchronised measurements from the thermal imaging camera and from a film thermal sensor (described in Section 4.8), which was held in contact against the specimen web were recorded. An emissivity value of 1.0 (maximum possible value) gave excellent agreement between the thermal film sensor and the thermal imaging camera. The disagreement between the two systems was in a range of ±0.5°C. Emissivity values for oxidised steel in the literature fall between 0.95 and 1.0.

4.8 Thermal film sensor

The thermal film sensor used (RS PT100 no 237-1607), Figure 4-18 is a very thin stainless steel plate, 2mm×10mm, has a resistance of ~100Ω at 20°C and which increases linearly with temperature. Its temperature range lies between -50°C and +260°C. Because of its small physical size it has a fast thermal response.

The thermal film sensor was calibrated attached to a standard mercury thermometer in an oven heated stepwise from +20°C to +100°C. The film sensor was connected in a circuit with a precision resistance of 100Ω and was connected as a half bridge on one BEDO channel, allowing the temperature variation to be synchronously recorded with the acquisition of the loadcell and actuator outputs. The thermal film sensor was kept in contact with the specimen web with a plastic screw, lodged into a small steel support, itself fixed onto the web by two tiny spot welds as shown in Figure 4-19.

Figure 4-18: Thermal film sensor

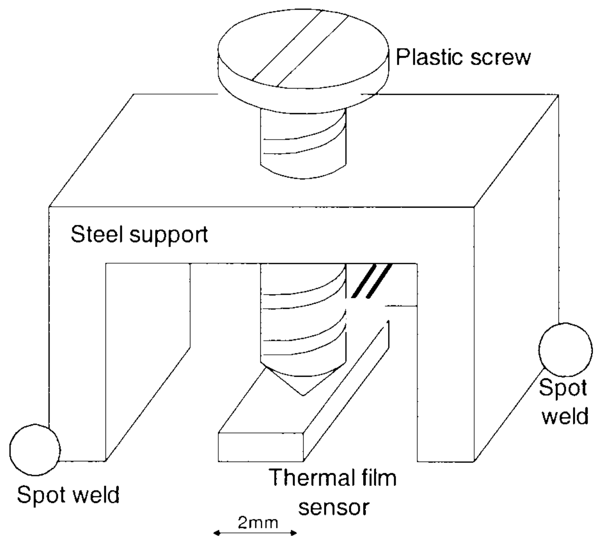

Figure 4-19: Fixation of the thermal film sensor

4.9 Real time substructure testing method

Darby et al. (1999) and Blakeborough et al. (2001) have developed a real time substructure testing method at the Structural Dynamics Laboratory of Oxford University. Figure 4-20 shows a schematic of the test setup and control loop of the method. The principal points of the testing procedure are:

1. A full or large scale model is built of a critical component of a structure, in this example a knee-element joint in a steel frame.

2. Loads are input to a numerical model of the surrounding structure in order to generate displacements, which are applied to the test specimen by the actuators.

3. Moments and forces measured from the two rig loadcells and mid span reaction force measured from the actuator's loadcells are used as input for the calculation of the next displacement increment.

4. (1). to (3). are repeated until the test ends.

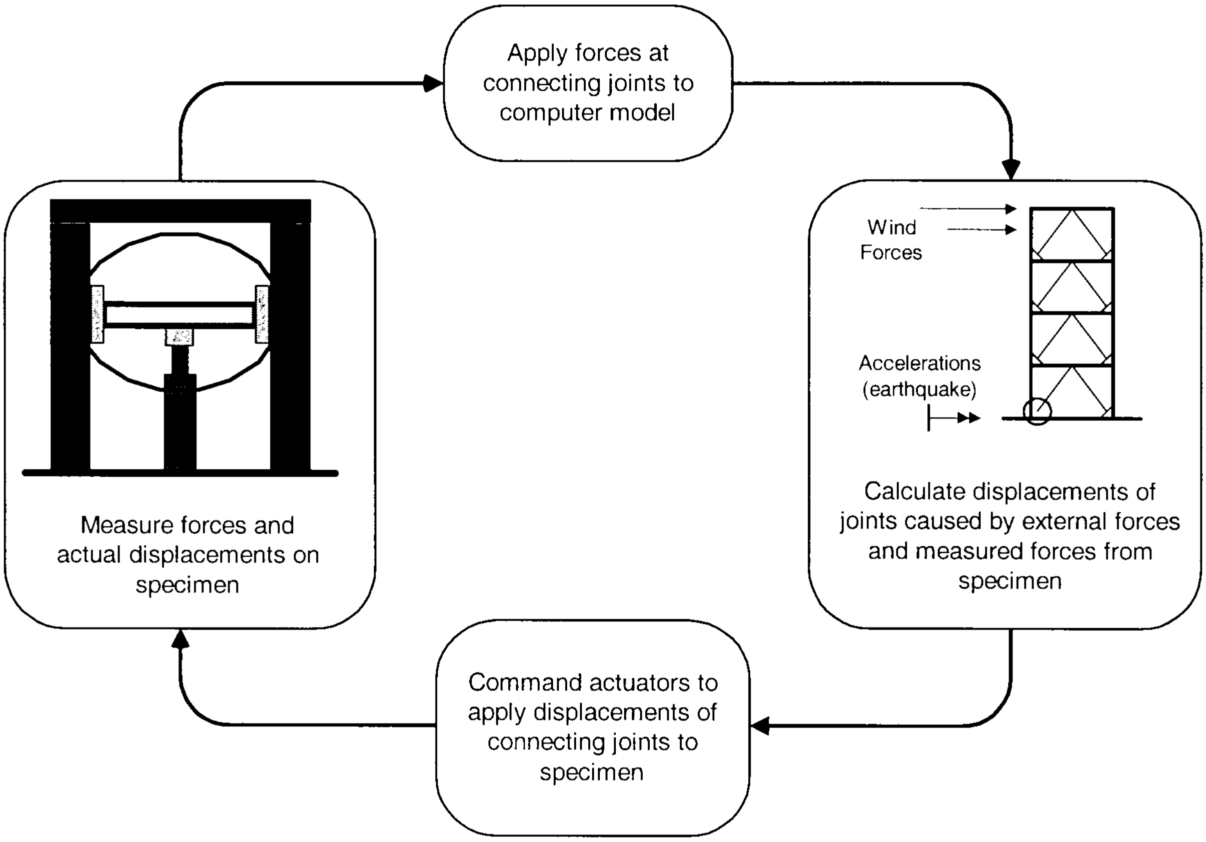

Figure 4-20: Real time substructure testing increment loop

For the physical test and numerical model to interact correctly, the measured forces must be fed back to the numerical model, the next displacement increment must be calculated and the corresponding command signal must be transmitted to the actuators within the duration of a single time step – typically of the order of 10ms. The implementation of the control loop therefore requires the development of sophisticated software both for rapid structural analysis and for actuator control.

Chapter 5

Performance of knee elements

5.1 Introduction

Different knee element designs have been selected in Section 3.9 for testing and the available testing facilities and set up have been presented in Chapter 4.

In this chapter the knee element test results are presented and analysed. First a list of the tested elements, their material characteristics and the general testing procedure is given. In order to evaluate the performance of the knee elements and make comparisons between the different designs, analysis criteria have been chosen. The element characteristics have been evaluated against these criteria and are presented in tables. Descriptions of the degradation of the knee element until failure are given for each type. Performances obtained with cyclic loading and earthquake loading have been compared and the influences of low cycle fatigue and steel grade are discussed. Based on the analysis and the observations made during the testing, design guidelines for the optimal knee element are given.

The second part of the chapter is devoted to thermal imaging analysis. The developed method to evaluate effective plastic strains and Von Mises stresses in cyclic loading using a thermal imaging camera is described. Possible improvements for the method are also given.

5.2 Knee element testing

5.2.1 List of tested knee elements

Sixteen knee elements listed in Table 5.1 were tested by cyclic loading and 3 knee elements, listed in Table 5.2 were tested dynamically using the substructure testing method, described previously in Section 4.9. A scalled accelerogram from the 1940 El Centro earthquake was used for the substructure testing method. The test numbers do not represent the chronological order of the testing.

Test	Type	Section	Features	Steel Grade [N/mm^2]
1	1	UC 152×152×30	12.5mm holes	290
2	1	UC 152×152×30	12.5mm holes	290
3	1	UC 152×152×30	12.5mm holes	340
4	2	UC 152×152×30	20mm holes	290
5	2	UC 152×152×30	20mm holes	290
6	3	UC 152×152×30	15mm holes (type a)	340
7	4	UC 152×152×30	15mm holes (type b)	430
8	5	UC 152×152×30	unaltered	340
9	5	UC 152×152×30	unaltered	340
10	6	UC 152×152×30	4 full stiffeners	340
11	7	UC 152×152×23	unaltered	340
12	8	UC 152×152×23	4 partial stiffeners	340
13	9	UC 152×152×23	2 full stiffeners	340
14	10	UC 152×152×23	4 full stiffeners	340
15	11	UB 203×102×23	unaltered	340
16	12	UB 203×102×23	4 full stiffeners	340

Table 5.1: List of knees tested by cyclic loading

Test	Type	Section	Features	Steel Grade [N/mm^2]
17	5	UC 152×152×30	neutral	340
18	5	UC 152×152×30	neutral	325
19	11	UB 203×102×23	neutral	340

Table 5.2: List of knees tested dynamically

(The section types were defined in section 3.9)

5.2.2 Steel Grade

In Tables 5.1 and 5.2, it can been seen that beams with various steel grades were used, which was not intentional. The knee elements were fabricated from a set of beams provided by Corus. The steel beams were received with a steel certificate indicating that they were made of S275 steel. However for logistical reasons, a steel producer may give his client a set of beams, in which some possess higher steel grades, believing that stronger steel is better. Contrary to static design, in a seismic design, replacing an element by a stronger one than that originally designed can lead to unforeseen modes of failure. The adage '*stronger is better*' is not valid for seismic designs. Hardness tests were performed on each knee element and four quite distinct groups of results were obtained. For each group, one tensile test was performed. The results are given in Table 5.3. Values for f_y between 290 and 430N/mm^2 were found.

Test	f_y $[N/mm^2]$	$f^t_{\max}$ $[N/mm^2]$	$f^e_{\max}$ $[N/mm^2]$	$f^t_{\max}/f_y$ $[-]$	$f^e_{\max}/f_y$ $[-]$
1	290	515	475	1.78	1.49
2	325	575	485	1.77	1.48
3	340	602	507	1.77	1.48
4	430	700	595	1.63	1.38

Table 5.3: Results of the tensile tests

For all the steels tested, the true strain $\varepsilon^t_{f\,\max}$ (when $f^t_{\max}$ is reached) was between 18 and 19% and the ultimate true strain ε^t_u between 26 and 27%.

True stress and true strain are obtained from the nominal stress σ_e and nominal strain ε_e with:

$$\varepsilon_t = \ln\left(\frac{\ell}{\ell_0}\right) = \ln\left(1 + \varepsilon_e\right) \tag{5.1}$$

$$\sigma_t = \frac{F \cdot \ell}{A_0 \cdot \ell_0} = \sigma_e \cdot (1 + \varepsilon_e) \tag{5.2}$$

where ℓ_0 and A_0 are respectively the initial length and initial section area.

5.2.3 Testing procedure

The testing of each knee element was carried out in steps, called subtests. A total of 227 subtests were performed (with an average of 12 subtests per specimen). The testing procedure used was based on the "Recommended testing procedure for assessing the behaviour of structural steel elements under cyclic load" (ECCS 1986). In the first step increasing cyclic displacements are imposed until hysteresis curves in the force displacement plot are observed, as shown in Figure 5-1 a). A number n of constant displacement cycles of amplitude $2^i \cdot \delta_y$ are then imposed (with i=0,1,2,3,...), as shown in Figure 5-1 b). When the response of the knee element suggested that failure might occur in the next step, smaller amplitude steps were imposed.

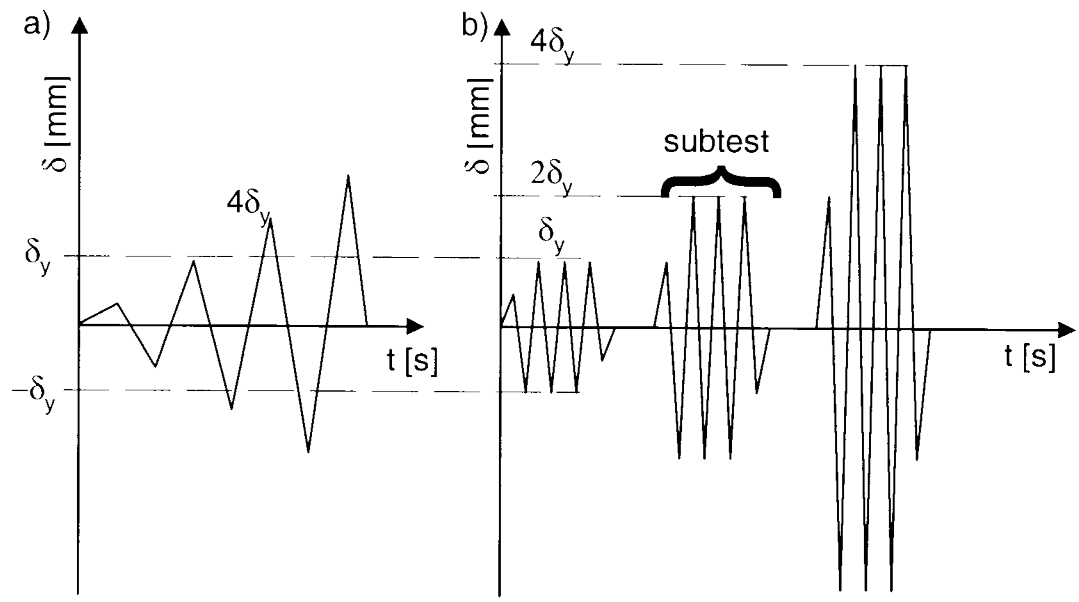

Figure 5-1: Testing procedure

Because of the test rig flexibility (described previously in Section 4.5) the imposed displacements of the knee elements were not equal to those of the actuator stroke. As only the actuator strokes were controlled during testing the above procedure could not be strictly followed. The actuator base plate flexibility was asymmetric (as it was lifting when actuators were in tension) which resulted in noticeable differences between the absolute values of the negative and positive displacements of the test specimen.

5.3 Analysis criteria

A large quantity of data was accumulated from the measurement equipment. In order to evaluate the performance of the tested knee elements, it was necessary to process this data and use performance criteria to determine indicative characteristics systematically; e.g. the yield load, the yield displacement and the initial stiffness.

5.3.1 Yield force and displacement

The yield force and displacement are important characteristics since the yield force determines the onset of yielding and the yield displacement is used to calculate the ductility. Different yield criteria exist and are used in practice. Three different methods are illustrated in Figure 5-2. The yield point is taken when:

(a) A difference ΔF between the force-displacement curves and the extended line of the initial stiffness is found. ΔF may take a fixed value or be expressed as a fraction of the total force F.

(b) The stiffness is found to be a percentage ζ (e.g. 50%) less than the initial stiffness. The yield force is then obtained by the intersection of the tangent of the force-displacement curve with the elastic curve.

(c) When the total displacement exceeds the elastic displacement by an amount $b = \zeta \cdot a$. This criterion is known as the proof load.

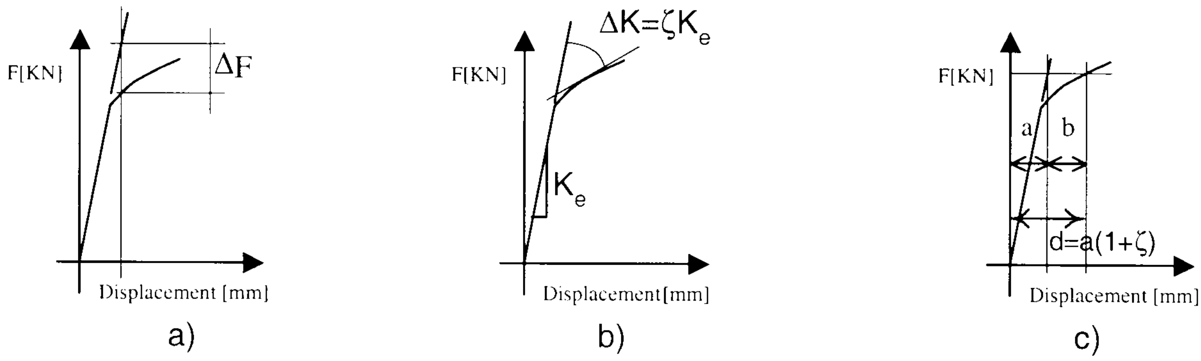

Figure 5-2: Yield criteria

These three methods were applied to the test data and gave different results. Criteria a) and c), gave almost identical results for some values of ΔF and ζ and their yield points on the force displacement curves also seemed more realistic than criterion b). The difficulty of accurately finding the tangent to real dataset makes criterion b) hard to apply in practice.

The yield displacement is very sensitive and significantly different values are obtained if the parameter ΔF in criterion a) or ζ in criterion c) are only slightly changed. However for the same change in these parameters the yield load changes only moderately.

Criteria a) and c) were used and the mean value was taken. When significant differences were found between the two criteria, the yield force and displacement were visually estimated on the force-displacement curve.

5.3.2 Plastic energy dissipation

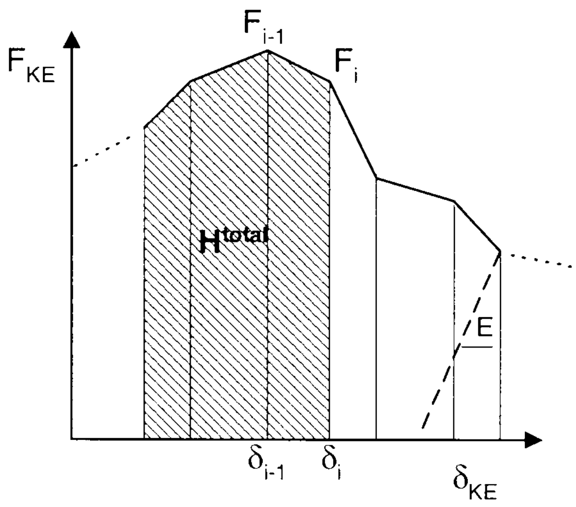

Figure 5-3: The dissipated plastic strain energy deduced from the force-displacement plot

From Figure 5-3, we can deduced the dissipated plastic strain energy H_n^{pl} at time step n with:

$$H_n^{pl} = H_n^{total} - H_n^{el} = \left[\frac{1}{2}\sum_{i=1}^{n}(\delta_i - \delta_{i-1})\cdot(F_i + F_{i-1})\right] - \frac{F_n^2}{2\cdot E} \qquad (5.3)$$

5.3.3 Ultimate displacement

The ultimate displacement depends on the definition of failure. Two approaches were considered.

Energy approach

Let η be the ratio between the real absorbed energy $H_{c,r}$ in a cycle and the energy $H_{c,epp}$ that might be absorbed for an identical cycle by an elastic-perfectly-plastic element with identical stiffness and yield load. η will be close to unity for small amplitudes in the plastic range, though it might take higher values (up to 1.4) due to strain hardening for larger amplitudes. When the section starts to degrade η starts to decrease. Failure was considered to have occurred when η dropped to value smaller than $\zeta \cdot \eta_{\max}$. For ζ =0.85 consistent results were obtained and this value was therefore used for all the data.

Force approach

The ultimate displacement was taken when the reaction force F was reduced by a percentage γ compared to the maximum reaction force experienced in a previous cycle of the same displacement intensity, as shown in Figure 5-4. For γ=10% consistent results were obtained and this value was therefore used for all the data.

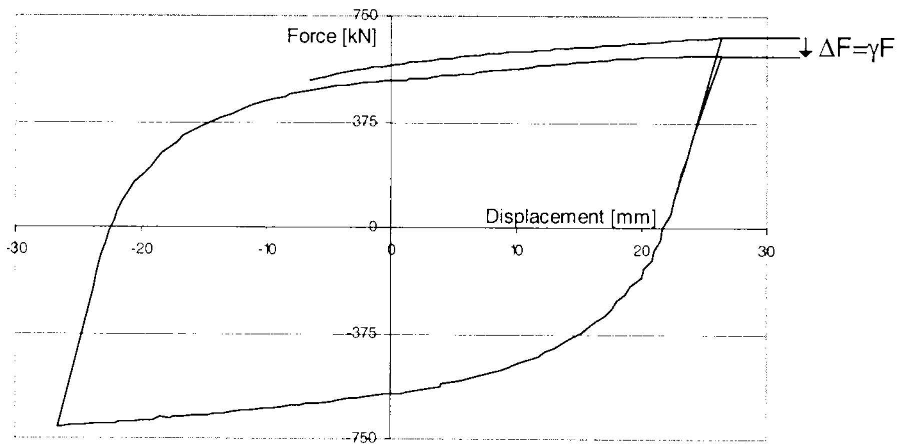

Figure 5-4: Force-displacement hysteresis curve showing degradation

Remarks

Both approach were used and the mean value was taken. Both methods gave similar results for the following reasons:

1. Because of the testing procedure used (described previously in Section 5.2.3) the maximum imposed displacement hardly varied within a subtest.

2. When η and F started decreasing, significant degradation was observed for each additional cycle and the failure criteria would then be met within a few additional cycles.

For other testing procedures larger differences may be expected between the two methods and a different percentage for ζ and γ would need to be considered.

5.3.4 Ductility, remaining strength capacity ratios

The displacement ductility is defined by:

$$\mu = \frac{\delta_u}{\delta_y} \tag{5.4}$$

Ductility accuracy depends directly on the accuracy with which the yield displacement is determined.

The remaining strength capacity ratio, is given by:

$$\chi_y^{\max} = \frac{F_{\max}}{F_y} \tag{5.5}$$

5.4 Results

The amplitudes and numbers of cycles that each knee element has experienced are given in Appendix A.

5.4.1 Yielding mode

From the observations made during the physical testing and from the thermal imaging analysis (presented later in Section 5.5) the yielding mode for each knee element could be identified.

All knee elements started yielding in shear with their energy dissipation area situated outside of the connection areas. The knee elements n°1-5 (with perforated web), showed plastic strain patterns stretching horizontally between the holes. The knee element with perforated web section n° 6 showed patterns stretching vertically. The knee element with perforated web section n° 7 showed patterns stretching vertically at first, followed rapidly by horizontally stretching pattern. Knee element n° 7, was intended to combine the horizontal and vertical yielding mode, and did indeed behave that way. For the other knee elements yielding stretched over the entire web area between the stiffeners, with the exception of small strips adjacent to the roots of the flanges and the stiffener welds. All yielding modes conformed to those predicted by the finite element modelling.

5.4.2 Cyclic loading

All knee elements showed a number of very large stable hysteresis curves at first, as shown in Figure 5-5 a) which shows force versus central deflection for knee element n°8 (subtest VII). The corners of the hysteresis curves are flattened off which can be explained by:

1. The data acquisition system frequency was set too low to have enough data points to accurately capture the corner point. In later tests the frequency was increased but the corner was less but still flattened.

2. The data acquisition records one channel at a time and a small Δt remains between each channel reading. Force and displacement may not have been perfectly synchronised. By interpolating the displacement to compensate for the delay Δt, the corner can be modelled perfectly, but this does not prove that the data acquisition system is the cause of the delay.

3. The real knee element deflection was calculated by subtracting the mean movement of the loadcell front from the global central deflection measured with cable extension position transducers. These transducers are made of cable on a roll-spring. These transducers are not perfectly instantaneous and the cables may vibrate.

Figure 5-5 b) shows the moments at the ends of knee element n°8 in the same subtest. The moments at both ends are similar but not identical. The differences increase when significant strength degradation has occurred as in Figure 5-5 c) showing at the extremities moments of knee element n°2. These large differences indicate that extended damage initially occurs at first only in one part (or one side) of the knee element. Failure of knee elements will be further discussed in Section 5.4.6.

Figure 5-5 d) shows a superposition of five subtests of knee element n°13. For an amplitude in the cyclic displacement up to 13mm, the reaction force of the knees increases quite significantly (from F_y=340kN to F=570kN, an increase by a factor 1.7); for larger displacements it increases only very moderately (to $F_{\max}$=637kN for a displacement of 27mm).

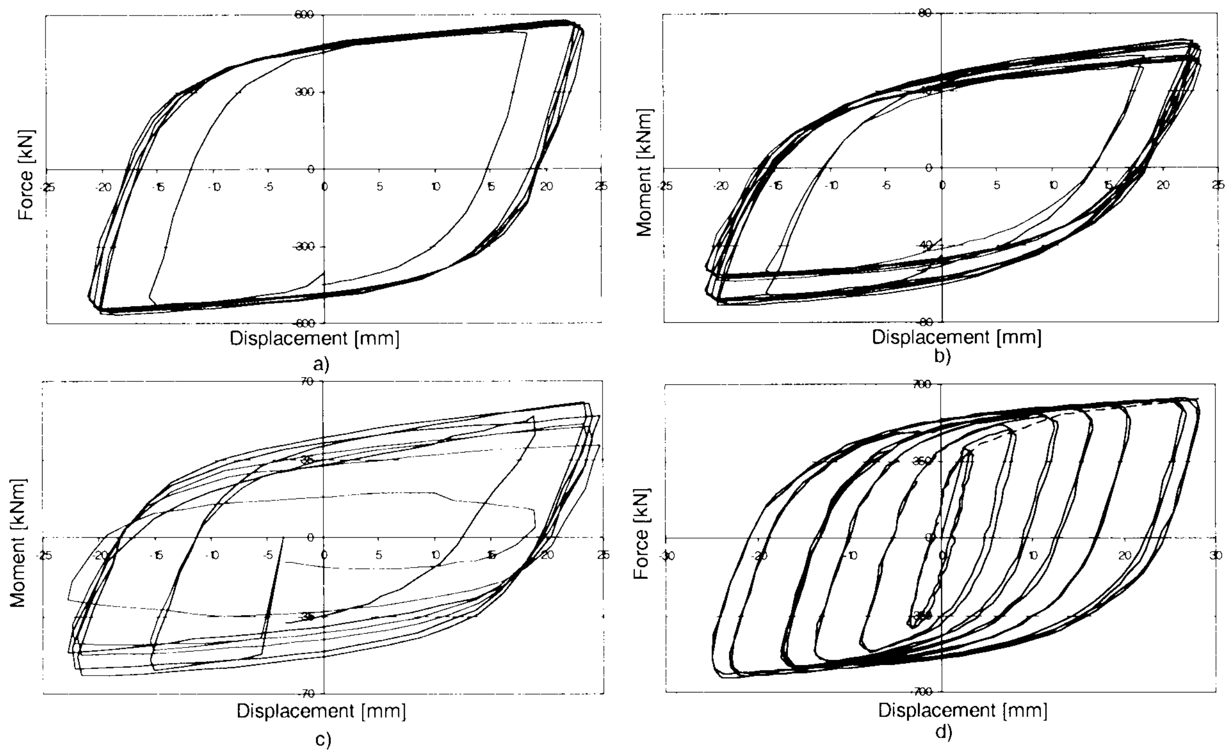

Figure 5-5: Stable hysteresis curves: a) & d) F-δ; b) M-δ; c) M-δ at failure.

5.4.3 Main characteristics shown by the knee elements

The results obtained by processing the physical testing data using the previously defined analysis criteria (Section 5.3) are given in Table 5.4.

Because of the test rig anchor failure, described previously in Section 4.5, tests 6, 10 and 11 had to be stopped prematurely and failure of the knee elements did not occur. The knee elements n°17 to 19 were used by other researchers in another project and not all subtests have been monitored. For these tests the maximum force, the maximum displacement and the plastic energy dissipation measured within the abbreviated test data are given. All these values and the ones calculated from them (ductility and force ratio), would have been higher if completion of the test had been possible. These values are marked with a $*$.

The results presented in Tables 5.4 are generally consistent. Very similar results have been found when identical knee elements have been tested. The identical knee element groups are {n°1 and 2}, {n°4 and 5}, {n°8, 9 and 18} and {n°15 and 19}. Their loading procedures were not identical which explains the discrepancy in the plastic energy

Test	*Section abreviation*	*Steel* f_y	F_y $[kN]$	δ_y $[mm]$	$F_{\max}$ $[kN]$	δ_u $[mm]$	$\chi_y^{\max} = F_{\max}/F_y$	μ $[-]$	H_{pl} $[kJ]$
1	UC30H12	290	300	2.3	484	24	1.6	10	320
2	UC30H12	290	300	2.3	480	24	1.6	10	325
3	UC30H12	340	325	2.4	579	26	1.8	11	385
4	UC30H20	290	225	1.7	380	18	1.7	11	240
5	UC30H20	290	230	1.9	406	25	1.8	13	205
6	UC30H15a	340	300	2.0	530*	20*	1.8*	10*	235*
7	UC30H15b	430	380	2.1	650	29	1.7	14	605
8	UC30N	340	350	2.1	599	35	1.7	17	1150
9	UC30N	340	360	2.4	597	40	1.7	17	1160
10	UC304FS	340	350	1.8	615*	15*	1.8*	8*	240*
11	UC23N	340	330	1.7	555*	17*	1.7*	10*	340*
12	UC23PS4	340	335	1.7	601	23	1.8	14	365
13	UC23FS2	340	340	2.0	637	28	1.9	14	720
14	UC23FS4	340	340	1.8	660	30	1.9	17	580
15	UB23N	340	365	1.8	614	25	1.7	14	215
16	UB23FS4	340	380	1.7	690	30	1.8	18	765
17	UC30N	340	350	2.4	542*	19*	1.5*	8*	425*
18	UC30N	325	330	2.2	500*	21*	1.5*	10*	664*
19	UB23N	340	365	2.1	563*	17*	1.5*	8*	657*

Table 5.4: Tested knee element characteristics

dissipation. More damage is done by one large amplitude cycle than by a multitude of small amplitude cycles dissipating the same plastic energy. This is remarkably evident in the comparison of knee elements n°15 and 19. Knee element n°19 was subjected to a few moderate earthquakes and experienced many small cycles, thus dissipating more than three times more energy than knee element n°15 under cyclic loading, without undergoing failure.

The yield displacements were larger than those calculated beforehand with a simple finite element model or with an analytical formula that takes into account the deflection due to bending and shear (Equation 3.40). Values in the range of 1.1-1.2mm for the sections without holes and in the range of 1.3-1.4mm for the sections with holes were expected. In practice the actual behaviour deviates substantially from the idealised model; the differences could come from the flexibility of the rig (the effect of which will be estimated later with finite element modelling, Section 6.7.2) and/or from small amounts of slack in the bolt connections, despite particular attention having been given to making them as tightly fitted as possible.

$\chi_y^{\max}$ values found are very high, especially for those knee elements with stiffeners where the values are in the range of 1.8 to 2.0.

5.4.4 Other useful characteristics

Two additional ratios have been identified for each knee elements. The first ratio $\chi_{e.y}^{\delta=\delta_{design}}$ is a very useful piece of information for the design of a knee braced frame and will be used in the 5-storey building example of Section 7.3. The second ratio $\chi_{e.y}^{y}$ is used to evaluate the accuracy of the analytical formula for the yield load established in section 3.8.1.

As seen in Section 5.4.2 the reaction force increases significantly due to strain hardening. When designing a knee braced frame the knee element reaction force at the maximum design deflection δ_{KE}^{design} is a very useful parameter. This force normalised to the yield force gives:

$$\chi_{e.y}^{\delta=\delta_{design}} = \frac{F_{\delta=\delta_{design}}}{F_y} \tag{5.6}$$

The maximum design deflection will be different for each building design. It is in the designer's interest that the knee element is capable of substantial energy dissipation through adequate deformation. However the knee element deflection is limited by the serviceability limit state condition on the interstorey drift d_r. Eurocode-8 (2001) gives the following restriction:

$$\frac{d_r}{\nu} \leq c \cdot h \tag{5.7}$$

where ν is a reduction factor equal to 2 for importance category III (buildings for normal use such as apartments and offices), h the height of the storey and c a factor which takes the value of 0.005 if non-structural elements of brittle materials are attached to the structure and 0.0075 otherwise.

As a coarse estimation of δ_{KE}^{design}, the value δ_{KE} for which the serviceability limit state is reached can be taken. For a ratio $\delta_{Frame}/\delta_{KE}$=2.05 (obtained with Equation 3.9 for realistic angles α and β) and a storey height of 3m, $\delta_{KE}^{\max}$ =14mm. In Table 5.5, $\chi_{.y}^{\delta=14mm}$ are given for all tested knee elements.

$\chi_{.y}^{\delta=14mm}$ values are above 1.5 and reach 1.7 for knee elements with 4 full stiffeners. The value 1.7 will be used in the 5-storey building example of Section 7.3.

In Section 3.8.1 Equations 3.59, 3.61 and 3.62 were developed in order to estimate F_y. For each tested knee element F_y was calculated with these equations using f_y from

Test	Section abreviation	F_y $[kN]$	$F_{e.y}$ $[kN]$	$\chi_{e.y}^{y}$ $[-]$	$F_{\delta=14mm}$ $[kN]$	$\chi_{.y}^{\delta=14mm}$ $[-]$
1	UC30H12	300	242	1.24	450	1.5
2	UC30H12	300	242	1.24	450	1.5
3	UC30H12	325	283	1.15	510	1.6
4	UC30H20	225	197	1.14	360	1.6
5	UC30H20	230	197	1.17	365	1.6
6	UC30H15a	300	293	1.02	500	1.7
7	UC30H15b	380	332	1.14	580	1.5
8	UC30N	350	375	0.93	525	1.5
9	UC30N	360	375	0.96	530	1.5
10	UC30FS4	350	375	0.93	600	1.7
11	UC23N	330	345	0.96	500	1.5
12	UC23PS4	335	345	0.97	520	1.6
13	UC23FS2	340	345	0.99	575	1.7
14	UC23FS4	340	345	0.99	585	1.7
15	UB23N	365	385	0.95	580	1.6
16	UB23FS4	380	385	0.91	610	1.6
17	UC30N	350	375	0.93	520	1.5
18	UC30N	330	359	0.92	500	1.5
19	UB23N	365	385	0.95	570	1.6

Table 5.5: Tested knee element characteristics

the tensile tests and the physically measured t_w. The ratios of the real yield force to the predicted yield force (Equation 5.8) are given in Table 5.5. Because of residual stresses yielding is expected at smaller load than predicted. This is the case for knee elements n° 8 to 19 (sections without holes in the web), with $\chi_{e.y}^{y}$ just under unity. The simple Equation 3.59 give an excellent estimate of the yield load for these elements. For the knee elements n°1 to 7 (sections with perforated web) the yield load is largely underestimated. For better estimation of the yield load, finite element analysis is needed.

$$\chi_{e.y}^{y} = \frac{F_y}{F_{e.y}} \tag{5.8}$$

5.4.5 Earthquake loading

As can been seen in Tables 5.4 and 5.5 by comparing n°18 with n°8 and 9 or n°19 with n°15, there are not many differences in the response between the cyclically loaded knee elements and the seismically loaded ones. In Figure 5-6 it can be seen that the force-displacement curves of a knee element, submitted to the scaled 1940 El Centro earthquake using the real time substructure testing method of Section 4.9, fit inside a cyclic hysteresis loop of equal maximum amplitude (knee elements n°8 and 18). The data acquisition system frequency was set rather low and in addition vibrations were induced in the cable position transducers. As a result, the unloading paths are not always straight and some corners of the hysteresis curve are flattened off.

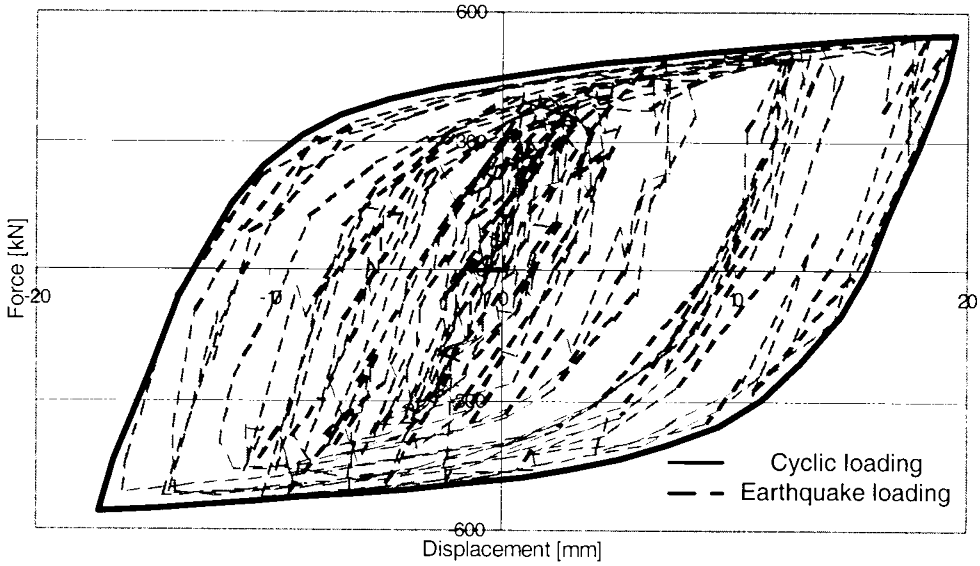

Figure 5-6: Comparison of the response of a cyclically loaded and an earthquake loaded knee element

5.4.6 Failure

Knee elements n°1 to n°5 (perforated web sections with horizontal yielding pattern)

For these knee elements the following steps in the failure process were observed:

1. Horizontal yield patterns appeared between the holes. The holes started to take a distorted shape.

2. Crack initiation developed at 4 points of the hole circumference in a direction making an angle of approximately 40° with the horizontal.

3. Horizontal cracks started to grow quickly and join the holes together, starting with the middle row.

4. Failure of the web (multiple horizontal cracks stretching over 200mm), causing loss of shear capacity. Subsequently some local web buckling also occurred. (Figures 5-7 and 5-8).

5. The bottom and top flanges (with a small strip of web) acted as small independent T-shaped beams, that have little stiffness and immediately yielded and buckle. Eventually the welds at the end-plates failed.

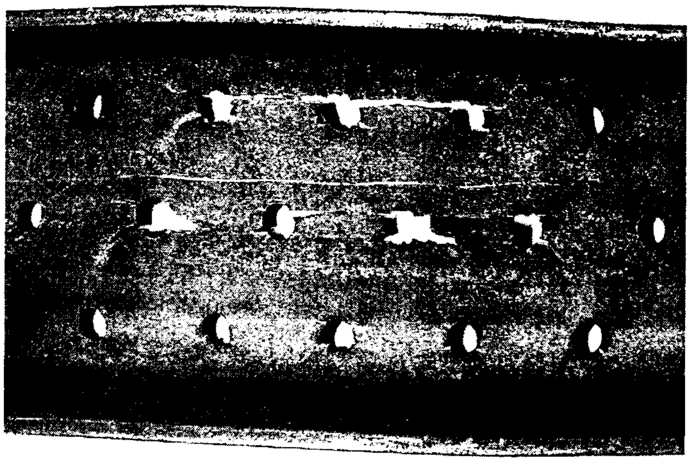

Figure 5-7: Failure of a knee element with 12.5mm diameter holes

It was observed that when the crack initiation took place (affecting 85% of the holes, within a couple of cycles) there was no noticeable decrease or change in the response (F-δ and M-δ plots). Furthermore, a significant increase of the displacement amplitude is necessary for crack propagation. This can be explained by the fact that the cyclic plastic deformation causes changes in the material mechanical properties which is the prerequisite for formation of microcracks. The cyclic plastic deformation in the plastic zone ahead of the crack tip determines the behaviour of fatigue macrocracks. Therefore additional cycles of higher amplitude are needed to allow higher plastic strains to build up between the holes enabling the crack to grow.

Crack initiation occurred on both sides (a side is defined as the beam-portion of the knee element between one end and the central connection), while crack growth initially

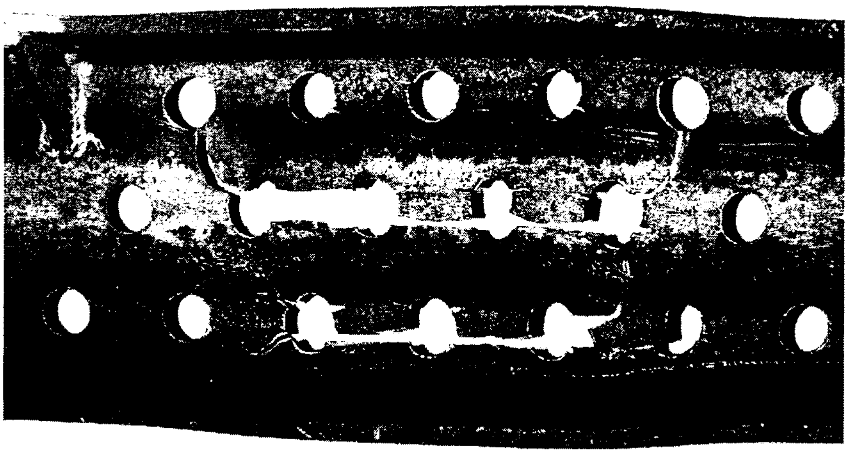

Figure 5-8: Failure of a knee elemnt with 20mm diameter holes

only occurred on one side ; eventually, after significant strength degradation, some cracks also grew on the other side of the knee.

Strength degradation occurred with the crack propagation. When the crack first grew a few millimetres and opened slightly, the response of the knee hardly reduced. However when the cracks propagated to join the holes, within a few additional cycles, failure of the web was achieved. The strength degradation is shown in Figure 5-9 for knee elements (a) n°1 (b) n°4 and (c) n°5. Crack propagation to web failure of one side occurs in less than two cycles for knee element n°1. Knee elements n°4 and n°5 are identical in design and made of the same steel but their loading procedures were different. Knee element n°4 was subjected to five cycles at the same displacement amplitude, while knee element n°5 was subjected to only 2.5 cycles. Knee element n°4 did fail for much smaller displacement and forces than knee element n°5. This indicates that low cycle fatigue occurred and affected the knee element performance significantly. Crack propagation was much slower for knee element n°4 than for knee element n°5, which is expected because the displacement and therefore the energy dissipated per cycle and the strain rate are smaller for knee element n°4.

Knee elements n°7 (perforated web section with vertical yielding pattern)

The failure process of knee element n°7 was similar to that of knee elements n°1 to 5. However this knee element showed more distorted hole shapes (Figure 5-10) than elements

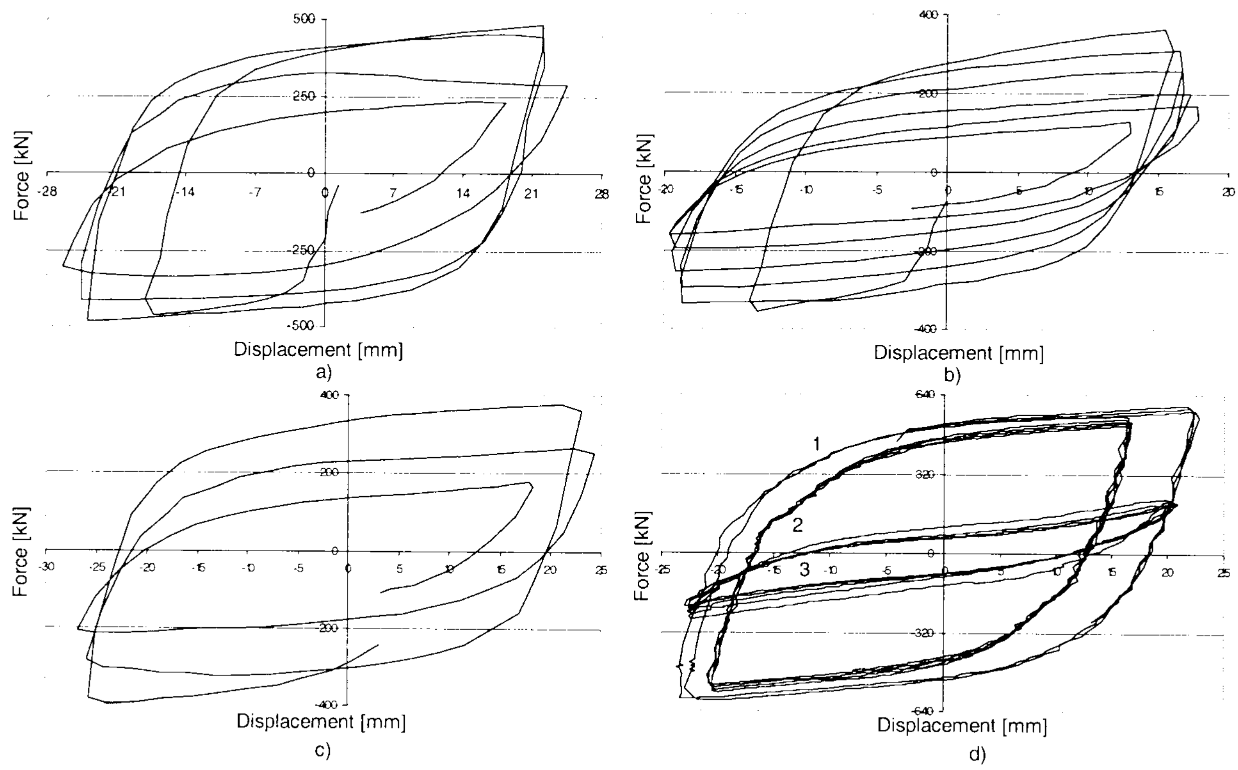

Figure 5-9: F-δ curves of failing knee elements (a) n°1, (b) n°4, (c) n°5 and (d) n°12 (curve 1: crack initiation, curve 2: reduced displacement, curve 3: residual strength after crack propagation)

n°1 to 5. Despite vertical yielding patterns having developed first, for large amplitude cycles horizontal yielding patterns developed in the bottom and top rows. Most holes showed crack initiation but only cracks around the holes from the bottom and top row grew and in the horizontal direction only.

Knee element n°8 and 9 (normal UC 152$\times$152$\times$30 sections)

For these knee elements the following steps in the failure process were observed:

1. Plastic buckling of the web as shown in Figure 5-11. A very slight twisting of the flanges was also observed. The reaction force dropped no more than a few percent.

2. Cracks tore apart the web in a spectacular manner and the flanges buckled (Figure 5-12). Curved diagonal cracks starting from the centre of the web rectangle developed, from which two additional cracks propagated more or less horizontally near the

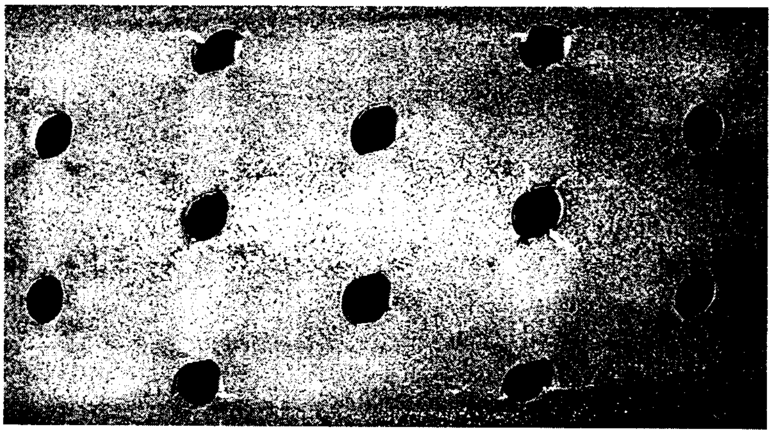

Figure 5-10: Hole distortion and crack growth in the top and bottom row of knee element n°7

bottom and the top flanges. Within a cycle the reaction forces dropped by a factor three.

3. Within a few additional cycles the welds between the end plates and the knee element extremities failed.

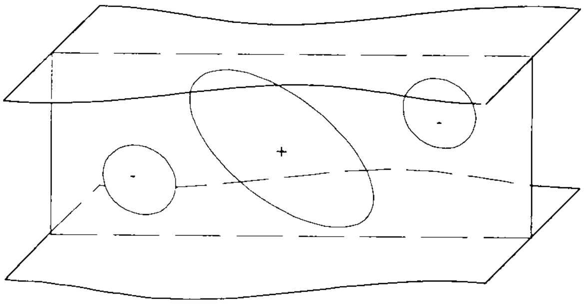

Figure 5-11: Buckling of the web

Knee element n°12 (UC 152×152×23 section with 4 partial stiffeners)

The partial stiffeners did prevent the beam from buckling. However the corners of the stiffeners introduced a stiffness discontinuity in the web, in a heat affected zone (due to the welding of the stiffeners) and therefore generated favourable conditions for crack initiation. When crack initiation was detected visually, the amplitude of the imposed displacements was reduced, with the hope of observing a slow progressive growth of the crack. However,

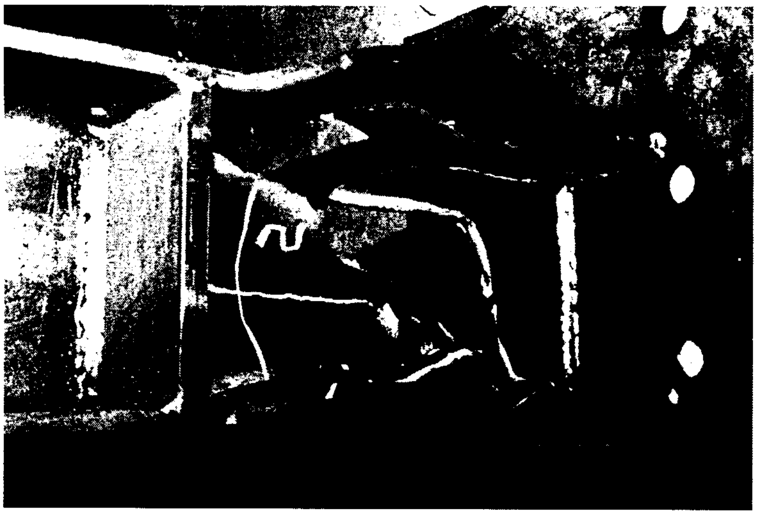

Figure 5-12: Failure of knee element n°8

little crack growth was seen in the next few cycles until the crack propagated rapidly to the state shown in Figure 5-13. Figure 5-9 (d) shows the force-displacement hysteresis curves (1 crack initiation, 2 reduced displacement, 3 residual strength after crack propagation).

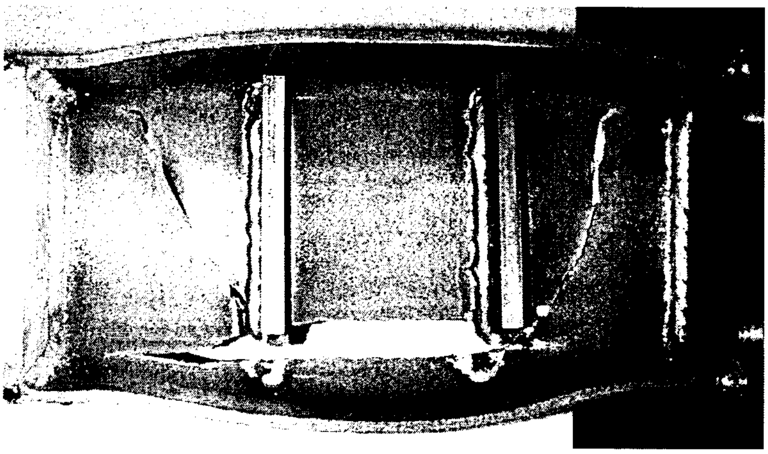

Figure 5-13: Failure of knee element n°12

Knee element n°13 and 14 (UC 152×152×23 section with 2 and 4 full stiffeners)

The stiffeners played their role in preventing the web from buckling early. However, severe buckling in the flange area opposite the central connection bolts occurred (Figure 5-14 a). Flange buckling also occurred near the knee element ends, but the buckle sizes were much smaller than the one in the central connection area. For knee element n°13 web buckling was observed in one part, but only after the flanges had buckled significantly. For knee element n°14 no web buckling was observed at all, and even higher loads than those for knee element n°13 were reached. As a result of the severe flange buckling, a crack propagated through half of the top flange (Figure 5-14 b). The central connection bolts also damaged the flanges so severely that the beam could not be loaded properly any longer (Figure 5-14 c).

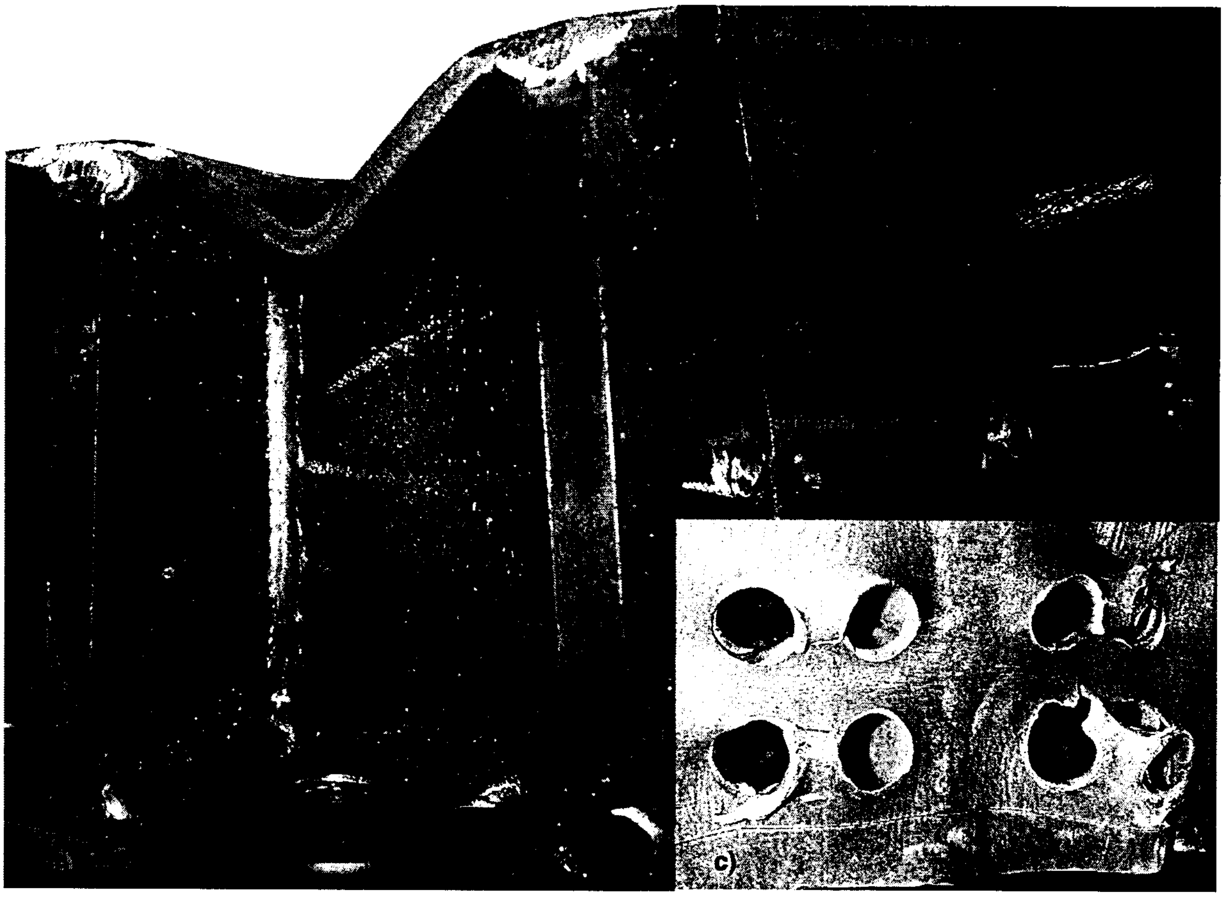

Figure 5-14: a) Flange buckling b) Crack in the flange c) The damaged bolt holes of the central connection

Knee elements n°15 and 19 (normal UB 203×102×23 sections)

The failure process of knee element n°15 was similar to the those of knee elements n°8 and 9. It showed a similar buckling pattern but, in step 2, two cracks inclined at approximately 45 degrees, propagated from the centre of the web rectangle (Figure 5-15). No other cracks were observed. Knee element n°19, which was dynamically loaded, was not brought to failure, though buckling occurred. No significant differences were observed between the buckling pattern of the cyclically loaded knee and the dynamically loaded one.

Figure 5-15: Failure of knee element n°15

Knee element n°16 (UB 203×102×23 section with 4 full stiffeners)

With 4 stiffeners knee element n°16 could resist higher displacements and forces than knee element n°15, however the two stiffeners did not totally prevent the web from buckling, which was followed by a crack propagation as shown in Figure 5-16. The weld between the stiffeners and the flanges failed completely.

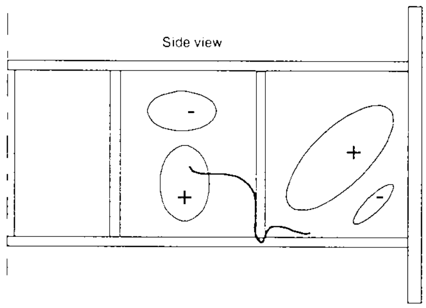

Figure 5-16: Failure of knee element n°16

5.4.7 Low cycle fatigue and ductility

Why low cycle fatigue models in shear could not be calibrated

From the comparison of knee elements {n°4 and 5} and {n°15 and 19}, it is seen that low cycle fatigue has to be taken into account. The ductility observed depends on the number of intermediate cycles that the knee element has experienced and can not be separated from the low cycle fatigue. Different low cycle theories were presented in Section 3.7.2. Yet these models have two or three parameters that need to be calibrated for each type of beam and yield mode. As never more than two data sets for knee elements of the same type and same steel were available, a realistic calibration could unfortunately not be completed. A large number (around 10) of tests of the same type would be required to calibrate a fatigue model as was done by Ballio and Castiglioni (1995).

Comparison with low cycle fatigue in bending

For comparison, the damage index was calculated, using Ballio's low cycle fatigue model (Equation 3.51 and Ballio, 1995), for two cantilevers (HEA220 and HEB 220) yielding in bending, experiencing the same number of cycles of equal ductility to knee element n°8. Knee element n°8 experienced six cycles of 3, 8, 13, 18, 21, 24 and 34mm and two cycles of 35mm before failure occurred. The damage index would be 1.85 for the HEA and 1.48 for the HEB. HEA and HEB are similar to UC-sections, and HEB possess thicker flanges than HEA-sections. The results are too sparse to conclude that knee elements yielding in shear are better than those yielding in bending, but the results do point in that direction.

Comparison of the low cycle fatigue resistance for the different knee elements.

A general trend can be recognised from the results in Table 5.4, in particular in analysing H_{pl} and μ. Sections with holes have their endurance reduced compared to a normal sections. Knee element n°4, which had a quite similar loading procedure to knee element n°9, dissipated 4.8 times less energy. UC30 which had a yield load only 6% higher than UC23 and only 4% smaller than UB23 was capable of dissipating much more energy and had a higher endurance. The stiffeners also enhanced the endurance by preventing web buckling.

5.4.8 Steel grade influence

From the available data there is no evidence that the steel grade has an influence on the endurance and performance, relatively to its yield load. However the sampling is too sparse to conclude that there is no influence. In theory, sections of lower steel grade are less prone to instabilities.

Varying the steel grade could be another effective means of varying the yielding shear load without the drawback of reducing the endurance of the knee element.

5.4.9 The best knee element design

Perforating the web is a simple and effective means of varying the yielding shear load to suit a particular structure. Taking into account the different steel grades, the yield load is reduced by 24% for the those with 20mm diameter holes, 14% for those with 15mm diameter holes and 6% for those with 12.5 mm diameter holes. The holes lower the yield load and the post-yield load and thus reduce the danger of buckling. Unfortunately, holes are favourable for crack initiation and propagation when the effective strain reaches a value of 10%. Because of the cracks, the endurance and energy dissipation capacity are decreased considerably. This probably outweighs the advantage gained in allowing the designer some flexibility in specifying the yield load.

With vertical web stiffeners attached to bottom and top flange and with fully penetrated welds at a spacing approximately equal to the section depth, web buckling is prevented for Universal Column sections and the buckling load is increased for Universal Beams. Universal Columns are also recommended because they are less prone to general lateral instabilities (torsional buckling). Web stiffeners hardly increase the yield force but increase the initial stiffness and the energy dissipation by avoiding buckling.

5.5 Thermal analysis method

A thermal imaging camera, the characteristics of which have been described in Section 4.7, was used to identify the dissipative areas and quantify the dissipation intensity. Furthermore a method, based on the heat diffusion and the plastic strain energy theory, was developed to deduce from the thermal imaging data the effective strains and the Von

Mises stress. This method required an image transform function to follow the area to analyse, which was moving and deforming under the imposed load.

5.5.1 Heat generation and diffusion

Yielding is an energy dissipating phenomenon which releases heat. The temperature increases locally where the material yields and the heat diffusion by conduction affects also the area surrounding the yielding zone. The general heat diffusion equation (Gebhart, 1993) is given by :

$$Q = \frac{\partial u}{\partial t} - \kappa \cdot \nabla^2 u \tag{5.9}$$

where $\partial u / \partial t$ is the variation of the temperature, Q is the equivalent temperature variation due to heat generation and κ a heat diffusion constant given by:

$$\kappa = \frac{k}{c_p \cdot \rho} \tag{5.10}$$

For steel the mass density is $\rho = 7850 kg/m^3$, the conductivity is $k = 50W/mK$ and the specific heat is $c_p = 450 J/kgK$, which gives κ=14.15mm$^2/s$.

Equation 5.9 can be rewritten to give the power density p (energy released per unit of volume and per second) (Gebhart, 1993):

$$p = c_p \cdot \rho \cdot \frac{\partial u}{\partial t} - k \cdot \nabla^2 u \tag{5.11}$$

By multiplying Equation 5.11 by δt $(= t_2 - t_1)$, the energy density dissipated between t_1 and t_2 is given by:

$$w_{1-2} = \frac{\Delta H_{1-2}}{V} = c_p \cdot \rho \cdot (u_2 - u_1) - k \cdot (t_2 - t_1) \cdot (\overline{\nabla^2 u}) \tag{5.12}$$

where $\overline{\nabla^2 u} = (\nabla^2 u_1 + \nabla^2 u_1)/2$ or $\overline{\nabla^2 u} = (\nabla^2 u_1 + 2 \cdot \nabla^2 u_{1.5} + \nabla^2 u_2)/4$ if intermediate thermal pictures are available. If the temperature is known for a grid of mesh $\Delta x = \Delta y$, $\nabla^2 u$ can be given by a discrete approximation function:

$$\nabla^2 u_{i,j} = \frac{u_{i+1,j} + u_{i-1,j} + u_{i,j+1} + u_{i,j-1} - 4 \cdot u_{i,j}}{4 \cdot \Delta x \cdot \Delta x} \tag{5.13}$$

In the case of a thermal imaging camera, the grid points are represented by the pixel centres.

The exchange of heat with the surrounding air has been neglected. The room temperature during the tests was in the range of 20-30$°C$ and maximum peak temperature of the steel was just above 100$°C$. Testing at a higher frequency is preferable so that air cooling becomes negligible. All tests were performed at frequencies between 0.4 to 1.5Hz. Higher frequencies for large amplitudes was not possible because the maximum available oil flow was reached.

5.5.2 Plastic strain dissipation

The plastic strain in a solid due to an external load can be evaluated using the plastic flow theory, a yield surface criterion and a material hardening rule.

The material hardening rule

The hardening rule describes the work hardening of the material and the change in the yield condition with the progression of plastic deformation.

The stress versus plastic strain curve was obtained from the uni-axial tests described in Section 5.2.2. The results differ from those of a cyclic loading tests, Figure 5-17 a). Cyclic loading tests will give a range of stress strain hysteresis loops as shown in Figure 5-17 b).

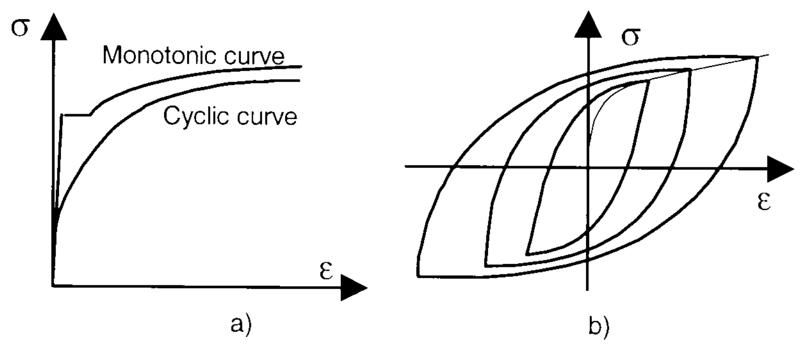

Figure 5-17: Monotonic and cyclic stress-strain curves.

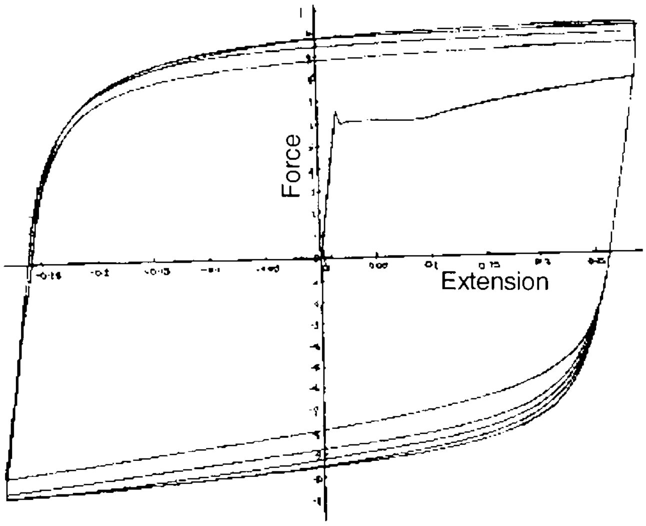

Figure 5-18: Cyclic material test on mild steel (source Corus).

Oxford University Engineering Department does not possess testing facilities that are designed for performing cyclic testing on steel samples. Initially, data of a cyclic test provided by Corus were used, Figure 5-18. We can see that a stabilized cycle is generally obtained after only a few cycles. Since the data given were from a test performed on a slightly different steel to that the one the knee element were made of, the material response had to be scaled. Using this scaled data was giving misleading results. Therefore, special grips were machined to fit on an Oxford University Instron machine to perform cyclic loading. Unfortunately the testing conditions were not optimal. As a result the first sample (steel with f_y =340N/mm^2) started buckling when when trying to perform the 5% hysteresis curve. In Figure 5-19 cyclic hysteresis curves for 1%, 2.5% and 5% strain are shown. The second sample (steel with f_y =430N/mm^2) started buckling when trying to perform the 7.5% hysteresis curve. The cyclic test was despite buckling continued. In Figure 5-20 cyclic hysteresis curves for 1%, 2.5% 7.5% and the attempt of 10% strain are shown.

The flow theory of plasticity

The normality rule specifies that at yield the direction of the increment of the strain vector is always normal to the yield surface. This implies that the direction of the strain

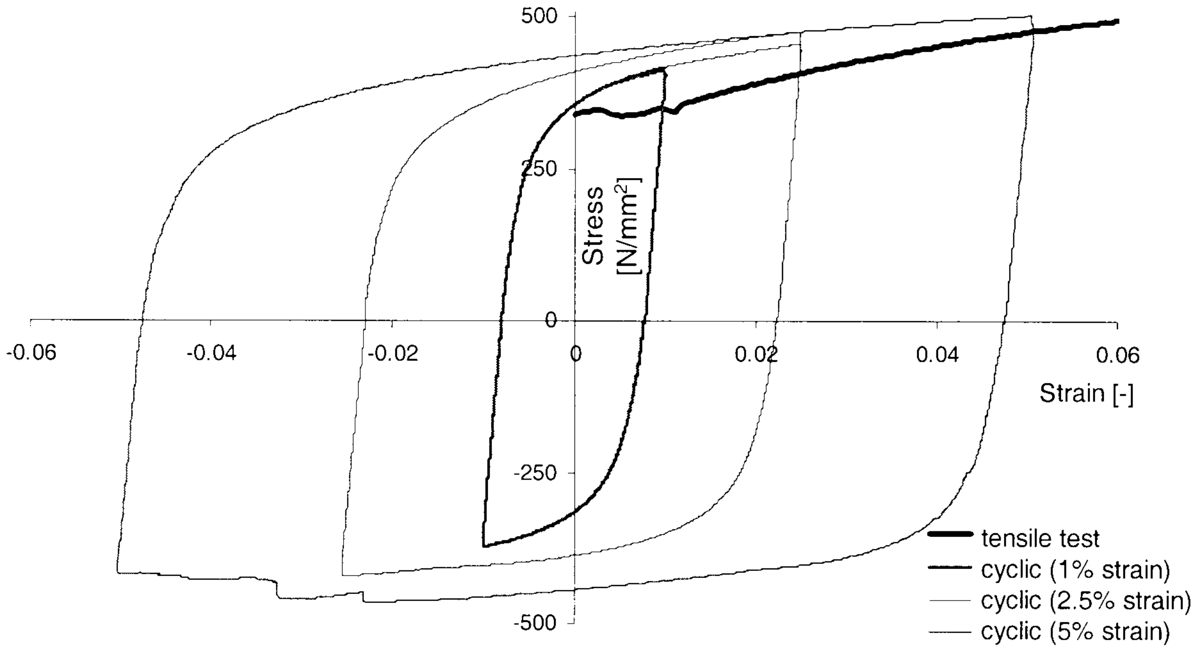

Figure 5-19: Tensile and cyclic material test results (steel with f_y =340N/mm^2)

increment vector depends only on the current stress state.

$$d\varepsilon_{ij}^{pl} = \lambda \frac{\partial f(\sigma_{ij})}{\partial \sigma_{ij}} \tag{5.14}$$

where $f(\sigma_{ij})$ is the yield surface function. The Von Mises yield surface criterion in term of principal stresses is:

$$(\sigma_1 - \sigma_2)^2 + (\sigma_2 - \sigma_3)^2 + (\sigma_3 - \sigma_1)^2 = 2\sigma_y^2 \tag{5.15}$$

and

$$\frac{\partial f(\sigma_{ij})}{\partial \sigma_1} = 2\sigma_1 - (\sigma_2 + \sigma_3) \tag{5.16}$$

and therefore:

$$\begin{aligned} d\varepsilon_1^{pl} &= \lambda(2\sigma_1 - (\sigma_2 + \sigma_3)) \\ d\varepsilon_2^{pl} &= \lambda(2\sigma_2 - (\sigma_1 + \sigma_3)) \\ d\varepsilon_3^{pl} &= \lambda(2\sigma_3 - (\sigma_2 + \sigma_1)) \end{aligned} \tag{5.17}$$

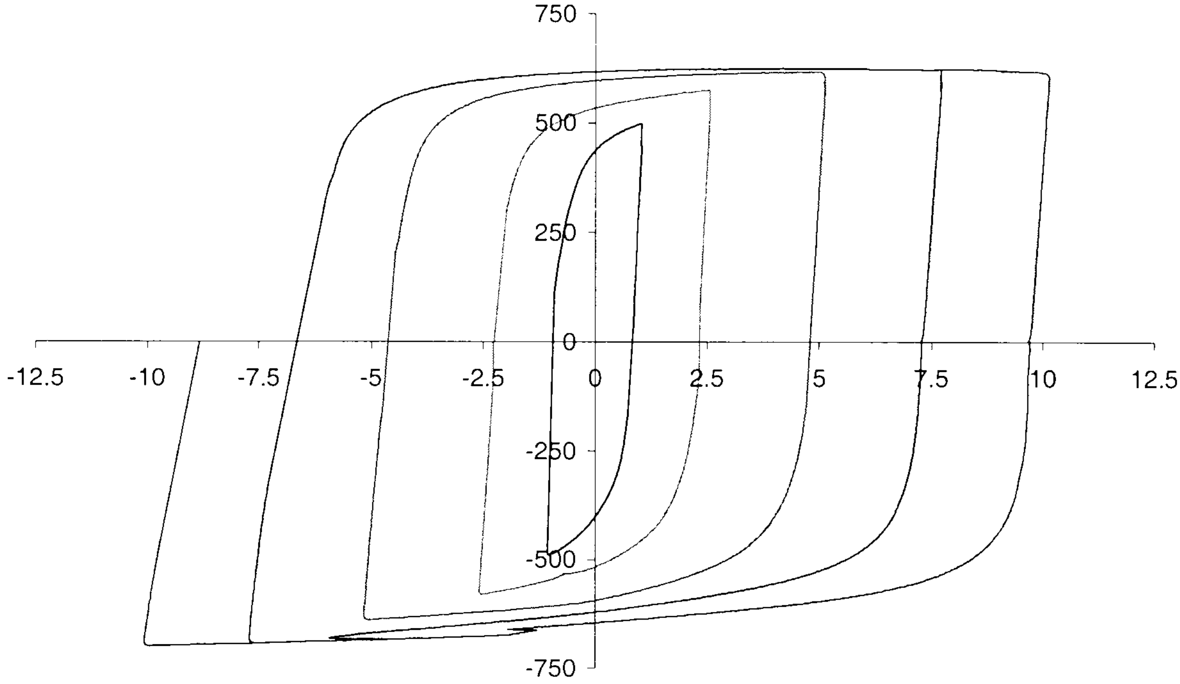

Figure 5-20: Cyclic material test results (steel with f_y =430N/mm^2)

where 2λ is a proportional factor, which represents an instantaneous modulus which changes value with increases in strains. $\sum d\varepsilon_i^{pl} = 0$, as in plastic flow deformation volume remains constant.

The effective (or equivalent) plastic strain increment is defined by:

$$d\bar{\varepsilon}_{eff}^{pl} = \sqrt{\frac{2}{3}\left(d\varepsilon_{ij}^{pl} d\varepsilon_{ij}^{pl}\right)} = \sqrt{\frac{2}{3}\left(d\varepsilon_1^2 + d\varepsilon_2^2 + d\varepsilon_3^2\right)} \tag{5.18}$$

Energy density

The energy density w_{pl} dissipated is then given by:

$$w_{pl} = \int_0^{\varepsilon_{ij}^{pl}} \sigma_{ij} \cdot d\varepsilon_{ij}^{pl} = \int_0^{\varepsilon_{eff}^{pl}} \sigma_{VM} \cdot d\varepsilon_{eff}^{pl} \tag{5.19}$$

From energy densities to effective strains

The energy density w_{pl} released in a half cycle of a specific effective strain, as shown in Figure 5-17 b, can be calculated using Equation 5.19 and a cyclic stress-strain curve (defined by the material hardening rule). This calculation performed for different effective strains, allows us to plot the energy densities versus effective strains and furthermore the energy densities versus the Von Mises stress, as shown respectively in Figure 5-21 a and b, (for steel with $f_y = 340N/mm^2$).

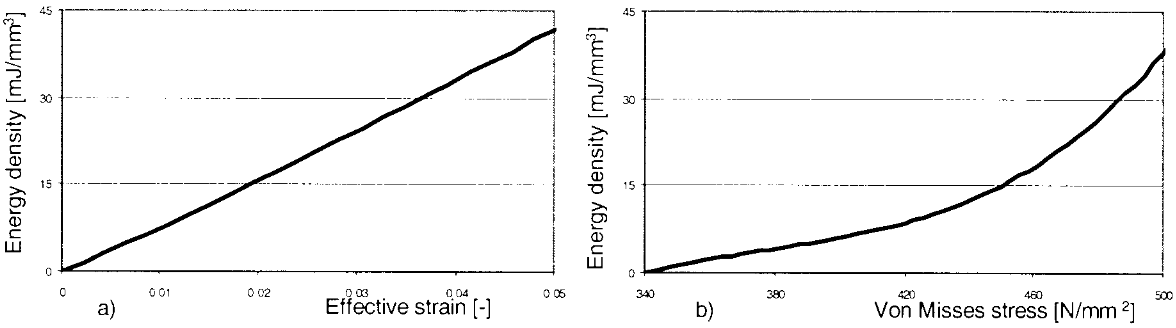

Figure 5-21: Energy density versus a) effective strain and b) Von Misses stress

5.5.3 Transform function

The beam is moving and deforming and therefore successive pictures cannot be simply superposed.

The easiest solution is to compare only pictures of the knee element at the same position and deformation state. Practically this was rarely possible, because the thermal imaging camera was only taking around 25 pictures per cycle and the testing rig had some flexibility, so that small shifts in both vertical and lateral movements were observed between two maxima.

The alternative solution is to follow the movement of each web point in order to extract the dissipated energy from the thermal images. A transform function was used to transform the deformed part back to its initial (or undeformed) shape. After the transform, pictures can be superposed and mathematical operations can be performed on them (such as subtraction, Laplacian,...). For knee elements with solid webs, a very simple transform function gave acceptable results. For the knee elements, with perforated webs, unhomogeneous deformations occurs and a more complex transform function was needed. Both transform function are presented below.

Simple transform function

$P_0(x_0,y_0)$, $P_1(x_1,y_1)$ and $P_2(x_2,y_2)$ are three reference points in the undeformed image and $P'_0(x'_0,y'_0)$, $P'_1(x'_1,y'_1)$ and $P'_2(x'_2,y'_2)$ are their new positions in the deformed image, both with their coordinates in the same orthogonal $Oxy-$system (Figure 5-22).

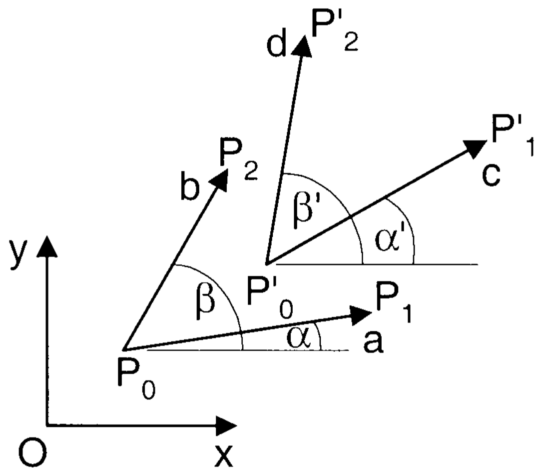

Figure 5-22: Movement and deformation of the reference points triangle

Each pixel $P_i(x_i,y_i)$ can be express as $P_i(a_i,b_i)$ in the $P_0P_1P_2$-system with:

$$\begin{pmatrix} a_i \\ b_i \end{pmatrix} = \begin{pmatrix} \cos\alpha & \cos\beta \\ \sin\alpha & \sin\beta \end{pmatrix}^{-1} \begin{pmatrix} x_i - x_0 \\ y_i - y_0 \end{pmatrix} = \frac{1}{\sin(\beta-\alpha)} \begin{pmatrix} \sin\beta & -\cos\beta \\ -\sin\alpha & \cos\alpha \end{pmatrix} \begin{pmatrix} x_i - x_0 \\ y_i - y_0 \end{pmatrix} \tag{5.20}$$

In the deformed image each pixel $P'_i(x'_i,y'_i)$ can be expressed as $P'_i(c_i,d_i)$ in the $P'_0P'_1P'_2$-system with:

$$\begin{pmatrix} c_i \\ d_i \end{pmatrix} = \begin{pmatrix} \cos\gamma & \cos\delta \\ \sin\gamma & \sin\delta \end{pmatrix}^{-1} \begin{pmatrix} x'_i - x'_0 \\ y'_i - y'_0 \end{pmatrix} \tag{5.21}$$

If it is assumed that in the triangle, the vertices of which are the three reference points, has experienced a linear transformation then $c_i \cdot \overline{P_0P_1} = a_i \cdot \overline{P'_0P'_1}$ and $d_i \cdot \overline{P_0P_2} = b_i \cdot \overline{P'_0P'_2}$. The coordinate of $P'_i(x'_i,y'_i)$, where the pixel $P_i(x_i,y_i)$ has moved to (in the $Oxy-$system) is obtained with:

$$\begin{pmatrix} x'_i \\ y'_i \end{pmatrix} = \begin{pmatrix} x'_0 \\ y'_0 \end{pmatrix} + \begin{pmatrix} \cos\gamma & \cos\delta \\ \sin\gamma & \sin\delta \end{pmatrix} \begin{pmatrix} \frac{\overline{P'_0P'_1}}{\overline{P_0P_1}} & 0 \\ 0 & \frac{\overline{P'_0P'_2}}{\overline{P_0P_2}} \end{pmatrix} \begin{pmatrix} \cos\alpha & \cos\beta \\ \sin\alpha & \sin\beta \end{pmatrix}^{-1} \begin{pmatrix} x_i - x_0 \\ y_i - y_0 \end{pmatrix} \tag{5.22}$$

Since the values of x' and y' may not be integers, the following linear interpolation function can be used:

$$T(i+\xi; j+\eta) = T(i,j)(1-\xi)(1-\eta) + T(i+1,j)\cdot\xi\cdot(1-\eta) + T(i,j+1)(1-\xi)\cdot\eta + T(i+1,j+1)\cdot\xi\cdot\eta \quad (5.23)$$

where i and j are the integer part and ξ and η the fractional part of x' and y' respectively.

The temperature of each point corresponding to a pixel of the undeformed image, can now be followed in successive images despite the object's significant movements and deformation. This simple transformation function was used for the thermal images of knee elements without holes. The images represent the rectangular section of the web between two stiffeners. The corners of the section were used as reference points. An executable was programmed in $MATLAB$; this programme first identified the reference points, then transformed the thermal images to their undeformed shapes and finally, using Equation 5.12, calculated the dissipated strain energy, from which the effective strains and Von Mises stresses were deduced.

Complex transform function

For knees with holes the deformation of the web is more unhomogeneous and the simple transform function gives unsatisfactory results. For these cases, a more sophisticated transform function was used, developed by researchers working on medical image analysis in the Oxford Engineering Science Department (Marias et al. 2000). Their prototype in-house software was used. The principle of their transform function is as follows:

Let the centre of the holes in the deformed image be $\overrightarrow{h_i^J}$, let the corresponding centre of the holes in the undeformed image be $\overrightarrow{h_i^I}$. $\widetilde{T}$ is a transform function from J to I such that $\widetilde{T}$=arg min $\left(\sum\left(T\left(h_i^J\right)-h_i^I\right)^2+\int \text{"}regulariser/smoothness\text{"} \quad in \quad \widetilde{T}\right)$.

The hole centres were taken as reference points. In order to identify the hole centre coordinates, a cold background $\sim 4°C$ (fridge temperature) was set behind the beam so that the holes were seen as cold spots on the thermal images. An executable was programmed in $MATLAB$, that found the hole centre coordinates on each thermal image. With the transform images, again, the dissipated strain energy, the effective strains and the Von Mises stresses were obtained.

5.6 Thermal analysis results

In this section the results of the thermal imaging camera with the thermal analysis method developed in Section 5.5 are presented. The results obtained with the thermal film sensor are also investigated.

5.6.1 Thermal film sensor

A thermal film sensor was fixed on a knee element, with a perforated web, between two holes where the maximum temperature increase was expected. Figure 5-23 gives the central deflection and the temperature increase of knee element n°7 versus time. The thermal film sensor measured the maximum temperature with approximately 2.5 seconds delay (time between the end of the test and the time when the temperature reached its maximum).In this example the thermal imaging camera was indicating a temperature increase of 40 degrees whereas the thermal film sensor was only able to measure an increase of 26 degrees. Especially for the perforated knee elements, the temperature at the hot points drops rapidly after the test because the temperature gradient is very high. With the delay the thermal film sensor will only measure the temperature after the gradient has dropped significantly.

This shows that even a small thermal film sensor (size $10 \times 2 \times 0.5$ [mm]) has a thermal inertia which causes an important time delay, causing it to fail to capture by a large amount the temperature peak. The thermal imaging camera has the advantage of giving 'instantaneous' measurements over an entire surface.

5.6.2 Image acquisition and reference points

During the time of the loan of the thermal imaging camera, knee element tests 7, 13 and 14 and the second part of knee element tests 3 and 6 were performed. In total 46 subtests were performed on these five knee elements and recorded successfully with the thermal imaging camera. For each subtest between 50 and 100 pictures were taken. The images corresponding to the peak displacements were carefully identified and transferred

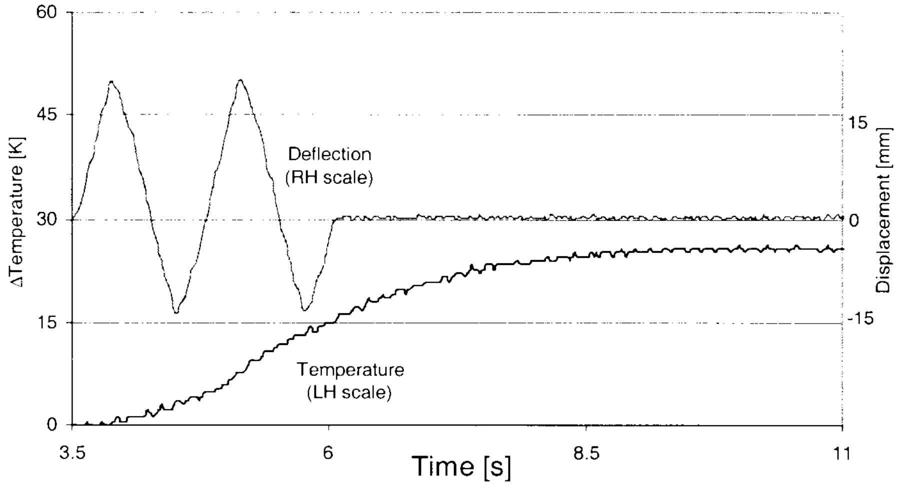

Figure 5-23: Central deflection and temperature increase between two holes of knee element n°7 versus time

with the procedure described in section 4.7. Further images corresponding to the state between the displacement peaks were also transferred for analysis. Figure 5-24 shows pictures recorded by the thermal imaging camera during testing.

In Figure 5-24 a), b) and c) the holes are visible as black circles representing the cold background (dark colour) that can be seen through them. In Figure 5-24 d) two cold rubber strips were attached on the stiffeners, represented in grey in Figure 5-25 b). To obtain better accuracy for the reference coordinate points, four small cold rubber patches were used instead of the strips for knee element n°13, Figures 5-24 e) and f). Two patches were attached to the stiffeners and two to the flange edges, as shown in Figure 5-25 a). Unfortunately, the patches and the strips did not have sufficient thermal inertia and were warmed up quite quickly. Some accuracy must have been lost through this process. The cold background behind the knee element with perforated web remained cold enough to determine the hole centres quite easily and accurately .

In Figure 5-24 d) the blue line at mid distance between the cold strips shows the position where the stiffener is placed on the other side. (Additional stiffeners were placed alternately, on one side only, Section 3.9). As expected this indicates that no yield in the web occurs where the stiffeners provide reinforcement.

In Figure 5-24 e) two strips of higher temperature (brighter colour) on the web on

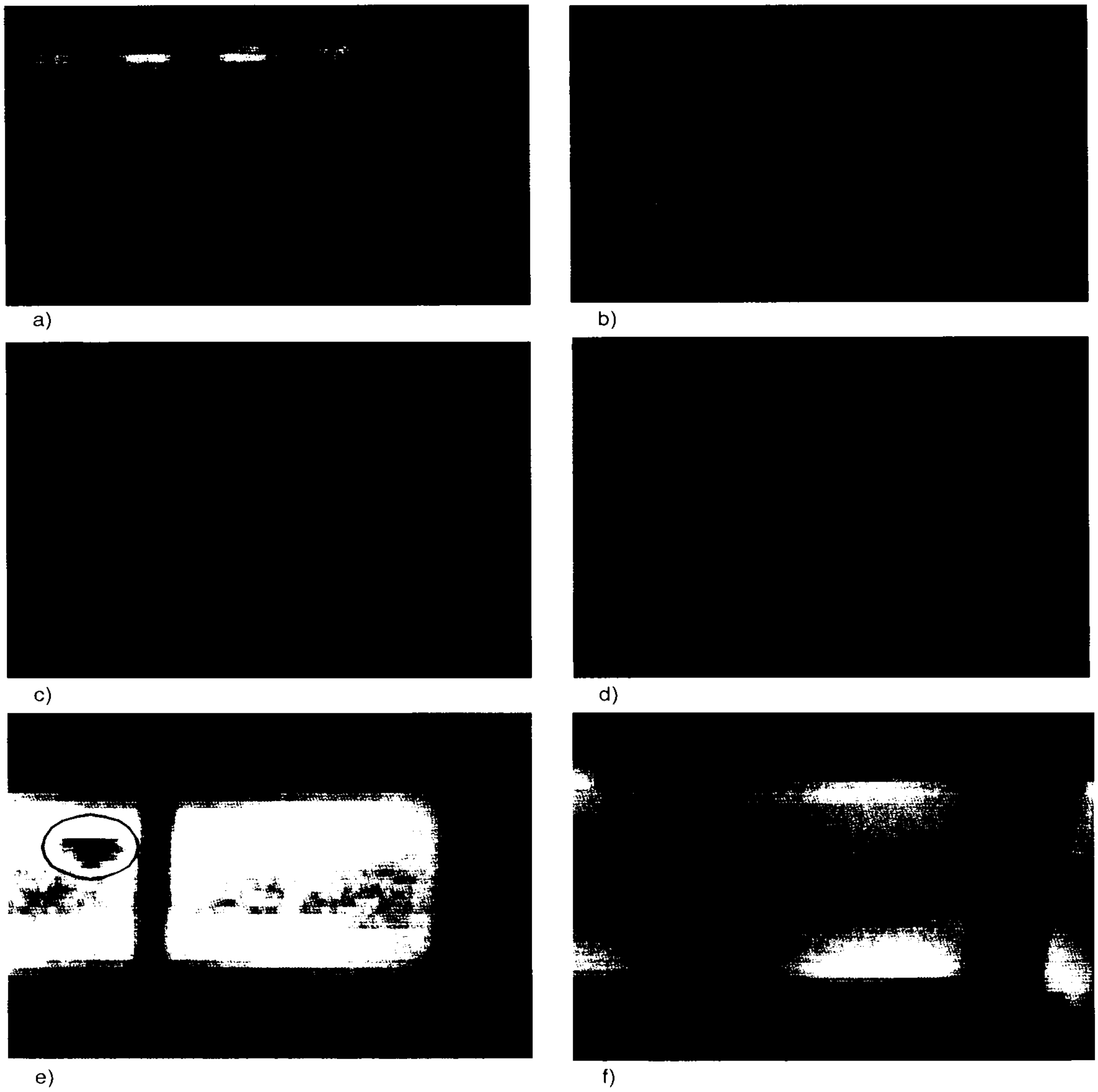

Figure 5-24: Thermal images taken during testing of the knee elements a) n°3, b) n°6, c) n°7, d) n°14, e) & f) n°13.

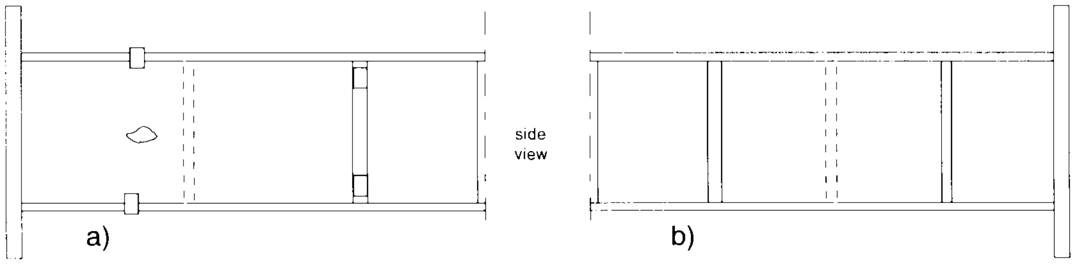

Figure 5-25: Cold patches and strips on knee elements a) n°13 and b) n°14

either side of the stiffeners can be seen. They are situated along the web-stiffener welds. This indicates that there is some interaction between the stiffeners and the web.

5.6.3 Emissivity variation

The knee element had a fully oxidised surface before testing. Using an emissivity ratio value of 1.0 in the software package *IRWIN*, good agreement with the thermal film sensor was obtained during the calibration test (Section 4.7). (The emissivity ratio of 1.0 is the maximum value allowed). During testing in central horizontal strips of the web most of the oxidised steel dust flaked off revealing shiny steel spots, Figure 5-26.

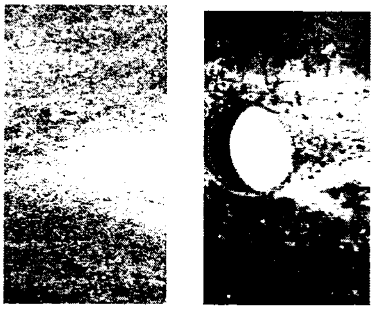

Figure 5-26: Shiny spots in the web

Unfortunately, shiny steel has a significantly lower emissivity than oxidised steel and also reflects emission from hotter surrounding objects. Before the testing of knee element n°13 a small spot was polished on the web and can be seen in Figure 5-24 e). In the central horizontal strips of the web zones, some zones are accredited by the thermal imaging as having lower temperature than the average surrounding temperature. This cold pattern expands as the oxidised steel dust continues to fall, Figures 5-24 e) and f). Since these cold patterns appear even for small deformations it was estimated that they are due to a change of emissivity alone, and not because of a local reduction in energy dissipation, which buckling would cause. Where shiny spots have appeared the temperature deduced from the thermal images are false and therefore the temperature information in the central horizontal strip where they appeared has been discarded. The fact that it concerns only horizontal central sections is surely related to the hot rolled production method. Knee element n°7 was not affected by this problem and a fine uniform shade of oxidised steel dust remained over the entire web during the test. (This knee element was the only one made of steel having a f_y =430mm^2).

To paint the web would have been inadequate, as the painting would have acted as an isolation layer, and may have cracked for high plastic strains and high temperatures. To polish the entire web and test under a blanket to protect it from parasite reflections seems conceivable, but was not performed because of the limited time period of the thermal camera loan.

5.6.4 Results

The complex transformation method described previously in Section 5.5.3 was applied successfully to the thermal images of the perforated web sections. Figure 5-27 (a) shows the thermal image knee element n°3 at peak displacement (downwards) and Figure 5-27 (b) shows the same image transformed to its initial shape using the complex transform method.

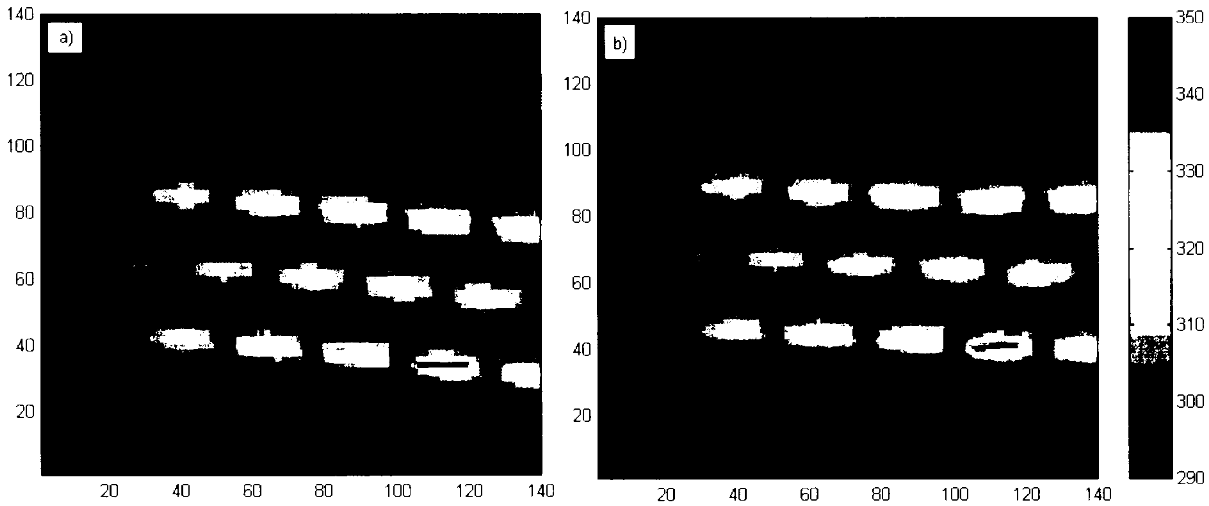

Figure 5-27: Transform temperature maping in [°K] from a) deformed shape, back to b) its initial shape.

Using Equation 5.12 and the relationships established in Section 5.5.2 for the energy dissipation density during half a cycle, the effective plastic strain and the Von Mises Stress in the web were mapped. Figure 5-28 shows the mapping of these quantities for knee element n°3. Images a) c) and e) are for an imposed displacement of 19mm and images b), d) and f) for an imposed displacement of 29mm corresponding to the failure amplitude. The propagation of two cracks occurred during that half cycle in the web area between the three holes of bottom line on the right hand side.

For knee elements n°3, 6 and 7 the crack propagated only after effective strains values of ~10% were reached between the holes. Of course, higher strains were reached at the crack tips. The strain at the tip could not be determined from the thermal images. The definition is to coarse, and the crack tip would be shiny and therefore have a different emissivity value.

The effective peak strains in the web of knee elements n°13 and 14 were around 5% at the amplitude for which failure was observed (Figure 5-29). For knee element n°14 in the last cycles the plastic strain was increasing in the web portion just above the central connection (which can just be seen on the right edge of Figure 5-29).

5.6.5 Improvements

Transform method The simplified method applied to the knee elements without holes gave relatively good results but could be refined by using a smoother transform function such as the one used for the knee elements with perforated holes (which used at least 15 reference points). For the knee elements without holes a more effective method of getting numerous reference points that can be followed easily and accurately needs to be drawn up. Dual synchronised thermal and normal cameras, low emissivity and isolation painting dots directly on the web or a grid of electric heated wires (detectable with today's cameras that possess better resolution) spanned at a few millimetres in front of the web, are methods to investigate. It is necessary to put the reference points as near as possible to the web, in case the knee element undergoes torsional deformation.

Emissivity and material characteristics Some additional work needs to be performed on the surface preparation and a method to accurately define its emissivity. Some material testing (tensile or cyclic testing) should be recorded with the thermal imaging camera to assess if Figure 5-21 are realistic and if the emissivity of the material varies when subject to high strains.

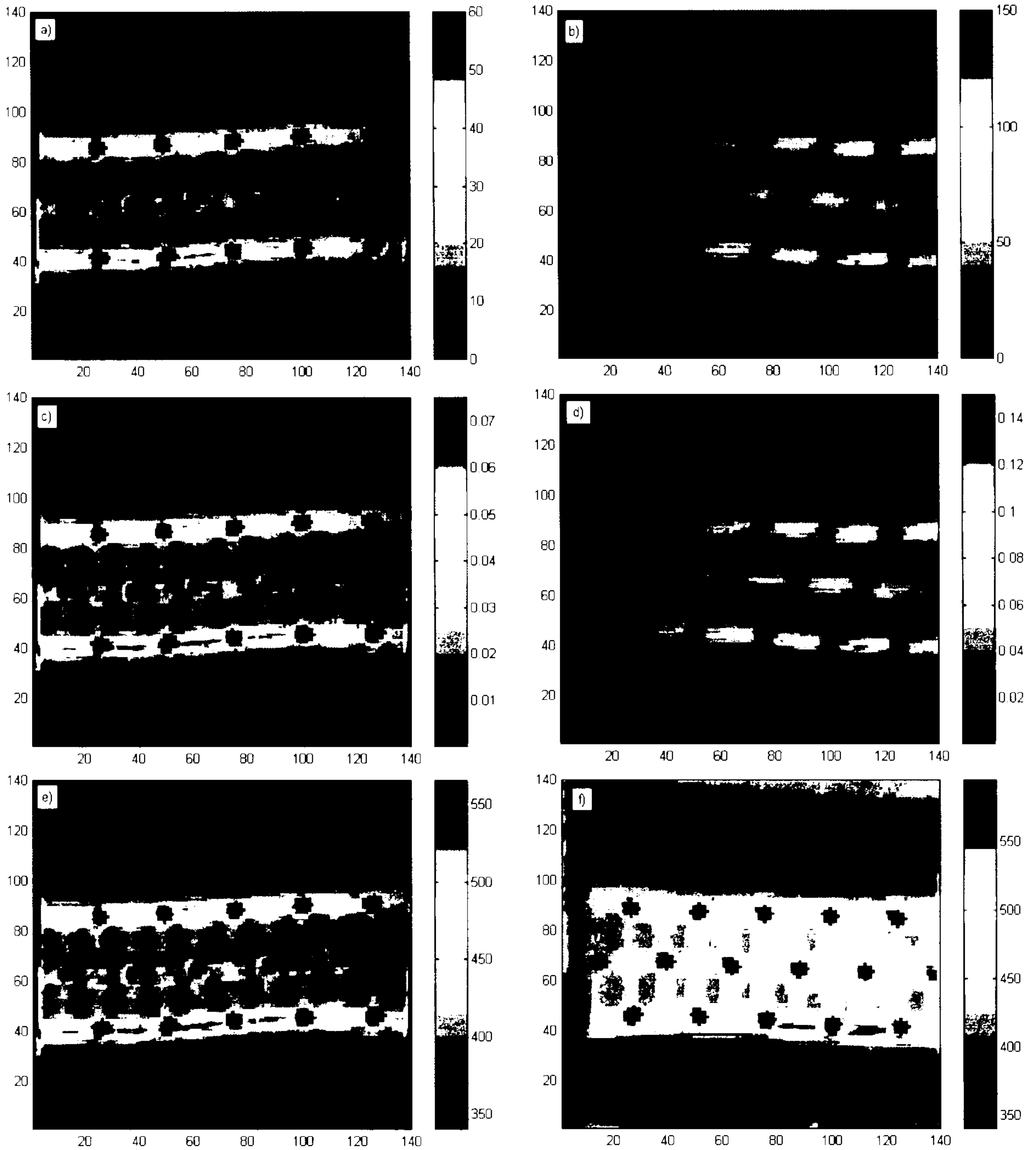

Figure 5-28: a) & b) Energy density [miliJ/mm^3], c) & d) Effective strain [-], and e) & f) Von Mises stress [N/mm^2]. a), c) & e) 19mm deflection. b), d) & f) 29mm deflection.

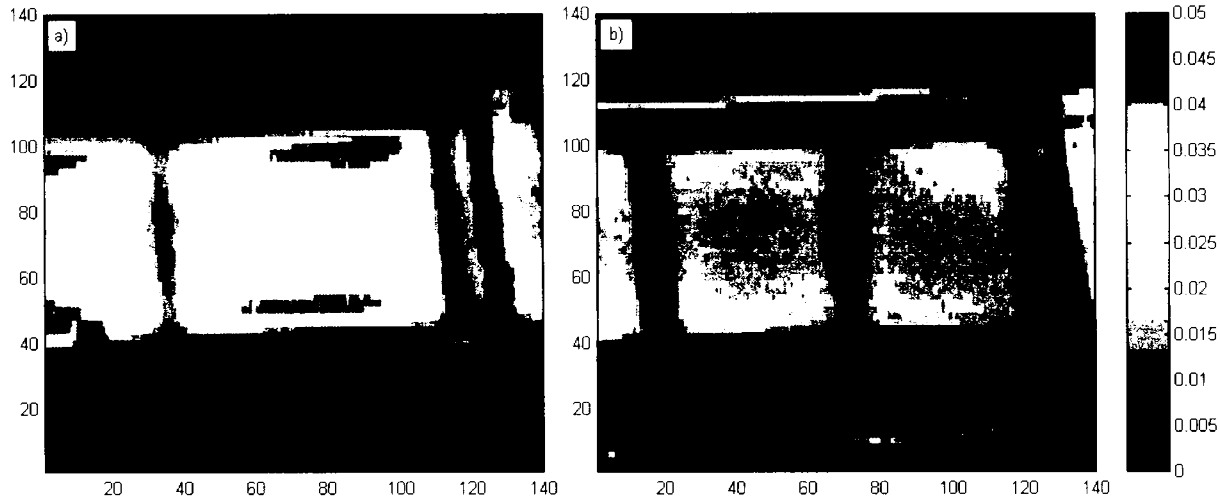

Figure 5-29: Plastic strain [-] of knee elements a) n°13 and b) n°14.

5.7 Conclusion

Physical testing yielded significant information and in particular allowed important conclusions to be drawn about buckling and failure. The measurement equipment generated a large quantity of data. Small executable programmes were written to help analyse the data and determine representative characteristics. From the results substantial conclusions and relevant design guidelines were drawn and are presented below.

5.7.1 Knee element performance

- Knee element yielding in shear shows great ductility and energy dissipation zones situated outside of the connection areas.
- Perforating the web is a simple and effective means of varying the yielding shear capacity to suit a particular structure though it slightly reduces the ductility and considerably reduces the endurance and the energy dissipation capacity. This outweighs the advantage gained in allowing the designer some flexibility in specifying the yield load.
- To prevent buckling under large plastic deformation, vertical web stiffeners attached to the bottom and top flanges should be added at a spacing approximately equal to the section depth.

- Stockier Universal Column sections are recommended because they are less prone to lateral instabilities. In addition (with stiffeners as recommended) web buckling is avoided.

- Knee element yield loads (without holes in the web) are accurately predictable (within $\pm 5\%$) using a simple formula (Equation 3.59) with a factor of 0.95 to account for residual stresses.

- To impose a realistic design deflection on a knee element (with stiffeners as recommended) requires a load of approximately 1.7 times the yield load. This is a factor the designer needs to take into account.

- Full scale cyclic loading of the knee element gives responses representative of what a knee element would experience in an earthquake.

- The number of knee elements of the same type and the same steel that were tested was insufficient to develop a low cycle fatigue model for beam yielding in shear.

- The influence of steel grade on the performance of the knee element could not be determined.

5.7.2 Thermal analysis

- Thermal imaging is an effective method for identifying the energy dissipation areas, where the element starts yielding and how the yielding pattern expands. (It can also detect friction by a bolt slip.)

- With reference points (that can be localised in each picture) and using a complex transform method, the images can be transformed back to their initial shape. This allows mapping of the energy density of a surface and the calculation of the effective plastic strain and the Von Mises stress for each equivalent pixel area.

- The results obtained were already of a very good quality and definition. Currently available thermal imaging cameras have better performance and these are promising tools for assessing plastic strain.

- The data gained can be useful in the calibration of a material rule and the improvement of a model for finite element analysis.

- Further consideration needs to be given to the emissivity and the surface preparation of the analysed part.

- A more effective method of establishing numerous reference points that can be followed easily and accurately needs to be developed.

- A small thermal film sensor was very useful for calibrating the thermal camera but failed to catch peak temperatures during testing. In addition it only gives the temperature at one point. Thermal film sensors are therefore not suitable for this application.

Chapter 6

Finite element modelling of knee elements

6.1 Introduction

In Section 3.8.1 extensive finite element analyses (FEA) were performed to evaluate the effects of drilling holes in the web on knee element characteristics such as the stiffness and the yield load. A selection of knee element designs was then physically tested and the results presented in Chapter 5. In this chapter the finite element models were refined. Details such as flexibility of the connections, the welds and the flange roots, which contribute to the response of the knee element, were modelled. Their contributions were evaluated by comparing different models. Imperfections and residual stresses were also included in the analysis.

Monotonic and cyclic calculations have been performed and the results compared with physical testing measurements.

A heat analysis simulating the diffusion of the plastic strain energy has also been performed and compared to thermal images taken during physical testing. The equivalent strain and the Von Mises stresses obtained with the FEA have been also compared with those deduced from the thermal images using the method developed in Section 5.5.

Detailed analyses of a web section with holes, where crack initiation and crack propagation take place, were performed. Finally instability calculations were performed in an attempt to determine critical or failure loads.

6.2 Geometrical model

Creating a model that is a very accurate replica of the structure using an extremely fine mesh of solid elements is not difficult. However, the analysis may converge very slowly (and in some case may even present some divergence problems) and create intermediate files of unmanageable sizes and may run for days on an average *UNIX* machine. In addition, the results may not be different or better than a simplified model. The designer is more interested in having a good simplified model that requires only a relatively small computing time, enabling him or her to acquire a good estimation of the knee element behaviour rapidly and eventually compare different designs. The use of shell elements reduces significantly the size of the problem. Shell elements have been used therefore for the global model. A model with a very fine mesh of solid elements was used only for the detailed analysis of a very small web portion with a hole.

All geometrical models were built using the solid modelling package *I-DEAS*.

6.2.1 Global model

Shell element

ABAQUS provides three categories of shell elements for static stress-displacement analysis: thin, thick and general purpose shell elements. The general-purpose elements provide robust and accurate solutions in all loadings for thin and thick shell problems. General-purpose elements allow transverse shear deformation and use thick shell theory for a certain shell thickness. They account for finite membrane strains and will allow for changes in thickness. They are, therefore, suitable for large-strain analysis involving materials with a non-zero effective Poisson's ratio. The thick shell elements are small-strain shell elements and the thin shells neglect transverse shear flexibility. Neither are therefore suitable for our analysis.

In the static finite element model general-purpose finite-strain 3-noded triangle shell elements and 4-noded quadrilateral shell elements were used. These elements use six degrees of freedom (3 displacement and 3 rotation components) at all nodes. Further element characteristics can be found in Section 3.6.6 (Finite-strain shell element formulation) in the *ABAQUS* Theory Manual (1998) and in the *ABAQUS* Standard User's

Manual (1998).

The size of the shell elements was chosen so that little noticeable difference would be found with a finer mesh, whilst retaining to a reasonable size in order to limit the number of elements and nodes in the model.

Shear capacity calculations taking into account stiffeners, welds and roots

The dissipative areas develop first in the parts of the web away from the root, the stiffeners and the welds. It was therefore decided to thicken the web where the root, the stiffeners and weld cordons prevent the web from yielding. Since the knee elements yield in shear, great care should be given to the area bearing the shear force. The I-section was modelled as shown in Figure 6-1. t_1 is the average measured thickness of the clear web. t_2 was set so that the modelled web area equals the shear area for a hot rolled section given by the Eurocode-3:

$$A_v = A - 2 \cdot B \cdot T + (t_1 + 2 \cdot r) \cdot T \tag{6.1}$$

$$t_2 = \frac{A_v - d \cdot t_1}{2 \cdot (T/2 + r)} \tag{6.2}$$

where d is the clear web height. t_2 =13.1mm for $UC23$, 14.4mm for $UC30$ and 13.1mm for $UB23$. t_1 =6.55mm for $UC23$, 6.85mm for $UC30$ and 5.75mm for $UB23$.

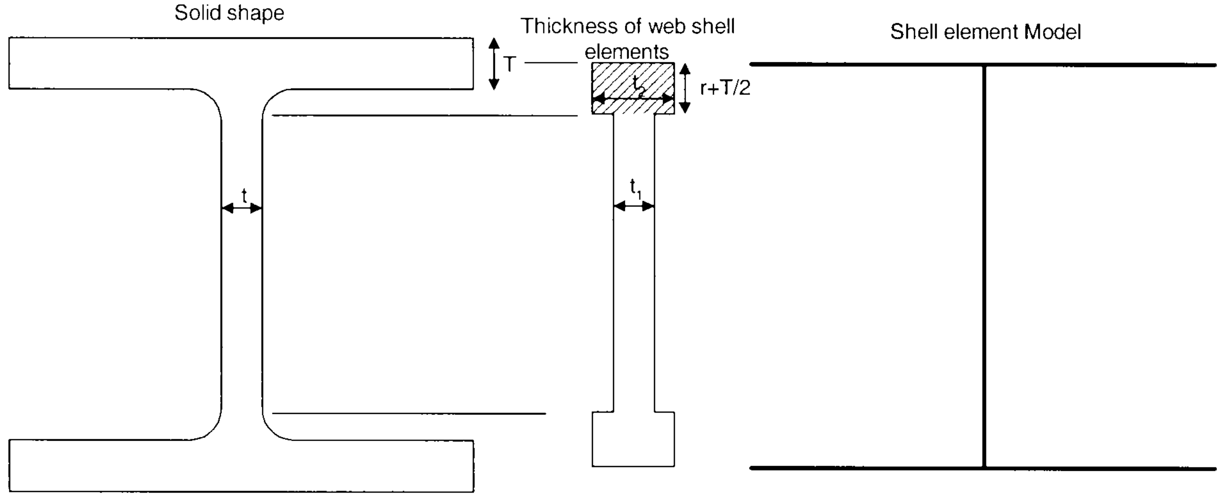

Figure 6-1: Geometric model of the beam section for finite element analysis.

Symmetry

Through consideration of symmetry only half of the knee element needed to be modelled. In Section 3.8.1 only a quarter of the knee element was modelled; at that stage of the research it was decided to simplify the central connection to a single stiffener (identical to the end plates) through which the load would be applied. This was done in order to reduce the computing time. For these analyses the beam was more realistically modelled.

6.2.2 Detailed model

Solid elements

In *ABAQUS* 8- and 20- node quadratic brick, 6- and 15- node prism and 4- and 10- noded tetrahedron solid elements are available. For a detailed model of a knee element portion 10-noded tetrahedron solid elements C3D10 were used.

6.3 Connections and boundary conditions

Tsai et al. (1995), Ramadan and Ghobarah (1995) and Popov et al. (1998) have assessed performance of beam-column joints and proposed improved connections for seismic design. Bernuzzi et al. (1996) have developed simple design criteria and simple prediction models of the joint response and Lo and Stiemer (1995) have proposed a practical method for incorporating connection models in plane frame analysis. However in the present research a simplified approach has been taken to the connection modelling for the following reasons:

1. The research concentrated on dissipative elements which have their dissipative area away from the connections.

2. In the physical testing, damage to the connection only occurred for the knee element with stiffeners subject to very large deformations and generally only after web buckling had occurred. The connections could be easily reinforced.

3. The ends of the knee element were solid-bolted to massive loadcells. During testing bolts were tightened after a few subtests, in order to suppress the influence of eventual bolt slip (in shear) or slack in the bolt (compression-tension). The rotational

and translational movement observed at the knee element supports came essentially from the testing rig flexibility. It was therefore more important to model this effect.

4. The connection behaviour can be added later in the global frame analysis (which is done for a building example in Section 7.3).

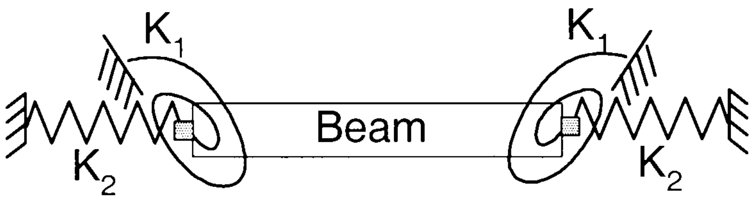

Figure 6-2: Knee element extremities in the FEA-model

The testing rig flexibility was evaluated in the physical testing (Section 4.4, Table 4.1) and included in finite element analysis using translational and rotational springs at the knee element extremities as shown in Figure 6-2. Since the test rig did not always show the same flexibility (anchor problems, Section 4.5), its stiffness has been re-evaluated in each subtest using the loadcell and cable transducer measurements. Since the whole end plate rotates about a specific axis the spring option was used in conjunction with a multi point constraint option.

6.4 Residual stresses

Residual stress inherited from the rolling process will affect the yield load of the knee element. In order to evaluate the residual stress influence, a commonly used residual stress model for hot-rolled I-sections was used, as shown in Figure 6-3 (ECCS 1984, Avery 1998). A user subroutine was written and was added to *ABAQUS* input files to generate residual stresses as initial conditions. The residual stress σ_r was taken as equal to half of the yielding stress f_y. When initial stresses are given, the initial stress state may not be an exact equilibrium state for the element model. Therefore, an initial static step, without external load, should be included to allow *ABAQUS* to achieve equilibrium.

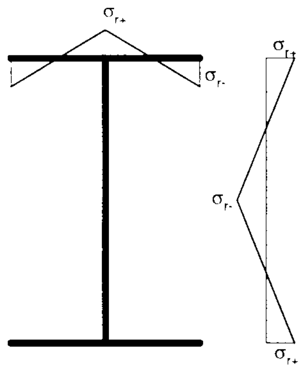

Figure 6-3: Typical I-section residual stress distribution

6.5 Buckling and imperfections

If the load is applied to the centroid of the cross-section and the members are perfectly straight, local buckling will not occur in the simulation. To activate buckling modes local imperfections of the member must be included. The most critical situation occurs when a member's local imperfection shape coincides with the critical buckling shape. *ABAQUS* provides eigenvalue buckling extraction for elastic buckling (Section 2.3.1 of the *ABAQUS* Theory Manual, 1998). The elastic buckling shapes, their eigenvalues and the buckling loads estimate as a multiple of the pattern of perturbation loads are obtained for the specified n-first mode using the buckle-option.

With the imperfection-option a geometric imperfection can be introduced into the model, as a linear superposition of buckling eigenmodes. The mode number and a scaling factor for each mode from the previously run buckling analysis are required. The algorithm used to integrate the perturbed coordinates in the analysis is given in section 7.5 of the *ABAQUS* Standard User's Manual (1998). The magnitude of local web and flange imperfections, were taken around of $1/150^{th}$ of the section depth, which is the tolerance value given for hot rolled steel sections in British Standard Code BS 4848 Part 1 (1972).

Concern about inelastic shear buckling in the web has already been mentioned in Section 3.6.3. In the physical testing inelastic shear buckling was effectively observed in some knee elements and was described in Section 5.4.6. To investigate inelastic buckling a load-deflection Riks analysis (Ramm 1981, Crisfield 1981) must be performed. The Riks method is very efficient in handling snap through. The Riks method uses the load magnitude as an additional unknown: it solves simultaneously for loads and displacements. An "arc length" along the static equilibrium path in load-displacement space is used to measure the progress of the solution. The procedure is described in section 2.3.1 of the *ABAQUS* Theory Manual (1998).

6.6 Material model

6.6.1 Monotonic loading

For evaluating the yield load, a tri-linear material law as shown in Figure 6-4 was appropriate. The tri-linear material was calibrated with the beginning of the tensile test curve presented in Section 5.2.2. In *ABAQUS*, the material is defined by the Young modulus and Poisson's ratio, the yield load and data-pair of the true-stress true-plastic-strain.

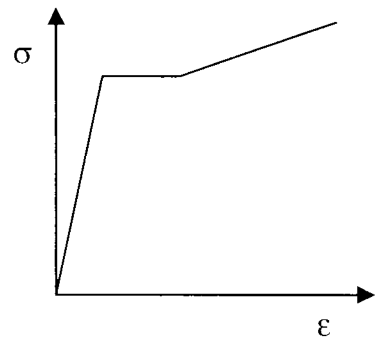

Figure 6-4: Tri-linear material law used for yield load evaluation.

6.6.2 Cyclic loading

For cyclic loading simulation a non-linear kinematic hardening model was needed. The non-linear hardening parameters can be calculated from a stabilized cycle subjected to symmetric strain cycles of a set of test data. A stabilized cycle is obtained by cyclic loading of the specimen over a fixed strain range until a steady-state condition is reached; that is, until the stress-strain curve no longer changes shape from one cycle to the next, Figure 5-18 from Section 5.5.2. For mild steel, a stabilized cycle is generally obtained after only a few cycles. Furthermore, in the material cyclic test it was observed that if the strain value is increased by small steps only one or two cycles are necessary to establish a new stabilised cycle.

The non-linear hardening parameters are the stabilised elastic range σ_y^s, C and γ and *ABAQUS* offers the possibility to calculate them from data pairs of stress and plastic strain (with the strain axis shifted to ε_0, Figure 6-5) with an exact match for the first data pair, and then achieving the best fit for the following data pairs using:

$$\sigma_i = \frac{C}{\gamma}(1 - e^{-\gamma \varepsilon_i^{pl}}) + \sigma_1 \tag{6.3}$$

$$\varepsilon_i^{pl} = \varepsilon_i - \frac{\sigma_i}{E} - \varepsilon_0 \tag{6.4}$$

The stabilised elastic range is given by:

$$\sigma_y^s = (\sigma_1 + \sigma_n)/2$$

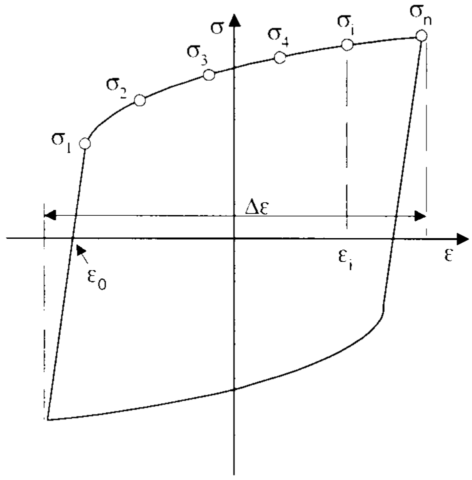

Figure 6-5: Stress-strain curve of a stabilized cycle

This calculation is very sensitive to the data pairs entered. The material model (Equation 6.3) with only three parameters does not allow for a very good fit of the hysteresis curves obtained from cyclic material test presented in Section 5.5.2 and plotted in Figure 5-19. Therefore the parameters were calibrated manually to match different aspects of these hysteresis curves. For example, the parameters of all three models presented in Figure 6-6 were calibrated such that the material model would give an exact match at a strain value of 2.5%, and a very good fit to the section preceding it. Material model 1 was given a low σ_y to model the low yield load in reversed loadings. Material model 2 was calibrated such that the energy dissipated in a cycle would be equal to the one found from the physical material test. Material model 3 was a best fit with $\sigma_y^s = f_y$.

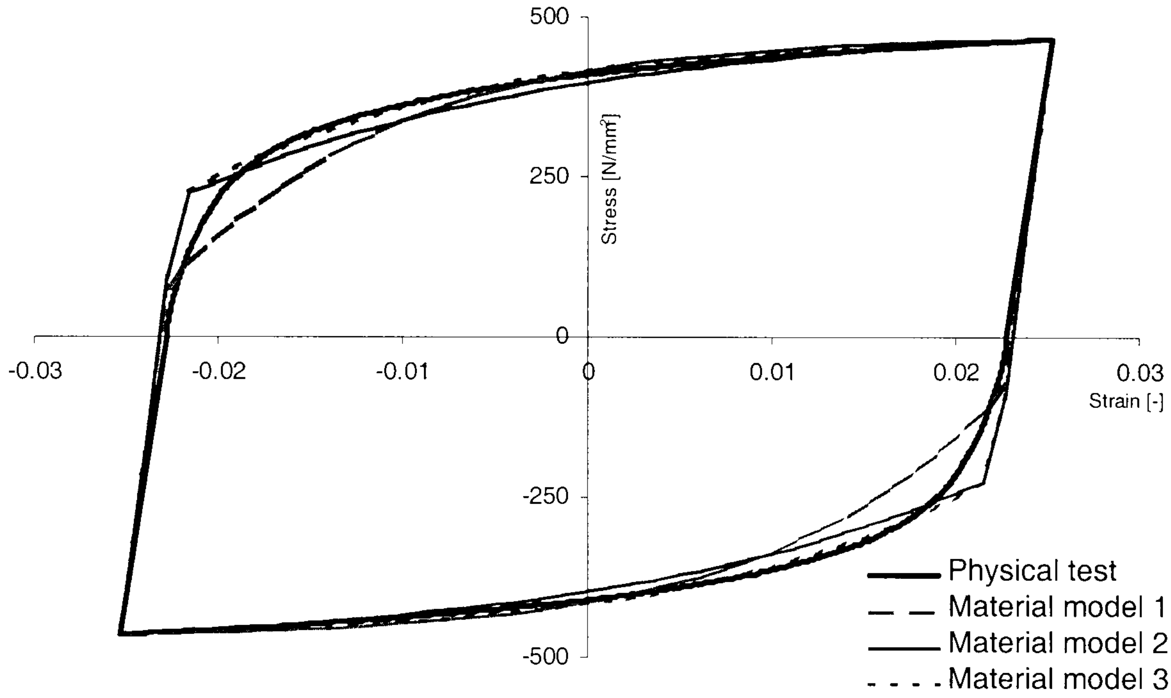

Figure 6-6: Material models for 2.5% reversed strain and comparison with the physical material test data.

In *ABAQUS* the plastic hardening model can be used in conjunction with the cyclic hardening-option. If this option is not used, no cyclic hardening will be considered and the behaviour will correspond to that of a saturated cycle; this may not provide accurate predictions of actual behaviour in initial cycles, but gives accurate results for stabilised cycles. In Section 5.4.5, not much difference was found between the stabilised cyclic loading and the earthquake loading and therefore modelling of stabilised cycle behaviour was chosen.

Further information on material modelling can be found in section 11.2.2 ("Models for metals subjected to cyclic loading") of the *ABAQUS* Standard User's Manual (1998).

In Figure 6-7 the material monotonic tensile tests are scaled to f_y and compared. Steels with f_y=290, 325 and 340N/mm^2 have the same normalised behaviour but f_y=430N/mm^2

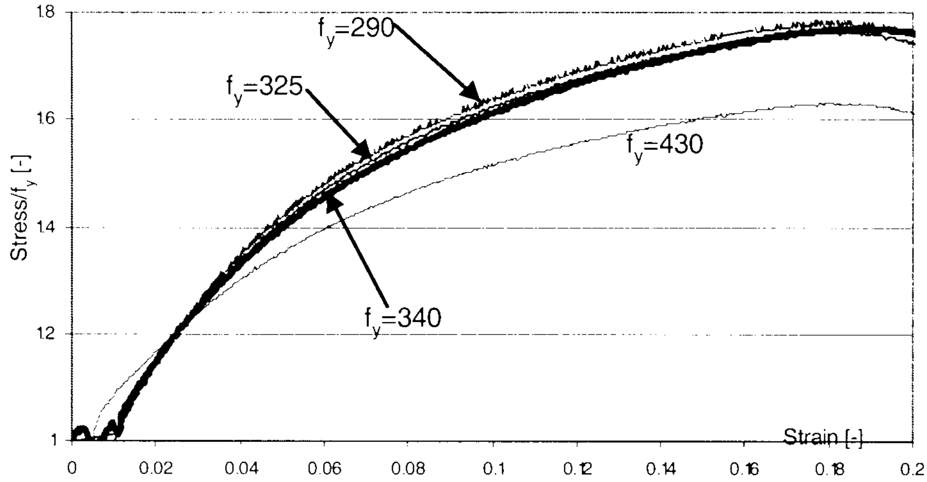

Figure 6-7: Results of the 4 material tensile tests. Stresses scaled to f_y.

is significantly different. Two cyclic material tests were performed; one for steel with f_y=430N/mm^2 and one for the steel with f_y=340N/mm^2. Two cyclic material tests were saved by scaling the curve for the steel with f_y=340N/mm^2 to f_y=290 and 325N/mm^2.

6.6.3 Strain rate

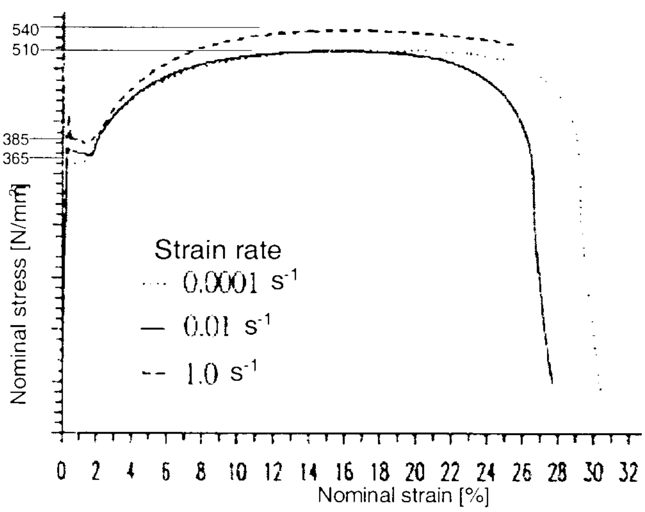

Figure 6-8: Plastic behaviour of steel at different strain rates. (Pan et al., 2001)

Many materials show an increase in their yield strength as strain rates increase: this effect becomes important in many metals when the strain rates range between 0.1 and 1 per second, and it can be very important for strain rates ranging between 10 and 1000 per second. Pan et al. (2001) did strain rate testing on different 2mm thick hot rolled steel sheets. One steel sheet that Pan used had a strain-stress plot (at very slow strain rate: $10^{-4}s^{-1}$) very similar (almost identical) to that of the tensile test of a knee element steel sample (with f_y =340kN/mm^2). Pan's results are shown in Figure 6-8. Based on his findings, he has proposed:

$$\sigma(\varepsilon,\dot{\varepsilon}) = \sigma(\varepsilon)\cdot\left(\dot{\varepsilon}\right)^{m} \tag{6.5}$$

$$\frac{\sigma_2(\varepsilon,\dot{\varepsilon}_2)}{\sigma_1(\varepsilon,\dot{\varepsilon}_1)} = \left(\frac{\dot{\varepsilon}_2}{\dot{\varepsilon}_1}\right)^{m} \tag{6.6}$$

where σ is true stress, $\dot{\varepsilon}$ the true strain rate and m is a material constant. For the steel shown in Figure 6-8, Pan estimated $m = 0.01$. The strain rate reached a maximum of 0.08 for the knee elements without holes and a maximum of 0.2 for knee elements with perforated web holes, though this peak value was restricted to a small area. In the material tensile test the strain rate was around 0.005.

With Equation 6.6, we can calculate the underestimation of the material stress which is less than 2.8% for knee elements without holes and less than 3.8% for knee elements with perforated web.

Pan also showed that the properties were slightly different (a couple of percent) if the test was performed in the longitudinal and transverse rolling directions. Ageing of the material tends also to increase slightly (around one percent) the response for strain rates corresponding to knee element applications.

Since the effects were estimated to be no more than a few percent, the influence of strain rate was not modelled.

6.7 Monotonic analysis

6.7.1 Yield load

The yield load was determined with a monotonic static analysis using the tri-linear material model as defined in Section 6.6. Displacement was imposed with very small step increments to get a very smooth response curve, so that the appropriate yield criteria could be applied accurately. The yield criteria that were used, were the same as for the physical testing (yielding criteria 1 and 3 defined in Section 5.3.1). The yielding point was taken when a difference of 10% of F was achieved for criterion 1 and when b=0.1·a for criterion 3. These criteria gave very similar results and the mean value was taken. The results are given in Table 6.1.

Test	*Section abreviation*	δ_y^{ph} $[mm]$	δ_y^{fem} $[mm]$	$\delta_y^{ph} - \delta_y^{fem}$ $[mm]$	F_y^{ph} $[kN]$	F_y^{fem} $[kN]$	$F_y^{ph} - F_y^{fem}$ $[kN]$	$\Delta F/F_y^{ph}$ $[\%]$
1	UC30H12	2.3	1.85	0.45	300	270	-30	-10
2	UC30H12	2.3	1.85	0.45	300	270	-30	-10
3	UC30H12	2.4	1.95	0.45	325	315	-10	-5
4	UC30H20	1.7	1.7	0.0	225	225	0	0
5	UC30H20	1.9	1.7	0.2	230	225	-5	-2
6	UC30H15a	2.0	1.85	0.15	300	315	15	5
7	UC30H15b	2.1	2.3	-0.2	380	390	10	3
8	UC30N	2.1	1.65	0.45	350	380	30	9
9	UC30N	2.4	1.65	0.75	360	380	20	6
10	UC304FS	1.8	1.65	0.15	350	385	35	10
11	UC23N	1.7	1.55	0.25	330	360	30	9
12	UC23PS4	1.7	1.55	0.15	335	365	30	9
13	UC23FS2	2.0	1.55	0.45	340	365	25	7
14	UC23FS4	1.8	1.5	0.3	340	365	25	7
15	UB23N	1.8	1.40	0.4	365	400	35	10
16	UB23FS4	1.7	1.35	0.25	380	405	25	7
17	UC30N	2.4	1.65	0.75	350	380	30	9
18	UC30N	2.2	1.60	0.6	330	365	35	11
19	UB23N	2.1	1.40	0.7	365	400	35	10

Table 6.1: Tested knee element characteristics

The error on the yielding forces is no more than 10%. Even by taking into account the residual stresses and the test rig flexibility the yield displacement is underestimated. The underestimation is less than 0.8mm: however, this difference makes up to 30% difference on the knee element ductility value.

6.7.2 Influence of rig flexibility and overthickness

Calculations have been performed with varying rotational and the axial spring stiffness at the extremities of knee-element n°1. The rotational spring stiffness K_1 and axial spring stiffness K_2 evaluated in the physical testing (Section 4.4, Table 4.1) were taken as reference values. Using the yield criteria it is found that the yield loads vary between 265 and

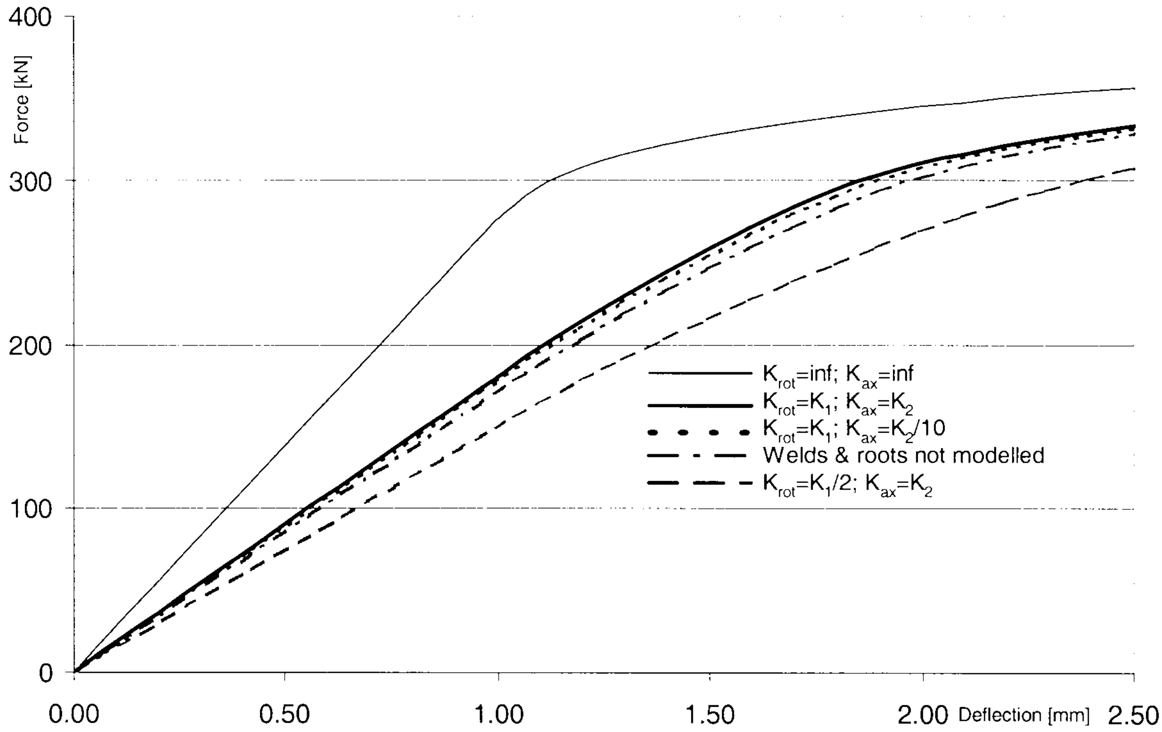

Figure 6-9: Influence of the boundary conditions on knee-element n°1

310kN as the yield displacements vary between 1.25 and 2mm. Figure 6-9 shows that the rotational spring stiffness has a large effect on the initial stiffness, the yield load and the yield displacement. The axial spring stiffness has almost no influence on the response. In the case of a perfect connection and an infinitely stiff testing rig, the yield displacements are approximately 1.05mm for the sections without holes and 1.25mm for the sections with holes. The force differences reduce with the displacement.

We can note in Figure 6-9 that the overthickness of a web portion (added to take into account the welds and the roots) for a small monotonic displacement increases the initial stiffness only slightly.

The rig flexibility and the overthickness influence over large cyclic loads has also been evaluated and will be presented later in Section 6.8.3.

6.7.3 Influence of residual stresses

Calculations have been performed including residual stresses as defined in Section 6.4. Figure 6-10 shows the knee element n°8 *FEA* results with and without residual stresses. The model including residual stresses starts yielding earlier than the one which does not include them. As yield develops the difference in response becomes negligible. The difference in response is less important for knee elements with perforated webs.

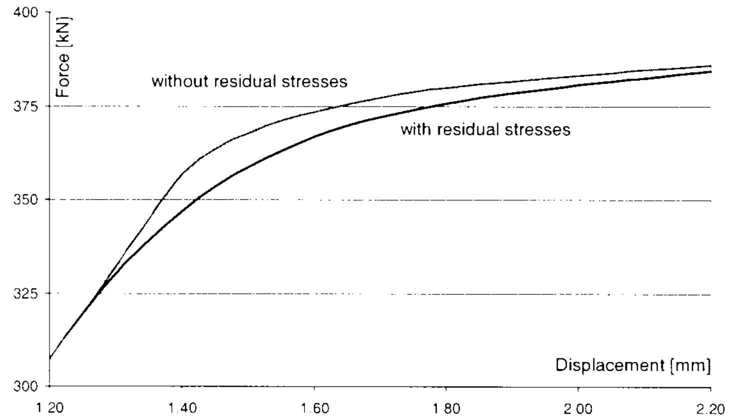

Figure 6-10: Influence of residual stress on the intial stiffness, yield load and yield displacement (specimen 5)

6.8 Cyclic analysis

6.8.1 Procedure

An initial calculation is performed with a single material law for all elements. The maximum plastic strain that each element has experienced is identified and the elements are categorised into several ranges based on plasticity level. A second calculation is then performed attributing a different material rule to the elements for each category. This procedure allows the use of a material rule which is more representative of the behaviour of steel for a certain cyclic strain amplitude. The different material rules are defined using the procedure of Section 6.6.2. For unaltered beams or beams with stiffeners, division of the elements into two categories is sufficient. Generally all the elements of the web not backed by stiffeners or in the flange root experience higher strains. For knee elements with perforated webs, the strains are more spread out and more categories are desirable and up to 5 material rules were used.

As in the monotonic analysis, the test rig flexibility was taken into account, the roots and welds were modelled with the overthickness t_2 and the non-linear hardening material model for cyclic loading was used.

6.8.2 Results

In Table 6.2 the results of a subtest for each knee element type are summarised. The results are very good; the errors on the maximum reaction force are less than 6%.

Test	*Section abreviation*	δ^+ $[mm]$	δ^- $[mm]$	F^+_{ph} $[kN]$	F^-_{ph} $[kN]$	F^+_{fem} $[kN]$	F^-_{fem} $[kN]$	$\overline{\Delta F}$ $[kN]$	$\overline{\Delta F}/F_{ph}$ $[\%]$
1	UC30H12	15	16	454	464	450	460	-4	-1
3	UC30H12	19	18.8	550	530	532	517	-16	-3
5	UC30H20	14	19	394	399	400	407	+7	+2
6	UC30H15a	15.5	15	523	522	508	507	-15	-3
7	UC30H15b	16.7	16.7	608	613	610	627	+8	+1
8	UC30N	17	19	549	556	568	587	+25	+5
10	UC304FS	10	12	586	596	607	613	+19	+3
11	UC23N	10.5	13.6	515	528	487	503	-27	-5
12	UC23PS4	12	10.5	567	537	542	528	-20	-4
13	UC23FS2	26	27.3	614	627	655	666	+40	+6
14	UC23FS4	15.5	17.3	603	608	599	602	-5	-1
15	UB23N	13.5	10.5	576	569	592	594	21	+4
16	UB23FS4	20.5	17	665	639	686	672	28	+4

Table 6.2: Finite element results of cyclicly loaded knee elements

Figure 6-11 shows the comparison of a finite element analysis using the three different material rules of Figure 6-6 with the physical test results for a subtest on knee element n°10. The finite element analysis (for all three material rules) overestimates the maximum reaction forces by only 3%. However, even with material rule 1, the FEA fails to follow the rugby ball shaped hysteresis curve and overestimates the dissipated energy (which are for the physical test 13.8kJ/cycle and for the FEA respectively 15.7, 16.2 and 16.4kJ/cycle).

Figure 6-12 compares the moments and axial forces obtained with the FEA and those measured during the testing. Despite the noticeable differences found in moments and axial forces, the value of the reaction force did not seem much affected.

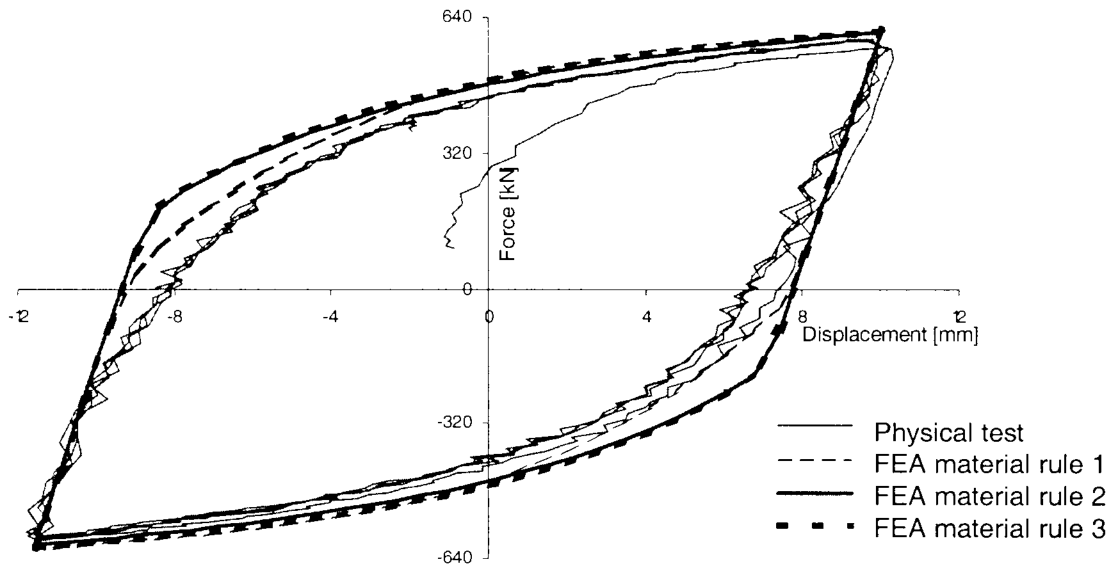

Figure 6-11: Comparison of finite element analysis calculation (for different material rules) with physical testing results of a subtest on knee element n°10.

6.8.3 Influence of rig flexibility and overthickness

Calculations have also been performed without the overthickness t_2. It was found that the overthickness increases the response by around 5% for the knee elements with perforated webs and by around 10% for the unaltered knee elements and those with stiffeners.

Reducing the rotational spring stiffness at the knee element extremities by a factor two reduces the response of the beam for large cyclic displacements (>10mm) by only around 1%.

6.9 Thermal analysis

6.9.1 Procedure

From the cyclic static analysis results of Section 6.8, the plastic strain energy densities (for example those at the deflection maxima and minima) are used for a thermal analysis in *ABAQUS* using the heat-transfer-option. For each element, the difference in plastic strain energy density is transformed into a heat flux over a short period of time. The heat flux heats the finite element locally which then affects its surrounding elements by diffusion.

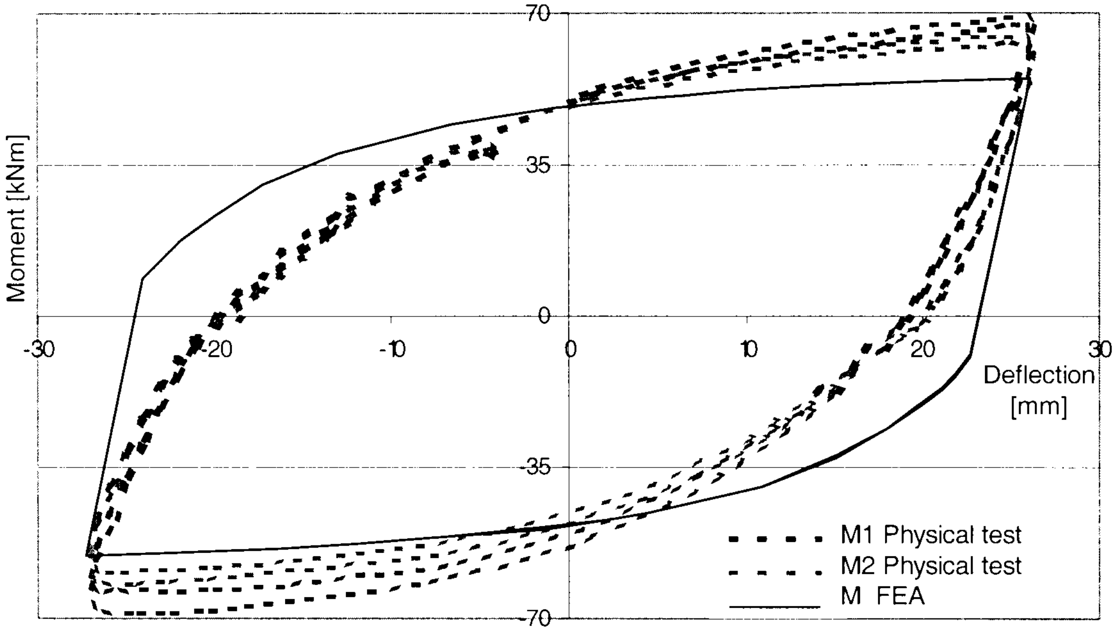

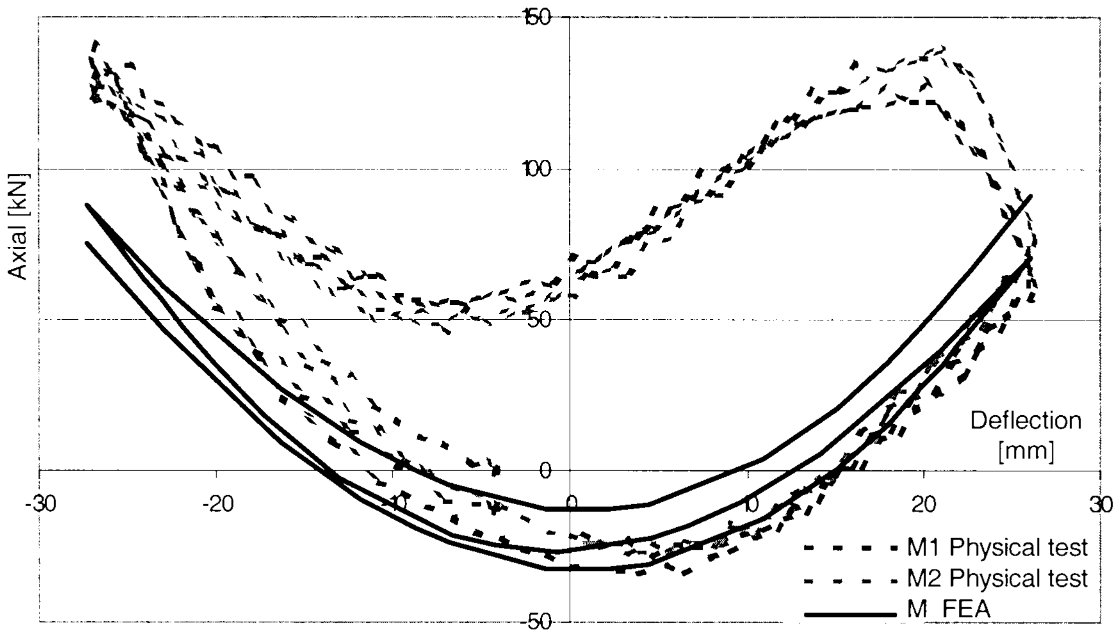

Figure 6-12: a) Moment and b) axial force plotted against deflection (knee element n°13).

The same thermal material characteristics given in Section 5.5.1 were used. (Density $\rho = 7850 kg/m^3$, conductivity $k = 50W/mK$ and the specific heat $c_p = 450J/kgK$). The time periods between the deflection maxima and minima were taken from the acquisition system timer. The results were then compared with the thermal images (Sections 5.6.4 and 5.5).

6.9.2 Results

Five knee element tests were recorded with the thermal imaging camera. For these knee elements a thermal simulation has been performed using the previously described procedure. Figure 6-13 shows the increase of temperature during half a cycle for knee element n°6. (The colour-bar of *ABAQUS* does not match with that of *MATLAB*). The maximum increase, excluding the peak values at the hole edges, was found to be $14°C$ with the FE and $13.6°C$ with the thermal images. The difference could be explained by the fact that the loss of heat through contact with the air is not modelled.

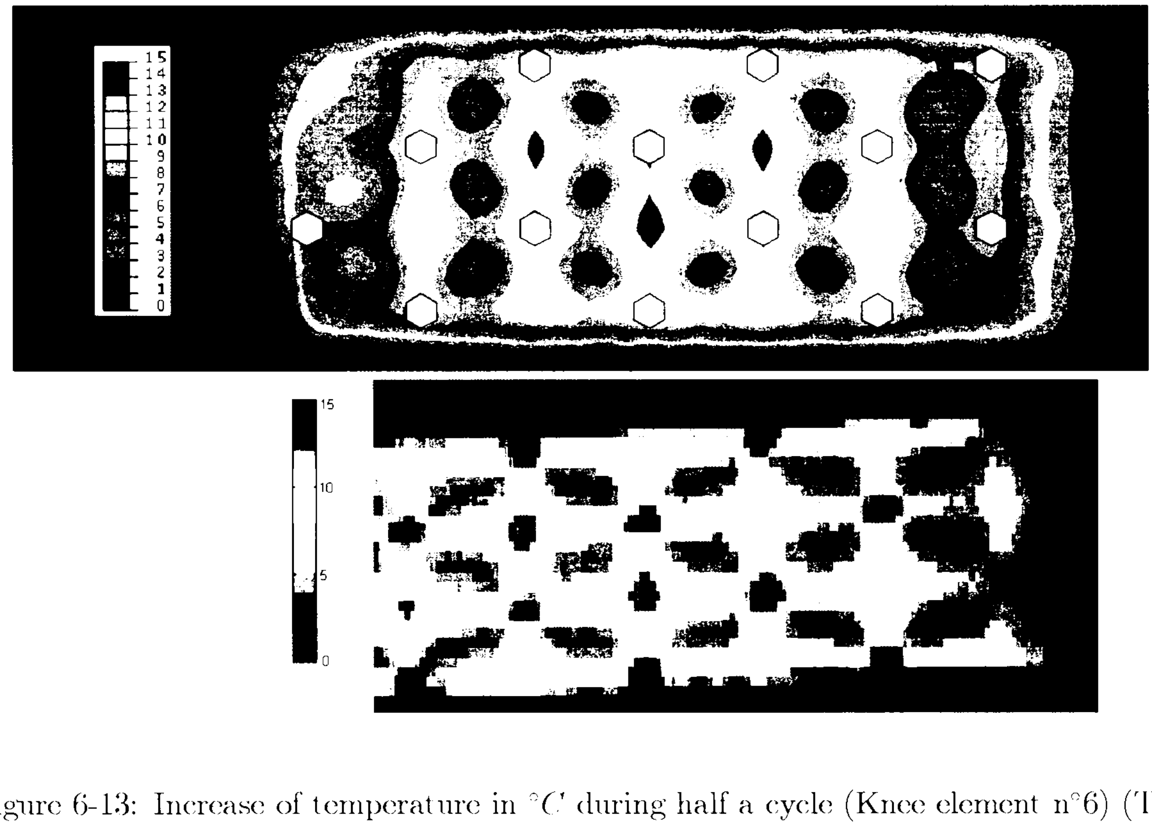

Figure 6-13: Increase of temperature in °C during half a cycle (Knee element n°6) (The top diagram shows the results of the FE-thermal analysis and the bottom diagram shows the results obtained with thermal images)

The strain energy can be compared instead of comparing the temperature difference. The strain energy is obtained easily by applying Equation 5.12 to the temperature matrix representing the thermal image. Because of the coarse pixel grid the Laplacian may not give very good results. However, because testing frequencies were between 0.67 and 1.5Hz, the Laplacian terms remained less than 10% of temperature increase. This was confirmed by the FE-thermal analysis, where the diffusion did not affect the temperature peak values by more than 10%. Figure 6-14 shows the plastic strain energy accumulated during half a cycle. Similar patterns as in Figure 6-13 are observed. The maximum plastic strain energy, excluding the peak values at the hole edges, was found to be $25mJ$ with the FEA and $24mJ$ with the thermal images. Unfortunately, the results of the other knee elements were not as good and consistent as for knee element n°6. Figures 6-15 to 6-18 show the comparison of the plastic strain energy for knee elements n°3, 7, 13 and 14. Table 6.3 summarises these results.

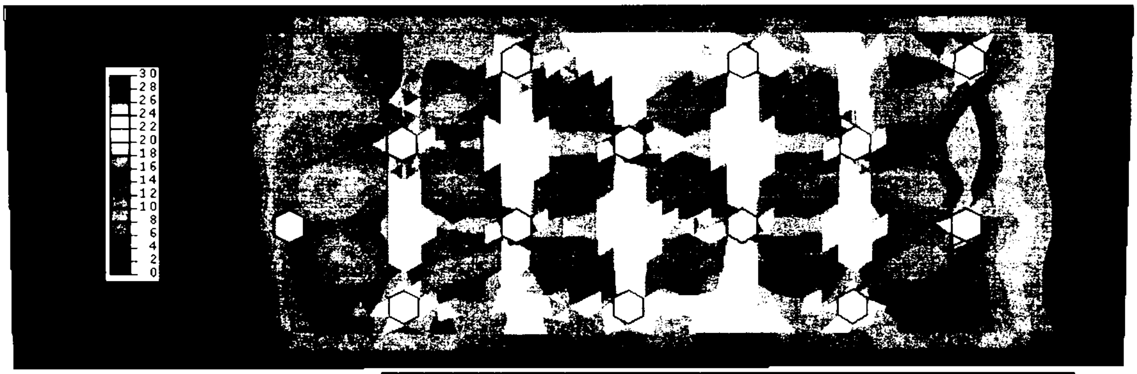

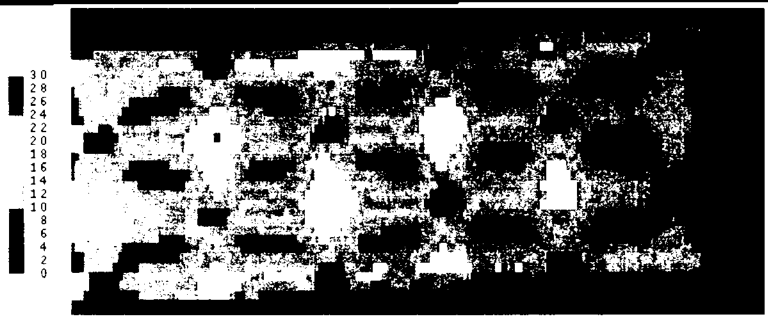

Figure 6-14: Plastic strain energy in mJ accumulated during half a cycle (KE n°6)

For knee elements n°13 and 14, higher strain energies are obtained with the FEA. The difference could be explained by the fact that the loss of heat through contact with the air was not modelled and that some oxidised steel dust flaked off revealing shiny steel

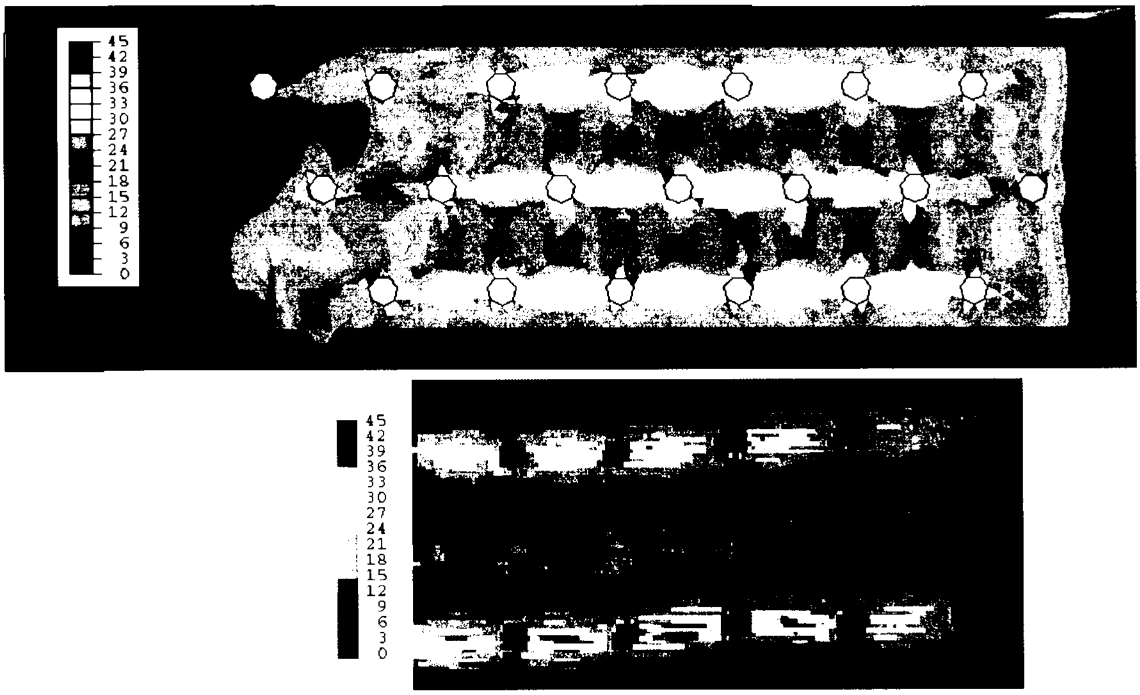

Figure 6-15: Plastic strain energy in mJ accumulated during half a cycle (KE n°3)

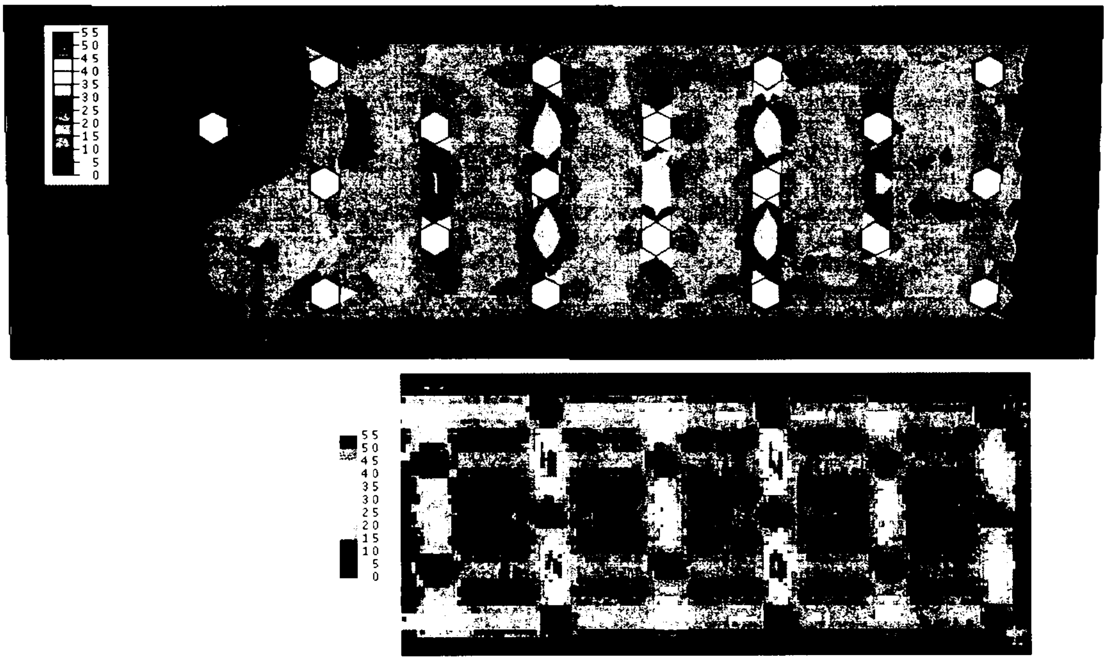

Figure 6-16: Plastic strain energy in mJ accumulated during half a cycle (KE n°7)

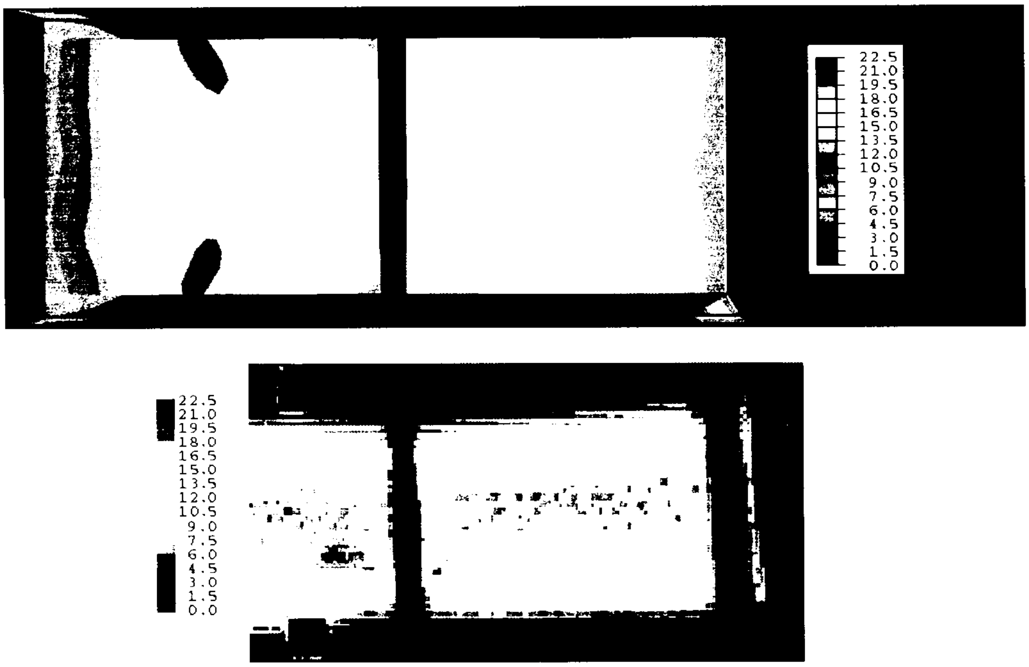

Figure 6-17: Plastic strain energy in mJ accumulated during half a cycle (KE n°13)

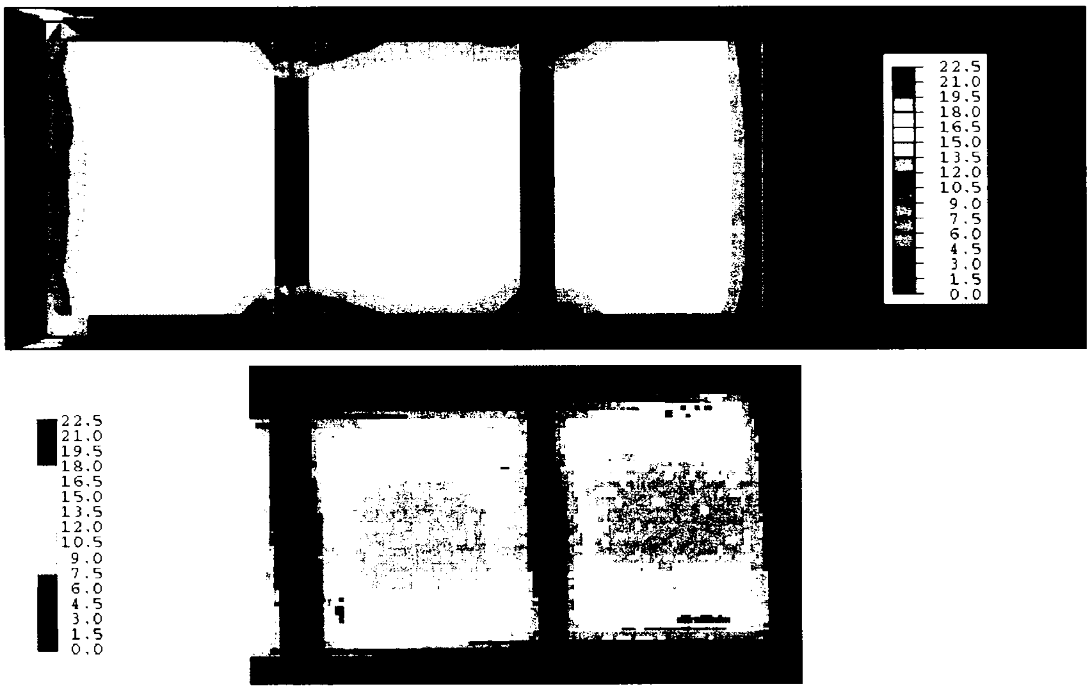

Figure 6-18: Plastic strain energy in mJ accumulated during half a cycle (KE n°14)

Test n°	Section abr.	Steel f_y N/mm^2	Finite element analysis ε^{max} %	σ_{VM}^{max} N/mm^2	w^{max} $miliJ$	Thermal images ε^{max} %	σ_{VM}^{max} N/mm^2	w^{max} $miliJ$	Δw %
3	UC30H12	340	4.5	498	37	5.1	505	43	+16
6	UC30H15a	340	3.0	481	25	3.0	480	24	-4
7	UC30H15b	430	3.4	618	38	4.6	640	51.5	+36
13	UC23FS2	340	2.5	483	20	2.4	470	19	-5
14	UC23FS4	340	2.6	491	20.2	2.3	465	18.7	-7

Table 6.3: Finite element results of the thermal analysis of cyclicly loaded knee elements

spots with lower emissivity.

For knee elements n°3 and 7, much higher strain energies are obtained with the thermal imaging. These quite important differences are not easily explained. One plausible explanation would be that some hole intervals deform more than others and therefore attract more plastic strain energy.

This was observed visually for knee element n°7. Most deformation appeared to take place in two vertical lines (containing two holes) and the flanges seemed bent above and underneath these two lines. In Figure 6-16, the thermal images show more concentrated high plastic strain energy patterns than the one obtained with the finite element analysis.

For knee element n°3, because of the oxidised steel dust flaking to revealing shiny steel spots with lower emissivity, it is difficult to establish whether the middle horizontal hole rows effectively dissipated and deformed less than the bottom and top ones. From the visual observations made during testing, the bottom and top hole rows were the only rows where crack propagations occurred, as shown in Figure 6-19.

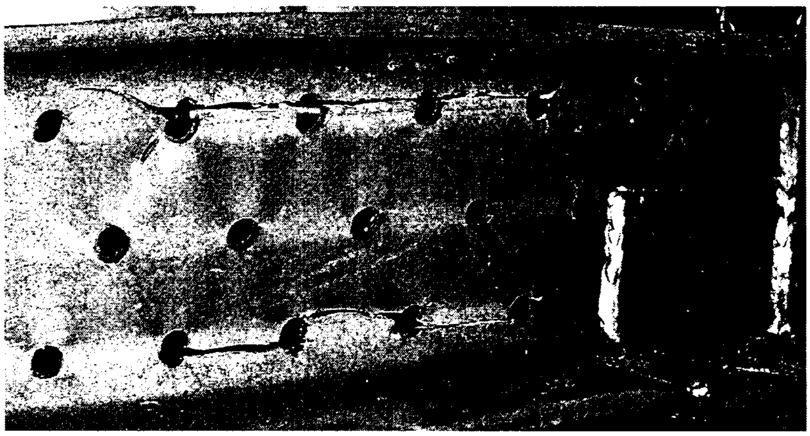

Figure 6-19: Crack propagations in the web of knee element n°3

The middle row had only very small crack initiation, even after the knee element had completely failed. In the knee elements n°1, 2 ,4 and 5 the first crack propagated in the middle row and either in the top or bottom row. It would appear that after a while most of the damage concentrates in the two weakest rows only. The third row still contributes to the energy dissipation but at a lower rate. If one row contributes half of what the two other rows contribute to the energy dissipation, the two more active rows will dissipate 20% more than if the dissipation were equally distributed between the three rows.

6.9.3 Conclusion

The thermal analysis gave very satisfying results. The FEA plastic deformation patterns matched the heat generation patterns. Differences were only found after oxidised steel dust flaked off or when the dissipation mechanism at a certain damage level did not split the energy dissipation equally between the hole rows or hole columns. The thermal imaging analysis is a promising method for understanding dissipation and failure mechanisms.

Ideally, thermal images of the tensile tests should have been taken, in order to determine the accuracy of the thermal analysis method and verify whether the emissivity at high strains remains constant. Unfortunately, the tensile tests were not performed during the thermal imaging camera loan.

6.10 Crack analysis

The knee elements with perforated webs showed a crack initiation and propagation when higher plastic strains between the holes eventually combined with low cycle fatigue gave favourable conditions for propagation. A very fine solid element model of a small section of web with a hole was built in order to investigate if the FEA could identify crack initiation locations. 10-noded tetrahedron solid elements were used. The web section was loaded by concentrated shear forces at the nodes of its four edges. These concentrated shear forces were taken from the half beam model that uses shell elements. Figure 6-20 shows a web section with a 12mm hole and the plastic strain due to the shear forces.

Peak strains are situated in four points in the hole edge at mid-thickness which correspond to the location of crack initiation observed during the testing. It is concluded that

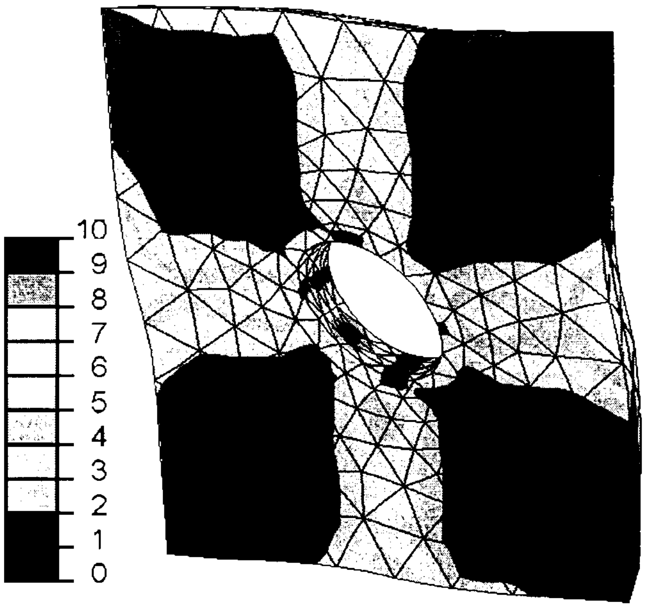

Figure 6-20: Plastic strain in % in a perforated web piece subject to the shear forces.

the FEA can identify probable crack initiation positions. However, in order to estimate the stress or strain peak and simulate crack initiation or propagation more advanced models are required. Such models were not investigated; such modelling constitutes a large research field outside of scope of this thesis, especially as knee-elements with perforated holes were recognized not to be the optimal design and possess reduced performance compared to unaltered knee elements or knee elements with adequate web stiffeners.

6.11 Instability

Knee elements without holes in the webs and without adequate stiffeners were subject to buckling. The results in Section 5.4.3 have indicated that plastic buckling failure loads were influenced by low cycle fatigue. In the finite element analysis low cycle fatigue could not be included and the buckling load is therefore overestimated. In this section the overestimation and sensitivity of a structure to imperfections are considered.

6.11.1 Procedure

The response of some structures depends on the imperfections in the original geometry. Hence, imperfections based on a single buckling mode tend to yield non-conservative results. By adjusting the magnitude of the scaling factors of the various buckling modes, the imperfection sensitivity of the structure can be assessed. A number of analyses were conducted to determine the most probable (lowest) critical load and to investigate the sensitivity of a structure to imperfections. The imperfect structure will be easier to analyse if the imperfection is large. If the imperfection is small, the deformation will be quite small (relative to the imperfection) below the critical load. The response will grow quickly near the critical load, introducing a rapid change in behaviour. Convergence problems may appear. On the other hand, if the imperfection is large, the post-buckling response will grow steadily before the critical load is reached. In this case the transition into post-buckling behaviour will be smooth and relatively easy to analyse. Therefore the maximum tolerance value given for hot rolled steel sections in British Standard Code were taken as the magnitude of the imperfection. The Riks method and the associated options (as described in Section 6.5) were used. A full cycle at a slightly subcritical load was performed first before starting the instability analysis from the yielded and deformed states.

Bi-linear axial springs were placed at the knee element supports in order to avoid mobilisation of most of the reaction forces by tension force deviation. The maximum value was set to the maximum axial force measured during the physical tests before failure.

Since the buckle-option calculates only elastic buckling shapes and their corresponding eigenvalues, it failed most of the time to predict correctly the web buckling mode (plastic shear buckling). It predicted flange buckling or global torsional buckling shapes with very high eigenvalues that indicated that their critical loads are unlikely to be reached. The web buckling mode can be forced by reducing the web thickness during the buckling analysis (easily done in shell element models). Of course, in the cyclic and Riks analysis the real thickness is used.

6.11.2 Results

For sections without stiffeners ($UC23N$, $UC30N$ and $UB23N$) plastic shear buckles appeared. For the sections with stiffeners the FEA failed to model the shear buckling failure mode. For the unstiffened sections the FEA does not give a clear sudden collapse of the knee element but merely a slight decrease in the reaction force, while the deflection and the buckle amplitudes increase, Figures 6-21 and 6-22.

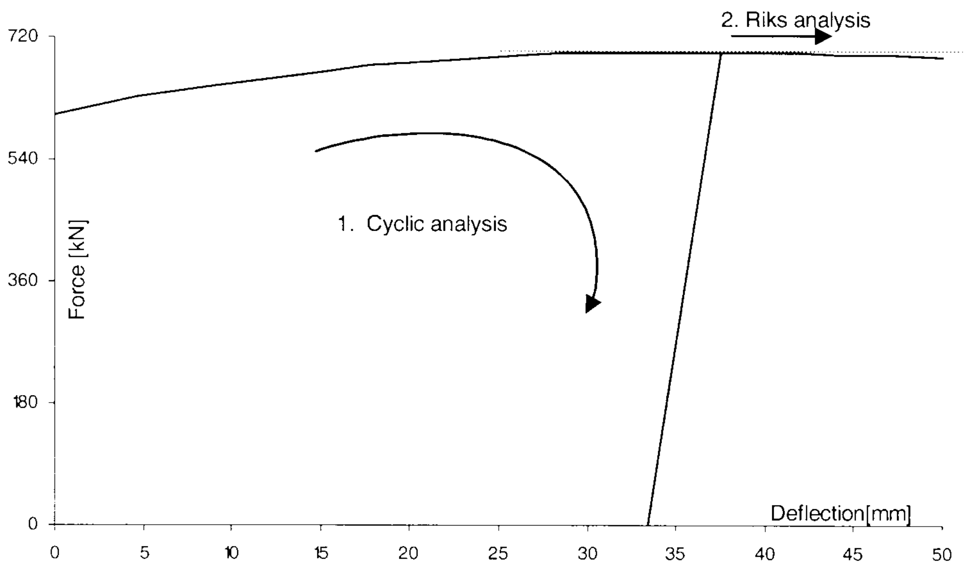

Figure 6-21: Mid-span applied force – mid-span deflection hysteresis plot of a $UC23N$ at maximum cyclic load before it decreases due to plastic shear buckling in the web.

The results of the finite element analysis are given in Table 6.4 and are compared with the physical testing results.

Test n°	Section $abr.$	Physical test δ_{max} $[mm]$	Physical test F_{max} $[kN]$	FEA δ_{max} $[mm]$	FEA F_{max} $[kN]$	Difference $\Delta\delta_{max}$ [%]	Difference ΔF_{max} [%]
	UC23N	>17*	>555*	37	698	-54	-20
		<28**	599			-24	-14
	UC30N	40	599	41	745	-3	-20
	UB23N	25	614	23	694	+9	-10

*Failure for this knee element was not achieved

**Imposed displacement increased too much at once

Table 6.4: Comparison of buckling load

The maximum forces calculated with the finite element analysis are 10 to 20% higher than those measured during physical testing. In Section 5.4.2 it was shown that low cycle fatigue reduces the maximum force and maximum displacement of the knee element. Low cycle fatigue was one aspect that could not be introduced in the $ABAQUS$ model.

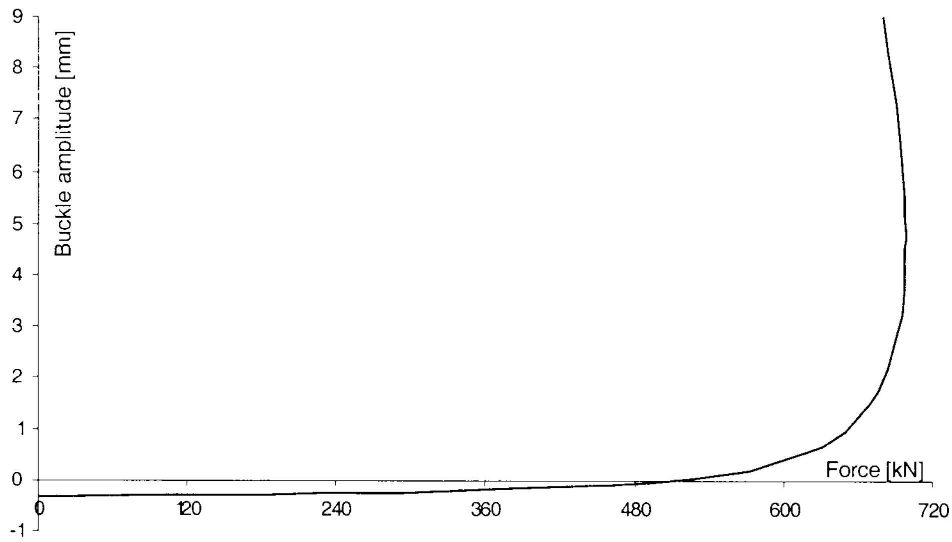

Figure 6-22: Mid-span applied force – web buckle amplitude plot for $UC23N$ failing by plastic shear buckling

The sensitivity of the buckle magnitude, of a single mode and of combinations of modes (e.g. flange buckling with web buckling) was assessed. The results are presented in Table 6.5 and show that the critical load varies by only a few percent.

Test	Section	1^{st} Mode		1^{st} Mode*		2^{nd} Mode		Combinations	
n°	*abr.*	$\delta_{\max}$ $[mm]$	$F_{\max}$ $[kN]$	$\delta_{\max}$ $[mm]$	$F_{\max}$ $[kN]$	$\delta_{\max}$ $[mm]$	$F_{\max}$ $[kN]$	$\delta_{\max}$ $[mm]$	$F_{\max}$ $[kN]$
	UC23N	37	698	40	714	41	709	39	705
	UC30N	41	745	42	767	41	754	41	760
	UB23N	23	684	23	694	24	687	23	697

*Imperfection taken $1/300^{th}$ of the depth (instead of a $1/150^{th}$)

Table 6.5: Comparison of buckling load

The buckle mode changes when the section is pulled down or pushed up, respectively Figure 6-23 a) and b) for the $UB23N$-section. During the physical testing it was actually observed that the buckle would switch sides of the web at each reversal. Figure 6-23 c) and d) shows respectively the buckle mode of the $UC23N$-section and the $UC30N$-section.

The buckling of the connections was not treated in this thesis, since knee element connections should be designed to withstand loads elastically and without buckling under the maximum load. Torsional buckling was not investigated as none of the knee elements

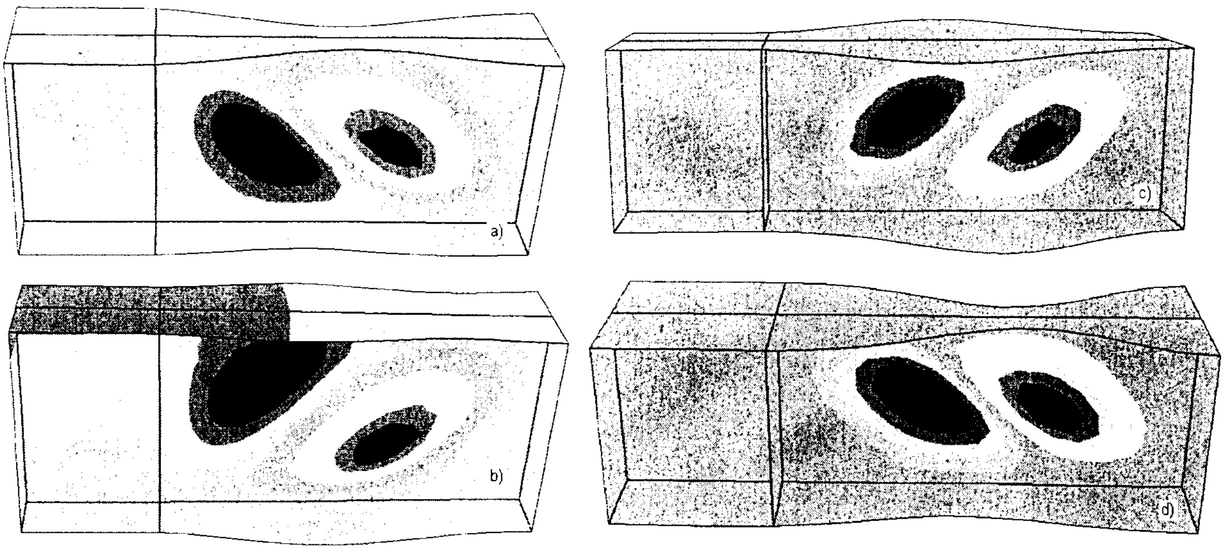

Figure 6-23: Buckling modes for the $UB23N$-section a) pulling and b) pushing. Buckling modes for c) the $UC23N$-section and d) the $UC30N$-section.

tested failed in that mode and the critical load of that buckling mode is much higher than the failure mode found in the physical tests. Torsional buckling did not affect the knee elements because they were so short.

6.11.3 Conclusion

It was found that even very sophisticated non-linear finite element modelling is unable to predict the failure by inelastic shear buckling for stiffened sections, and overestimates the buckling load by 10 to 20% for unaltered sections. Low cycle fatigue could not be modelled in the FEA.

6.12 Conclusion

From the FEA-results substantial conclusions and relevant guide-lines were drawn and are listed below.

- Residual stresses influence only the onset of yield, not the post-yield behaviour.
- The boundary conditions (rotational spring stiffness at the extremities) have an influence only at small level of plasticity.

- The flange and the root contribute up to 10% of the shear capacity of the analysed beams. When using shell elements, the welds, the roots and the part of the flange above the roots can be modelled efficiently with overthickness strips.

- Strain rate effects were not observed in dynamic testing, and such effects were estimated to have an influence of not more than a few percent.

- The most significant parameter in the cyclic test results is definitely the material law. Therefore, a cyclic test at different plastic strains should be performed and material laws matching these hysteresis curves should be created. Each element should be assigned a material law corresponding to the plastic strain range it experiences.

- A thermal analysis is easily performed to obtain the temperature increase due to the plastic strain energy and can be compared with the thermal images. Differences in the patterns or intensities of the plastic strain indicate that the dissipative mode in the FEA is not perfectly modelled. A more precise check can be performed by comparing the plastic strain energy from the static analysis with the thermal images converted into plastic strain energy images.

- It was not possible to build a model that agreed with all aspects of behaviour; shear forces, axial forces, moments and thermal dissipations. However, the models used gave excellent results for the reaction forces which are the most important parameter for the designer. The hysteresis curves given by the FEA were generally not rounded enough to follow the rugby ball shaped distribution found during the physical testing and therefore give a slightly higher global energy dissipation. The moments and axial forces obtained had some resemblance with those found during physical testing, though large differences in these quantities would not mean necessarily that the reaction force would be less accurate.

- Detailed solid element analysis allows identification of probable crack initiation sites.

- Riks analysis on a knee element with imperfections having been previously subjected to cyclic loading overestimates the critical load by 10 to 20% for the unaltered knee element and is unable to predict the failure mode for knee elements with stiffeners such as inelastic shear buckling under cyclically reversing loads. Low cyclic fatigue cannot be modelled in the finite element analysis. Large-scale experimental testing has therefore a key role to play in the further development of knee elements.

Chapter 7

Seismic behaviour of a knee braced frame building

7.1 Introduction

In Chapter 5 the response and the performance of knee elements have been investigated by physical testing and in Chapter 6 simulated with finite element analysis. In the present Chapter a knee element model for a non-linear dynamic analysis software has been created and calibrated against the physical testing results and for the non-tested sections against the finite element analyses. Using these elements, the non-linear static and dynamic analysis of a whole building have been performed.

Traditional seismic resistant design used to emphasize linear analysis concepts. In Eurocode-8 (2001), moment resisting frames and concentric and eccentric bracings can be designed using modified elastic analyses (Section 2.4.2), however this is not possible for knee braced frames. The concept of the method followed by Eurocode-8 for MRF, CBF and EBF of dividing the elastic response spectrum by a single factor to arrive at the inelastic spectrum may results in forces and displacement distributions which may have little resemblance to that experienced during an actual earthquake. This is the case when there is significant non-linearity or when discrete dampers are used (Kappos 1999), and it is believed to be the case for the knee braced frame. However, with the development of software that can perform non-linear (static and dynamic) analysis, the design approach can shift to pushover analysis and time-history analysis.

A non-linear pushover analysis method has been used to design a knee-braced frame of a 5-storey building example. Using non-linear dynamic time-history analysis, the performance of the knee braced frame design was assessed by submitting it to three representative artificially generated earthquakes and to a real scaled earthquake.

7.2 Knee element model for non-linear analysis

The *NonLinPro* software package (1997), which includes the executable *Drain-2Dx*, was chosen to perform the non-linear analysis. A model of a knee element, that takes into account the deflection due to shear and due to bending, that can yield both in shear and in bending and that fits the response observed in the physical tests has been created by assembling standard available elements in *NonLinPro*. Unfortunately *NonLinPro* does not allow the use of inclined spring elements which made the task very difficult. Only horizontal, vertical or rotational spring elements could be used.

The proposed knee element model simulates the deflection due to bending by two flexible beams and the deflection due to shear by two little cantilever beams placed in the centre, as shown in Figure 7-1. The rotation at point D is constrained to be the same as that at point B. The P-Δ effect is ignored for the two short cantilever beams but included for the flexible beams. At both beam supports, a rigid zone can be defined to simulate the offset at the connection. The plastic hinges will form just outside the rigid zones as shown in Figure 7-2. The axial behaviour is treated separately by a bi-linear truss element spanning between D and B. By doing so, the brace had to be divided into two half braces and point C into two points C'' and C'''. No axial deformation or axial forces will be generated by pure bending in a beam element (*NonLinPro* is a small displacement finite element program). When a beam element yields in bending and is axially loaded, no inelastic axial deformation is considered in *NonLinPro*. In theory, the plastic flow will be along the normal to the yield surface and in an axial-bending load combination, inelastic axial deformation is expected.

No physical data is available to assess the behaviour of a knee element to axial load when the web has undergone large plastic strains and when the flanges carry moments that are 2/3 of the moment needed to yield the flanges. In a global building model, because of the deformation of the frame, the knee element is in compression where the

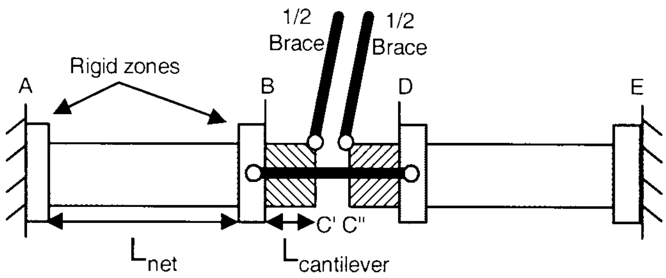

Figure 7-1: Knee element model for *NonLinPro*

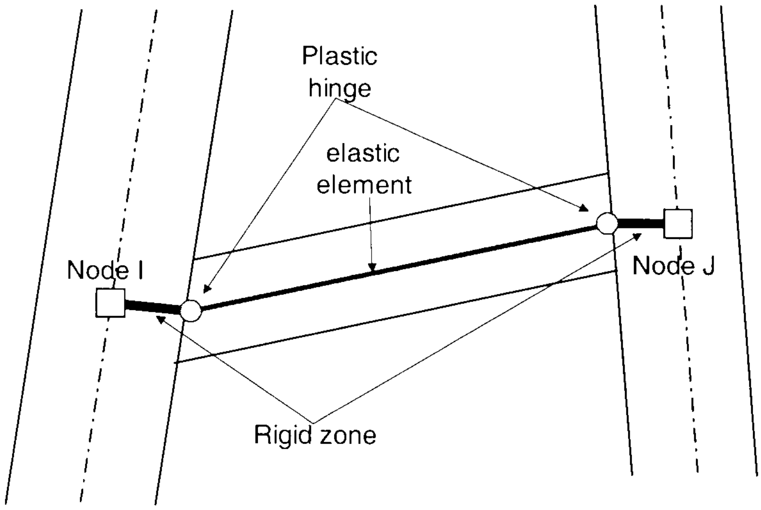

Figure 7-2: Beam element in *NonLinPro*

brace is pulling and in tension where the brace is pushing. If inelastic deformation is not allowed axially after the knee element has yielded in shear or bending, axial forces higher in magnitude than the shear forces are generated, which seems quite unrealistic. The tension truss bar $\overline{BD}$ was set arbitrarily to yield in tension for $N > 0.5 \cdot A_{fl} \cdot f_y^{\text{real}}$ and to buckle in compression for $N \geq 0.3 \cdot A_{fl} \cdot f_y^{\text{real}}$. It was verified that axial yielding or buckling took only place after the knee element had yielded in shear (with important axial stresses in the flanges induced by bending moment). This hypothesis is quite simplistic and the model could be improved by using a bending moment/axial load yield surface with inelastic deformation acting both in the axial direction and rotation.

The proposed model also fails to include the P-Δ effect due to the shear deformations. The P-Δ effect due to the shear deformations could be modelled easily if inclined spring elements were available.

Plastic hinges occur at points B and D of the cantilever beam. Since a bi-linear response is not representative enough of the knee element response, additional bi-linear rotational springs can be added at the points B and D. Additional springs can also be placed at points A and F to take the eventual connection flexibility into account.

Knee element models with two additional bi-linear springs at the points B and D and one additional linear springs at the points A and F have been calibrated using the physical test results or the finite element analysis. Shear force and the plastic energy dissipation were the calibration criteria. In Figure 7-3, the response of a knee element model of a $UC30N$-section is compared with physical test results (knee element n°9). The knee element model gives a good simulation of stabilised cyclic hysteresis.

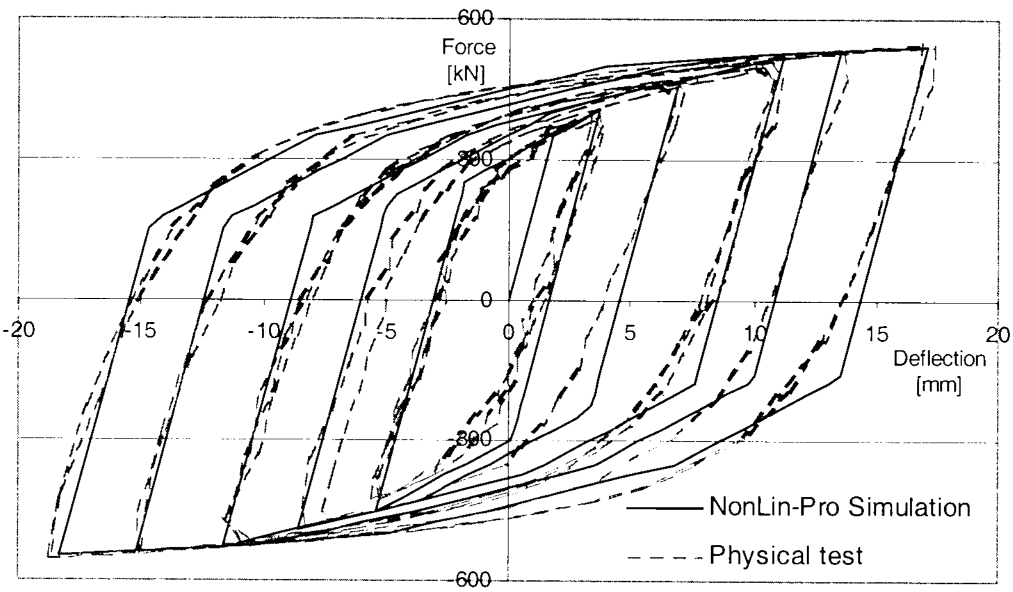

Figure 7-3: Cyclic response of a knee element model in $NonLinPro$ and comparison with the physical test results

7.3 Knee braced frame 5-storey building example

7.3.1 Building size

A simple 5-storey rectangular building with plan dimensions of 15.6m×10.4m (3bays×2bays with 5.2m wide bays) and with 3m high storeys, was used as the basic design. The knee element inclination α and brace inclination β were chosen so the line of action of the brace force goes through the intersection of the beam and the column centre lines and so the brace would connect the knee element at mid-span. For the given bay width and storey height $\alpha = \beta = 49°$. The brace makes an angle of $8°$ with the normal to the knee element axis. The knee element length was set to 0.95m. Each outside panel has one knee braced frame. Elevation of the long and short side of the building are shown in Figure 7-4. The building has therefore no eccentricity in mass or stiffness.

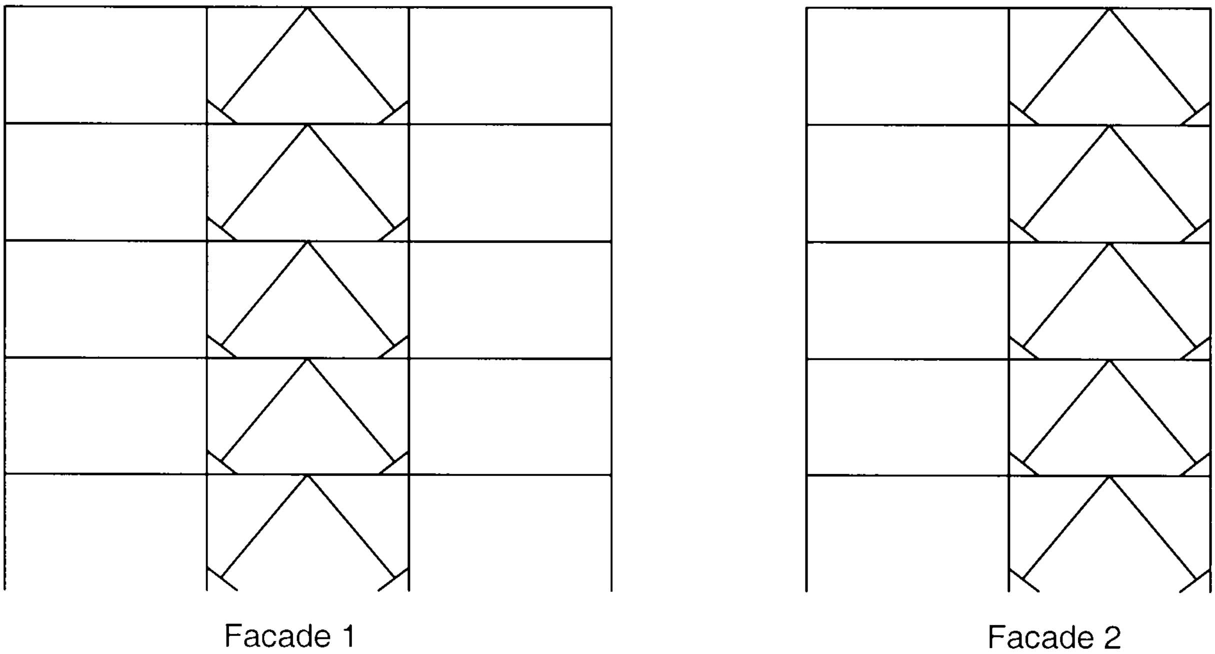

Figure 7-4: Facades of the 5-storey building

7.3.2 Choice of the sections and of the material

UB-sections were used for the beams, *UC*-sections for the columns. *SHS*-sections were used for the braces because of their high buckling resistance. *UC*-sections with adequate stiffeners as recommended in section 5.4.9 were used for the knee elements .

Standard $S235$-steel was used for knee elements and braces and standard $S355$-steel was used for beams and columns. High initial stiffnesses for the knee elements and braces and a high yield moment-stiffness ratio for the beams and columns are desirable.

The mean yield stress of the materials is generally 1.25 times the value given by the classification. The $S235$-steel real yield stress f_y is expected to be around 290N/mm^2 and this is the value used in the analysis. The modulus of elasticity for steel is E =210'000N/mm^2.

7.3.3 Connections, boundary conditions and construction details

The braces are pinned at both ends. Knee elements are built into the column and to the beam.

Beam-column connections are rigid connections. Under seismic actions more severe than the reference one, the moment resisting frame will participate in carrying the lateral loads and eventually some hinges in the beams could form and participate in the dissipative process. (This complies with Section 2.2.4 of Eurocode-8, 2001).

To avoid a massive section for the ground floor the column was pinned at the knee element connection as shown in Figure 7-5. Numerical examples have revealed that if the column is built in, it takes such an important percentage of the lateral load that it undergoes large moments and shear forces. Additionally the knee element at the ground floor will dissipate less energy.

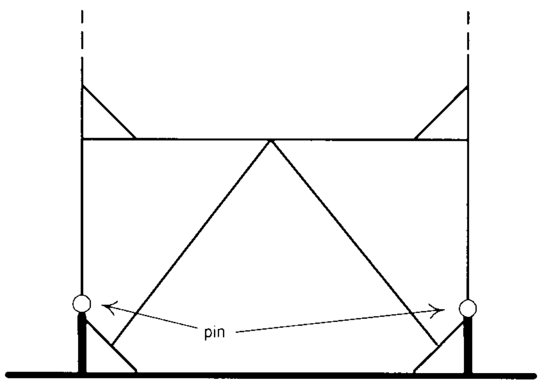

Figure 7-5: Ground floor details

In a moment resisting frame the column segments are generally assembled from storey mid-height to the next storey mid-height in order to have the column-to-column connections (column joints) where the bending moments are small. In knee braced frames the zones with the highest demand on the column are at the beam-column connection and at the knee element-column connection. At the storey mid-height the moment is already much decreased and therefore the column joint was located at that level.

The reinforced concrete floor diaphragm is attached to the top flange of the beam in order to transmit the lateral force to the bracing system. The floors avoid buckling of the beam due to compression and lateral torsional buckling of the top flange. If it is necessary to prevent lateral torsional buckling of the bottom flange, its lateral movement can be restrained by holding the bottom flange with a link to the floor, set at regular intervals.

7.3.4 Loads and load combinations

Non-seismic loads and load combinations

The standard loads are dead loads, wind loads, snow loads and imposed loads and the combinations to be considered are given in Appendix B.

Seismic loads and load combinations

ENV (1996) gives the actions to be considered in seismic design:

$$G\text{"} + \text{"}\gamma_I \cdot A_{Ed}\text{"} + \text{"} \sum_{i \geq 1} \Psi_{2i} \cdot Q_i \tag{7.1}$$

where G represents the deadload, A_{Ed} the seismic action, γ_I the importance factor, Q the variable actions and Ψ_{2i} the combination coefficient (given in Table 7.1). For buildings of intermediate size and normal use (e.g. apartments and offices) γ_I=1.0.

	Ψ_2
Imposed load B	0.3
Imposed load C	0.6
Snow	0.0
Wind	0.0

Table 7.1: Factors for seismic design situation

The mass m_i of storey i is obtained by calculating all the gravity loads with:

$$G \text{"} + \text{"} \sum \Psi_{Ei} \cdot Q_i \tag{7.2}$$

where Ψ_{Ei} are combination coefficients given by:

$$\Psi_{Ei} = \varphi \cdot \Psi_{2i} \tag{7.3}$$

Ψ_{2i} are the combination coefficients of Table 7.1 and φ the coefficient given in Table 7.2.

	φ
Imposed load B&C, top storey	1.0
Imposed load B&C, other storeys with correlated occupancies	0.8
Imposed load B&C, other storeys without correlated occupancies	0.5

Table 7.2: Factors for seismic design situation

Horizontal components

In general the horizontal components of the seismic action shall be considered as acting simultaneously. The action effect due to the combination of the horizontal components may be computed using the combinations:

$$\begin{aligned} &E_{Edx} \text{"} + \text{"} 0.3 \cdot E_{Edy} \\ &0.3 \cdot E_{Edx} \text{"} + \text{"} E_{Edy} \end{aligned} \tag{7.4}$$

Torsional effects

The accidental torsional effects need to be accounted for by amplifying the action effects in the individual load resisting elements by a factor δ. For a symmetric distribution of lateral stiffness structure δ is given by:

$$\delta = 1 + 0.6 \cdot \frac{x}{L_e} \tag{7.5}$$

where x is the distance of the element under consideration from the centre of the building and L_e is distance between the outmost lateral load resisting elements. For a rectangular building with bracing on the outside frames the accidental eccentricity factor is δ=1.3.

7.4 Non-linear pushover analysis

The use of static pushover analysis in seismic design has no rigorous theoretical background. It is based on the assumption that the response of the structure can be related to the response of an equivalent single degree of freedom ($SDOF$)-system. This implies that the response is controlled by a single mode and that the shape of this mode remains constant throughout the time history response. Clearly both assumptions are incorrect. However Miranda (1999) has shown that for buildings responding primarily in the fundamental mode the method provides a good approximation.

The pushover analysis proposed in Eurocode-8 (2001) uses an idealised elastic perfectly-elastic equivalent $SDOF$-system that dissipates the same energy for a control displacement as the multi-degree of freedom ($MDOF$)-system. There is only one unique formulation for such a $SDOF$-system. The pushover analysis is followed up to 1.5 times the target displacement.

The pushover analysis procedure in Eurocode-8 (2001) is still at a draft level and may be subject to modifications.

7.4.1 Method

The non-linear pushover in Eurocode-8 (2001) consists of the following steps.

1. A representative model of the structure should be built. Each element should be modelled at least with a bi-linear force-deformation relationship. Element properties should be based on mean properties of the materials. For the knee element, the model defined in Section 7.2 was used.

2. A non-linear pushover analysis should be performed and the maximum lateral displacement, which is defined in Section 7.4.2, should be determined. To validate the method the maximum lateral displacement should be at least 1.5 the target displacement (which is obtained in step 7). Two vertical distributions of the lateral loads

should be applied: a uniform pattern (proportional to mass regardless of elevation) and a modal pattern (obtained with Equation 2.3).

3. The displacement d_n at the control node should be read for each step increment.

4. F and d_n values should be transformed to those of an equivalent $SDOF$-system in order to draw the F^*-d^* plot with transformation procedure defined in Section 7.4.3.

5. The equivalent idealized elasto-perfectly-plastic model should be determined with the procedure defined in Section 7.4.4.

6. The target displacement d_t^* for the equivalent $SDOF$-system should be determined with the procedure defined in Section 7.4.5.

7. The target displacement d_t^* should then be transformed back into the target displacement d_t of the control node of the $MDOF$-system using $d_t = d_t^* \cdot \Gamma$. Γ is given by Equation 7.7 in Section 7.4.3.

8. $d_m \geq 1.5 \cdot d_t$ should be verified. If this condition is not satisfied the critical element section leading to the collapse should be enhanced.

9. The limitation of interstorey drift d_ν should be verified using Equation 5.7. If the condition is not satisfied the bracing stiffness should be increased.

10. It should be verified that the non-dissipative elements remain in the elastic range at the target displacement d_t. The strength and stability of the structural elements should be checked with the procedure defined in Section 7.4.6.

7.4.2 Maximum lateral displacement

The maximum lateral displacement d_m of the roof mass centre (called control node) is defined when one of the following conditions is met:

1. Enough plastic hinges are formed to obtain a plastic mechanism.

2. The second order (P-Δ) effects create an instability.

3. Failure of an element occurs and the load can not been carried by the remaining structure.

It is important to clarify to what extent the non-linear response of the knee element can be exploited without risk of low cycle fatigue failure. If a knee elements fails, the loss of stiffness and strength is such that the structure becomes unsafe.

Ballio and Castiglioni (1995) has developed low cycle fatigue models for I-sections yielding in bending. However in Section 5.4.7 it was explained that not enough test data was available to build or to calibrate the parameter of low cycle fatigue models for the knee elements. The pushover analysis only gives the maximum amplitude for each element but not the number of cycles that the element will have to resist. The number of cycles and amplitudes depend also on the characteristics of the earthquake and the building (duration, frequency content, etc.).

UC-sections with adequate stiffeners resisted more than 20 cycles of more than 22.5mm central deflections (+24 cycles of smaller amplitudes) without showing strength degradation. d_m^{KE} =22.5mm was taken as the exploitable knee element deflection for the pushover analysis in this building example. The number and amplitudes of cycles that the knee element will have to sustain will be determined in the time history analysis of Section 7.5.

7.4.3 Transformation to an equivalent $SDOF$-system

The displacements Φ_i are normalised so that the displacement at control node equals 1. The mass m^* of the equivalent $SDOF$-system is given by:

$$m^* = \sum m_i \cdot \Phi_i \tag{7.6}$$

The transformation factor is given by:

$$\Gamma = \frac{m^*}{\sum m_i \cdot \Phi_i^2} \tag{7.7}$$

And the force F^* and d^* for the equivalent $SDOF$-system are given by:

$$F^* = \frac{F_b}{\Gamma},\ d^* = \frac{d_n}{\Gamma} \tag{7.8}$$

7.4.4 Equivalent idealized elasto-perfectly-plastic system

An idealized elasto-perfectly-plastic system is determined, that has its yield force F_y^* equal to the force at maximum lateral displacement F_u^* and has a initial stiffness such as the area underneath the force-displacement curves from 0 to d_m^*, H_m^*, representing the energy is the same as for the equivalent $SDOF$-system, as shown in Figure 7-6. The yield displacement of the idealised system is given by:

$$d_y^* = 2 \cdot \left(d_m^* - \frac{H_m^*}{F_y^*} \right) \tag{7.9}$$

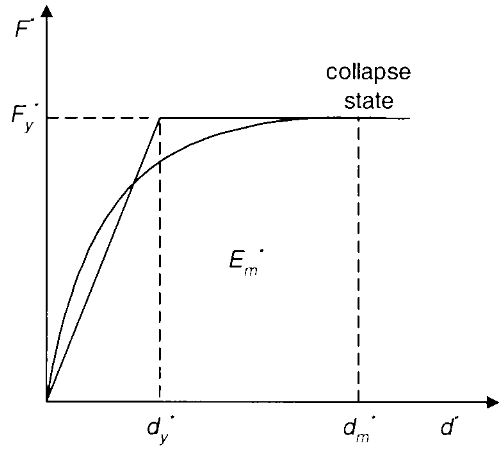

Figure 7-6: Equivalent idealised elasto-perfectly-plastic model

7.4.5 Target displacement of the equivalent $SDOF$-system

The period of the idealized elasto-perfectly-plastic system is given by:

$$T^* = 2\pi \sqrt{\frac{m^* \cdot d_y^*}{F_y^*}} \tag{7.10}$$

The target displacement of the structure with period T^* and unlimited elastic behaviour is given by:

$$d_{el}^* = \left(\frac{T^*}{2\pi} \right)^2 S_e\left(T^*\right) \tag{7.11}$$

Where $S_e\left(T^*\right)$ is the value of the elastic response spectrum at the period T^* given by Equation 2.1.

The target displacement of the equivalent $SDOF$-system is given by:

$$\begin{aligned} T^* &\geq T_C : \; d_t^* = d_{el}^* \\ T^* &< T_C : \; d_t^* = \frac{d_{el}^*}{q_u}\left(1 + (q_u - 1)\frac{T_C}{T^*}\right) \geq d_{el}^* \end{aligned} \tag{7.12}$$

where T_C is the edge period of elastic response spectrum define in Section 2.4.1 and where q_u is given by:

$$q_u = \frac{S_e \cdot m^*}{F_y^*} \tag{7.13}$$

The relationship between the different quantities can be visualized in Figures 7-7 which are in acceleration-displacement format.

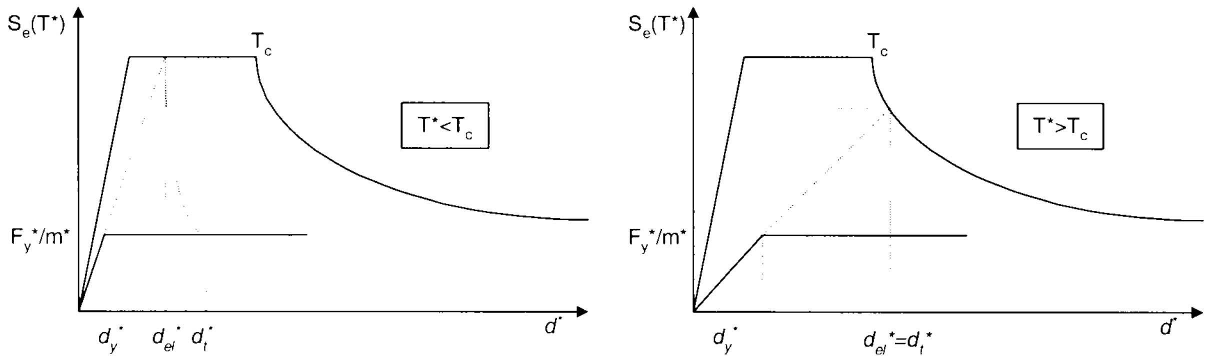

Figure 7-7: Graphic visualisation of the target displacement calculation

7.4.6 Strength and stability check for columns, beams and braces

The columns were designed to satisfy the strength and stability requirements of the design procedure given in Appendix C for a lateral displacement of at least d_m (which means no buckling or plastic hinges in the column).

The beams were designed to remain elastic for a lateral displacement of at least d_t but were allowed to form plastic hinges for higher lateral displacements.

Braces were designed to resist (without buckling) loads at which the knee element reaches its ultimate state. Buckling of the braces would be catastrophic since it would reduce considerably the stiffness of the structure and prevent the knee elements from dissipating as much energy as they should. In Section 3.3 it was shown that a high brace stiffness is very much recommended, because it confers the building with a high initial stiffness, improves the energy dissipating capacity and the global ductility. In Section 5.4.3 it was shown that the ratio $F_{\max}/F_y$ can take values up to 1.9. The brace should therefore be conservatively designed to resist, without buckling, twice the force at which the knee element, it is attached to, starts yielding. The procedure of the buckling load calculation is given in Appendix C.

7.4.7 Choice of the knee element and brace section sizes

This section does not pretend to be a rigorous method but just a help in selecting the section's size at the beginning of the iterative design procedure.

The bracing system takes the majority of the horizontal force because its lateral stiffness is much larger than that of the moment resisting frame. For a large deformation of the knee element, the part taken by the bracing system decreases but remains substantial. Using Equations 3.10 and 3.12, an estimation of the shear force in knee element can be given:

$$S_q^{KE,i} \approx \frac{c \cdot F_q^{KBF,i}}{4} \cdot \frac{\sin(\alpha + \beta)}{\cos(\beta)} \tag{7.14}$$

where α is the knee element inclination, β the brace inclination, c the proportion of the lateral force taken by the braces and F^{KBF} is the accumulated lateral force at each storey i given by:

$$F_q^{KBF,j} = \sum_{i=j}^{n} F_i^{Sd}(q) \tag{7.15}$$

where F_i^{Sd} is the static horizontal force calculated with the design spectrum (Equation 2.2) in function of a behaviour factor q (which has been determined in Section 7.4.9 for the 5-storey building example). The average of the uniform pattern (proportional to mass regardless of elevation) and the modal pattern (from Equation 2.3) should be taken.

In Section 5.4.4 it was shown that the reaction force of a the knee elements (UC-sections with 4 full stiffeners) submitted to a 14mm central deflection was around 1.7 times its yield load. To make use of the non-linear response of the knee element, the knee element should be chosen so that:

$$S_y^{KE.i} \approx \frac{S_q^{KE.i}}{1.7} \tag{7.16}$$

Since the knee element has a maximum shear capacity the axial load in the brace should not exceed:

$$N_{\max}^{Brace.i} = \frac{2 \cdot S_{\max}^{KE.i}}{\sin(\alpha + \beta)} \tag{7.17}$$

with:

$$S_{\max}^{KE.i} = 2 \cdot S_y^{KE.i} \tag{7.18}$$

7.4.8 Sections complying with the strength and stability checks

Table 7.3 gives the sections that comply with the strength and stability checks (Section 7.4.6) for the forces calculated using the pushover analysis method (Section 7.4.1). A ground acceleration, a_g, of 3.5m/s^2 for the no collapse requirement was taken. This corresponds to a 475 year return earthquake for the most seismic region of Italy and for a very seismic region of Greece, (Romeo and Pugliese, 2000).

	Braces	Knee-elements		Columns*	Beams
5	SHS 120x120x8	UC 152x152x23	roof	-	UB 254x146x31
4	SHS 150x150x10	UC 152x152x37	4-5	UC 203x203x60	UB 254x146x31
3	SHS 150x150x12.5	UC 203x203x46	3-4	UC 203x203x86	UB 254x146x31
2	SHS 150x150x16	UC 203x203x60	2-3	UC 254x254x107	UB 254x146x31
1	SHS 150x150x16	UC 203x203x71	1-2	UC 254x254x167	UB 254x146x43

*Columns are spliced at mid height according to Section 7.3.3.

Table 7.3: Structural element sections of the knee braced frame

The progressive increase, down the building, of the column, brace and knee element capacity can be observed. Strength irregularities would introduce weaknesses into the design.

The 5 natural periods of the building are: 0.565s; 0.20s; 0.12s; 0.09s and 0.07s. The first mode frequency is a bit low, but not excessively so. State expected period value is $T = 0.05 \cdot H^{0.75}$ (Aproximate expression in Eurocode-8, 2001) where H is the building height (for H=15m, T=0.38s). The displacement of the floor in the first mode (normalised to the control node =roof) is [0.13; 0.31; 0.52; 0.77; 1.00].

7.4.9 Non-linear pushover analysis results

This section presents the results of the pushover analysis performed for the two lateral load patterns, the modal pattern and the uniform load pattern.

The modal pattern results

The ultimate displacement is d_m=184mm, when the fourth floor knee element reaches a central deflection of 22.5mm (which correspond to the amplitude where there is a danger of failure by low cycle fatigue of the knee element). The yield displacement is d_y=28mm when the fourth floor knee elements start yielding.

The displacement shape normalised to the control node (at roof level) is [0.13; 0.31; 0.52; 0.77; 1.00] and the transformation factor is Γ=1.312.

Figure 7-8 shows the F^*-d^* curve and the response of the equivalent elasto-perfectly-plastic $SDOF$-system.

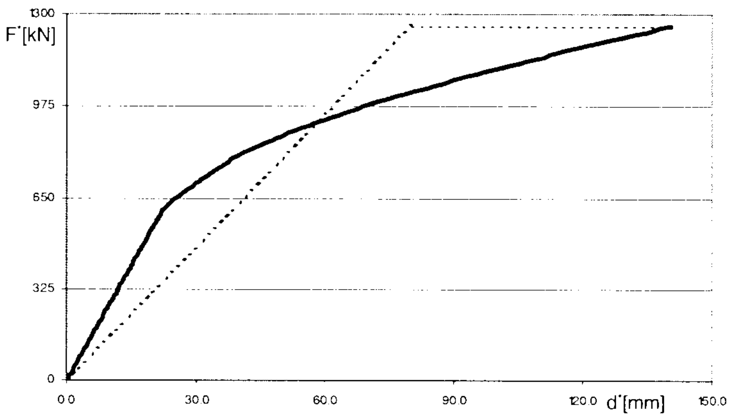

Figure 7-8: $F^* - d^*$ curve for the modal load pattern and the response of the equivalent elasto-perfectly-plastic $SDOF$-system

For the elastic perfect plastic equivalent $SDOF$-system T^*=0.76s, d_y^*=80mm and d_m^*=140mm. For that system the target displacement d_t^*=d_{el}^*=92mm. The target displacement for the building is then d_t=121mm. It is noticed that the period of the $SDOF$-system is higher by a factor T^*/T_1=1.35. Its ductility is $\mu^* = d_m^*/d_y^*$ =1.75 and its used ductility is $\mu^*_{used} = d_t^*/d_y^*$ =1.15.

Table 7.4 gives the interstorey drift of the building for d_m and d_t.

Storey	$d = d_t = 121mm$ Interstorey-drift d_v	KE-deflection δ	$d = d_m = 184mm$ Interstorey-drift d_v	KE-deflection δ
5	25	10	37	17
4	30	14.5	46	22.5
3	28	13.5	42	21.5
2	23	11.5	35	18.5
1	15	6.5	24	11.5

Table 7.4: Interstorey drifts and knee element deflections

The serviceability limit state (for $d = d_t$) is satisfied since $d_v \leq d_{\max} = 30mm$ (obtained with Equation 5.7 and with c =0.005, the factor to use when non-structural elements of brittle materials are attached to the structure). The deflections are quite non-homogeneous throughout the height. The first floor knee element is the one that participates the least in the energy dissipation.

Table 7.5 gives the yield sequence of the knee elements and beams expressed in terms of the ratio $F_b/F_{b.t}$, where F_b is the base shear force at the base of the building when the particular element yields and $F_{b.t}$ is the base shear force at target displacement d_t. The beams in the central section yield at the knee element connection, except for the third floor beam which yields at one of the column-beam connections. In the time-history analyses (Section 7.5) the same hinge locations were found.

Storey	KE left	KE right	Beam left	Beam right
5	0.60	0.61	-	-
4	0.56	0.55	-	-
3	0.57	0.56	1.11*	1.08
2	0.60	0.60	1.05	1.07
1	0.76	0.74	-	-

*plastic hinge at column-beam connection

Table 7.5: Yield sequence

Other indicative quantities can be deduced from the results, such as the behaviour factor q, the multiplier α_u/α_1, the global ductility μ and the used ductility:

$$q = \frac{S_e(T_1) \cdot \sum m_i}{F_{b.t}} \tag{7.19}$$

The behaviour factor q is defined here as the ratio between the shear base force of the non-linear system and that of an elastic system with 5% damping ratio.

$$\frac{\alpha_u}{\alpha_1} = \frac{F_{b.m}}{F_{b.y}} \tag{7.20}$$

$$\mu = \frac{d_m}{d_y} \tag{7.21}$$

$$\mu_{\text{used}} = \frac{d_t}{d_y} \quad \left(\leq \frac{\mu}{1.5}\right) \tag{7.22}$$

For the modal pattern, these quantities are: q=2.36, α_u/α_1=2.1, μ=6.6 and μ_{used}=4.4. The behaviour factor q is very low, despite the fact that the structure possesses an important ductility. Is is noticed that a dissipative structure with elasto-perfectly-plastic behaviour requires significantly less ductility than a structure showing significant strain hardening; μ/μ^*=6.6/1.75=3.8.

The uniform pattern results

The pushover analysis is repeated using an uniform load pattern (proportional to mass regardless of elevation). The ultimate displacement is d_m=160mm, when the second floor's knee element reaches a central deflection of 22.5mm. The yield displacement is d_y=26mm when the second floor's knee elements starts yielding.

The displacement shape normalised to the control node is [0.245; 0.52; 0.73; 0.895; 1.00] and the transformation factor is Γ=1.242.

Figure 7-9 shows the F^*-d curve and the response of the equivalent elasto-perfectly-plastic $SDOF$-system.

For the elastic perfect plastic equivalent $SDOF$-system T^*=0.70s and d_y^*=74mm and d_m^*=129mm. For that system the target displacement is d_t^*=d_{el}^*=85mm. The target displacement for the building is then d_t=105mm. T^*/T_1=1.24, $\mu^* = d_m^*/d_y^*$ =1.75 and $\mu_{\text{used}}^* = d_t^*/d_y^*$ =1.15.

Table 7.6 gives the interstorey drift of the building for d_m and d_t.

The serviceability limit state is again satisfied since $d_v \leq d_{\max} = 30mm$ for a lateral displacement of d_t. The knee elements of the two last floors participate less to the lateral deflection and therefore not much in the energy dissipation.

Table 7.7 gives the yield sequence of the knee elements and beams expressed in terms of the ratio $F_b/F_{b.t}$. The beams yield, without exception, in the central section at the

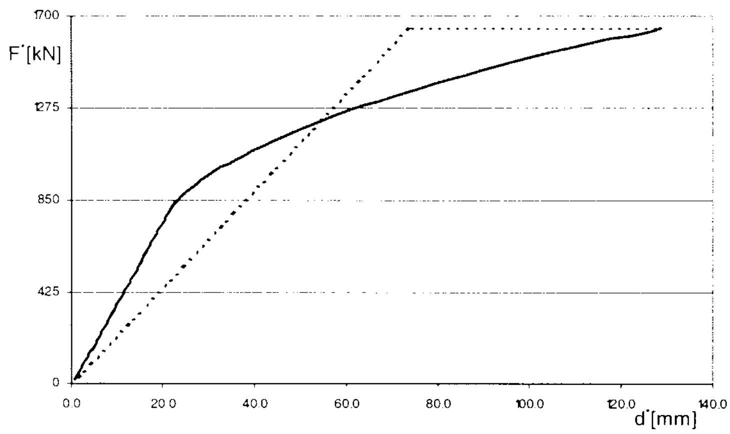

Figure 7-9: $F^* - d^*$ curve for the uniform load pattern and the response of the equivalent elasto-perfectly-plastic $SDOF$-system

Storey	$d_t = 105mm$		$d_m = 160mm$	
	Interstorey-drift d_v	KE-deflection δ	Interstorey-drift d_v	KE-deflection δ
5	12	3.5	16	5.5
4	18	7	27	12
3	22	10	35	17.5
2	28	14.5	42	22.5
1	25	13	39	21.5

Table 7.6: Interstorey drifts and knee element deflections

knee element connection.

Storey	KE left	KE right	Beam left	Beam right
5	0.83	0.84	-	-
4	0.68	0.67	-	-
3	0.61	0.60	-	-
2	0.57	0.55	1.06	1.09
1	0.62	0.61	1.08	1.05

Table 7.7: Yield sequence

For this load pattern: q=1.90, α_u/α_1=2.1, μ=6.2, μ_{used}=4.1 and μ/μ^* =6.2/1.75=3.5.

Earthquakes for various intensities

By varying d_m from 0 to 184mm for the modal pattern and from 0 to 160mm for the uniform pattern, the ground acceleration value a_g for which d_t=d_m can be determinate. This allows the evaluation of the mean lateral displacement and the location of possible damage in the structure for a given a_g. Figure 7-10 shows a plot of d against a_g for both load patterns. The onset of yield of the knee elements and the beams are indicated by KE for the knee elements and B for the beams. Both are followed by the storey number. This results are not exact; in general the mean-plus-one standard deviation on the inelastic displacement can be up to 50% of the inelastic displacement, Whittaker et al.(1998).

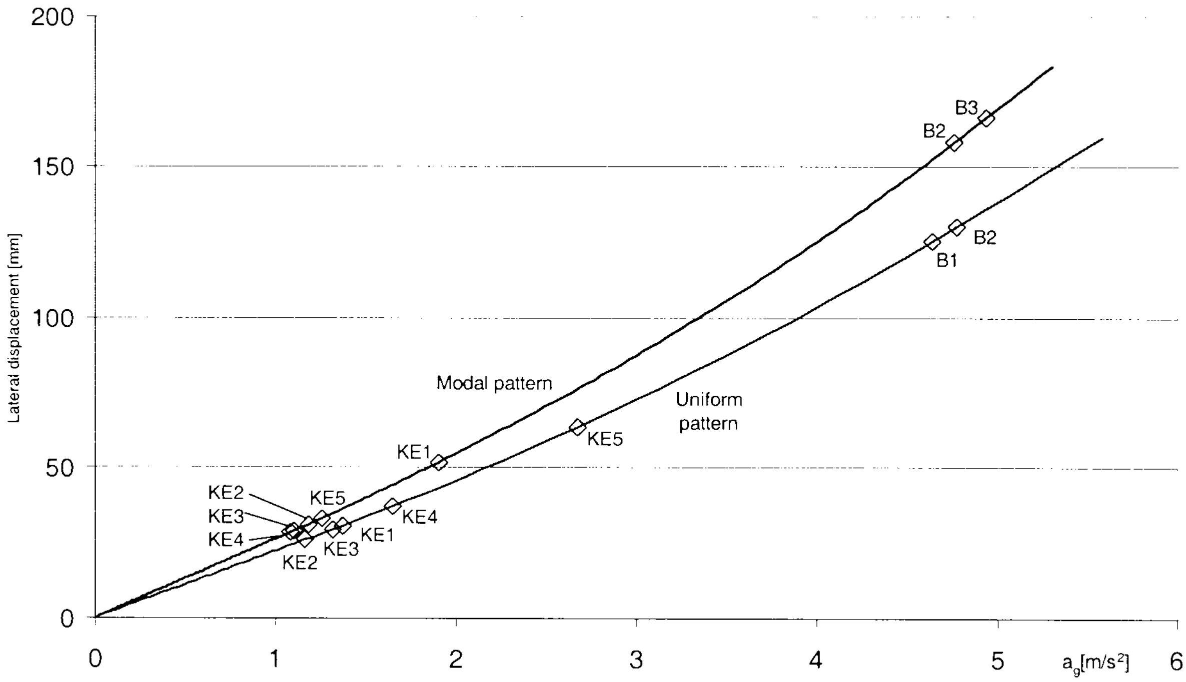

Figure 7-10: Roof mean displacement for a given ground acceleration a_g

7.4.10 Other non-linear pushover analysis methods

Significant post-yield stiffness can make the results with the pushover method of Eurocode-8 using an elasto-perfectly-plastic equivalent $SDOF$-system produce a conservative design. Various methods using the non-linear pushover analysis results with other load patterns exists in codes or are suggested in the literature.

Variant load pattern

Krawinkler (1998) showed that deformation estimates obtained from pushover analysis using the fundamental modal load pattern may be in some cases very inaccurate (on the high and low side), especially for structures where higher mode effects are significant. Higher mode effects are generated when the structure's dynamic characteristics change after the formation of the first local mechanism. By applying more than one load pattern the problem can be mitigated but usually not eliminated. Krawinkler (1998) therefore recommends the use of a variant load pattern, that is one updated at each step. In *FEMA*-356 (2000), two lateral load patterns have to be selected from two lists (one load pattern from each list). For example a modal load pattern and an adaptive load pattern can be selected. Procedures for developing adaptive load patterns include the use of story forces proportional to the deflected shape of the structure (Fajfar and Fischinger, 1988, Vidic et al., 1994), the use of load patterns based on mode shapes derived from secant stiffness at each load step (Eberhard and Sozen, 1993), and the use of load patterns proportional to the story shear resistance at each step (Bracci et al., 1995, Krawinkler, 1998). Use of an adaptive load pattern will require more analysis effort, but may yield results that are more consistent with the characteristics of the building under consideration.

Bi-linear equivalent *SDOF*-system with post-yield stiffness $\alpha_{SH} \cdot K$

A bi-linear equivalent *SDOF*-system with post-yield stiffness $\alpha_{SH} \cdot K$ can be used instead of the elastic perfectly plastic *SDOF*-system used in Eurocode-8 (2001). However this does not have a unique formulation and the choice of the post-yield stiffness $\alpha_{SH} \cdot K$ needs to be chosen with care. The initial stiffness can be chosen such as to keep the area underneath the force-displacement (H_m^*) the same. With this condition d_y^* is determined by:

$$d_y^* = \frac{2 \cdot F_m^* \cdot d_m^* - 2 \cdot H_m^* - \alpha_{SH} \cdot K \cdot (d_m^*)^2}{F_m^* - \alpha_{SH} \cdot K \cdot d_m^*} \tag{7.23}$$

FEMA-356 (2000), includes the use of bi-linear equivalent *SDOF*-system in the pushover analysis method and defines the period of the equivalent *SDOF*-system as follows:

$$T_e = T_i \sqrt{\frac{K_i}{K_e}} \tag{7.24}$$

where T_i is the fundamental elastic period, K_i the lateral elastic stiffness of the building and K_e the effective lateral stiffness as defined in Figure 7-11. The displacement demand is obtained with the same spectra and transformation factor as those used in Eurocode-8. The maximum displacement at the top of the building is obtained by multiplying the

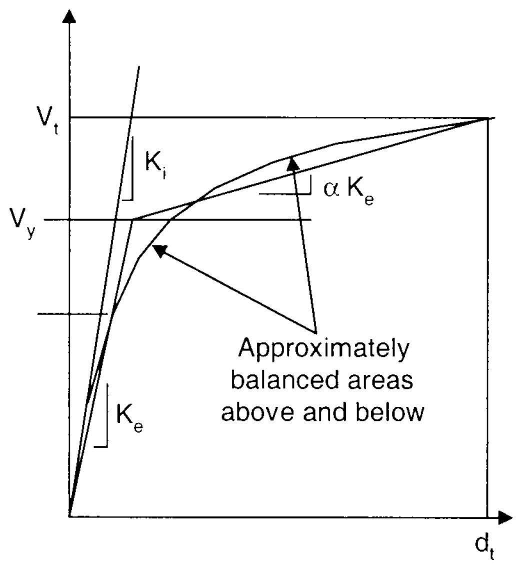

Figure 7-11: Definition of the effective lateral stiffness K_e ($FEMA$-356) on the shear force-displacement plot of the pushover analysis.

displacement demand (calculated for T_e with Equation 7.11) by the transformation factor Γ (obtained with Equation 7.7). In $FEMA$-356, the displacement is then multiplied by three other modification factors, however they are all equal to one in this case. For the 5-storey building example, $K_e \approx K_i$, α_{SH} ≈16%, and the target displacement d_t is 90mm for the modal load pattern and 84mm for the uniform load pattern. The target displacements are, as expected, smaller than those calculated with the elasto-perfectly-plastic equivalent $SDOF$-system of Eurocode-8 (2001).

Capacity spectrum

The capacity spectrum originally developed by Freeman (1978), has been incorporated in ATC-40 (Applied Technology Council, 1996). This method idealises the non-linear structures as an elastic $SDOF$-system with secant stiffness period and viscous damping corresponding to the hysteretic damping, both taken at the extreme displacement. This method is an iterative procedure with the following steps:

1. The pushover curve is transformed into the capacity diagram using the procedure of Section 7.4.3.

2. The ductility ratio is calculated with $\mu = D_i/u_y$ (where D_i is the displacement

demand).

3. The period T_{eq} of an equivalent elastic system with secant stiffness k_{sec}, as shown in Figure 7-12 a), is calculated with :

$$T_{eq} = T_i \cdot \sqrt{\frac{\mu}{1 + \alpha\mu - \alpha_{SH}}} \tag{7.25}$$

4. The equivalent viscous damping ξ_{eq} is obtained by equating the energy dissipated in a vibration cycle of the inelastic system to that of an equivalent linear system with viscous damping, Figure 7-12 b).

$$\xi_{eq} = \frac{1}{4\pi}\frac{H_D}{H_S} = \frac{2}{\pi}\frac{(\mu - 1)(1 - \alpha_{SH})}{\mu(1 + \alpha\mu - \alpha_{SH})} \tag{7.26}$$

5. The equivalent viscous damping is modified with:

$$\widehat{\xi}_{eq} = \xi + \kappa \cdot \xi_{eq} \tag{7.27}$$

where κ is a modification factor κ (which is a around 0.95 in this case) and ξ is the viscous damping ratio of the structure in the elastic range.

6. The response spectrum is plotted in its acceleration-displacement (A-D) format (called demand diagram) for $\widehat{\xi}_{eq}$.

7. Demand point is defined as shown graphically in Figure 7-13.

8. If D_t is significantly different than D_i, the procedure is repeated with $D_i = D_t$.

In the first step, D_i is the displacement demand obtained from the demand diagram with 5% viscous damping ratio. For the 5-storey building example, the damping viscous ratio is 20% and the target displacement d_t is 72mm for the modal load pattern and 66mm for the uniform load pattern. These displacements are much smaller than those calculated with Eurocode-8 (2001). However Chopra and Goel (1999) have shown that the ATC-40 procedure tends to be unconservative and may in some cases underestimate the inelastic displacement by up to 50%.

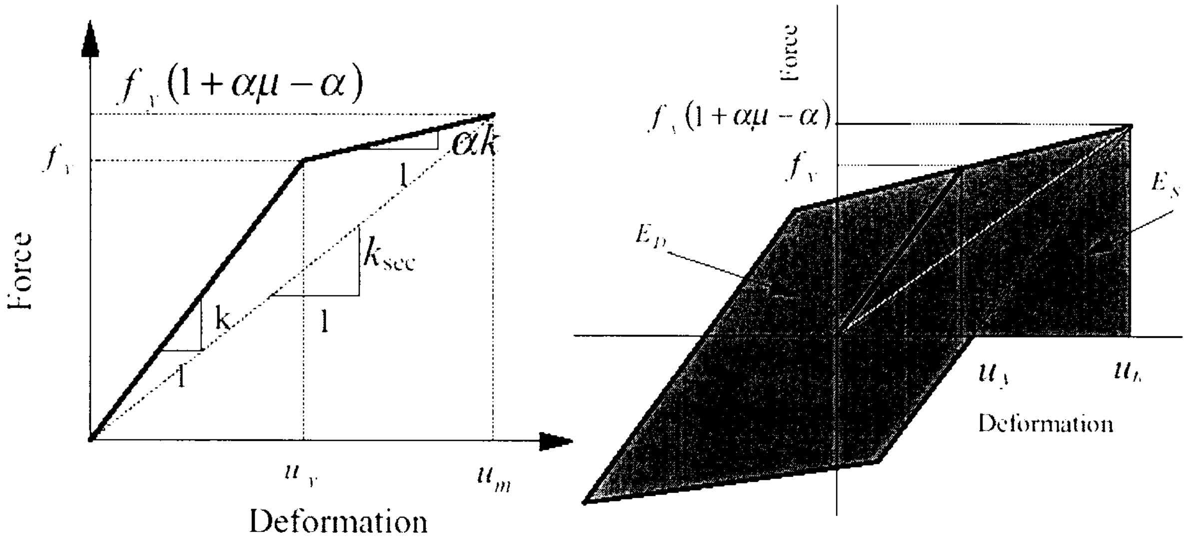

Figure 7-12: a) Bi-linear force-deformation relationship and the secant stiffness. b) Hysteretic energy dissipation for the calcution of the equivalent viscous damping.

7.5 Dynamic analysis

In this section three earthquake ground motions, compatible with prescribed response spectra of Eurocode-8 (2001), have been generated for a time history analysis of the 5-storey building example. In addition, the scaled El Centro earthquake has been used. Time-history analysis using a minimum of three artificial accelerograms is an alternative design method proposed in Eurocode-8 (2001).

7.5.1 Artificial earthquakes

To generate artificial earthquake the *SIMQKE-I* code was used. *SIMQKE-I* generates statistically independent accelerograms, performs a baseline correlation on the generated motions to ensure zero final ground velocity and calculates the response spectra. The option used generates ground motions whose response spectra match, a specified smooth response spectra. The basis for the spectrum compatible motion generation is the relationship between the response spectrum values for arbitrary damping and the expected Fourier amplitudes of the ground motion (Gasparini and Vanmarcke, 1976). The earthquakes are synthesized by superimposing sinusoidal components with pseudo-random phase angles, and by multiplying the resulting stationary trace by a user specified function representing

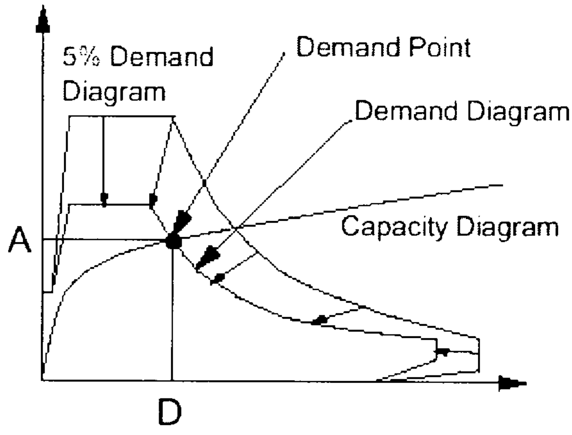

Figure 7-13: Determination of the displacement demand using the capacity spectrum diagram.

the variation of ground motion intensity with time. Its equation expression is:

$$x(t) = I(t) \cdot \sum_{i=1}^{n} A_i \cdot \sin(\omega_i \cdot t + \phi_i) \tag{7.28}$$

where ϕ_i is the phase angle, ω_i the frequency, A_i the wave amplitude and $I(t)$ the ground motion intensity time function.

The program *SIMQKE-1* also has the capability to adjust, by iteration, the ordinates of the spectral density function to improve the agreement between computed and specified response spectra. Even without the last step, the average response spectrum (of a set of simulated motions) matches the smooth target spectrum very closely.

A trapezoidal intensity envelope was used for the ground motion intensity time function $I(t)$, as shown in Figure 7-14 a). The earthquake duration was taken 20 seconds with a stationary part of 13 seconds (>10 seconds which is the minimum duration prescribed in Eurocode-8, 2001). The pseudo velocity response spectra, Figure 7-14 b), derived from the acceleration elastic spectra (damping of 5%, soil category B and a_g=1m/s^2) of the Eurocode-8 (2001) was used.

Eurocode-8 (2001) specifies that the generated accelerograms should comply with the following rules:

1. The mean of the zero period spectral response acceleration values (calculated from the individual time history) is not smaller than $a_g \cdot S$.

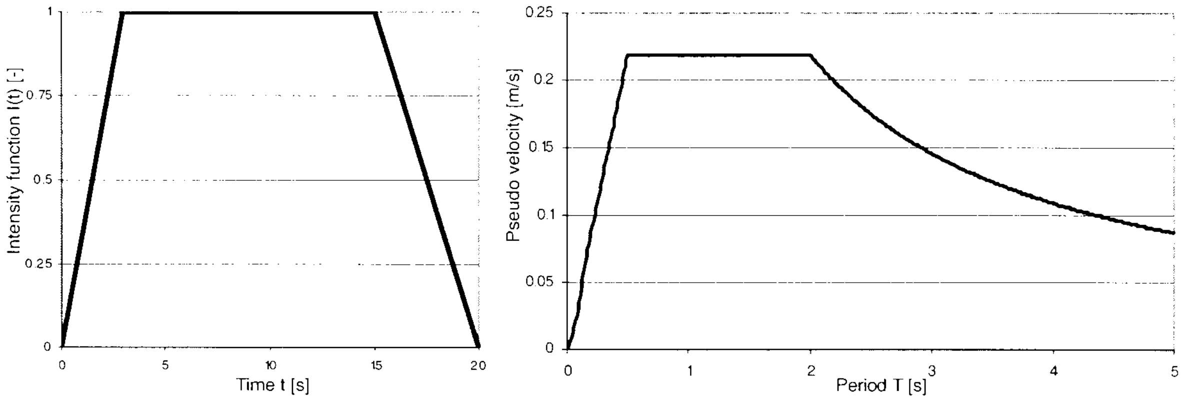

Figure 7-14: a) Trapezoidal intensity function. b) Pseudo velocity response spectra.

2. In the period range T_B to T_C, the elastic response spectrum when averaged from all time histories is not smaller than $2.5 \cdot a_g \cdot S$ (sampled at no fewer than 5 periods).

3. No value of the mean spectrum calculated from all time histories is more than 10% below the corresponding value of the elastic response spectrum.

Three artificial earthquakes (with a_g=3.5m/s^2) that comply with the above conditions were generated and their accelerograms and their acceleration spectra are shown respectively in Figure 7-15 and Figure 7-16. The response spectra envelope of the Eurocode-8 (2001) is also plotted.

7.5.2 Scaled earthquake record

An accelerogram from the 1940 El Centro earthquake which has been scaled such as its peak acceleration is 3.5m/s. was also used to perform a time history analysis. Its accelerogram and its acceleration spectra are shown in Figure 7-17. It is noticed that the response for periods in the range of 0.53-0.65s is slightly above the response spectra envelope of Eurocode-8 (2001). Since the first natural period of the building is 0.565s. It is expected that the building will respond significantly to this earthquake.

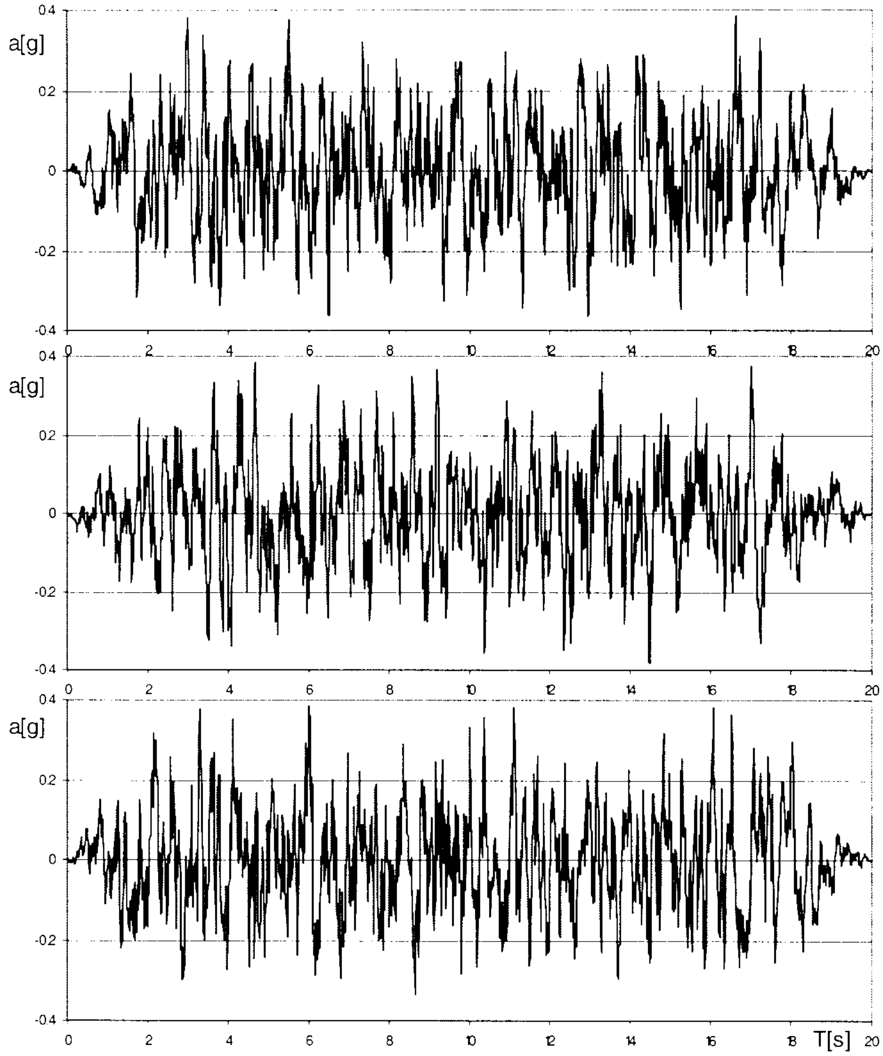

Figure 7-15: Accelerograms of three artificially generated earthquakes

7.5.3 Time history analysis

Non-linear dynamic time-history analysis of the building was carried out using the *NonLinPro* program (1997). Figure 7-18 shows the top displacements of the building for the three artificial earthquakes and the scaled 1940 El Centro earthquake (with a_g=3.5m/s^2).

All interstorey drifts remained below 23mm for the three artificial earthquakes and below 27mm for the El Centro earthquake (which is smaller than 30mm, the maximum drift allowed in Eurocode-8, obtained with Equation 5.7). The strength and stability conditions were met and no inelastic deformation outside of the knee elements occurred. Using Equation 7.19, the behaviour factors were determined and are given in Table 7.8.

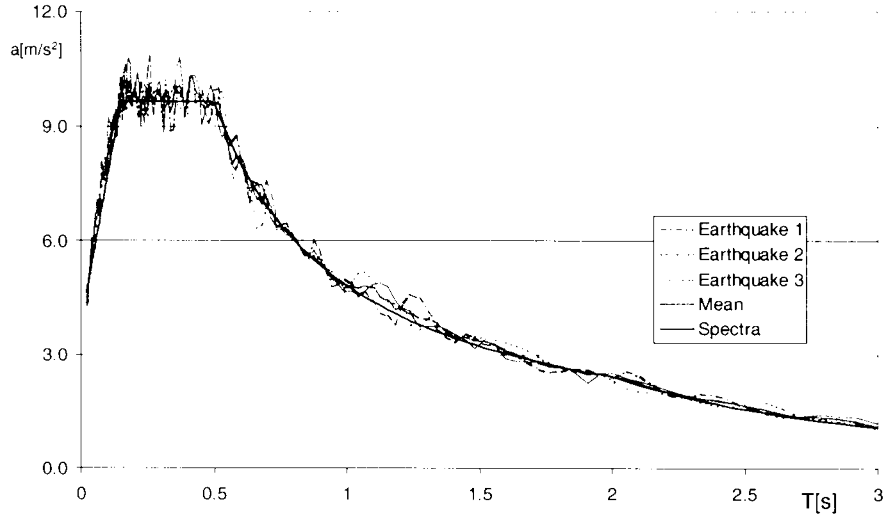

Figure 7-16: Acceleration spectra of the three artificially generated earthquakes

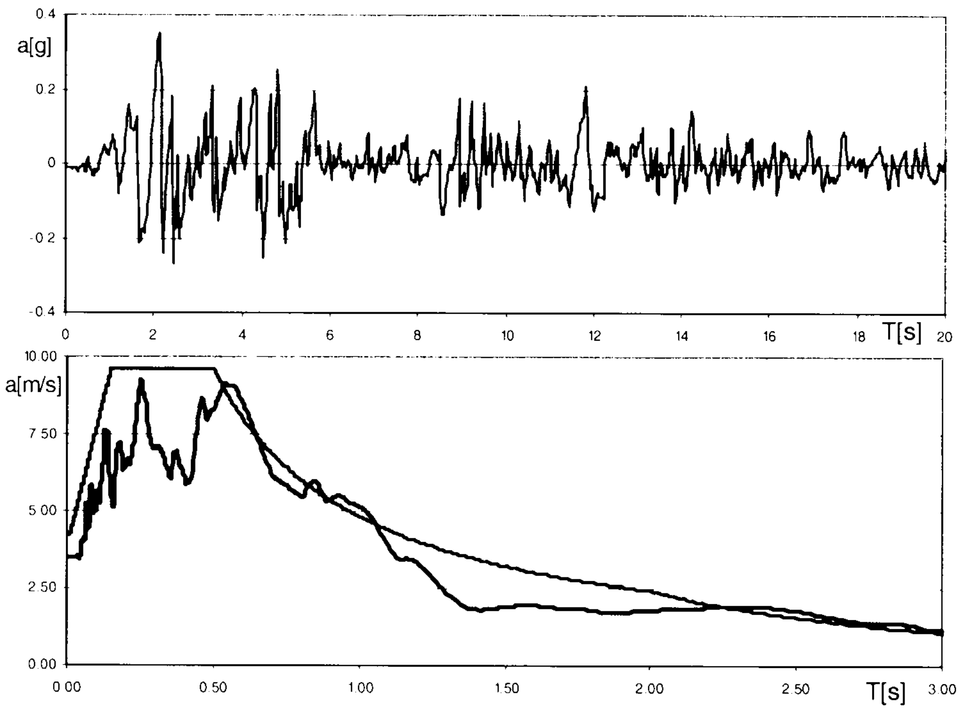

Figure 7-17: Accelerogram and the acceleration spectra of the 1940 El Centro Earthquake

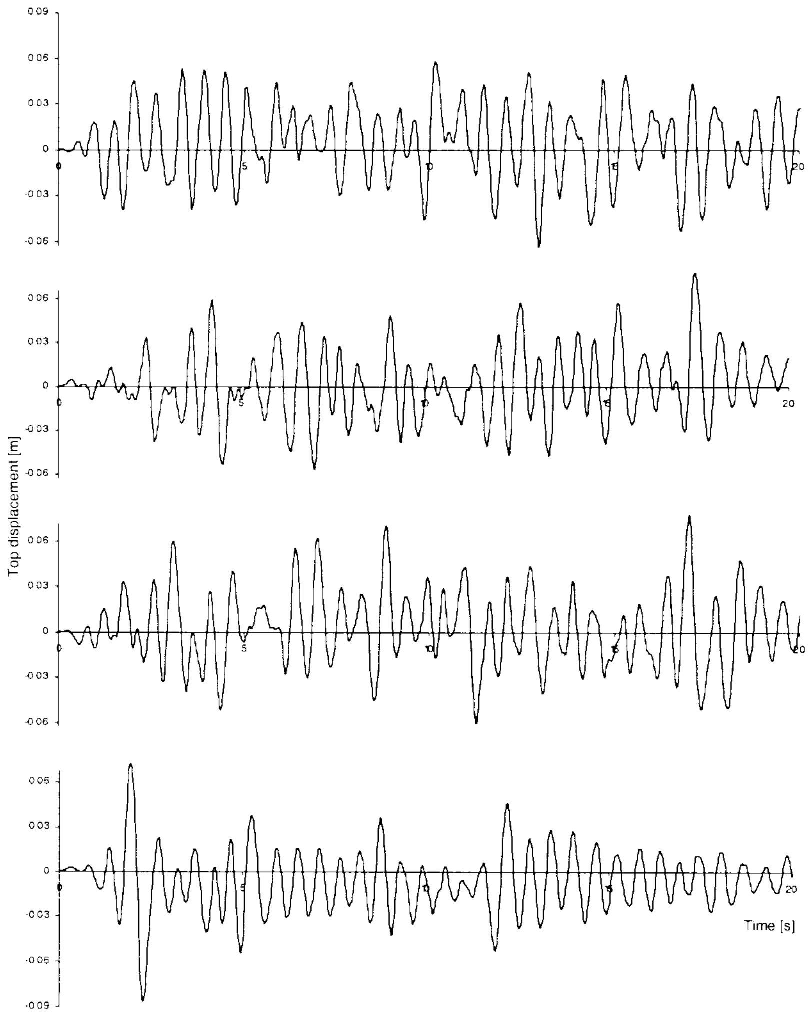

Figure 7-18: Building lateral displacement at the top for 3 artificial earthquakes and the scaled El-Centro earthquake.

The largest energy input and energy dissipation occurred for Earthquake n°1. (The dissipated energy is given for the knee braced frame, and not for the whole building). Knee elements at various stories are always yielding in pairs at the first significant acceleration peak of the earthquake. It was clearly seen that the building deformed mainly in its first mode and that higher mode effects were very small and limited. Furthermore, no soft storey behaviour (which is when the majority of the displacement concentrates in one storey) was observed. However the lower stories deformed less than the upper stories. For earthquake n°2 the maximum interstorey drifts were from bottom to top: {9; 13; 19; 22; 20 mm}. It was noticed that the maximum interstorey drifts were not reached all at the

Earth-quake n°	Max. displ a_g=3.5m/s^2 [mm]	$q_{3.5}$ [-]	Dissipated Energy [kJ]	KE yielding at first peak KE n°	a_g at which yield starts [m/s^2]	Max. displ a_g=5.6m/s^2 [mm]	$q_{5.6}$ [-]
1	64	2.6	531	1:2:3:4	0.7	119	3.4
2	78	2.7	469	1:2:3	0.8	98	3.5
3	77	2.4	494	3:4	0.7	104	3.2
El-Centro	86	2.7	254	2:3:4:5	0.8	111	3.7

Table 7.8: Time history analysis results

same time. These differences in interstorey drifts can be explained by the fact that in the pre-dimensioning, the knee element sections were chosen such as to satisfy both the modal and the uniform load pattern. To satisfy the uniform load pattern larger sections were needed for the lower stories. A more uniform maximum interstorey drifts throughout the storeys would probably be obtained by using in the pre-dimensioning a variant load pattern, as proposed in Section 7.4.10, instead of a uniform load pattern.

Figure 7-19 a) shows the knee element response (left fourth storey) to Earthquake n°2. The knee element dissipated 51.5kJ and underwent 15 plastic cycles of which none were more than 10mm. Figure 7-19 b) shows the knee element response (left fourth storey) to El Centro earthquake. The knee element dissipated 28.5kJ and underwent 9 plastic cycles of which 1 was more than 10mm. The knee elements in the fourth storey were the ones with the highest deflection amplitudes, followed by the knee elements of the third storey. The responses of these knee elements were similar to those observed during the physical test using the real time substructure testing method (Figure 5-6, Section 5.4.5).

The earthquake intensities at which inelastic deformation occurs, were determined and are given in Table 7.8. For non-dissipative structures the difficulty lies in choosing a realistic damping ratio. It was taken to 2% for the first and second natural frequency of the building. In *NonLinPro* the damping is assembled from the stiffness and mass terms as follows:

$$C = \alpha \cdot M + \beta \cdot K \tag{7.29}$$

and the frequency dependent damping ratio is given by:

$$\xi(\omega) = \frac{1}{2}\left(\frac{\alpha}{\omega} + \beta \cdot \omega\right) \tag{7.30}$$

The time history analysis was also repeated for earthquakes with a_g=5.4m/s^2 and

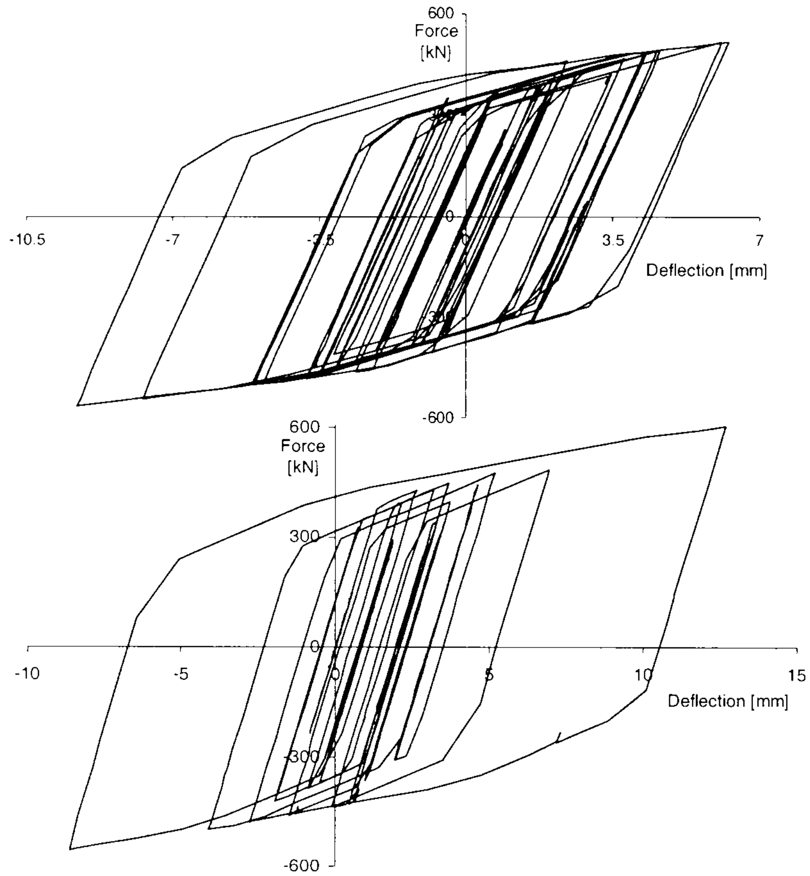

Figure 7-19: Knee element response (forth storey) to earthquake n°2 and scaled El-Centro earthquake.

a_g=5.6m/s^2. For a_g=5.6m/s^2, the top displacement and the q-factors are given in Table 7.8. The strength and stability conditions were still met and no inelastic deformation occurred away from the knee elements. However hinges would form in the third floor beams for the El Centro earthquake scaled such as a_g=5.7m/s^2. The knee element maximum deflections were smaller than 14mm for the artificial earthquakes and 18mm for El Centro earthquake. All interstorey drifts remained below 31mm for the three artificial earthquakes and below 37mm for the El Centro earthquake. For the three artificial earthquakes with a_g=5.4m/s^2, all interstorey drifts remained below 30mm.

7.5.4 Comparison with the pushover analysis results

The time history analysis results have been compared with those obtained with the three different pushover methods. Table 7.9 gives the interstorey drifts for the three artificial earthquakes (with a_g=3.5m/s^2) and those calculated with the pushover methods for the uniform and modal load patterns.

St.	Time-history				Eurocode-8			FEMA-356			ATC-40		
n°	1	2	3	Max.	Uni.	Mod.	Max.	Uni.	Mod.	Max.	Uni.	Mod.	Max.
5	19	20	18	**20**	12	25	**25**	10	19	**19**	8	15.5	**15.5**
4	23	22	21	**23**	18	30	**30**	15	24	**24**	12	19	**19.5**
3	15	19	18	**19**	22	28	**28**	18	21	**21**	15	17	**17**
2	13	13	17	**17**	28	23	**28**	22	17	**22**	17	13	**17**
1	9	9	11	**11**	25	15	**25**	19	9	**19**	15	7	**15**

Table 7.9: Comparison of the inter-storey drift in [mm] obtained for different methods

Eurocode-8 (2001) largely overestimates all the interstorey drift demands (by 25-125%). $FEMA$-356 also overestimates all the interstorey drift demands with the exception of the last storey which is underestimated by 1mm (=5%). ACT-40 largely underestimates all interstorey drifts demands (by 1-25%) with the exception of the first storey. This confirms Chopra and Goel (1999) findings that ACT-40 may be unconservative. ACT-40 is therefore not recommended for the design of knee braced frames.

From these three pushover methods, $FEMA$-356 gave the closest results to those obtained with the time history analysis. Eurocode-8 (2001) and $FEMA$-356 use the same spectra and the difference (of ~23%) is due only to the bi-linear idealisation. These two methods are based on the more than 40 years old finding of Veletos and Newmark (1960) that in the medium and long period range an elastic-perfectly-plastic $SDOF$-system has approximately the same displacement demand than an elastic $SDOF$-system with 5% of viscous damping ratio. Since then it has been confirmed by a large number of researchers. Miranda (2000) has performed a statistical study on time history analysis performed with a large number of recorded ground motions and determined the average inelastic displacement ratio $\Delta_{inelastic}/\Delta_{elastic}$ and its coefficient of variation (COV) for different levels of inelastic deformation (or ductility ratios) and for periods between 0.05 and 30 seconds. The COV takes values around 0.15 for ductility ratio of 1.5 to values around 0.40 for ductility ratio of 6. In the short period range, the displacement demand is higher for the inelastic system and increases with ductility ratios. This is taken into account in the inelastic spectra developed by Newmark-Hall (1982), Krawinkler-Nassar (1992), Vidic-Fajfar-Fischinger (1994) and Borzi (2000). Krawinkler and Seneviratna (1998) showed that the effect of stiffness degradation and pinching does not have a significant effect on the inelastic displacement demand except for very short periods. They also showed that strength degradation has a significant effect, which magnitude unfortunately cannot be put into a simple equation.

The author believes that *FEMA*-356 is a practical and reliable method to use during the design process of structures that have positive post yield stiffness as the knee brace frame exhibits.

7.6 Conclusions

7.6.1 Knee braced frame simulation and its performance

A knee element model for the non-linear static and dynamic analysis was built. An example of a 5-storey building was designed using the non-linear pushover analysis method of Eurocode-8 (2001) for a ground peak acceleration a_g=3.5m/s^2. Its performance was assessed by performing non-linear dynamic time-history analyses. The 5-storey building was submitted to three artificial generated earthquakes and to the scaled El Centro earthquake.

The pushover analysis showed that the knee braced frame possesses a high global ductility μ (6.6 for the modal load pattern and 6.2 for the uniform load pattern) and possesses an important post-yield stiffness (~16%). The 5-storey building met the strength, stability and serviceability conditions when submitted to the three artificial earthquakes with a_g=5.4m/s^2. Furthermore the 5-storey building still met the strength and stability conditions for the three artificial earthquakes with a_g=5.6m/s^2 and no inelastic deformation occurs outside of the knee elements. The maximum knee element deflections are smaller than 18mm, which is smaller than the critical deflection at which low cycle fatigue failure may be expected.

The time history analysis also showed that the knee elements would start yielding and the structure benefit from its damping effect, already for earthquake with $a_g \geq$0.8m/s^2. This shows that the knee elements can be designed to yield for small earthquakes or early on in a strong one and still be able to withstand the largest event for a given site without collapse or risk of premature failure.

It can be concluded that the knee element designed in this thesis confer knee braced frame structures with an excellent seismic resitance.

The pushover analysis design method does not necessarily lead to the optimal design. Optimisation has not been undertaken in the present work and all the results were therefore obtained with a non-optimised building example. Better results may be expected for an optimised structure. Optimisation method for knee braced frames similarly to the one of Papadrakakis et al. (2000) for moment resisting frames could be developed.

7.6.2 Non-linear pushover analysis

The time history analysis results have been compared with those obtained with the three different pushover analysis (Eurocode-8, $FEMA$-356 and ACT-40). The pushover analysis method of $FEMA$-356 gave the closest results to those obtained with the time history analyses. The author believes that this is a practical and reliable method to use during the design process. However the author would recommend a final check with time history analysis. The Eurocode-8 methods which differs with $FEMA$-356 only in the bi-linear idealisation of the equivalent $SDOF$-system, gave too conservatives results. This will be always the case for structures with significant strain hardening as the knee braced frame exhibits. The ACT-40 method is not recommended as it yields unconservative results.

7.6.3 Improvements

In the non-linear simulation it was found that important compression and tension forces built up in the knee elements due to the frame interaction. Therefore the current knee element model could be improved by including interaction moment-axial yield criteria, with inelastic axial deformation and shortening of element due to large deformations. However this required to physically assess the behaviour of a knee element to axial load when the web has undergone large plastic strains and when the flanges carry important moments.

Chapter 8

Conclusions and future work

8.1 Summary of work and conclusions

8.1.1 Review

In this work the different strategies for seismic design have been briefly reviewed. For ordinary buildings, the advantages of adding damping to structures, and in particular the advantage of steel hysteretic dampers have been demonstrated. A brief review of how codes treat the design of hysteretically damped structures was included. It was explained that after the 1994 Northridge and the 1995 Kobe earthquakes research on dissipative structures was encouraged, for which the replacement of the damaged (dissipative) elements is easier and more economical. The knee element, which is the replaceable dissipative component of such a system, the knee braced frame, has been paid little attention. This has been part of the motivation for undertaking the present research.

8.1.2 Preliminary work on knee braced frames and knee elements

An analytical study of the knee braced frame was performed in which the ideal knee element characteristics were identified. A simple equation giving a very good approximation to the relationship between the knee element deflection and the interstorey drift dependent on the geometry of the structure has been derived. It was shown that the dissipative mechanism of web yielding in shear is advantageous because it is independent of the applied moment, does not affect the connections and extends the dissipative zones over the whole beam. Standard hot rolled sections that yield for a given knee element length were identified. Inelastic shear buckling and of low cycle fatigue, which are the most probable failure modes for the knee element were reviewed. It was shown that the UC-sections are the most appropriate standard hot rolled sections to resist these two failure modes.

The interest in lowering or adjusting the yield load of the knee-element, to suit a particular structure, oriented the research on deliberately weakened UC-sections. The weakening of the sections was achieved by drilling holes in the section's web. These weakened UC-sections were analysed and the hole pattern optimised using finite element analysis. A selection of the best designs were chosen and built for physical testing. In addition, specimens made of UC-sections and UB-sections unaltered or with web stiffeners (different configurations) were tested physically.

8.1.3 Physical testing of knee elements

Innovative loadcells were designed, built and calibrated to monitor the axial force, shear force and bending moment at the knee element connections. Displacement transducers were used to monitor the knee element deformation. For some tests a thermal imaging camera and a thermal film sensor were used to observe and locate the sites of energy dissipation in the web. Furthermore, a method to map the effective plastic strain in the web on the basis of the thermal images was developed and improvements for the method have been also suggested.

Step increasing cyclic displacements were imposed on the specimens (with a cycle frequency between 0.5-2Hz). A few specimens were tested using the innovative real time substructure testing method (which simulates the loading that a knee element in a building subject to an earthquake would experience). In total nineteen knee-elements of twelve different designs (all loaded about their strong axis) were tested. Sections loaded about their minor axis have a low yield load and a high out-of-plane stability, but in practice are difficult to provide with an adequate mid beam connection and have not been considered in the present work.

The performance of the specimens was evaluated by observations made during the testing and against a list of criteria needed to analyse systematically the large quantity of data produced in the tests. It was found that perforating the web is an effective means of varying the yield load; however, local deformation at four points round each hole, roughly 40° round from the beam longitudinal axis horizontal, accelerate crack initiation which is followed by crack propagation as plastic strain builds in the web. The reduction of endurance reduces the advantage gained in allowing the designer some flexibility.

Unaltered sections showed great ductility and energy dissipation but failed prematurely due to inelastic shear buckling. Web buckling can be prevented with web stiffeners stretching from the bottom flanges to the top flanges at a spacing approximately equal to the section depth for the tested UC-sections. Partial stiffeners introduce stiff points from which cracks propagate and they are therefore not recommended. Stiffeners on only one side are sufficient. For UB-sections with stiffeners spaced at approximately half the section depth, buckling is not completely eliminated, only put off to a higher load or deflection. As predicted the stockier Universal Column sections with stiffeners are the most appropriate knee elements. In addition, their yield load is predictable within ±5% using a very simple formula. No significant differences between the knee elements cyclically loaded and those seismically loaded were found. Cyclic loading at a cycle frequency between 0.5-2Hz has therefore been found adequate to assess the seismic response of knee elements.

Not enough knee elements of the same type and the same steel were tested to be able to calibrate existing low cycle fatigue models or develop a low cycle fatigue models for beams yielding in shear. However, the few identical knee element groups confirmed clearly that more damage was done by one large amplitude cycle than by a multitude of small amplitude cycles dissipating the same amount of plastic energy and that low cycle fatigue needs to be taken into account. The results were also compared with published results of beam yielding in bending. The results were too sparse to conclude that the knee elements yielding in shear are better than those yielding in bending but the results point in that direction.

The knee element response (UC-sections with adequate stiffeners) at a deflection of 14mm (which corresponds roughly to the knee element deflection for which the serviceability limit state of the frame is reached) is approximately 1.7 times its yield load. The knee element ultimate load can reach 1.9 times its yield load.

8.1.4 Thermal imaging

Thermal imaging was found to be an effective method for identifying energy dissipation regions, initial yield locations and the modes of yield pattern expansion. Thermal imaging was also found capable of detecting energy dissipation by friction of a slipping bolt.

With numerous reference points that can be easily followed, and using a complex transform method, the image of the structure can be transformed back to its undeformed shape. This allows superposition of the images and meaningful mathematical processing of the data. This in turn allows the mapping of the energy dissipation rate, the calculation of the effective plastic strain and the Von Mises stress for each equivalent pixel area. It was concluded that some attention should be given to the surface preparation and to the determination of the emissivity of the analysed surface. The results, despite being obtained with an outdated thermal imaging camera with very limited performance, were of a very good quality and definition. Currently available thermal imaging cameras are therefore powerful tools for assessing plastic strain. On the contrary the thermal film sensor failed to catch peak temperatures during testing and in addition gave only localised information. However, the thermal film sensor was useful for the determination of the surface emissivity.

8.1.5 Finite element modelling of the knee elements

The finite element models were refined to match the physical test results. Material characteristics were determined from a uni-axial specimen for both monotonic and cyclic loading. Details, such as the connection flexibility, the welds and the flange roots, all of which contribute to the response of the knee element, were modelled. In addition, the effect of imperfections and residual stresses were also included. Both monotonic and cyclic analyses were performed.

It was shown that shell elements give accurate results and reduce the computing time and result file size over solid elements. However, solid element models may be used to analyse stress concentrations in a small portion of a structural element.

The material properties have been found to be the most sensitive component in the analysis. In *ABAQUS* the cyclic material behaviour is only defined by three parameters. This was found to be insufficient. This problem was circumvented using different material rules for different plastic strain levels. An initial analysis with a single material rule was used to classify the elements into plastic strain categories. A second calculation was then performed attributing a different material rule to each category. In general four material rules were sufficient.

The welds and roots can be modelled by giving an increased thickness to the shell elements where they are situated. Connections can be modelled by rotational and translational springs. It has been found that the strain rate can be neglected and that the residual stresses slightly influence the yield load, but have no effect on the post-yield behaviour. It was found that imperfections have almost no influence except when the load is close to the buckling load.

The finite element analysis gave excellent results with less than 6% error for large hysteresis loops. However, it fails to give the rugby ball shape found in the physical testing and therefore overestimates the dissipative energy by about 16%. Important differences are found in moments and axial forces but they seemed not to affect the accuracy of the reaction force (shear force).

A heat analysis simulating the diffusion of the heat generated by plastic straining was also performed and compared to thermal images taken during physical testing. The equivalent strain and the Von Mises stresses obtained with the finite element analysis were also compared with those deduced from the thermal images using the method developed earlier. Satisfying results were obtained. Large differences were found only when elements approach the failure mechanism and when the damage and dissipation would be distributed unequally. Thermal imaging is therefore an excellent tool for understanding energy dissipation and the failure mechanisms.

A detailed analysis with a solid element model of a small square section of the web with a central hole suggested that severe local deformation occurred where crack initiation occurred. Crack propagation has not been modelled.

Instability calculations performed in an attempt to predict the critical or failure loads showed that even a very sophisticated analysis (Riks analysis) including the effects of imperfections was unable to predict the failure of highly inelastic shear bucking, and overestimated the critical load in the best case by 10 to 20%. In addition, low cycle fatigue cannot be modelled in *ABAQUS*. Large-scale experimental testing has therefore a key role to play in further development of knee elements and determining their ultimate load and endurance.

8.1.6 Dynamic simulation of knee braced frame buildings

A knee element model for the non-linear dynamic analysis was built and gave realistic responses including energy dissipation. The element was integrated into a complete 5-storey building model. The building was design using the non-linear pushover method of Eurocode 8 (2001). Non-linear pushover analysis revealed that the knee braced frame possesses a high global ductility (>6) but significant post-yield stiffness (~16%). The displacement demand obtained with the non-linear pushover method of Eurocode 8 (2001) was checked against the maximum displacement observed in the time history analyses using artificially generated earthquakes. It was found that Eurocode 8 produces very conservative design for structures with significant post-yield stiffness because it uses an elastic-perfectly plastic idealisation. The time history analysis showed that the designed knee braced frame building can resist an earthquake with a peak ground acceleration of a_g=5.6m/s^2 (with damage located exclusively in the knee elements), and also provides the building with a beneficial dissipative effect for earthquake as weak as a_g =0.8m/s^2. This shows that the knee elements can be designed to yield for small earthquakes and still be able to withstand the largest event for a given site without risk of collapse or failure. All the results were obtained with a non-optimised building example but the results obtained confirmed the excellent properties of knee brace frames and the adequacy of the knee elements designed and developed in this thesis.

8.2 Suggestions for future work

Since the present research leaves many questions unanswered, a short list of suggestions for future work is given below:

- Development of a low cycle fatigue model of a *UC*-section yielding in shear. This requires numerous specimens to be tested with different loading histories e.g. as Ballio and Casteglioni (1995) did for sections yielding in bending.

- Assessment of the behaviour of a knee element under axial load when the web has undergone large plastic strains and when the flanges carry significant moments. Non-linear simulations of an entire building showed that relevant tension and compression forces may be present in knee elements due to frame interaction.

- Verification that stiffener spacing equal to section depth prevents inelastic shear buckling for larger UC-sections than the those tested in the present research.

- Development of a better method of acquiring reference points for the thermal imaging analysis technique. Development of an adequate surface preparation method and verification that the emissivity does not vary due to large plastic deformation. Calibration on a uni-axial cyclic test could provide useful information.

- Improvement of the current knee element model for non-linear simulation of the whole building by including interaction moment-axial yield criteria, with inelastic axial deformation and element shortening due to large deformations.

- Development of an optimisation method for knee braced frames and design guidelines for the designer.

- Estimation of the adequacy of various existing design procedures.

- Development of the knee element replacement method after a moderate earthquake. This methods needs to take into account the elastic energy still stored in some structural members after the earthquake. Careful design of the knee element connections are needed.

Appendix A

Summary of the knee element tests

Test	*Section abreviation*	*Imposed cyclic displacements* *Number of cycles* × {*Amplitude* [*mm*]}
1	UC30H12	6×{↗1.5; ↗2.4}; 4×{2; 5; 8.5; 11.5; 15.5; 19.5}; 3×{24}
2	UC30H12	6×{↗2.4}; 4×{2.4; 5.1; 8.2; 10.2; 15.5; 19.5}; 3×{24}
3	UC30H12	2×{2.4; 3.2; 3.3; 5.2; 9.1; 8.9; 9.2; 13.4; 12.2; 8.9; 12.2; 15.6; 18.9} 2×{24.5; 26}
4	UC30H20	10×{↗2}; 6×{1.5; 4; 6; 9; 12; 15; 18}
5	UC30H20	6×{↗1.5}; 6×{↗3}; 3×{2.3; 5.5; 9.2; 12.6; 16.5; 20; 25}
6	UC30H15a	2×{1.9}; 12×{3.1}; 2×{3.3; 4.6; 7.6; 8.2; 11; 15; 15.3; 5; 11.5; 20}
7	UC30H15b	2×{2.3; 4.9; 5.1; 8.4; 11.8; 16.4; 16.7; 18.8; 19.5; 20.5; 21; 19.5; 29}
8	UC30N	10×{↗2}; 10×{↗3.8}; 6×{3; 8; 13; 18; 21; 24; 34}; 2×{35}
9	UC30N	6×{↗3}; 4×{2; 5; 7.9; 11.2; 14.4; 18.4; 20.2; 22; 23.9; 25.9; 35; 40}
10	UC30FS4	4×{2; 4.5; 4.7; 11; 13.5; 15}
11	UC23N	8×{2.3}; 12×{2}; 4×{5; 8.5; 11.5; 15.4}; 12×{12}; 4×{17}
12	UC23PS4	1×{2}; 4×{4.2}; 3×{4.7; 11.3; 7; 11.5; 18.2; 23; 18.5; 23}
13	UC23FS2	2×{3.6; 8.4; 13.2; 16.9; 19; 24.3; 26.3; 21; 22.7; 26.7; 28}
14	UC23FS4	2×{3.4; 8.2; 12.8; 16.4; 21.5; 24.6; 26.2; 28.5}; 1×{30}
15	UB23N	6×{↗1.7;↗3.1}; 2.5×{2.8; 7; 12; 15.5; 17.4}; 1×{25}
16	UB23FS4	15×{1.7}; 4×{4.7; 7.9; 8; 11.4; 18.2; 17.8; 4.1; 9.5; 11; 18.7; 30}

6×{↗2}; 4×{3; 5} means the knee element experienced 6 increasing cyclic amplitudes (see Figure 5-1a) with a maximum amplitude of 2mm , 4 cycles of 3mm and 4 cycles of 5mm.

Test	*Section abreviation*	*Maximum response amplitude to the El Centro earthquake (for different scaling) [mm]*
17	UC30N	{16; 13; 12.3; 19}
18	UC30N	{2.5; 9.7; 13.8; 14.2; 15; 15.6; 16; 16.8; 21}
19	UB23N	{2.2; 3; 4.2; 4.2; 4.9; 4.9; 10.2; 11.9; 15; 15.2; 15.2; 17}

Appendix B

Non-seismic loads and design situations for a 5-storey building

B.1 Loads

From the ENV (1996), an average values for the surface dead loads were chosen and are given in Table B.1 and B.2.

Roof	$q[kN/m^2]$
Steelwork	0.50
Concrete slab ($t = 150mm$)	3.75
Roof and finishing	1.50
Ceiling and services	0.50
Total	6.25

Table B.1: Roof deadload

Storeys	$q[kN/m^2]$
Steelwork	0.50
Concrete slab ($t = 150mm$)	3.75
Ceiling and services	0.50
Total	4.75

Table B.2: Storey deadload

A perimeter deadload of 2.2kN/m^2 was taken, which represents the weight of secondary elements, cladding and isolation panels. For the roof an imposed load category C of 3kN/m^2 and for the storeys an imposed load category B of 2.5kN/m^2 were considered. On the roof a snow load of 0.6kN/m^2 was considered. For the wind a local pressure of

$0.75 kN/m^2$ and a global pressure of $1 kN/m^2$(which is the addition of the average pressure acting on the front and on the back side of the building) were considered.

B.2 Permanent and transient design situation

ENV (1996) gives the actions to consider for a persistent and transient design situations for ultimate states verification:

$$\gamma_G \cdot G\text{"} + \text{"}\gamma_{Q1} \cdot Q_1\text{"} + \text{"} \sum_{i>1} \Psi_{0i} \cdot \gamma_{Qi} \cdot Q_i \tag{B.1}$$

where γ_Q and Ψ_0 are given in Table B.3.

	γ_Q	Ψ_0
Imposed load B	1.50	0.7
Imposed load C	1.50	0.7
Snow	1.50	0.6
Wind	1.50	0.6

Table B.3: Factors for the permanent and transient design situation

For the deadload, since its action is unfavourable, a factor of γ_G=1.35 was taken.

B.3 Allowance for imperfections

The effects of imperfections was taken into account. These effects are given in terms of an initial rotation ϕ at the base of the column but can be converted into equivalent horizontal forces $\phi \cdot F_i$. A value of ϕ=1/400 was considered (Table 5.3, C-EC3, 1993).

B.4 Serviceability for non-seismic load combinations

The recommended values for the serviceability limit state are for vertically displacement of floors $\delta=(1/250)\cdot L$ and of roofs $\delta=(1/200)\cdot L$. For lateral displacements of multistorey buildings, $\delta=(1/500)\cdot H$ for the top displacement and $\delta=(1/300)\cdot h$ for interstorey drift, (Table 4.1, C-EC3, 1993).

Appendix C

Strength and stability procedure for structural elements

C.1 Braces

The braces are only axially loaded members and should satisfy the buckling and the tension resistance, respectively the Equations 5.4.2 and 5.4.3, of C-EC3 (1993):

$$N_{Sd} \leq f_y \cdot A/\gamma_{M0} \tag{C.1}$$

$$N_{Sd} \leq N_b = f_c \cdot A/\gamma_{M1} \tag{C.2}$$

where the partial safety factors $\gamma_{M0} = \gamma_{M1}$ =1.05, f_c is the compression stress which depends on the slenderness ratio $\lambda = \ell/i$ (Table 5.14 of C-EC3, 1993), ℓ is the buckling length, i is the radius of gyration. In this case ℓ is equal to the length of the brace since it is restrained in position but not in rotationat its ends.

C.2 Columns

Columns and beams have to resist axial loads, shear loads and bending moments (biaxial bending for the columns). The shear capacity has to be checked with Equation 5.5.1 of C-EC3 (1993).

$$V_{pl.Rd} = A_{web} \cdot (f_y/\sqrt{3})/\gamma_{M0} \tag{C.3}$$

Only the low shear check is necessary, if Equation 5.6 of C-EC3 (1993) is satisfied:

$$V_{Sd} \leq 0.5V_{pl.Rd} \tag{C.4}$$

If not the high shear condition applies.

C.2.1 Low shear

To avoid buckling in compression or torsional buckling in biaxial bending the two following equations need to be satisfied:

$$\frac{N_{Sd}}{N_{b.z.Rd}} + \frac{k_y \cdot M_{y.Sd}}{M_{c.y.Rd}} + \frac{k_z \cdot M_{z.Sd}}{M_{c.z.Rd}} \leq 1.0$$

$$\frac{N_{Sd}}{N_{b.z.Rd}} + \frac{k_{LT} \cdot M_{y.Sd}}{M_{b.Rd}} + \frac{k_z \cdot M_{z.Sd}}{M_{c.z.Rd}} \leq 1.0 \tag{C.5}$$

where k_y, k_z and k_{LT} are defined with the procedure 5.3 of C-EC3 (1993) and where:

$$M_{c.Rd} = f_y \cdot W_{pl.y}/\gamma_{M0} \tag{C.6}$$

$$M_{b.Rd} = f_b \cdot W_{pl.y}/\gamma_{M1} \tag{C.7}$$

f_b is obtained from Table 5.18(a) of C-EC3 (1993) in function of λ_{LT} given by:

$$\lambda_{LT} = \frac{[k/C_1]^{0.5} L/i_{LT}}{[1 + (L/a_{LT})^2/25.66]} \tag{C.8}$$

$$i_{LT} = [I_w/I_t]^{0.5} \tag{C.9}$$

$$a_{LT} = [I_x \cdot I_w/W^{2}_{pl.y}]^{0.25} \tag{C.10}$$

where I_t is the torsional constant and I_w is the warping constant.

C.2.2 High shear

The same conditions as for low shear have to be satisfied. In additionally the following equation needs to be satisfied:

$$M_{y.Rd} \leq M_{VN.Rd} \tag{C.11}$$

where $M_{VN.Rd}$ is given by Equation 5.6.1.5 of C-EC3 (1993):

$$M_{VN.Rd} = M_{Nf.Rd} + \frac{(M_{N.Rd} - M_{Nf.Rd})}{[1 - (2V_{Sd}/V_{pl.Rd} - 1)^2]} \tag{C.12}$$

where $M_{Nf.Rd}$ is the plastic resistance consisting of the flanges only and $M_{N.Rd}$ is the plastic resistance of the whole section.

References

- ABAQUS (1998), Abaqus User's Manual I-III and Theory Manual Version 5.8, Hibitt, Karlsson & Sorensen, INC.

- Agrawal A K, Kosaka H and Yamanaka H, (1994), "Stability Of Active-Tendon Structural Control With Time-Delay", *Journal of Engineering Mechanics*, 120(10), 2240-2243.

- Aguire M and Sanched R, (1992), "Structural seismic dampers", *Journal of Structural Engineering*, 118(5), 1159-1171.

- Aiken I, Nims D K, Whittaker A S and Kelly J M, (1993), "Testing of passive dissipation systems", *Earthquake Spectra*, 9(3).

- ALGA, S.p.A, *http://192.107.65.2/GLIS/HTML/gn/turchi/g5turchi.htm*, (June 2001).

- Allen H G and Bulson P S, (1980), "Background to Buckling", Mc Graw Hill.

- Aristazabal-Ochoa J D, (1986), "Disposable Knee Bracing: Improvement in Seismic Design of Steel Frames", *Journal of structural Engineering*, 112(7),1544-1553.

- ATC, (1996), "ATC-40; Seismic evaluation and retrofit of concrete buildings", *Report 40*, Applied Technology Council.

- Avery P, (1998), "Advanced analysis of steel frame structures comprising non-compact sections", *PhD-thesis*, School of Civil Engineering, Queensland University of Technology.

- Azhari M and Bradford M A, (1993), "Inelastic initial buckling of plates with and without residual stresses", *Engineering Structures*, 15(1), 31 39.

- Bachmann H and Weber B, (1995), "Tuned vibration absorbers for 'Lively' structures", *Structural Engineering International*, 5(1), 31-36.

- Balendra T, Yu C H and Lee F L, (2001), "An economical structural system for wind and earthquake loads", *Engineering Structures*, 23, 491–501.

- Balendra T, Lim E L and Liaw C Y, (1997), "Large-Scale Seismic Testing of Knee Braced Frame", *Journal of Structural Engineering*, 1(1), 11-19.

- Balendra T and Liaw C Y, (1995), "Earthquake-resistant steel frame with energy dissipating knee element ", *Engineering Structures*, 17(5), 334-343.

- Balendra T, Lim E L and Liaw C Y, (1994), "Ductile knee braced frames with shear yielding knee for seismic resistant structures", *Engineering Structures*, 16(4), 263-269.

- Balendra T, Sam M-T and Lee C-Y, (1991), "Preliminary studies into the behaviour of knee braced frames subject to seismic loading", *Engineering Structures*, 13, 67-74.

- Balendra T, Sam M-T and Lee C-Y, (1991), "Design of Earthquake-Resistant Steel frames with Knee bracing", *Journal of Constructional Steel Research*, 18, 193-208.

- Balendra T, Sam M-T and Lee C-Y, (1990), "Diagonal brace with ductile knee anchor for aseismic steel frame", *Earthquake Engineering & Structural Dynamics*, 19, 847-858.

- Ballio G and Castiglioni C A, (1995), "A Unified Approach for the Design of Steel Structures under Low and or High Cycle Fatigue", *Journal of Constructional Steel Research*, 34(1), 75-101.

- Bernuzzi C, Zandonini R and Zanon P, (1995), "Experimental analysis and Modelling of semi-rigid steel joints under cyclic reversal loading", *Journal of Constructional Steel Research*, 38 (2), 95-123.

- Bertero V V, Anderson J C, Krawinkler H, (1994), "Performance of steel structures during the Northridge earthquake", *Report*, College of Engineering, University of California at Berkley, UCB/EERC-94/09.

- Blakeborough A, Clément D, Williams M S and Woodward N, (2002), "Loadcell for Measuring Axial Force, Shear Force and Bending Moment in Large Scale Structural Experiments", *Journal of Experimental Mechanics* , 42(1), 115-122.

- Blakeborough A, Williams M S Darby A P and Williams D M, (2001), "The development of real time substructure testing", *Philosophical Transactions of the Royal Society of London, Series A*, 359(1786), 1869-1892.

- Blakeborough A, Merrinan P A and Williams M S (Eds.), (1997), "The Northridge, California Earthquake of 17 January 1994", Field report by EEFIT, Earthquake Engineering Field Investigation Team, London.

- Borzi B and Elnashai A S, (2000), "Refined force reduction factors for seismic design", *Engineering Structures*, 22, 1244-1260.

- Borzi B, Calvi G M, Elnashai A S, Facciolo E and Bommer J J, (2000), "Inelastic spectra for displacement-based seismic design", *Soil Dynamics and Earthquake Engineering*, 21, 47-61.

- Bourahla N, (1990), "Knee bracing system for earthquake resisting steel frames", *PhD-thesis*, Department of Civil Engineering, University of Bristol, UK.

- BS 4848, (1972), "Hot-rolled structural steel section", British Standards Institution, BSI, London.

- BS 5950, (1992), "Tolerances on rolled cross sections", British Standards Institution, BSI, London.

- BS 6399, (1997), "Standard wind loads", British Standards Institution, BSI, London.

- Bracci J M, Kunnath S K and Reinhorn A M, (1995), "Simplified Seismic Performance and Retrofit Evaluation", *Journal of the Structural Division*, American Society of Civil Engineers, New York.

- Burdekin F M (Ed.), (1997), "Seismic design of steel buildings after Northridge and Kobe earthquakes", *Society for Earthquake & Civil Engineering Dynamics*, SECED, The Institution of Structural Engineers, London.

- BRI, (1996), "Survey Report for building damage due to the 1995 Hyogo Ken Nanbu Earthquake", *Report*, Building Research Institute, Ministry of Construction.

- Campenon Bernard, (2000), "Dispositif permettant de limiter le deplacement relatif de deux elements d'une structure comprenant un tel dispositif", Brevet d'invention 0001597 de Campenon Bernard SGE, 5 Ferdinand de Lesseps, 92500 Rueil Malmaison, France, auprès de l'institut national de la propriete industrielle de Paris.

- Calado L, (1995), "Experimental research and analytical modelling of the cyclic behaviour of bolted semi rigid connections", *Proceedings of the 1st European conference on steel structures*, Eds. Kounadis and Balkema, Rotterdam.

- Calado L and Azevedo J, (1989), "A model for predicting the failure of structural steel elements", *Journal of Constructional Steel Research*, 14(1), 41-64.

- Capra A, (2000), "Dispositif de protection parasismique à comportement elasto-plastique", Mémoire de présentation, Campenon Bernard SGE.

- Capra A and Wastiaux M, (2000), "Seismic design of the second Tagus crossing", Mémoire de présentation, Campenon Bernard SGE.

- Celesco, 7800 Deering Avenue Canoga Park, CA91309, *http://www.celesco.com* (July 2001).

- Chandler A M and Pomonis A (Eds.), (1997), "The Hyogo-Ken Nanbu (Kobe) Earthquake of 17 January 1995", Field report by EEFIT, Earthquake Engineering Field Investigation Team, London.

- Chandler A M and Lam N T K, (2001), "Review Article: Performance-based design in earthquake engineering: a multi-disciplinary review", *Engineering Structures*, 23, 1525–1543.

- Chang C C and Yang T Y, (1995) "Control of Buildings using Active Tuned Mass Dampers", *Journal of Engineering Mechanics*, 121(3), 355-366.

- Chang K C, Soong T T, Oh S T and Lai M L, (1995), "Seismic behaviour of steel frame with added visco-elastic dampers", *Journal of Structural Engineering*, 121(10), 1418-1426.

- Chopra A K and Goel R K, (1999), "Capacity-demand-diagram methods for estimating seismic deformation of inelastic structure: SDOF-system", *Report No. PEER-1999/02*, Pacific Earthquake Engineering Research Centre, College of Engineering, University of California, Berkeley.

- Colajanni P and Papaia M, (1995), "Seismic response of braced frames with and without friction dampers", *Engineering Structures*, 17(2), 129-140.

- Constantinou M C, Tsopelas P, Hammel W and Sigaher A N, (2001), "Toggle-brace-damper seismic energy dissipations systems", *Journal of Structural Engineering*, 127(2), 105-112.

- Crisfield M A, (1981), "Fast incremental iteration solution procedure that handle snap through", *Computer with Structures*, 13, 55-62.

- Darby A P, Blakeborough A and Williams M S, (1999), "Real time substructure tests using a hydraulic actuator", *Journal of Engineering Mechanics*, 125(10), 1133-1139.

- Darby A P, (2001), "Energy dissipation and ductility of filled rectangular hollow steel sections", *http://www.bath.ac.uk/ace/people/darby.html*, (December 2001).

- Daali M L and Korol R M, (1995), "Adequate ductility in steel beams under earthquake loading", *Engineering Structures*, 18(2), 179-189.

- Eberhard M O and Sozen M A, (1993), "Behavior-Based Method to Determine Design Shear in Earthquake-Resistant Walls", *Journal of the Structural Division*, American Society of Civil Engineers, New York, 119(2), 619–640.

- ECCS, (1984), "The residual stress distribution", *Technical Report*, Technical Committee 8, European Convention for Constructional Steelwork.

- ECCS, (1986), "Recommended Testing Procedure for assessing the behaviour of structural Steel Elements under Cyclic Loads", *Technical Report N°45 (First Edition)*, Technical Committee of the European Convention for Constructional Steelwork.

- Ehrgott R C and Masri F. (1993), "Structural control applications of an electrorheological device", *Proceedings of the International Workshop on Structural Control*, 115-129.

- Engelhard M D and Sabol A S, (1998), " Reinforcing of steel moment connections with cover plates: benefit and limitation", *Engineering Structures*, 20(4-6) 510-520.

- ENV, (1996), "Design values of actions", British Standards Institution, BSI, London.

- EPSRC Engineering Instrument Pool, Rutherford Appleton Laboratory, Didcot, Oxon, OX110QX, UK, *http://www.eip.rl.ac.uk*, (June 2001).

- Eurocode-3, (1993), "Design of steel buildings", The Steel Construction Institute, Silwood park Ascot, Berkshire SL5 7QN, UK.

- Eurocode-8, (1998), "Earthquake resistant design of structures", *Second Draft*, The Steel Construction Institute, Silwood park Ascot, Berkshire SL5 7QN, UK.

- Eurocode-8, (2001), "Design of structures for earthquake resistance", *Third Draft*, European Committee for Standardization, Central Secretariat, rue de Stassart 36, B1050 Brussels.

- Fajfar P, (2000), "A Non-linear Analysis Method for Performance-Based Seismic Design", *Earthquake Spectra*, 16(3), 573-592.

- Fajfar P, (1999), "Capacity spectrum method based on inelastic spectra", *Earthquake Engineering and Structural Dynamics*, 28, 979-993.

- Fajfar P, (1992), "Equivalent ductility factors, taking into account low-cycle fatigue", *Earthquake Engineering and Structural Dynamics*, 21, 837-848.

- Fajfar P and Fischinger M, (1988), "N2--A Method for Non-Linear Seismic Analysis of Regular Structures", *Proceedings of the Ninth World Conference on Earthquake Engineering*, Tokyo-Kyoto, Japan.

- FEMA, (1997), "FEMA 273: Guidelines for the seismic rehabilitation of buildings", Federal Emergency Management Agency, Washington DC.

- FEMA, (2000), "FEMA 356: Seismic Rehabilitation of Buildings", Federal Emergency Management Agency, Washington DC.
- FEMA, http:\\www.fema.gov, Federal Emergency Management Agency, (July, 2002).
- Filiatrault A and Cherry S, (1988), "Seismic Design of Friction Damped Steel Plane Frames by Energy Methods", *Report N° UBC-EERL-88-01*, Earthquake Engineering and Research Laboratory, Civil Engineering Department, University of British Columbia, Vancouver, Canada.
- Filiatrault A and Cherry S, (1990), "Seismic Design Spectra for Friction Damped Structures", *Journal of Structural Engineering*, 116(5), 1334-1355.
- Filiatrault A, Tremblay R and Kar R, (2000), "Performance evaluation of friction spring seismic damper", *Journal of Structural Engineering*, 126(4), 491-499.
- Fiero E, Perry C, Sedarat H and Scholl R, (1993), "Seismic Retrofit in San Francisco Using Energy Dissipation Devices", *Earthquake Spectra*, 9(3).
- Freeman S A, (1978), "Prediction of response of concrete buildings to severe earthquake motion", *Publication SP-55*, American Concrete Institute.
- Freeman S A, (1998), "Development and use of capacity spectrum method", *Proceedings of 6^{th} U.S. National Conference on Earthquake Engineering*, Seattle.
- Frey F, (1993), "Mecanique des structures II", *Swiss Federal Institute of Technology Press*, Lausanne, Switzerland.
- Gasparini D A and Vanmarcke E H, (1976), "SIMQKE: A program for artificial motion generation; user's manual and documentation", *Report n° 2*, Department of civil Engineering, Massachusetts Institute of Technology, Cambridge, Massachusetts.
- Gavin H A M, Alhan C and Oka N, (2001), "Fault Tolerance of Semi-Active Seismic Isolation", *Technical Report*, Department of Civil and Environmental Engineering, Duke University, Durham, North Carolina.
- Gebhart B, (1993), "Heat conduction and mass diffusion", *McGraw-Hill*, London.

- Giacchetti R, Whittaker A S, Bertero V V and Aktan H M, (1989), "Seismic Response of a building retrofitted with friction slip devices", *Proceedings of the First International Meeting on Base Isolation and Passive Energy Dissipation*, Assisi, Italy.

- Graesser E J and Cozzarelli F A, (1991), "Shape Memory Alloys as New Materials for Aseismic Isolation", *Journal of Engineering Mechanics*, 117(11).

- Hodgson D E, (1988), "Using Shape Memory Alloys", Shape Memory Applications, Inc., Sunnyvale, California.

- Holmes W T and Sommer P, (1996), " Northridge earthquake of January 17, 1994", *Reconnaissance Report*, Earthquake Research Institute, Oakland CA.

- Hjelmstad K D and Popov E P, (1983), "Cyclic behaviour and design of link beams", *Journal of Structural Engineering*, 109(10).

- Inoue T, (1996), "Analysis of plastic buckling of steel plates in shear based on the Tresca yield criterion", *International Journal of Solids and Structures*, 33(26), 3903-3923.

- Johnson E A, Ramallo J C, Spencer B F and Sain M K, (1998), "Intelligent Base Isolation Systems", *Proceedings of the Second World Conference on Structural Control*, Kyoto, Japan, June 28 – July 1, 1998.

- Kalyanaraman V, Mahadevan K and Thairani V, (1998), "Core loaded earthquake resistant bracing system", *Journal of Constructional Steel Research*, 46(1-3), 437-439.

- Kappos A J, (1999), "Evaluation of behaviour factors on the basis of ductility and overstrength studies", *Engineering Structures*, 21, 823-835.

- Kasai K and Popov E P, (1986), "General behaviour of steel shear link beams", *Journal of Structural Engineering*, 112(2), 362-386.

- Krawinkler H and Seneviratna G D P K, (1998), "Prons and cons of a pushover analysis for seismic performance evaluation", *Journal of Structural Engineering*, 20(4-6), 452-464.

- Krawinkler H and Nassar A A, (1992), "Seismic design based on ductility and cumulative damage demand and capacities", in "Non-linear seismic analysis and design of reinforced concrete buildings", Fajfar P and Krawinkler H (Eds.), Elsevier, New York.

- Lo D S K and Stiemer S F, (1995), "A practical method for incorporating flexible connections in plane frame analysis", *Canadian Journal of Civil Engineering*, 22, 871-882.

- Malhotra P K, (1998), "Seismic strengthening of liquid-storage Tanks with Energy dissipating anchors", *Journal of Structural Engineering*, 124(4).

- Manhaeim D N and Popov E P, (1983), "Plastic shear hinges in steel frames", *Journal of Structural Engineering*, 109(10).

- Marias K, Behrenbruch C P, Brady M, Parbhoo S and Seilalian A M, (2000), "Non-rigid registration of temporal mammogram pairs via a combination of boundary and internal landmarks", *Proceedings of the International Workshop on Digital Mammography (IWDM)*.

- Miller D K, (1998), "Lesson learned from the Northridge earthquake", *Engineering Structures*, 20(4-6), 249-260.

- Miranda E, (2000), "Inelastic displacement ratios for structures on firm sites", *Journal of Structural Engineering*, 126(10), 1150-1159.

- Miranda E, (1999), "Approximate seismic lateral deformation demands in multi-storey buildings", *Journal of Structural Engineering*, 125(4), 417-425.

- Miranda E, (1993), "Evaluation of site-dependent inelastic seismic design spectra", *Journal of Structural Engineering*, 119, 1319-38.

- Mofid M and Peyman K, (2000), "Non-linear analysis of disposable knee bracing", *Computers and Structures*, 75, 65-72.

- Moghaddam H A and Estekanchi H E, (1999), "Seismic behaviour of offcentre bracing systems", *Journal of Constructional Steel Research*, 51, 177–196.

• NonLinPro, (1997), "NonLinPro user's manual", Advanced Structural Concepts, Golden, CO.

• Ove Arup and Partners, (1999), "Design Procedures for buildings incorporating hysteretic damping devices", *Proceedings of the 68th Annual Convention*, Santa Barbara, California, Structural Engineers Association of California.

• Pall A S and Marsch C, (1982), "Response of friction damped braced frames", *Journal of Structural Division*, ASCE, 108(ST6), 1313-1322.

• Pan C-L, Wu S and Yu W-Y, (2001), " Strain rate and aging effect on the mechanical properties of sheet steels", *Thin-Walled Structures*, 39, 429-444.

• Papadrakakis M, Lagaros N D and Plevris V, (2000), "Optimum design of structures under seismic loading", *Proceedings of the European Congress on Computational Methods in Applied Science and Engineering*, (ECCOMAS 2000), Barcelona, 11-14 September 2000.

• Park Y J and Ang A, (1985), "Mechanistic seismic damage model for reinforced concrete", *Journal of Structural Engineering*, 111(4), 722-739.

• Plumier A, Dexter J D, Fisher J W, Frank K H, Kaufmann E J, Krawinkler H, Leon R T, Miller D K, Popov E P and Tsai K C, (Eds), (1997), "Metallurgy, Fracture Mechanics, Welding, Moment connections and frame systems behaviour", *Report N° SAC-95-09*, FEMA.

• Plumier A, (2000), "General report on ductility", *Journal of Constructional Steel Research*, 55(1-3), 91-107.

• Popov E P, Yang T s and Chang S P, (1998), "Design of steel MRF connections before and after 1994 Northridge earthquake", *Engineering Structures*, 20(12), 1030-1038.

• Povov E P, Balan T A and Yang T S, (1998), "Post-Northridge Earthquake seismic steel moment connections", *Earthquake spectra*, 14(4), 659-677.

• Porter D M, Rockey K C and Evans H R, (1975), "Collapse behaviour of plate girders loaded in shear", *Structural Engineer*, 53(8), 313-325.

- Prakash V, Powell G H and Campell S, (1998), "Drain-2Dx: base program description and user guide, *Report N° UCB/SEMM-93/17*, University of California, Berkley.

- Ramadan T and Ghobarah A, (1995), "Behaviour of bolted link-column joints in eccentrically braced frames", *Canadian Journal of Civil Engineering*, 22, 745-754.

- Ramm E, (1981), "Strategies for tracing the non-linear response near limits points", *Non-linear Finite Element Analysis in Structural Mechanics*, Spring-Verlag, Berlin.

- Ricles J M and Popov E P, (1994), "Inelastic link element for EBF seismic analysis", *Journal of structural Engineering*, 120(2), 441-463.

- Romeo R and Pugliese A, (2000), "Seismicity, seismotectonics and seismic hazard of Italy", *Engineering Geology*, 55, 241-266.

- RS Components Ltd, Birchington Road, Corby, Northants, NN179RS, UK, *http://rswww.com*, (June 2001).

- Sam M-T, Balendra T and Lee C-Y, (1995), "Earthquake resistant steel frames with energy dissipating knee elements", *Engineering Structures*, 17, 334-344.

- Santosa S, Banhart J and Wierzbicki T, (2000), "Bending crush resistance of partially foam-filled sections", *Advanced Engineering Materials*, 2(4), 223-227.

- Sasaki K, (1989), "Experimental Evaluation of Nitinol for Energy Dissipating Devices", *Report UCB/SEMM-89/20*, Department of Civil Engineering, University of California, Berkeley.

- Shen J, Kitjasateanphun T and Srivanich W, (2000), "Seismic performance of steel moment frames with reduced beam sections", *Engineering Structures*, 22, 968-983.

- Shukla A K and Datta T K, (1999), "Optimal use of visco-elastic dampers in building frame for seismic force", *Journal of Structural Engineering*, 125(4), 401-409.

- Symans M D and Constantinou M C, (1998), "Semi-active control systems for seismic protection of structures: a state-of-the-art review", *Engineering Structures*, 21, 469-487.

- SZS C5 (1992), "Schweizerische Zentralstelle für Stahlbau", Stahlbau Tabellen, Seefeldstrasse 2, 8034 Zürich, Switzerland.

- Tehranizadeh M, (2001), "Passive energy dissipation device for typical steel frame building in Iran", *Engineering Structures*, 23, 643–655.

- Tsai K C, Wu S and -Popov E P, (1995), "Experimental performance of seismic steel moment beam column joints", *Journal of Structural Engineering*, 121(6), 925-931.

- Tsai K C, Chen H W Hong C P and Su Y F, (1993), "Design of steel triangular plate energy absorbers for seismic-resistant construction", *Earthquake Spectra*, 9(3), 505-528.

- Usami T and Kumar S, (1998), "Inelastic seismic design verification method for steel bridge piers using a damage index based hysteretic model", *Engineering Structures*, 20(4-6), 472-480.

- Vanmarcke E H, (1976), "Structural Response to Earthquakes", Edited by Lomitz C and Rosenblueth E, published by Elsevier Publishing Co, Amsterdam.

- Vidic T, Fajfar P and Fischinger M, (1994), "Consistent inelastic design spectra: strength and displacement", *Earthquake Engineering & Structural Dynamics*, 23, 507-521.

- Villaverde R, (1999), "Aseismic roof isolation system: Analytic and shake table studies", *Earthquake Engineering & Structural Dynamics*, 28, 217-234.

- Whittaker A S, Constantinou M and Tsopelas P, (1998), "Displacement estimate for performance based seismic design", *Journal of Structural Engineering*, 124(8), 905-911.

- Whittaker A S, Bertero V V, Thompson C L and Alonso L J, (1991), "Seismic Testing of Steel Plate Energy Dissipation Devices", *Earthquake Spectra*, 7(4).

- Witting P R and Cozzarelli F A, (1992), "Shape Memory Structural Dampers: Material Properties, Design and Seismic Testing", *Report NCEER-92-0013*, State University of New York, Buffalo.

- Xu Y L and Zhang W S. (2001). "Modal analysis and seismic response of steel frames with connection dampers", *Engineering Structures*, 23, 385-396.

- Zahrai S M and Bruneau M, (1999). "Cyclic testing of ductile end diaphragms for slab-on-girder steel bridge", *Journal of Structural Engineering*, 125(9), 987-996.

Bibliography

- Bachmann H, (1995), "Vibration Problems in Structures, Practical Guidelines", Birkhäuser Verlag Basel.

- Booth E, (1998), "Earthquake engineering in the 1990s: achievements, concern and future directions", *Proceeding Institution of Civil Engineers Structures and Buildings, 128, 154-166.*

- Bilham R, Rundle E, Klein J F and Turcotte D, (1995), "Global Fatalities in the Past 2000 s: Prognosis for the Next 30. In Reduction and Predictability of Natural Disasters", *Internal Report*, Santa Fe Institute Studies in the Sciences of Complexity.

- Building Seismic Safety Council, (1997), "NEHRP Recommended Provisions for the Development of Seismic Regulations for New Buildings and Other Structures", FEMA, Washington DC.

- Clough R W and Penzien J, (1979), "Dynamics of Structures (Seismological background, deterministic analysis of earthquake response)", McGraw-Hill.

- Gioncu V, (2000), "Framed structures. Ductility and seismic response. General Report", *Journal of Constructional Steel Research*, 55(1-4), 125-154.

- ISE, (2000), "Seismic design of bridges", Conference Proceedings, Institution of Structural Engineers, 11 Upper Belgrave Street, London SWX 8BH, with the participation of the Institution of Structural Engineers SECED, French Association for Earthquake Engineering, l'Ecole Nationale des Ponts et Chaussees & the American Concrete Institute.

- Key D, (1988), "Earthquake design practices for buildings", Thomas Telford.

- Mazzolani F M and Piluso V, (1999), "Theory and design of seismic resistant steel frames", Spon London.
- Murr L E, Staudhammer K P and Meyer M A, (1986), "Metallurgical applications of shock-wave and high-strain rate phenomena", Marcel Dekker INC, New York.
- Nethercot D A, (2000), "Frame structures: global performance, static and stability behaviour. General report", *Journal of Constructional Steel Research*, 55, 109-124.
- Robson D, (1999), "Finite Element Assessment of Connections and Bracing System for Structural Design", *Project Work Report D2461*, Oxford University Civil Engineering.
- Rosenblueth E, (1980), "Design of earthquake resistant structures", Pentech Press, London.
- SCI, (1992), "Steel Designer's Manual", Fifth Edition, The Steel Construction Institute, Silwood park Ascot, Berkshire SL5 7QN, UK.
- SIA, (1996), "Dynamische Probleme bei Bruecken und Hochbau" (Dynamic problems in bridges and buildings), SIA D0138 Switzerland.
- Skinner R J, (1993), "An introduction to seismic isolation", Wiley Chichester.
- Suresh S, (1998), "Fatigue of material", Second Edition, Cambridge University Press.
- Warburton G B, (1976), "The dynamical behaviour of structures", Second Edition, Pergamon Press, Oxford.
- Williams M S and Todd J D, (2000), " Structures; theory and analysis", Macmillan Press London.

Software

- ABAQUS, Version 5.8 and Version 6.2, Hibitt, Karlsson & Sorensen, INC.
- Drain-2DX, Version 1.1, University of California, Berkley.
- HP-VEE, Hewlett-Packard Company.
- I-DEAS, Version 6, Structural Dynamics Research Corporation.
- IRWIN PRO 2.0, Flir Systems AB, Rinkebyvägen 19, SE-182 11 Danderyd, Sweden
- MATLAB, Version 5.2 and Version 6 Release 12, Mathworks, INC.
- NonLinPro, Version 2.18, Advanced Structural Concepts, Golden, CO.
- PROKON, Version 1.6, Prokon Software Consultant Ltd.
- SIMQKE-I, NISEE Computer Application.